

DISSERTATION

DEVELOPMENT OF A MULTIDISCIPLINARY TOOLKIT FOR THE COLLOIDAL  
NANOPARTICLE SYNTHESIS OF COPPER SELENOPHOSPHATE,  $\text{Cu}_3\text{PSe}_4$ , A  
PROMISING MATERIAL FOR PHOTOVOLTAICS

Submitted by

Jennifer M. Lee

Department of Chemistry

In partial fulfillment of the requirements

For the Degree of Doctor of Philosophy

Colorado State University

Fort Collins, Colorado

Spring 2021

Doctoral Committee:

Advisor: Amy L. Prieto

Chris J. Ackerson

Chuck S. Henry

Kristen S. Buchanon

Copyright by Jennifer Minkyung Lee

All Rights Reserved

## ABSTRACT

### DEVELOPMENT OF A MULTIDISPLINARY TOOLKIT FOR THE COLLOIDAL NANOPARTICLE SYNTHESIS OF COPPER SELENOPHOSPHATE, $\text{Cu}_3\text{PSe}_4$ , A PROMISING MATERIAL FOR PHOTOVOLTAICS

Colloidal nanoparticle (NP) synthesis is a toolkit to expand the accessible phase space of semiconductor materials. As the demand increases for materials with coveted physical properties that enable advances in applications such as energy conversion and storage, an increase in the diversity of materials to meet these applications is required. Strategies to tune the complexity of the material include composition, stoichiometry, and morphology. Ternary copper-based chalcogenide nanoparticles have been an area of intense focus due to their application as photovoltaic absorbers and their non-toxic, earth-abundant composition. By virtue of its solution-based regime, colloidal nanoparticle synthesis provides a method to expand the phase space accessible to semiconductor materials. However, multinary nanoparticles syntheses are quite complex due to their hybrid composition (i.e. inorganic core/organic surface ligands) and unique chemical composition (i.e. materials with bonds anomalous to the hard-soft acid-base principle), introducing synthetic challenges arising from the diversity of species and interactions. The reaction system is dependent on the reaction as a whole and not as a summation of individual components, and characterization of only the final product overlooks this inherent complexity. Thus, all species and interactions, including organic, organometallic, inorganic, and solid-state, must be considered to control the speciation toward balanced reactivities and advance rational, generalizable syntheses of compositionally complex NPs.

To that effect, we explored and developed a toolkit to access and evaluate complex solid-state materials through colloidal nanoparticle synthesis. Outlined in the introduction (Chapters 1-3) were the strategies employed which include: (1) elucidation and understanding of reaction landscapes to guide rational syntheses, (2) investigation of chalcogenide precursor to monomer transformations and the subsequent impact on reactivity (probing the role of solvent as a starting reagent), and (3) methods and techniques for characterization of all phases and components, including overlooked species such as gaseous or amorphous species.

This research resulted in the first reported colloidal nanoparticle (NP) synthesis of copper selenophosphate,  $\text{Cu}_3\text{PSe}_4$ , a promising photovoltaic material (Chapter 4). The main strategy employed for the directed solution-phase synthesis was the bond installation of P, yielding P-containing binary starting reagents ( $\text{Cu}_3\text{P}$  and  $\text{P}_4\text{Se}_3$ ), to map a synthetic landscape and to overcome the hard-soft acid-base (HSAB) compatible Cu-Se pair. In route to the synthetic design of  $\text{Cu}_3\text{PSe}_4$ , the origin of the Cu-Se impurities was examined by sequential and complimentary use of XRD (crystalline nanoparticle core), XPS (nanoparticle surface), and finally STEM/EDS (elemental composition) to ultimately prevent the formation of these impurities and optimize the synthesis. Rational synthesis of phase-pure  $\text{Cu}_3\text{PSe}_4$  NPs involved the selenization of phase-pure  $\text{Cu}_3\text{P}$  NPs with Se powder in 1-octadecene precursor (Se/ODE). Phase-purity was confirmed via STEM/EDS, XRD, and Rietveld refinement. We also found that product formation was acutely sensitive to the Se precursor and the solvents used. Robust evaluation of failed reactions was key to understanding the final reaction conditions.

Ongoing research focuses on the development and advancement of multidisciplinary characterization methods such as in situ (XRD, ssNMR) and ex situ (XRD,  $^1\text{H}$  NMR, and IR) characterization to observe speciation changes and to elucidate complex reaction schemes and

landscapes in solution-based reactions. The goal is to intersect molecular and material mindsets to inform on how extended materials of unique chemical compositions can be rationally made. This includes the characterization of the precursor to monomer transformation(s), the non-innocent role of solvent, and the gaseous reaction headspace (Chapter 5). In collaboration with Justin P. Joyce (Shores/Rappé groups, CSU), the intermediates and the schemes by which they are formed and subsequently delivered were modeled. Specifically, we considered the role of chalcogen bonding between experimentally identified dialkyl selenide monomer and nucleophilic  $\text{Cu}_3\text{P}$  toward the formation of P-Se bonds within the  $[\text{PSe}_4]^{3-}$  tetrahedral structure. Further, collaborations with the Neilson group at CSU and the Hu group at FSU were established to collect in situ diffraction and in situ solid state  $^{31}\text{P}$  NMR data, respectively, of the solution-based ternary nanoparticle synthesis (Chapter 6). This required development and optimization of a capillary preparation for solution-based reactions that could withstand high temperatures and remain under inert conditions.

Through the use of  $\text{Cu}_3\text{PSe}_4$  as a case study, a preliminary toolkit with general strategies and considerations for the synthesis of analogous materials was built. A diverse landscape was mapped, and a plethora of opportunities were inspired (Chapter 7). Future work could focus on the refinement or expansion of these strategies and the development of a criterion to screen what materials could be synthesized by these methods. For example, the dual Lewis acidic and basic classifications of chalcogenide monomers could be exploited to rationalize an electronically complementary precursor and template bonds between the two species. Refinement of this idea would effectively expand HSAB principles which could contribute to the rationalization of nanoparticle syntheses with complex and unique compositions. Expansion of strategies could include the implementation of a new synthetic knob such as photoinitiation in which nanoparticle syntheses are performed under light as opposed to heat. This could offer the opportunity to target

metastable phases as opposed to thermodynamic phases which are often favored under elevated temperatures. Alternatively, future work could investigate material properties through iterative characterization and synthetic optimization to implement  $\text{Cu}_3\text{PSe}_4$  NPs into devices. The specific aim would be to gain fundamental chemistry understanding of how a material performs to make systematic device improvements.

Ultimately, our goal is to contribute to the evolution of how the nanoparticle synthesis community designs novel syntheses, focusing on building and developing processes as opposed to continued trial-and-error or sole focus on device applications. Not only can we come up with better ways to understand and characterize materials, we can also come up with better ways to make materials. I hope to inspire new directions and perspectives on a toolkit for colloidal nanoparticles, and I hope that any of these pursuits challenge and expand the knowledge of the NP community.

## ACKNOWLEDGEMENTS

First and foremost, I am grateful for my partner Max. He was my punching bag but never took my shit. He challenges me intellectually and emotionally, and even after all of these years together, I still manage to learn new things about him. Max is a true companion in every capacity. This past year was frenzied and nothing went as planned, but I had Max and that made all the difference. Thank you for being the reason that I always have something to look forward to. Thank you for letting me grow old with you.

I am my inspiration, but I would never have the confidence to announce it proudly if it weren't for the unrelenting support of my family and friends. What I was uniquely capable of through my parents' teachings and culture were passion, grit, and survival. My parents reminded me of the good when I focused on the bad, that my creativity would set me apart from the ignorant people that I would always inevitably face, and that my hard work would amount to not just something but something significant and valuable. To my brother Andrew who provides excellent company. Thank you for teaching uhm mah and ah bbah to Zoom. To everyone in my knitting, drunk baking, game night, brunch, traveling, hiking, skiing, adventuring, Mishawaka/Red Rocks/concerts, political activism, virtual hangouts, booze writing, Bobs/Road/Marmot/Ramskellar/Mayor/MCHC/Bar (RIP), let's-end-the-night-at-Steakout, my-afternoon-isn't-going-well-let's-play-hooky crews and bandits, thank you! Special shout-out to Justin for all the science discussions over too many beers. Thank you for not taking orientation seriously with me and letting me latch onto you when I had no understanding of group theory, solid-state, or even inorganic chemistry. To Kim, my soonduboo. I'm so grateful that we can talk about anything, relate to one another, and that you're always down. All of our happy hours and

Friday the 13<sup>th</sup> experiences. We're so hardcore. To Eve, my adventure buddy without whom I wouldn't have discovered a love for skiing or backpacking. Thank you for always answering my arguably dumb solid-state questions. To Lily, my lab mate without whom I would not have survived our group. Thank you for letting me talk your ear off and fixing my horrible drafts. To Hailey, who surprises me endlessly with her many talents. Thank you for making me laugh with your sassy remarks and always answering my organic questions in my favor. To Chris, my writing partner who kept me accountable. Thank you for serendipitously finding me at the exact moments I needed a coffee break and offering company. To Annalise, Jaz, Leslie, and Angela, my ladies who I could always depend on. Thank you for always being down to drink, hang out, adventure, and answer my questions. To Joe and Ryan, thank you for staying in CO and always understanding and looking out for me. I appreciate you all so much. I initially arrived at graduate school with the intention of a reality show contestant, "I didn't come here to make friends, I came here to win." To win was to meet you and share these incredible experiences with.

A career in chemistry would not be possible without the wonderful and fantastic guidance of the gracious mentors I auspiciously met along the progression of my career. People who I looked up to, who intimidated me with their excellence. People who taught me all the diverse aspects on how to be and what it means to be a scientist. People who provided unconditional support and saw potential in me when I didn't see it for myself. To Yugang and Steve, who gave me my first break in advanced research as an undergraduate even though I didn't have much direction. Their mentorship created a confidence in my chemistry ability, especially when I felt like an imposter. Yugang taught me synthesis and a passion for making things, what it actually means to work hard, how to rationalize methods, and how to be a good lab mate. He always knew exactly what to say and continued to root me on even though I couldn't fathom how I could possibly initiate the

daunting task of independent research. Long days and nights in lab without any judgement if I didn't know the right answer or if I didn't feel like coming in because I was too hungover to work. Thank you for instilling a passion for chemistry and always pushing me to be ambitious. Thank you to Nancy Levinger for uplifting me no matter the situation. I will cherish our late night Bawarchi dinners as we graded exams. A conversation with you is honest, a rarity these days. Last but not least, thank you to Amy. Amy was more than my advisor or my boss, she was also my mentor and in a lot of ways my friend. Her type of leadership and teaching was something I always strived for. I learned clear communication and how to pursue rigorous chemistry. Amy taught me to say what I mean, that the intent had to align with what was actually written or spoken. She was there when I needed a shoulder to lean on but also knew how to push me to get my shit together. Amy's method of motivating me was subtle, which was exactly what I needed when anything and everything sent me over the edge. She never told me I did a good job if she didn't mean it, so I worked my ass off to make sure what I accomplished deserved a wholehearted and earnest "nice job." Thank you for taking me into your group, taking a chance on me, and showing me an unparalleled kindness. Thank you to all my mentors. I don't necessarily do well with authority and prefer to pave my own route, even if it means making mistakes. The mentorship of these extraordinary people taught me that not only was it okay to ask for help, but that it should be encouraged. No innovation or enterprising pursuit happens without a team.

My career would not be possible without those who I've acknowledged. This experience taught me to be bold and to be radical. A go-getter and ambitious. To be unabashedly myself, even though I struggled with imposter's syndrome, haters, and doubters. So much bureaucracy, so much bullshit. Even so, I learned to tackle problems creatively and excelled with a little help from all those I acknowledged. I humbly leave here knowing less than when I started.

## TABLE OF CONTENTS

ABSTRACT.....	ii
ACKNOWLEDGEMENTS.....	vi
CHAPTER 1. GENERAL CONSIDERATIONS TO ENABLE RATIONAL SOLUTION-BASED SYNTHESIS OF COVETED MULTINARY SEMICONDUCTOR NANOPARTICLE (NP) MATERIALS.....	1
1.1. Introduction.....	1
1.2. Defining the Thermodynamics Versus Kinetics (TvK) Problem .....	7
1.3. Reaction Pathway Studies in Traditional Solid-State Chemistry .....	10
1.4. Non-Classical Nucleation: Additional Considerations NP Syntheses.....	13
1.5. Reaction Pathway Studies for NP Syntheses: From Brute Force to Elegant Approaches .....	15
1.6. Perspective .....	21
REFERENCES .....	23
CHAPTER 2. INVESTIGATING THE FORMATION OF CHALCOGENIDE SPECIES AND THEIR ROLES IN NANOPARTICLE (NP) SYNTHESSES TO INFORM ON REACTION MECHANISMS AND PATHWAYS.....	27
2.1. Tertiary Phosphine Chalcogenides: Mechanism of Chalcogen Delivery and Reactivity Trends.....	28
2.2. Diorganyl Dichalcogenides: Reactivity Trends and Extrapolation from Binary to Ternary Systems.....	32
2.3. Alkylamine-chalcogenides: Chalcogen Dissolution and Reduction.....	33
2.4. Multiple Roles of 1-Dodecanethiol (DDT): Sulfur Precursor, Stabilizing Ligand, and Solvent .....	37
2.5. Thiourea and Selenourea: Chemical Decomposition.....	38
2.6. In situ Evolution of Gaseous Chalcogenide Species from Elemental Chalcogen Interaction with 1-Octadecene (ODE) .....	39
2.7. Evolution of Dialkyl Selenide Species from Elemental Selenium Reaction with 1-Octadecene (ODE).....	47
2.8. Perspective .....	48
REFERENCES .....	50
CHAPTER 3. CHARACTERIZATION OF NANOPARTICLE (NP) SYNTHESSES.....	53
3.1. Characterization for Elucidating Reaction Mechanisms.....	53
3.1.1. NMR Spectroscopy: Solution-based, 2D, and Solid-state Techniques.....	54
3.1.2. Infrared (IR) Spectroscopy for Solution Composition and NP Ligand Identification .....	61
3.1.3. Mass Spectrometry to Support the Presence of Reaction Species Interactions.....	65
3.1.4. UV-Vis Spectroscopy .....	66
3.2. Characterization for Elucidating Reaction Pathway .....	68

3.2.1. X-ray Diffraction (XRD) .....	69
3.2.3. Thermal Analysis .....	69
3.2.4. X-ray Photoelectron Spectroscopy and X-ray Absorption Spectroscopy .....	70
3.2.5. Ex Situ Transmission Electron Microscopy (TEM) .....	72
3.3. Prospects in NP Reaction Characterization: Understanding the Complexity of NP Syntheses .....	76
3.3.1. Using Mass Conservation to Rationalize NC Growth via In situ FTIR and UV-Vis Spectroscopies .....	77
3.3.2. In situ Synchrotron X-ray Scattering Studies .....	81
3.3.3. Outlook of In situ X-ray Diffraction for NP Synthesis .....	83
3.4. Characterization Summary and Perspective .....	85
REFERENCES .....	87
CHAPTER 4. DIRECTED ROUTE TO COLLOIDAL NANOPARTICLE SYNTHESIS OF THE COPPER SELENOPHOSPHATE $\text{Cu}_3\text{PSe}_4$ .....	91
4.1. Overview .....	91
4.2. Introduction .....	91
4.3. Results and Discussion .....	93
4.3.1. Investigation of Pathway Route (P-Se) + Cu .....	94
4.3.2. Investigation of Pathway Route (Cu-P) + Se .....	94
4.4. Conclusion and Outlook .....	102
REFERENCES .....	103
CHAPTER 5. MOLECULAR-LEVEL DESIGN PRINCIPLES FOR THE COLLOIDAL NANOPARTICLE SYNTHESIS OF COPPER SELENOPHOSPHATE, $\text{Cu}_3\text{PSe}_4$ : PROBING SELENIUM PRECURSOR EVOLUTION AND DELIVERY .....	105
5.1. Overview .....	105
5.2. Introduction .....	106
5.3. Results and Discussion .....	110
5.3.1. Experimentally Characterized Active Monomer(s) or Species .....	110
5.3.2. Role of Chalcogen Bonding .....	117
5.3.3. Role of Solvent .....	123
5.4. Conclusion and Outlook .....	131
REFERENCES .....	135
CHAPTER 6. IN SITU CHARACTERIZATION SUITE FOR THE REACTION LANDSCAPE ELUCIDATION OF COLLOIDAL COPPER SELENOPHOSPHATE, $\text{Cu}_3\text{PSe}_4$ , NANOPARTICLE (NP) SYNTHESIS .....	139
6.1. Introduction .....	139
6.2. Experimental .....	140
6.3. Materials Characterization .....	142
6.4. Results and Discussion .....	143
6.5. Conclusion and Outlook .....	152
REFERENCES .....	155

CHAPTER 7. OUTLOOK ON THE SYNTHETIC AND CHARACTERIZATION TOOLKITS FOR SOLUTION-BASED NANOPARTICLES (NPs) OF COMPOSITIONAL COMPLEXITY: USING COPPER SELENOPHOSPHATE, $\text{Cu}_3\text{PSe}_4$ , AS A CASE STUDY.....	159
7.1. Introduction.....	159
7.2. Experimental.....	159
7.3. Expansion of a Synthetic Toolkit.....	161
7.4. Computation to Navigate the Interdisciplinary Nature of NP Synthesis.....	172
7.5. Material Properties Exploration as a Feedback Loop for Better NP Syntheses .....	175
7.6. Perspective .....	178
REFERENCES .....	180
APPENDIX A. CHAPTER 4 SUPPORTING INFORMATION.....	186
APPENDIX B. CHAPTER 5 SUPPORTING INFORMATION .....	207
APPENDIX C. DESK MOTIVATION .....	230

## CHAPTER 1

# GENERAL CONSIDERATIONS TO ENABLE RATIONAL SOLUTION-BASED SYNTHESIS OF COVETED MULTINARY SEMICONDUCTOR NANOPARTICLE (NP) MATERIALS<sup>1</sup>

### 1.1. Introduction

There is an urgent need for semiconductors with diverse applications to meet the demands of a technologically driven society.<sup>1-3</sup> While theorists have long predicted useful materials that engender coveted physical properties that enable applications such as energy conversion or energy storage, synthetic guidelines for these materials remain elusive and the feasibility of rationalizing a synthesis for these materials has not been well assessed.<sup>4-10</sup> Traditionally, many of these materials were predicted for the bulk and targeted by solid-state syntheses which often require high temperatures that bypass metastable phases. Although much work is being focused here to develop clever strategies for syntheses,<sup>5,6,11,12</sup> we direct our attention instead to the implementation of colloidal nanoparticle synthesis as a way to target some of these more elusive materials due to the added advantages of the solution-phase.<sup>13-16</sup> The added degrees of freedom from not only the minimization of the diffusion barrier but also the resulting diverse speciation could contribute to the overall entropic stabilization of the reaction system to yield metastable phases.

Colloidal semiconductor nanoparticles possess an inorganic crystalline core stabilized by surface surfactants.<sup>14,15,17-24</sup> Due to their unique hybrid structures, they can simultaneously exploit the useful properties of their bulk counterpart yet maintain industrial applicability because they are

---

<sup>1</sup> This chapter was excerpted and modified from an invited review for the journal's 50<sup>th</sup> anniversary in *J. Solid State Chem.* **2019**, 273, 243-286 by Jennifer M. Lee, Rebecca C. Miller, Lily J. Moloney, and Amy L. Prieto with Jennifer M. Lee and Rebecca C. Miller as equal contribution first authors. All sections from the review were expertly crafted and written collaboratively by all authors and were adapted, expanded, or rewritten into this chapter to encompass ideas presented in this dissertation. To that effect, new sections were also written to highlight exemplary manuscripts not evaluated in the review. All figures not explicitly referenced were created by the authors for the JSSC review.

solution processible. They possess composition-, size-, and shape-dependent optoelectronic properties,<sup>25–28</sup> giving rise to flexible tunability of materials properties. They are often synthesized one of two ways: by hot injection in which precursors are rapidly injected into hot solvent to induce nucleation then a growth stage as the cooled reaction temperature equilibrates back to the original reaction temperature, or by heat-up in which all precursors are present at the start of the reaction and are steadily heated to initiate nucleation and growth.<sup>17,29</sup>

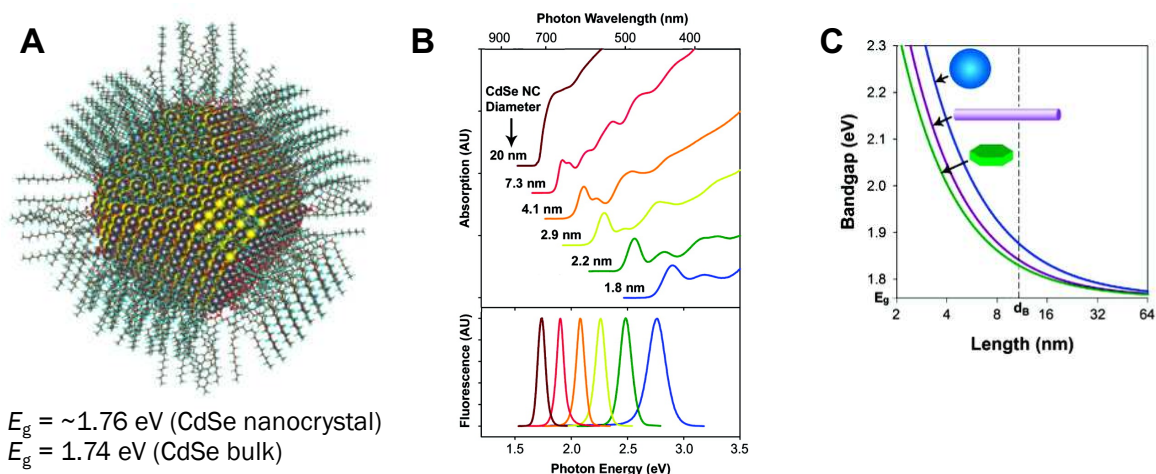


**Figure 1.1.** (A) Calculated atomic surface of a 5 nm diameter nanocrystal (NC) passivated with oleate and hydroxyl ligands. The bandgap ( $E_g$ ) for CdSe NCs are  $\sim 1.76$  eV which is near that of its bulk counterpart (1.74 eV) with the advantage that it can be tuned by shape, size, and morphology. Adapted with permission from ref 24. (B, C) The tunability of the CdSe NC by size and shape, respectively. Adapted with permission from ref. 17.

Over the last thirty years, the nanoparticle community has achieved elegant syntheses owing to the careful work on CdE (E = chalcogenide) systems,<sup>23,30</sup> specifically how the components of a reaction can lead to the composition, size, and morphology of NPs. The field is striving to move past reports of cause and effect in which understanding is extrapolated from characterization of the final products upon tuning the reaction variables and toward identification of reaction pathways which may inform rational planning. Classic examples from the CdE literature over the years show how the evolution of precursors can lead to greater control over the

rate of nucleation and growth as well as how the subtle interplay between closely related structures can lead to control over morphology.<sup>31-33</sup>

However, the models and synthetic strategies built from these systems are not necessarily relevant to systems of increased compositional complexity. It is currently very difficult to predict the results of a targeted reaction product when the roles of ubiquitous reactants are not well understood across different systems. This has often resulted in synthetic strategies for multinary systems that come from a trial-and-error basis with the intent of studying material properties without assessment of the synthesis. While synthetic organic chemists have long developed mechanistic approaches to the synthesis of complex molecules and benefits from a known toolbox of functional groups and their associated reactivities to rationalize the choice of synthetic pathway and enables a retrosynthetic approach, the nanoparticle synthesis community let alone the solid-state synthesis community have not.<sup>5,6</sup> In contrast, a large part of the challenge for understanding NP synthetic strategies and adapting knowledge to new material systems lies in their inherent complexity and diversity of their phase space which inhibits chemists from having a comparable toolbox. These syntheses often rely on empirical knowledge of the crystal chemistry but ultimately lacks a systematic approach that can be extrapolated to the synthesis of new materials.

Common language may also play a role. General terms are sometimes used to imply differing meaning, depending on the context of the study. Thus, we wish to define a few terms we will use in our discussion of NP syntheses and characterization. They are as follows. Note: deconvolution of some of these terms is onerous; however, these descriptions are our best attempt at clarity of speech and meaning.

- “*Nanoparticles (NPs)*” as solid-phase particles with nanoscale dimensions. Specifically, the term nanocrystal (NC) should imply single crystallinity, but the term nanoparticle encompasses a wider range of nanostructures, including those which are polycrystalline.
- “*Precursors*” as the starting compounds for the constituent elements of the final NP
- “*Active species*” or “*Monomers*” as the compounds that undergo nucleation
- “*Precursor Conversion*” for the reaction(s) taking place during the transformation of precursors to active species
- “*Solvent System*” as the non-precursor components of the reaction solution. These are typically high boiling point solvents but could include additive compounds. We won’t use “surfactant” because it implies that this compound necessarily interacts with the surface of the NP, and this isn’t always known.
- “*Bound Ligand*” and “*Free Ligand*” for describing molecular interactions with the NP surface. Bound ligands are at the NP interface whereas free ligands are molecules with potential for being ligated but are solubilized and unattached to NP surfaces.
- “*Reaction Mechanism*” refers to the chemical processes occurring between specific species within the reaction system. In Figure 1.2, this could refer to the chemical equations that describe each of the arrows.
- “*Reaction Pathway*” refers to the route(s) taken by the reaction system from precursors to end products or the evolution of the solid phase components. o “Conversion” pathway refers to the preservation of a solid-state intermediate followed by end product formation via incorporation or expulsion of elemental species. Note: the word “conversion” is also commonly used to describe the transformation of precursors to active species.

- “*Consumption*” pathway refers to the dissolution of a solid state intermediate, providing active monomers in solution, usually at different conditions (temperature, coordination, concentration, etc.) than the conditions during the intermediates’ initial nucleation(s).
- “*Coalescence*” refers to the adhesion and/or merging of two solid state intermediates in solution followed by transformation to the end product.

An added layer of complexity comes from the solvent, our “advantage” over the solid-state community. We are learning more that the role of the solvent is beyond a heat-transfer medium and/or surface-passivating ligand but is dynamic and can additionally participate in the reactivities of different precursors.<sup>33–37</sup> This requires synthetic strategies for the nanoparticle synthesis community to be highly interdisciplinary, requiring not just knowledge of the solid state but also that of molecular organic or inorganic interactions.<sup>6,38–41</sup> In order to start building this toolbox, we must understand all possible routes from precursors to end products.

Presented in Figure 1.2 is a general guide on the processes by which starting materials, intermediates, and final products are formed in NP syntheses. These processes can be highly complex with many important, dynamic components and the possibility for multiple mechanisms and pathways to simultaneously exist. As viewed from left to right, we typically think of NP precursors being introduced into the solvent system and reacting or dissolving to form active species or monomers (the blue-, yellow-, and red-atom containing compounds dissociate from their gray counterions). Moieties from the solvent system may complex the NP constituent element and alter their reactivity, as shown in the circular inset labeled “various monomer-ligand complexes” with purple lightning bolts and light blue trapezoids on the darker blue atoms. Thus, due to dissociation or reaction of precursors and complexation by solvent molecules, the composition of the solvent system may change. Throughout the course of the reaction, these solvent concentrations

are constantly in flux, depicted by the purple, light blue, and gray bar graphs at the bottom of Figure 1.2. The active species may then proceed along various routes which include direct nucleation of the end product or the formation of any number of solid-state intermediates (crystalline or amorphous particles or clusters). Possible intermediates may then transform in different ways: (1) “consumption” as dissolution to produce elemental active species once more (though under different reaction conditions and possibly with different complexation), (2) “conversion” as incorporation of an active species into an intermediate, or (3) “coalescence” as attachment of solid intermediates prior to end product arrangement. The intricacy of this depiction also functions to highlight the convoluted impact each synthetic parameter may have.

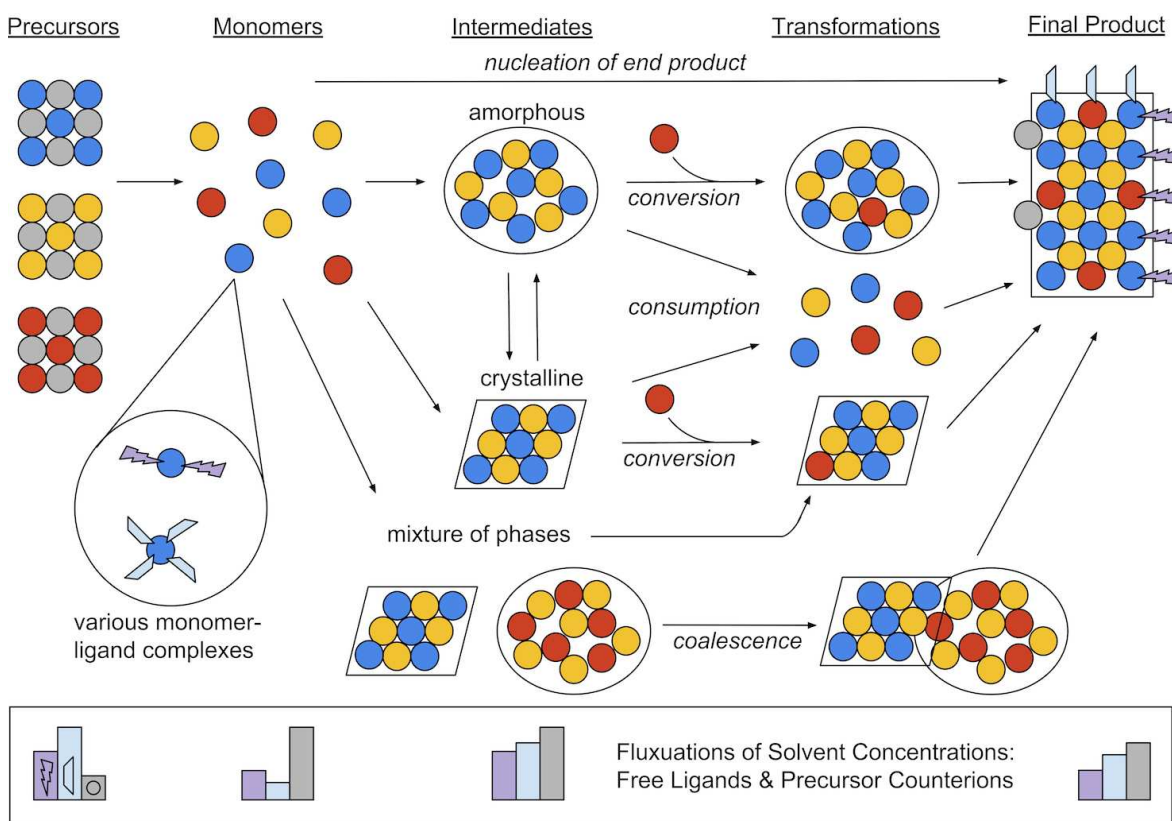


**Figure 1.2.** Potential reaction routes for the transformation of precursors to end NP products. Generally, syntheses follow the evolution of the underlined components but may involve multiple simultaneous processes. Constituent elements are depicted as red, yellow, and blue circles. Solvent molecules capable of complexation (ligands) are depicted in purple lightning bolts and light blue trapezoids. A simplistic description of the solvent system’s dynamic nature is shown in bar graphs at the bottom with exaggerated concentration changes.

Nanoparticle syntheses are inherently quite complex. Thus, studies exploring the full reaction landscape through a complete understanding of the synthesis techniques involved, how they work, and what limits they have should subsequently widen the available qualitative kinetic and thermodynamic knowledge of a material system. The reaction pathways can then be directed to access lower energy routes to desired phases, trap metastable phases, and attain novel products. Further, this knowledge can elucidate possible synthetic strategies for other systems, and as more reaction pathways are explored, patterns across systems could be revealed and may pave a more universal understanding of materials synthesis, building strategies toward a nanoparticle synthesis-by-design toolkit.

Reaction pathway studies are traditionally explored for bulk solid-state syntheses to understand the rate-limiting step, the diffusion of components, and finally the formation of the desired phase.<sup>6,11</sup> Although bulk solid-state synthesis and solution-based NP synthesis differ in many ways, the desire to gain fundamental reaction pathway insights to enable greater control over materials design exists in both fields. Here we draw parallels from bulk solid-state pathway studies with a non-exhaustive compilation of solution-based NP studies. These solution-based NP studies demonstrate the excitement but also difficulty in exploring reaction pathways due to the involvement of coinciding concepts drawn from different fields: solid-state chemistry, inorganic chemistry, coordination chemistry, and synthetic organic chemistry. We hope to highlight exemplary studies that demonstrate the evolution of thoughtful reaction pathway studies as a strategy for targeted synthesis and showcase where the field can further advance.

## **1.2. Defining the Thermodynamics Versus Kinetics (TvK) Problem**

Reaction pathways are often defined by thermodynamic- or kinetic-control.<sup>5,8,11,42–45</sup> The goal of understanding thermodynamics and kinetics is to provide rational predictions. Lacking one

branch means there is missing predictive power. Reactions that occur under thermodynamic control often have higher activation barriers and yield the products that are the most stable at thermodynamic equilibrium, achieved by sufficiently high reaction temperature and reaction time. To increase product yield, conditions can be tuned to destabilize the starting materials and/or stabilize the product. Alternatively, a reaction may proceed under kinetic control if the activation energy can be lowered, thus, the product that forms the fastest may be stabilized despite not being the lowest-energy configuration in the system. When studying a kinetically controlled reaction, the rate-limiting step and the transition state therein must be understood. Thus, creating new pathways and manipulating the interactions at the intermediate states are more important than stabilization of the products. To increase yield, the temperature could be lowered just enough for the reaction to proceed, then the product can be isolated immediately upon completion so that the competitive and reverse reaction is suppressed.

A third pathway was defined by Chamarro et al. for the formation of metastable products.<sup>5</sup> Known as thermo-kinetic coupling, the stability of a metastable product is enforced by coupling the pathway to the formation of a stable byproduct with a low enthalpy of formation (Figure 1.3).

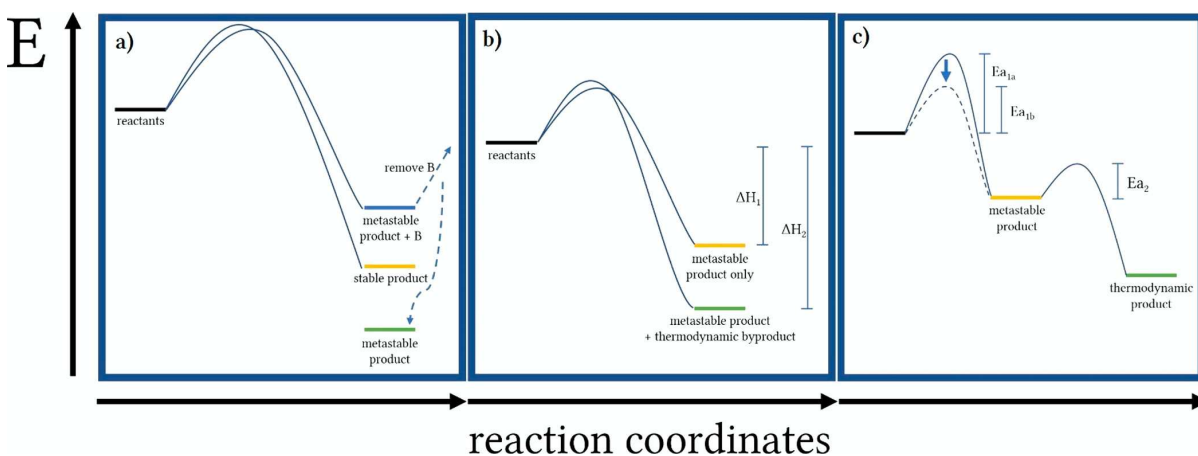


**Figure 1.3.** (a) Exploitation of LeChatlier's principle to stabilize metastable phases (thermodynamic control). (b) Thermo-kinetic coupling reaction pathway. (c) Trapping the metastable phase by lowering the activation energy of its formation (kinetic control). Reprinted with permission from ref 5. Copyright 2018 American Chemical Society.

For example, the underlying driving force in metathesis reactions to yield a metastable product is the simultaneous formation of a thermodynamically stable salt. However, the authors caution that a pathway is not necessarily kinetic just because a metastable product is formed. Metastable products can be realized by exploitation of LeChatlier's principle, maintaining a nonequilibrium condition throughout the reaction by removing the products as they are formed.

Moreover, metastable products can be formed due to the stabilization by external parameters such as temperature or pressure, known as kinetic trapping (Figure 1.4).<sup>11</sup> True kinetic control of reactivity requires a catalyst or lowered diffusion which decreases the activation barrier. Typically, true kinetic products do not persist for long times even when the conditions in which they are stable are held as constant as possible. A simple experiment, then, to test thermodynamic- vs kinetic-control is to subject the product to the conditions in which it was synthesized for extended periods of time.

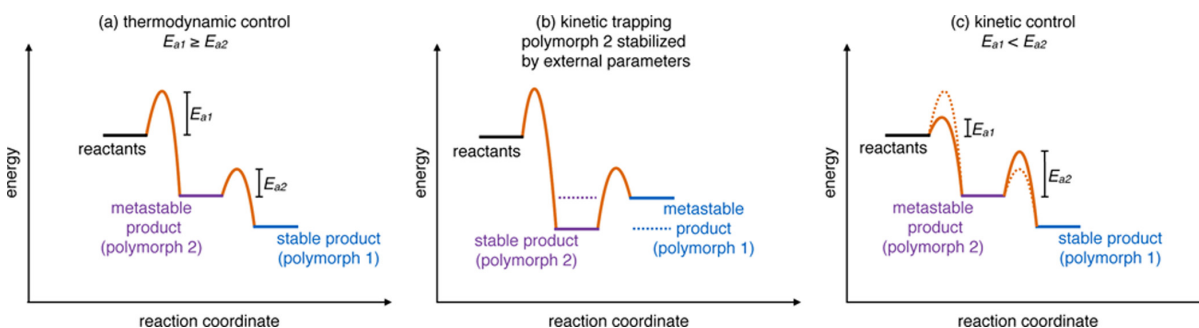


**Figure 1.4.** (a) Thermodynamic, (b) kinetic-trapping, and (c) kinetic reaction pathways. Reprinted with permission from ref 11. Copyright 2017 American Chemical Society.

The distinction between thermodynamic- versus kinetic-control are clear for well-defined pathways with full deconvolution of intermediate speciation. However, this is not the case in complex multinary or multicomponent nanoparticle systems in which even the solution plays a dynamic role. Such convolutions include precursor to monomer transformation, the existence of multiple, simultaneous, yet energetically different intermediates, and competitive formation of

multiple products (Figure 1.2).<sup>7,46</sup> Many of these studies do exist but are often for homonuclear NPs.<sup>47,48</sup> Despite the use of only one element, these systems are, in fact, quite complex and require rigorous studies over extended periods of times to elucidate reaction pathways and mechanisms. Although a nontrivial task, we believe the field can be evolved to incorporate more complex systems. However, we must be mindful over how the terms thermodynamics and kinetics are used for more complex systems. Often, these terms are used carelessly to describe the growth of NPs such as “formation kinetics” and is especially worse for complex NP syntheses which could have multiple simultaneous reaction pathways. We must make sure that when we use these terms, we provide robust characterization and define the route we are probing. We can first look towards the solid state community as a foundation then build up towards the goal of synthesis by design.<sup>6</sup>

### 1.3. Reaction Pathway Studies in Traditional Solid-State Chemistry

Jiang et al. demonstrated the importance of reaction pathway studies to expedite the synthesis of  $\text{Fe}_2\text{SiS}_4$ .<sup>49</sup> Key limitations of the  $\text{Fe}_2\text{SiS}_4$  synthesis from the elements were resolved via in situ XRD. As the reaction proceeded, Fe-S binaries ( $\text{Fe}_{1-x}\text{S}$ ,  $\text{FeS}_2$ ) formed up to the peritectic point (743 °C), at which point,  $\text{FeS}_2$  decomposed incongruently into  $\text{Fe}_{1-x}\text{S}$  and elemental S liquid. The authors hypothesized that access to the liquid phase and the high reactivity of S increased mobility and initiated consumption of  $\text{Fe}_{1-x}\text{S}$  and Si to yield  $\text{SiS}_2$  and the targeted ternary  $\text{Fe}_2\text{SiS}_4$ . The peritectic point was investigated by the synthesis of the intermediate binary  $\text{FeS}_2$  which was subsequently reacted with Si. Indeed,  $\text{FeS}_2$  instantaneously decomposed at 743 °C. To bypass the peritectic point and drive a reaction with elemental Si more rapidly, two methods based in Si bond installation were developed to sidestep sluggish Si reactivity: (1) reaction of  $\text{SiS}_2$  with FeS and (2) reaction of Fe-Si binary mixtures (to target the correct overall stoichiometry of  $\text{Fe}_2\text{SiS}_4$ ) with elemental S. Both routes were successful in initiating  $\text{Fe}_2\text{SiS}_4$  generation at lower temperatures

(682 °C and 586 °C, respectively) than the FeS<sub>2</sub> peritectic. When Si was installed into the starting material, its reactivity transformed which subsequently changed its role in the reaction. The authors offered that perhaps breaking Si bonds in the binaries blocks a thermodynamic equilibrium pathway. While the reaction pathway from the elements goes from fast Fe sulfurization to sluggish Si sulfurization, the pathway starting with Fe-Si binaries blocks fast Fe sulfurization in favor of Si reactivity (Figure 1.5). Thus, “a reaction will spontaneously access the chemical space that offers the most immediate available free energy release, rather than the most stable global minimum.” Neither pathway leads directly to the ternary but through a series of intermediates.

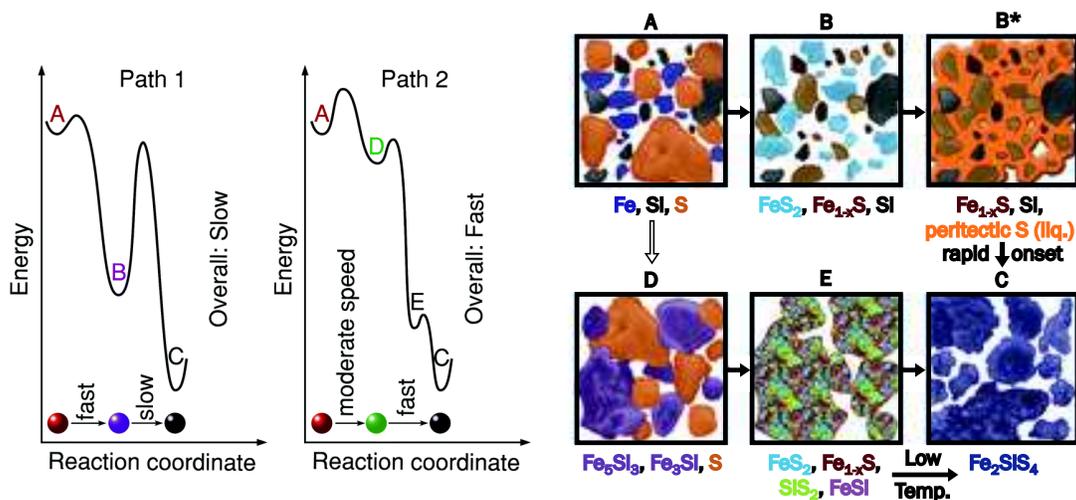


**Figure 1.5.** Path 1 describes the reaction pathway for the synthesis Fe<sub>2</sub>SiS<sub>4</sub> (species C) from the elements (species A). While the route to species B is quite favorable, the barrier to overcome sluggish Si incorporation is quite steep. Alternatively, Path 2 describes Fe-Si binaries (Species D) as the starting point toward the synthesis of Species C. This overcomes the activation barrier required for Si incorporation because breaking Fe-Si bonds directs a different reaction pathway. Adapted with permission from ref 49. Copyright 2017 Royal Society of Chemistry.

We, thus, posit that complex multinary systems generally do not follow a pathway towards the most stable global minimum but through a series of intermediates in a dynamic landscape controlled by different reaction parameter knobs and their cascading consequences. Jiang et al. successfully directed the route towards Fe<sub>2</sub>SiS<sub>4</sub> through alternate intermediates and omniscient characterization of all species via in situ XRD. Strategies such as the bond installation of elements

with sluggish reactivities and the robust characterization of all species could be essential to control syntheses of other systems.

In situ monitoring of a reaction, or “panoramic synthesis,” was also independently explored by the Kanatzidis group to, alternatively, discover new compounds.<sup>50</sup> The authors argued that analysis after synthesis completion is a missed opportunity to study intermediates which could lead to the discovery of new materials or elucidate how final products are formed. Panoramic synthesis provides total phase awareness by in situ synchrotron powder X-ray diffraction which tracks and provides information on all occurring crystalline phases for a particular temperature range. Using the Cs/Sn/P/Se system as a test case, six unknown phases were detected in addition to seven known phases (Figure 1.6). Three of the unknown phases were identified as  $\text{Cs}_4\text{Sn}(\text{P}_2\text{Se}_6)_2$ ,  $\alpha\text{-Cs}_2\text{SnP}_2\text{Se}_6$ , and  $\text{Cs}_4(\text{Sn}_3\text{Se}_8)[\text{Sn}(\text{P}_2\text{Se}_6)]_2$  by some of the following strategies: (1) ex situ preparation of unknowns due to the established relationship between temperature and phase; (2) “chemical analogy” in which in situ PXRD patterns are compared with calculated PXRD patterns of known compounds possessing similar unit cell parameters to elucidate crystal structure parameters and elemental composition; (3) rationalization that an unknown structure that grows simultaneously to the consumption or conversion of a known structure suggests that these phases share similar structural building blocks; and (4) computational software to solve structures.

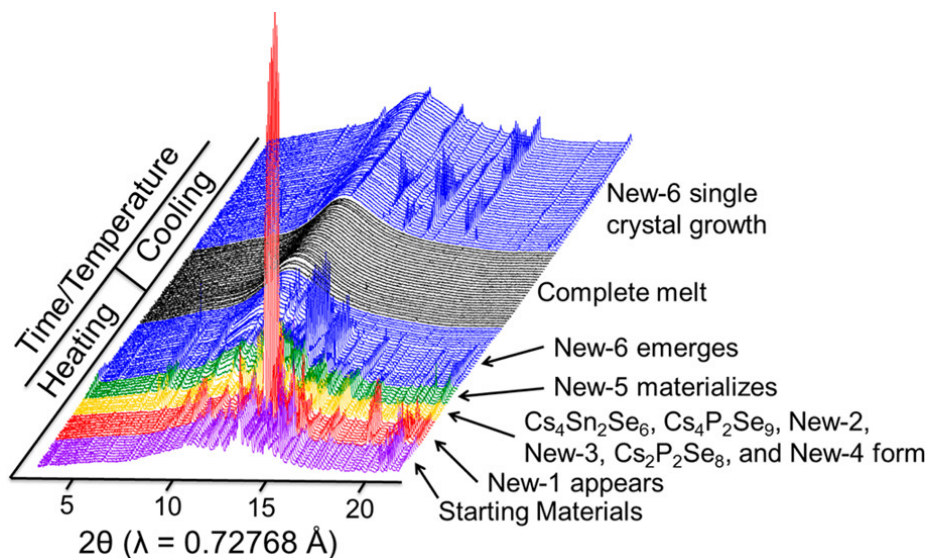


**Figure 1.6.** In situ XRD data identifying the formation or consumption/conversions of different phases as a function of ramp stages (time and temperature). Reprinted with permission from ref 50. Copyright 2017 American Chemical Society.

Both examples provide a framework of in situ methods developed by the solid-state community to elucidate reaction pathways, and thus synthetic toolbox strategies, for the potential extrapolation to the nanoparticle community. While the addition of the solution-phase increases the complexities of these systems while also limiting the availability of in situ characterization methods that can sufficiently characterize all intermediate species, these challenges provide a creative opportunity to interface mature molecular and bulk characterization techniques to elucidate reaction pathways of nanoparticle syntheses. In order for the nanoparticle synthesis community to start the building of a toolkit for rational syntheses, additional considerations and complexities must be considered such as nucleation and growth.

#### 1.4. Non-Classical Nucleation: Additional Considerations for NP Syntheses

An additional consideration in understanding reaction pathways for nanoparticle syntheses lies in their formation, specifically the nucleation stage. The classical nucleation theory portrays the formation of nanoparticles by monomer addition, in which a supersaturation of monomers

leads to nucleation seeds that monomers can continue to grow off of (Figure 1.7).<sup>51-53</sup> However, through careful characterization and understanding, this simplistic model has evolved beyond a macroscopic view to recognize dynamic chemical processes in which molecular rearrangements occur at very short times scales (Figure 1.7).<sup>54-58</sup> Non-classical nucleation pathway processes include precursor to monomer transformation in which the speciation of precursors can change due to interactions with each other, evolution of solid intermediate species that aren't the target material in progress toward the final product, and formation of the final product by conversion, consumption, etc. of these species. These processes can happen linearly and/or simultaneously, thus the deconvolution of these processes is non-trivial. It is also common to misattribute the characterization or identification of certain species to some process. While mature characterization methods can be used to study isolated species or processes, our goal is to move toward characterization of simultaneous hybrid species.

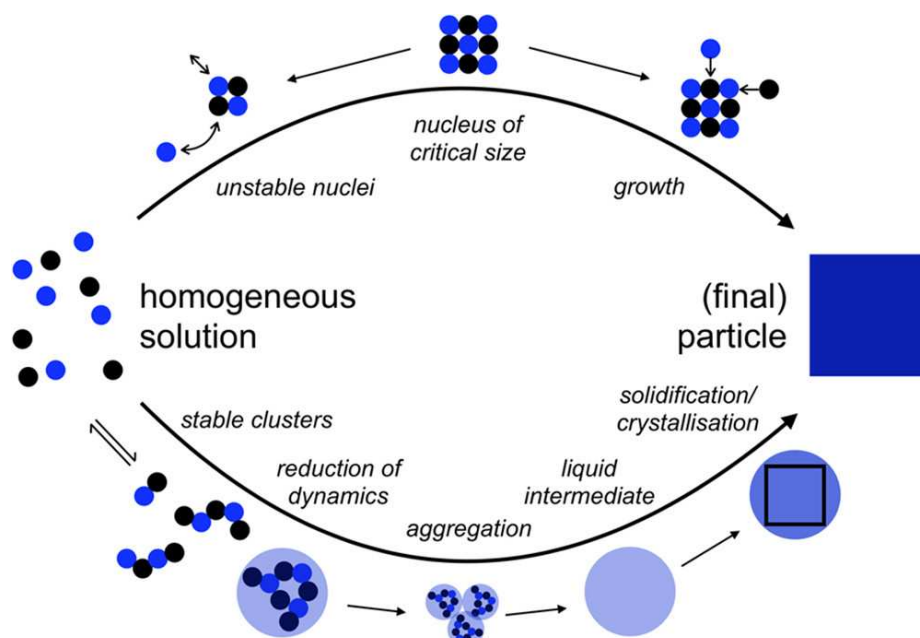


**Figure 1.7.** The top pathway describe classical nucleation in the final product is formed by monomer addition to nuclei. The bottom pathway represents nonclassical nucleation in which the final product is formed by more diverse and dynamic processes. Reprinted with permission from ref<sup>55</sup>. Copyright 2019 American Chemical Society.

Presented here are select exemplary examples of how the nanoparticle synthesis community has evolved from the elucidation of reaction landscape by systemic yet uncontrolled parameter changes (i.e. requiring the synthesis of every parameter permutation to elucidate phase space) to the robust characterization of speciation in order to elucidate reaction pathways for the controlled synthesis of a target nanoparticle system. Despite what appears to be brute force strategies in some cases, we acknowledge and enforce the significance and value of the preliminary studies as a progression must exist in order to achieve the ultimate goal of synthetic control. Due to the complexities of nanoparticle synthesis and the diverse chemical bonds and structures of different systems, no synthetic control let alone synthetic design of unique structures would exist without a significant amount of data achieved by initially screening many reactions. Further these studies defined a foundation and pioneered a field for rational syntheses.

### **1.5 Reaction Pathway Studies for NP Syntheses: From Brute Force to Elegant Approaches**

A study by Ramasamy et al. explored the phase space of Cu-Sb-S family by keeping the synthesis method, injection order, and cationic precursor identities constant but varying the Cu:Sb ratio, anionic precursor identity, and temperature.<sup>59</sup> Four Cu-Sb-S phases including  $\text{CuSbS}_2$  (chalcocite),  $\text{Cu}_{12}\text{Sb}_4\text{S}_{13}$  (tetrahedrite),  $\text{Cu}_3\text{SbS}_3$  (skinnerite), and  $\text{Cu}_3\text{SbS}_4$  (fematinite) were synthesized (Figure 1.8). Because the authors focused on the characterization of optoelectronic properties such as bandgaps and absorption spectra, there was limited discussion and analysis on the compiled effects of tuning several synthetic knobs. However, much can be elucidated based on the final products such as differences in the phases yielded suggesting differences in reaction pathways. The anionic precursor identity impacts monomer speciation once in solution, impacting the reactivity of that constituent element through parameters such as but not limited to sterics, coordination environment, oxidation state, and polarizability (Chapter 2). These parameters can

consequently influence the reaction pathway. In this study, the speciation of the anionic precursors, 1-DDT/t-DDT vs. Se/OLA, upon monomer transformation is not simply elemental sulfur but thiols and polysulfides coordinated by amines, respectively. Additionally, temperature can impact the thermodynamics of a reaction, directing the route toward one phase that is more favorable than another at a specific temperature. For example, synthesis of  $\text{Cu}_{12}\text{Sb}_4\text{S}_{13}$  required higher temperatures than  $\text{Cu}_3\text{SbS}_4$  for a given set of parameters. This study highlights the permutation of phases accessible for a given system of multiple constituent elements and select variables. While this could aid in synthetic optimization of nanoparticle synthesis, it requires significant trial-and-error and is specific to the system under investigation. Further probing of the intermediates and parameters on their impact on the reaction pathways would be required to elucidate rationalizations that could be extrapolated into other analogous systems.

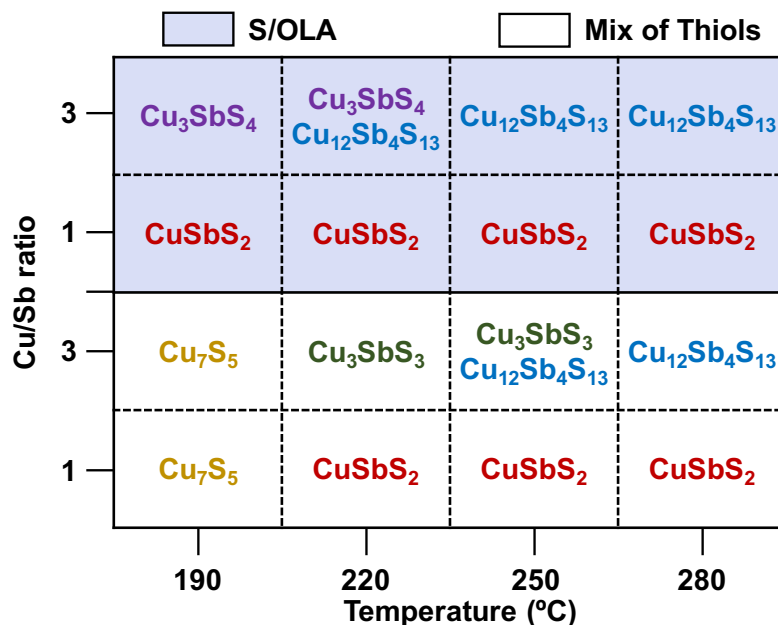


**Figure 1.8.** Phases of Cu-Sb-S synthesized by systematic changes of parameters. Adapted with permission from ref 59. Copyright 2014 American Chemical Society.

An evolution from the Ramasamy et al. study can be exemplified by the controlled phase space of  $\text{Cu}_2\text{SnSe}_3$  NPs to target a specific morphology by Wang et al.<sup>60</sup> Through the optimization

of the NP synthetic conditions for the wurtzite and cubic phases, the authors recognized that subtle but critical temperature changes and precursor identity could be extrapolated to control the formation of polytype NPs. The synthesis of the metastable wurtzite-phase (R1, Figure 1.9) was resolved by balancing the use of lower temperatures (220–280 °C) and high reactivity precursors diphenyl diselenide,  $\text{Ph}_2\text{Se}_2$ , and tin acetate,  $\text{Sn}(\text{Ac})_4$ . To achieve the thermodynamically stable cubic phase (R3, Figure 1.9), higher nucleation temperatures (255–310 °C) and lower reactivity precursors Se powder and tin (II) chloride,  $\text{SnCl}_2$ , were chosen to suppress the potential nucleation of the wurtzite-phase (R2, Figure 1.9) and to balance the reactivity of all precursors to prevent formation of binary impurities, namely  $\text{SnSe}$ . The summation of these rationalizations was then used to synthesize tetrapods with a cubic phase core and termination of four wurtzite phase arms (R4, Figure 1.9). A high enough injection temperature was used to nucleate the cubic phase upon injection of the cold precursors into the reaction flask. The temperature then dropped far enough to grow the wurtzite phase from the four equivalent (111) faces on the core. While this demonstrates a clever use of temperature understanding, a rationalization for the precursors was not given beyond balanced reactivity learned empirically. Further, while the authors reported that the wurtzite phase was formed by Sn insertion into Cu-Se binary intermediate, the role of an intermediate was not experimentally supported. The pursuit of understanding the speciation and their reactivities could have further probed the success of the tetrapod synthesis and pushed the strategy of qualitative balance towards true synthetic design. However, this study demonstrated a level of control and prediction which provided some guidelines for the controlled synthesis of both cubic (thermodynamic) and wurtzite (metastable) phases of  $\text{Cu}_2\text{SnS}_4$  to ultimately yield a unique tetrapod polytype. Despite an achievement in control, the study still required a high quantity of reactions and permutations of precursor choices. Further, the study was specific to the material

system because it only manipulated the crystal phase for a given stoichiometry of elements. What we aim is to expand synthetic control to *any* material system, and we believe this could be achieved through the understanding of how speciation or intermediates impact reaction pathway.

Reaction	Phase	Precursors in Flask	Injected Precursors	Injection Temperature	Growth Temperature	Shape
R1	Wurtzite	Ph <sub>2</sub> Se <sub>2</sub> , Cu-Oleate	Sn(Ac) <sub>4</sub>	230 °C	240 °C for 30 min	
R2	Polytype 1	Ph <sub>2</sub> Se <sub>2</sub> , CuCl, SnCl <sub>2</sub>	No injection	No injection	310 °C for 60 min	
R3	Cubic	Se	CuCl, SnCl <sub>2</sub>	300 °C	300 °C for 5 min	
R4	Polytype 2	CuCl	Ph <sub>2</sub> Se <sub>2</sub> , Sn(Ac) <sub>4</sub>	290 °C	280 °C for 15 min	

**Figure 1.9.** Phases of Cu-Sb-S synthesized by systematic changes of parameters. Adapted with permission from ref 60. Copyright 2014 American Chemical Society.

Gary et al. carefully identified the growth of toward the synthesis of InP and used reaction pathway studies to synthesize well-defined, monodisperse InP NPs.<sup>61</sup> The authors initially investigated the separation of nucleation and growth through optimized P precursor composition to improve the size dispersity of InP NPs. The P precursor composition was balanced by alignment of each precursor's reactivity to a specific reaction step: tris(trimethylsilyl)phosphine (P(SiMe<sub>3</sub>)<sub>3</sub>) which would induce fast nucleation by rapid consumption and tris(triphenylsilyl)phosphine (P(SiPh<sub>3</sub>)<sub>3</sub>) which would provide a monomer reservoir for controlled growth by slow consumption. Despite well-defined nucleation and growth steps, the reaction still yielded inhomogeneous InP NPs. This result contrasted classical nucleation theory and suggested that precursor conversion rate was not sufficient to obtain monodisperse InP. The authors evolved their studies to map out the reaction pathway for the formation of InP QDs. They hypothesized that the deviation of the InP system from classical nucleation theory was due to the formation of magic-sized cluster (MSC)

intermediates, supramolecular precursors to quantum dots, which were detected via UV-Vis spectra with lowest energy electronic transition (LEET). To probe this, the authors varied the stability of MSCs through synthesis and isolation of InP MSCs terminated by carboxylate, amine, or phosphonate ligands (Path A, B, and C, respectively), and illuminated a reaction landscape summarized in Figure 1.10.

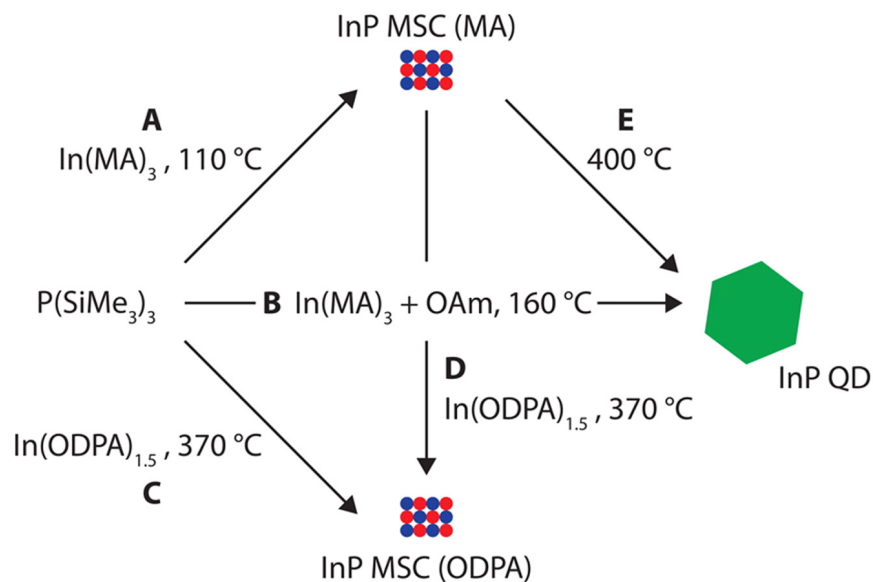


**Figure 1.10.** Reaction pathways of InP detailing the routes from molecular precursors (indium myristate,  $\text{In}(\text{MA})_3$ , indium octadecylphosphonate,  $\text{In}(\text{ODPA})_{1.5}$ , octylamine (OAm), and  $\text{P}(\text{SiMe}_3)_3$ ), InP MSCs, and QDs. Reproduced with permission from ref 61. Copyright 2015 American Chemical Society.

While carboxylate-terminated MSCs (Path A) and phosphonate-terminated MSCs (Path C) could be isolated, only Path A could further move toward the growth of polydisperse InP QDs (Path E). The use of amine ligands (Path B) bypassed the formation of MSCs altogether but resulted in some uniform growth of InP QDs. Interestingly, carboxylate-capped MSCs could be replaced by phosphonate ligands but not vice versa (Path D). Because of the elucidation of Path E, the authors further investigated if purified carboxylate-terminated MSCs could be directly substituted for molecular precursors as single-source precursors. Indeed, high quality InP QDs were synthesized, successfully eliminating the role of precursor conversion in InP monomer

generation to simplify the overall reaction scheme and follow classical nucleation theory. This study serves several important points on characterization of intermediates and reaction pathway studies. By understanding the reaction pathway intermediates, the authors swiftly optimized synthesis of a traditionally heterogeneously growing material system. Because MSCs are not predicted by classical nucleation theory, their characterization provides guidelines for other systems which may be observing heterogenous growth. Further, we hope that the nanoparticle community begins to embrace potential roadblocks in syntheses as opportunities to pivot their research and gain deeper understanding on the synthesis of new materials. The complexity of nanoparticle syntheses does not always lend to simple elucidation of reaction pathways nor the alignment of identified intermediates to the correct pathway. However, it is not unusual for our studies to reveal surprise findings, so it is imperative we meet these challenges to undergo rapid development of useful, yet general synthetic tools as opposed to ones that are only useful for a specific materials system.

We hope to have demonstrated through exemplary reaction pathway studies, not limited to the ones discussed here, on the evolution from continued trial-and-error to some modicum of swift rationalization. From the elucidation of phase space to the characterization of intermediates, we acknowledge that all components of methodology including brute force are not only important but required to continue progression in this field. This is because the nanoparticle community is dynamic and draws from the inspiration of many different chemistries including organic and solid-state chemistries. However, this has a lot to do with necessity as both molecular and bulk species must be considered in the elucidation of reaction pathways. Here, we demonstrated through the Ramasamy et al. report that characterization of molecular precursors as they transform into monomers in solution and transform into reactive intermediates could have been further used in

the community to understand how precursors behave.<sup>59</sup> This was demonstrated in the Gary et al. study in the use of a single-source precursor to bypass a nucleation event that was characterized through the illumination of a reaction pathway landscape.<sup>61</sup> Characterization of the bulk was also important to elucidate trends from parameter changes as exemplified by the report from Wang et al.<sup>60</sup> Through investigation of the final products they could then extrapolate how temperature and precursor reactivity balance played a role in the crystal phases, ultimately using these elucidations for the controlled synthesis of a unique polytype. Ultimately, we hope to have built a framework for a toolkit which enables full and total synthetic design of colloidal nanoparticles.

## 1.6. Perspective

In order to understand the reaction pathways for the synthesis of NPs, we aim to robustly characterize all reaction components, especially those that are overlooked such as amorphous phases or the gaseous reaction headspace. Through these studies, we hope to develop general strategies for the controlled or directed syntheses of ternary Cu chalcogenide nanoparticle systems and to advance methodologies to characterize not only individual processes but the reaction on the whole. Due to the interdisciplinary nature of NP synthesis, the goal is to intersect molecular and material mindsets to inform on how extended materials of unique chemical compositions can be rationally made. We close with challenges and important considerations for furthering NP synthetic strategies which we hope we have described well:

- adopt more uniform and specific diction
- characterize dynamic processes, not just final products
- thoroughly consider all aspects and components present, even if something is traditionally regarded as benign

- know the limitations of the techniques used, both inherent to the technique and in relation to the materials studied
- use complementary techniques to find evidence in areas for which other techniques are blind

Through robust characterization of reaction speciation in colloidal nanoparticle syntheses and specific diction, our objective is to build a multidisciplinary toolkit that connects the intersection of diverse chemistries. We are interested in not only probing this speciation by a combination of techniques, in this dissertation we explore both experimental and computational methods, but exploiting it to control synthetic pathways. Our objectives are to enhance our ability to purpose-build functional materials and advance the science of predictive synthesis.

## REFERENCES

- (1) Coughlan, C.; Ibáñez, M.; Dobrozhan, O.; Singh, A.; Cabot, A.; Ryan, K. M. Compound Copper Chalcogenide Nanocrystals. *Chem. Rev.* **2017**, *117* (9), 5865–6109.
- (2) Gao, M. R.; Xu, Y. F.; Jiang, J.; Yu, S. H. Nanostructured Metal Chalcogenides: Synthesis, Modification, and Applications in Energy Conversion and Storage Devices. *Chemical Society Reviews*. The Royal Society of Chemistry March 11, 2013, pp 2986–3017.
- (3) Fan, F.-J.; Wu, L.; Yu, S.-H. Energetic I–III–VI<sub>2</sub> and I<sub>2</sub>–II–IV–VI<sub>4</sub> Nanocrystals: Synthesis, Photovoltaic and Thermoelectric Applications. *Energy Environ. Sci.* **2014**, *7* (1), 190–208.
- (4) Yu, L.; Kokenyesi, R. S.; Keszler, D. A.; Zunger, A. Inverse Design of High Absorption Thin-Film Photovoltaic Materials. *Adv. Energy Mater.* **2013**, *3* (1), 43–48.
- (5) Chamorro, J. R.; McQueen, T. M. Progress toward Solid State Synthesis by Design. *Acc. Chem. Res.* **2018**, *51* (11), 2918–2925.
- (6) Soderholm, L.; Mitchell, J. F. Perspective: Toward “Synthesis by Design”: Exploring Atomic Correlations during Inorganic Materials Synthesis. *APL Mater.* **2016**, *4* (5), 053212.
- (7) Alberi, K.; Nardelli, M. B.; Zakutayev, A.; Mitas, L.; Curtarolo, S.; Jain, A.; Fornari, M.; Marzari, N.; Takeuchi, I.; Green, M. L.; et al. The 2019 Materials by Design Roadmap. *J. Phys. D: Appl. Phys.* **2019**, *52* (1), 013001.
- (8) Aykol, M.; Dwaraknath, S. S.; Sun, W.; Persson, K. A. Thermodynamic Limit for Synthesis of Metastable Inorganic Materials. *Sci. Adv.* **2018**, *4* (4), eaaq0148.
- (9) Sun, W.; Bartel, C. J.; Arca, E.; Bauers, S. R.; Matthews, B.; Orvañanos, B.; Chen, B.-R.; Toney, M. F.; Schelhas, L. T.; Tumas, W.; et al. A Map of the Inorganic Ternary Metal Nitrides. *Nat. Mater.* **2019**, *18* (7), 732–739.
- (10) Yu, L.; Zunger, A. Identification of Potential Photovoltaic Absorbers Based on First-Principles Spectroscopic Screening of Materials. *Phys. Rev. Lett.* **2012**, *108* (6), 068701.
- (11) Martinolich, A. J.; Neilson, J. R. Toward Reaction-by-Design: Achieving Kinetic Control of Solid State Chemistry with Metathesis. *Chem. Mater.* **2017**, *29* (2), 479–489.
- (12) Fallon, M. J.; Martinolich, A. J.; Maughan, A. E.; Gallington, L. C.; Neilson, J. R. Low-Temperature Synthesis of Superconducting Iron Selenide Using a Triphenylphosphine Flux. *Dalt. Trans.* **2019**, *48* (43), 16298–16303.
- (13) Wang, X.; Zhuang, J.; Peng, Q.; Li, Y. A General Strategy for Nanocrystal Synthesis. *Nature* **2005**, *437* (7055), 121–124.
- (14) Loiudice, A.; Segura Lecina, O.; Buonsanti, R. Atomic Control in Multicomponent Nanomaterials: When Colloidal Chemistry Meets Atomic Layer Deposition. *ACS Mater. Lett.* **2020**, *25*, 14.
- (15) Yarema, O.; Yarema, M.; Wood, V. Tuning the Composition of Multicomponent Semiconductor Nanocrystals: The Case of I–III–VI Materials. *Chem. Mater.* **2018**, *30* (5), 1446–1461.
- (16) Mazing, D. S.; Korepanov, O. A.; Aleksandrova, O. A.; Moshnikov, V. A. Synthesis of Ternary Metal Chalcogenide Colloidal Nanocrystals in Aqueous Solutions. *Opt. Spectrosc. (English Transl. Opt. i Spektrosk.)* **2018**, *125* (5), 773–776.

- (17) Smith, A. M.; Nie, S. Semiconductor Nanocrystals: Structure, Properties, and Band Gap Engineering. *Acc. Chem. Res.* **2010**, *43* (2), 190–200.
- (18) Chen, G.; Seo, J.; Yang, C.; Prasad, P. N. Nanochemistry and Nanomaterials for Photovoltaics. *Chem. Soc. Rev.* **2013**, *42* (21), 8304.
- (19) Yin, Y.; Alivisatos, A. P. Colloidal Nanocrystal Synthesis and the Organic-Inorganic Interface. *Nature* **2005**, *437* (7059), 664–670.
- (20) Talapin, D. V.; Lee, J.-S.; Kovalenko, M. V.; Shevchenko, E. V. Prospects of Colloidal Nanocrystals for Electronic and Optoelectronic Applications. *Chem. Rev.* **2010**, *110* (1), 389–458.
- (21) Kovalenko, M. V.; Manna, L.; Cabot, A.; Hens, Z.; Talapin, D. V.; Kagan, C. R.; Klimov, V. I.; Rogach, A. L.; Reiss, P.; Milliron, D. J.; et al. Prospects of Nanoscience with Nanocrystals. *ACS Nano* **2015**, *9* (2), 1012–1057.
- (22) Reiss, P.; Carrière, M.; Lincheneau, C.; Vaure, L.; Tamang, S. Synthesis of Semiconductor Nanocrystals, Focusing on Nontoxic and Earth-Abundant Materials. *Chem. Rev.* **2016**, *116* (18), 10731–10819.
- (23) Yin, Y.; Alivisatos, A. P. Colloidal Nanocrystal Synthesis and the Organic–Inorganic Interface. *Nature* **2005**, *437* (7059), 664–670.
- (24) Boles, M. A.; Ling, D.; Hyeon, T.; Talapin, D. V. The Surface Science of Nanocrystals. *Nat. Mater.* **2016**, *15* (2), 141–153.
- (25) Aldakov, D.; Lefrançois, A.; Reiss, P. Ternary and Quaternary Metal Chalcogenide Nanocrystals: Synthesis, Properties and Applications. *J. Mater. Chem. C* **2013**, *1* (24), 3756.
- (26) Buhro, W. E.; Colvin, V. L. Shape Matters. *Nat. Mater.* **2003**, *2* (3), 138–139.
- (27) Kumar, S.; Nann, T. Shape Control of II–VI Semiconductor Nanomaterials. *Small* **2006**, *2* (3), 316–329.
- (28) Alvarado, S. R.; Guo, Y.; Ruberu, T. P. A.; Tavasoli, E.; Vela, J. Inorganic Chemistry Solutions to Semiconductor Nanocrystal Problems. *Coord. Chem. Rev.* **2014**, *263–264*, 182–196.
- (29) Carey, G. H.; Abdelhady, A. L.; Ning, Z.; Thon, S. M.; Bakr, O. M.; Sargent, E. H. Colloidal Quantum Dot Solar Cells. *Chem. Rev.* **2015**, *115* (23), 12732–12763.
- (30) Murray, C. B.; Norris, D. J.; Bawendi, M. G. Synthesis and Characterization of Nearly Monodisperse CdE (E = S, Se, Te) Semiconductor Nanocrystallites. *J. Am. Chem. Soc.* **1993**, *115* (19), 8706–8715.
- (31) Milliron, D.; Hughes, S. M.; Cui, Y.; Manna, L.; Li, J.; Wang, L. W.; Alivisatos, A. P. Colloidal Nanocrystal Heterostructures with Linear and Branched Topology. *Nature* **2004**, *430* (6996), 190–195.
- (32) Park, J.; Joo, J.; Soon, G. K.; Jang, Y.; Hyeon, T. Synthesis of Monodisperse Spherical Nanocrystals. *Angew. Chemie - Int. Ed.* **2007**, *46* (25), 4630–4660.
- (33) García-Rodríguez, R.; Liu, H. Mechanistic Insights into the Role of Alkylamine in the Synthesis of CdSe Nanocrystals. *J. Am. Chem. Soc.* **2014**, *136* (5), 1968–1975.
- (34) Wang, F.; Tang, R.; Buhro, W. E. The Trouble with TOPO; Identification of Adventitious Impurities Beneficial to the Growth of Cadmium Selenide Quantum Dots, Rods, and Wires. *Nano Lett.* **2008**, *8* (10), 3521–3524.
- (35) Dhaene, E.; Billet, J.; Bennett, E.; Van Driessche, I.; De Roo, J. The Trouble with ODE: Polymerization during Nanocrystal Synthesis. *Nano Lett.* **2019**, *19* (10), 7411–7417.
- (36) Mourdikoudis, S.; Liz-Marzán, L. M. Oleyamine in Nanoparticle Synthesis. *Chem.*

- Mater.* **2013**, *25* (9), 1465–1476.
- (37) Liu, Y.; Yao, D.; Shen, L.; Zhang, H.; Zhang, X.; Yang, B. Alkylthiol-Enabled Se Powder Dissolution in Oleylamine at Room Temperature for the Phosphine-Free Synthesis of Copper-Based Quaternary Selenide Nanocrystals. *J. Am. Chem. Soc.* **2012**, *134* (17), 7207–7210.
- (38) Das, A.; Shamirian, A.; Snee, P. T. Arsenic Silylamide: An Effective Precursor for Arsenide Semiconductor Nanocrystal Synthesis. *Chem. Mater.* **2016**, *28* (11), 4058–4064.
- (39) García-Rodríguez, R.; Hendricks, M. P.; Cossairt, B. M.; Liu, H.; Owen, J. S. Conversion Reactions of Cadmium Chalcogenide Nanocrystal Precursors. *Chem. Mater.* **2013**, *25* (8), 1233–1249.
- (40) Sowers, K. L.; Swartz, B.; Krauss, T. D. Chemical Mechanisms of Semiconductor Nanocrystal Synthesis. *Chem. Mater.* **2013**, *25* (8), 1351–1362.
- (41) Schaak, R. E.; Williams, M. E. Full Disclosure: The Practical Side of Nanoscale Total Synthesis. *ACS Nano* **2012**, *6* (10), 8492–8497.
- (42) Wang, Y.; He, J.; Liu, C.; Chong, W. H.; Chen, H. Thermodynamics versus Kinetics in Nanosynthesis. *Angew. Chemie Int. Ed.* **2015**, *54* (7), 2022–2051.
- (43) Bianchini, M.; Wang, J.; Clément, R. J.; Ouyang, B.; Xiao, P.; Kitchaev, D.; Shi, T.; Zhang, Y.; Wang, Y.; Kim, H.; et al. The Interplay between Thermodynamics and Kinetics in the Solid-State Synthesis of Layered Oxides. *Nat. Mater.* **2020**, *19* (10), 1088–1095.
- (44) Sun, W.; Dacek, S. T.; Ong, S. P.; Hautier, G.; Jain, A.; Richards, W. D.; Gamst, A. C.; Persson, K. A.; Ceder, G. The Thermodynamic Scale of Inorganic Crystalline Metastability. *Sci. Adv.* **2016**, *2* (11), e1600225.
- (45) Martinolich, A. J.; Neilson, J. R. Toward Reaction-by-Design: Achieving Kinetic Control of Solid State Chemistry with Metathesis. *Chem. Mater.* **2017**, *29* (2), 479–489.
- (46) Lee, J. M.; Miller, R. C.; Moloney, L. J.; Prieto, A. L. The Development of Strategies for Nanoparticle Synthesis: Considerations for Deepening Understanding of Inherently Complex Systems. *J. Solid State Chem.* **2019**, *273*, 243–286.
- (47) Whitehead, C. B.; Finke, R. G. Nucleation Kinetics and Molecular Mechanism in Transition-Metal Nanoparticle Formation: The Intriguing, Informative Case of a Bimetallic Precursor,  $\{[(1,5\text{-COD})\text{Ir}^{\text{I}}\text{-HPO}_4]_2\}^{2-}$ . *Chem. Mater.* **2019**, *31* (8), 2848–2862.
- (48) Finney, E. E.; Finke, R. G. Nanocluster Nucleation and Growth Kinetic and Mechanistic Studies: A Review Emphasizing Transition-Metal Nanoclusters. *J. Colloid Interface Sci.* **2008**, *317* (2), 351–374.
- (49) Jiang, Z.; Ramanathan, A.; Shoemaker, D. P. In Situ Identification of Kinetic Factors That Expedite Inorganic Crystal Formation and Discovery. *J. Mater. Chem. C* **2017**, *5* (23), 5709–5717.
- (50) Haynes, A. S.; Stoumpos, C. C.; Chen, H.; Chica, D.; Kanatzidis, M. G. Panoramic Synthesis as an Effective Materials Discovery Tool: The System Cs/Sn/P/Se as a Test Case. *J. Am. Chem. Soc.* **2017**, *139* (31), 10814–10821.
- (51) Thanh, N. T. K.; Maclean, N.; Mahiddine, S. Mechanisms of Nucleation and Growth of Nanoparticles in Solution. *Chem. Rev.* **2014**, *114* (15), 7610–7630.
- (52) Kwon, S. G.; Hyeon, T. Formation Mechanisms of Uniform Nanocrystals via Hot-Injection and Heat-up Methods. *Small* **2011**, *7* (19), 2685–2702.
- (53) Finney, E. E.; Finke, R. G. Nanocluster Nucleation and Growth Kinetic and Mechanistic Studies: A Review Emphasizing Transition-Metal Nanoclusters. *J. Colloid Interface Sci.*

- 2008, 317 (2), 351–374.
- (54) De Yoreo, J. J.; Gilbert, P. U. P. A.; Sommerdijk, N. A. J. M.; Penn, R. L.; Whitelam, S.; Joester, D.; Zhang, H.; Rimer, J. D.; Navrotsky, A.; Banfield, J. F.; et al. Crystallization by Particle Attachment in Synthetic, Biogenic, and Geologic Environments. *Science* **2015**, 349 (6247), aaa6760–aaa6760.
- (55) Gebauer, D.; Wolf, S. E. Designing Solid Materials from Their Solute State: A Shift in Paradigms toward a Holistic Approach in Functional Materials Chemistry. *J. Am. Chem. Soc.* **2019**, 141 (11), 4490–4504.
- (56) Bøjesen, E. D.; Iversen, B. B. The Chemistry of Nucleation. *CrystEngComm*. Royal Society of Chemistry 2016, pp 8332–8353.
- (57) Lee, J.; Yang, J.; Kwon, S. G.; Hyeon, T. Nonclassical Nucleation and Growth of Inorganic Nanoparticles. *Nat. Rev. Mater.* **2016**, 1 (8), 16034.
- (58) Li, J.; Wang, H.; Lin, L.; Fang, Q.; Peng, X. Quantitative Identification of Basic Growth Channels for Formation of Monodisperse Nanocrystals. *J. Am. Chem. Soc.* **2018**, 140 (16), 5474–5484.
- (59) Ramasamy, K.; Sims, H.; Butler, W. H.; Gupta, A. Selective Nanocrystal Synthesis and Calculated Electronic Structure of All Four Phases of Copper–Antimony–Sulfide. *Chem. Mater.* **2014**, 26 (9), 2891–2899.
- (60) Wang, J.-J.; Liu, P.; Seaton, C. C.; Ryan, K. M. Complete Colloidal Synthesis of  $\text{Cu}_2\text{SnSe}_3$  Nanocrystals with Crystal Phase and Shape Control. *J. Am. Chem. Soc.* **2014**, 136 (22), 7954–7960.
- (61) Gary, D. C.; Terban, M. W.; Billinge, S. J. L.; Cossairt, B. M. Two-Step Nucleation and Growth of InP Quantum Dots via Magic-Sized Cluster Intermediates. *Chem. Mater.* **2015**, 27 (4), 1432–1441.

## CHAPTER 2

### INVESTIGATING THE FORMATION OF CHALCOGENIDE SPECIES AND THEIR ROLES IN NANOPARTICLE (NP) SYNTHESSES TO INFORM ON REACTION MECHANISMS AND PATHWAYS<sup>2</sup>

Selection of a chalcogen (E) precursor for solution-based NP synthesis is typically based on solubility, ease of use, and desired reactivity. However, this often devolves into a game of trial-and-error to balance the reactivities of all species in the desired end compound and to avoid unintended byproducts. Discussed herein are some of the considerations we believe to be important not only when judiciously selecting a chalcogen precursor, specifically sulfur and selenium, but also in understanding its role and behavior when investigating the reaction system as a whole. Beyond balanced reactivities in a reaction system, selection of the chalcogen precursor must also consider how it may impact the identity of the active chalcogenide monomers due to the reaction solvents, the reaction mechanism for chalcogenide species evolution and subsequent delivery, and the interactions of the dissolved chalcogenide monomers with all other components to direct the reaction pathway. For example, octadecene (ODE) is typically touted as a non-coordinating and “innocent” bystander as motivation for its use with chalcogen powders. A contradicting and surprising discovery is found in a report from Bullen et al. in which ODE reacts with Se powder, suggesting ODE is an active reagent and may play an unexpected role in the reaction landscape.<sup>1</sup> This underscores the importance of understanding the roles of all participants and not discounting alternative considerations without the appropriate experimental data.

---

<sup>2</sup> This chapter was adapted or excerpted from an invited review for the journal’s 50<sup>th</sup> anniversary in *J. Solid State Chem.* **2019**, 273, 243-286 by Jennifer M. Lee, Rebecca C. Miller, Lily J. Moloney, and Amy L. Prieto with Jennifer M. Lee and Rebecca C. Miller as equal contribution first authors. The excerpted section from the review (Section 2.1) was written by Jennifer M. Lee with insights and edits from all authors. It was further expanded upon to encompass ideas presented in this dissertation.

The value of the studies highlighted is their specificity in studying the transformation of precursor to monomer (Chapter 1, Figure 1.2) exhaustively, emphasizing how even understanding one process of the inherently complicated NP synthesis warrants its own body of literature. This allows elucidation of reactivity trends and prediction of how a precursor might interact in a reaction system as a whole (i.e. precursor reactivity, decomposition, activation, species evolved, etc.). In other words, these studies can be used as initial resources for rational chalcogen precursor selection as well as subsequent systematic changes in chalcogen precursors to balance the parameters required for a specific reaction system.

### **2.1. Tertiary Phosphine Chalcogenides ( $R_3P=E$ ): Mechanism of Chalcogen Delivery and Reactivity Trends**

In general, basic structural properties, the mechanism of delivery, and reactivity trends of tertiary phosphine chalcogenides ( $R_3P=E$ ) are well-reviewed.<sup>2-4</sup> Here, we briefly summarize a few key points. For the phosphine chalcogenide series, the reactivity order via bond dissociation energies (BDEs) of the phosphine chalcogenides follows  $S < Se < Te$ . Although Te will not be compared in this section, one exemplary work we would like to highlight is by Yarema et al. who demonstrated impressive size and composition control of Cu-In-Te and Ag-In-Te ternary NPs from trioctylphosphine telluride (TOPTe) despite its unstable nature. Due to its ability to equilibrate with its dissociated counterparts within hours, the chalcogenide speciation can be incredibly difficult to balance with other constituent elements.

Determination of mechanistic details on the delivery of the chalcogen from  $R_3P=E$  was pioneered by the Bawendi and Alivisatos groups using nuclear magnetic resonance (NMR) (see Chapter 3).<sup>6,7</sup> For phosphine chalcogenides, chalcogen atoms can be cleaved by two mechanisms: (1) an acid/base reaction in which the chalcogen transfers as reduced  $E^{2-}$  and (2) a redox reaction

in which it transfers as  $E^\circ$ .<sup>2</sup> Both mechanisms are known to be important in metal chalcogenide NP syntheses depending on the reaction conditions. In 2017, mechanism 1 was further probed by Frenette et al. who characterized the expected anhydride and tertiary phosphine oxide byproducts but additionally observed  $H_2Se$  generated by phosphine selenide decomposition.<sup>8</sup> The headspace was collected into carbon disulfide ( $CS_2$ ) by cannula transfer and analyzed via  $^{77}Se$  NMR. Interestingly, the authors discovered that binary quantum dots (QDs) could be synthesized by cannula transfer of this gaseous Se species into a separate flask of cadmium carboxylate, suggesting that phosphine selenide activation by a metal complex was not solely necessary for phosphine-chalcogenide bond cleavage. However, the authors acknowledged this observation did not necessarily disprove the previously proposed mechanism but provided it as an alternative route to QD formation. This highlights the difficulty in pinpointing an active precursor and identifying all interactions in even binary, but still complicated, NP systems.

The Vela Group has made significant strides toward understanding the reactivity trends of tertiary phosphine chalcogenide families through comprehensive empirical evidence complemented by theoretical calculations.<sup>4,9</sup> From DFT calculations, they rationalized that the BDE of the phosphorus-chalcogen ( $P=E$ ) bond in tertiary phosphine chalcogenides determined its reactivity such that an increasing  $P=E$  BDE gave rise to lower reactivity of the phosphine chalcogenide precursor. For any given phosphine, the Se reactivity is greater than that of S because S is smaller, more electronegative, and therefore, forms stronger bonds. Moreover,  $P=E$  bond strength increases with increasing electron-donating ability of the R functional groups as this helps stabilize the partial positive charge on the P atom. This theoretical model was supported by empirical CdS and CdSe syntheses in which the aspect ratios of the nanorods were tuned by the reactivity of the  $P=E$  bond (Figure 2.1).<sup>9</sup> Here, they saw the production of low aspect ratio NPs

with diphenylpropylphosphine chalcogenide (DPPE), where the functional group was electron-withdrawing. When trioctylphosphine chalcogenide (TOPE) with a more electron-donating group was used, high aspect ratio particles formed. The general trend followed that as the P=E BDE decreased, thereby increasing reactivity, the aspect ratio and length of the NPs also decreased, meaning shorter and wider nanorods (Figure 2.2). This trend was explained by the heightened reactivity of the phosphine chalcogenide, initiating faster and more uncontrollable reaction with the cadmium precursor, which led to lower selectivity for anisotropic 1D growth. The authors hypothesized this outcome was a nucleation-dominated phenomenon because more reactive precursors are known to nucleate more rapidly and in greater concentration, leading to less precursor for growth. Further, high precursor concentrations were also reported to favor anisotropic growth, so the rate of chalcogen release during growth may have also contributed.

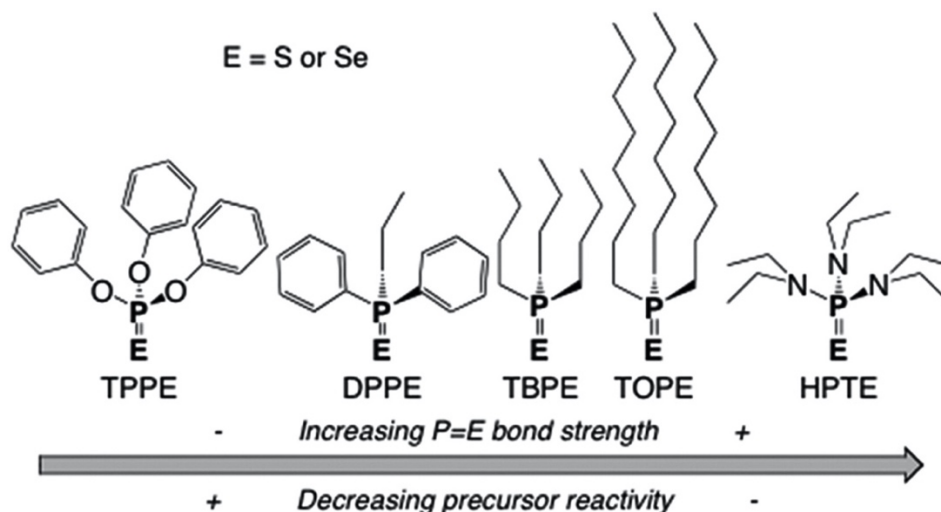


**Figure 2.1.** Reactivity trend of tertiary phosphine chalcogenides: triphenylphosphite (TPP), diphenylpropylphosphine (DPP), tributylphosphine (TBP), trioctylphosphine (TOP), hexaethylphosphorotriamide (HPT). Reprinted with permission from ref 9. Copyright 2012 American Chemical Society.

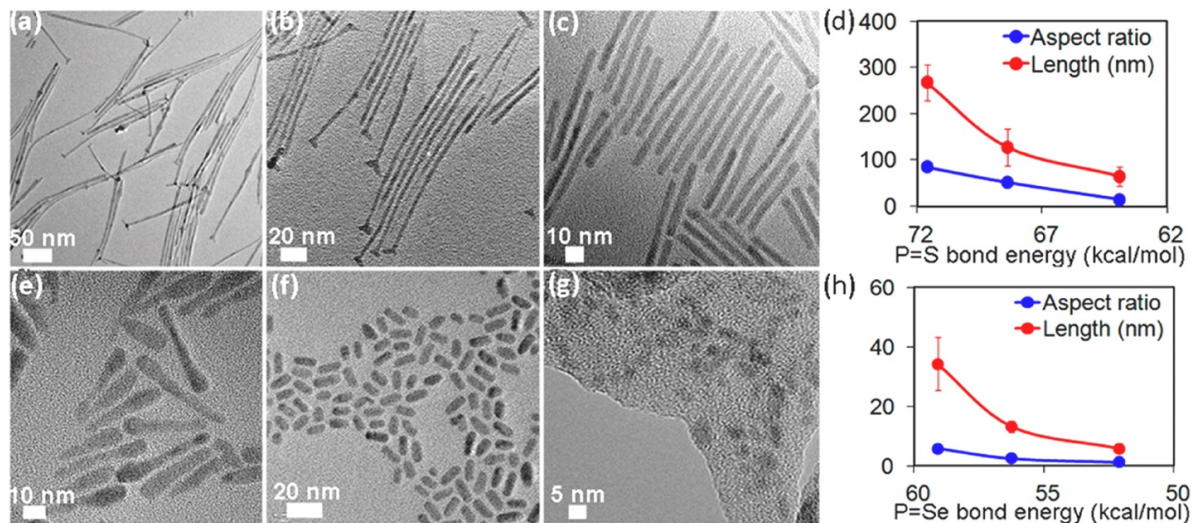


**Figure 2.2.** Change in nanorod aspect ratio as a function of precursor reactivity. Images of CdS nanorods made with (a, b, c) TOPS, TBPS, and DPPS, respectively. (d) Plot of CdS nanorod length (nm) and aspect ratio as a function of calculated P=S bond strength. CdSe nanorods made with (e, f, g) TOPSe, TBPSe, and DPPSe, respectively. (h) Plot of CdSe nanorod length (nm) and aspect ratio as a function of calculated P=Se bond strength. Reprinted with permission from ref 9. Copyright 2012 American Chemical Society.

The strength of this report lies in establishing reactivity trends for the different series of tertiary phosphine chalcogenides. This enables selection of a chalcogen precursor due to the assignment of a quantitative value, i.e. BDE, instead of arbitrarily selecting a chalcogen precursor because it is common in the literature. This can be viewed as analogous to tuning a reaction with temperature and time parameters as they can be treated as “continuous” parameters (as in, there are no gaps in identifying a quantifiable value). As our knowledge of reactivity trends of tertiary phosphine chalcogenides expands, instead of these trends looking “step-wise,” we are now filling in gaps so that a precursor can be strategically selected along a continuous plot. For example, in the first attempts of a ternary synthesis, one could select tertiary phosphine chalcogenides that possess BDEs at extreme ends; then, depending on the reaction products, one could rationalize a precursor with a BDE more suitable for the reaction system and conditions. This would hopefully lead to predictive control of the reaction outcome as we are now equipped with a standard base knowledge of how we might use this class of precursors.



found that the chalcopyrite phase formed from precursors with weaker C–Se bonds via a fast-nucleating  $\text{Cu}_{2-x}\text{Se}$  NP intermediate, while the metastable wurtzite-like phase formed from precursors with stronger C–Se bonds through a slow-nucleating umangite  $\text{Cu}_3\text{Se}_2$  phase. While a range of dichalcogenides were tested en route to the formation of thermodynamically stable chalcopyrite and metastable wurtzite phases of  $\text{CuInSe}_2$ , more mechanistic insight is required for the general use of dichalcogenides for ternaries. While ex situ X-ray diffraction (XRD) enabled the discovery of these respective reaction pathways, rigorous molecular-level studies analogous to those presented in Section 2.1 (Chapter 2) could elucidate rational synthesis principles. However, tertiary phosphine chalcogenides have the advantage of being monitored by the P nuclei, which gives rich mechanistic insight. NMR spectroscopies such as  $^1\text{H}$ ,  $^{13}\text{C}$ , and most importantly,  $^{77}\text{Se}$  could be used in addition although we acknowledge this is not always an accessible technique.

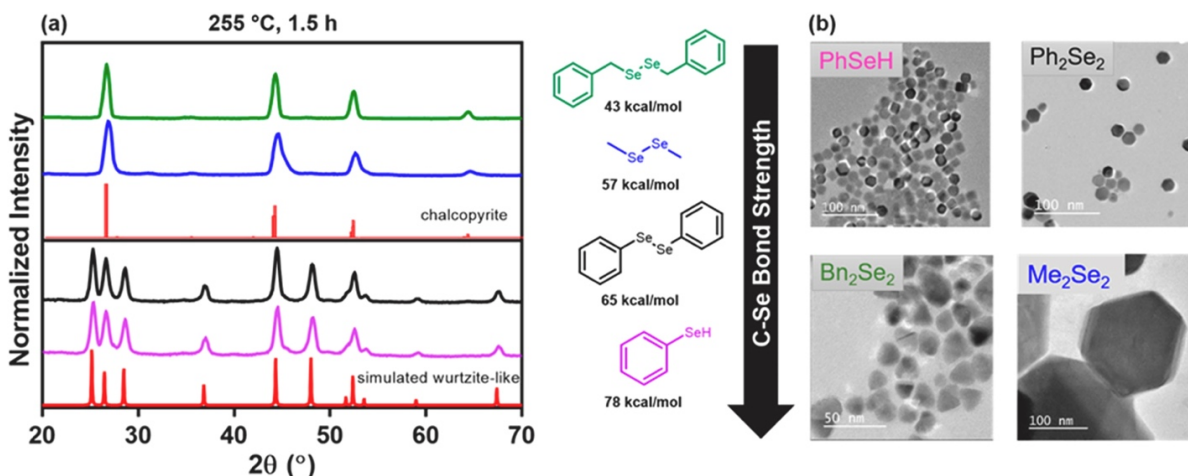


**Figure 2.4.** (a) Powder X-ray diffraction (PXRD) patterns of  $\text{CuInSe}_2$  NPs derived from the corresponding diselenide and benzeneselenol ( $\text{PhSeH}$ ) precursors, and the reactivity scale of DFT calculated BDEs of C–E bonds. (b) TEM of the resulting NPs synthesized by the corresponding diselenide. Reprinted with permission from ref 11. Copyright 2018 American Chemical Society.

### 2.3. Alkylamine-chalcogenides: Chalcogen Dissolution and Reduction

Generally, the simplest method to prepare a chalcogen precursor is mixing elemental powders of S or Se, which can exist respectively as  $\text{S}_8$  and  $\text{Se}_8$  rings as well as polymeric chains,

with a high boiling point organic solvent. Solvents such as primary alkylamines or phosphines are common and versatile because they are reducing and have the dual capability of acting as a surface ligand, coordinating to the surfaces of NPs to stabilize the surface. Specifically, oleylamine (OLA) is desirable and widely used due to its multiple roles: (1) as a reducing agent from either its olefin or amine functional groups; (2) as a neutral, labile coordinating ligand group through the lone pair on the amine; and (3) as a long chain alkylamine affording controlled NP growth and a high boiling point synthetic parameter.<sup>13</sup> However, delivery of the chalcogen in these cases is not straightforward as the possible identities of active and non-active species are difficult to detect and categorize. Efforts to achieve mechanistic insight exist with the aim to uncover how these might affect the reaction pathway of NP formation.

While several mechanisms have been proposed for the case of sulfur, seminal work from the Ozin group proposed that sulfur solubilized in octylamine (via sonication at 80 °C), existed mainly as alkylammonium polysulfides.<sup>14</sup> Octylamine was studied as a model compound for other common primary alkylamines because it can be bought commercially at a higher purity. OLA is typically used at 70% tech grade purity, for reference. Upon heating (2 h at 130 °C), the polysulfide ions reacted with excess alkylamine to liberate H<sub>2</sub>S, indicated indirectly by the transformation of PbO-coated paper to PbS in the presence of the reaction flask headspace. Byproducts of the H<sub>2</sub>S liberation reaction, such as thioamides, reacted further to continue evolving H<sub>2</sub>S although it remained unclear how and if these species contributed to the reaction pathway. Although studying octylamine instead of OLA afforded simplification of data, OLA has further functionality in the C-9 alkene<sup>13</sup> that we suspect could contribute to the identity of the reaction byproducts. Moreover, the composition and grade of OLA can influence the outcome of a reaction. While this study is a valuable resource for initial understanding of the potential reaction mechanisms in which S could

interact with a primary alkylamine, it cannot account for all the unexpected side reactions that might occur as a result of OLA's impurities.

Regarding Se dissolution in alkylamines, early reports of directly dissolved Se powder in OLA often exhibited uncontrolled reactivity of NPs.<sup>15</sup> An alternative route was developed in 2010 in which Wei et al. demonstrated sodium borohydride, NaBH<sub>4</sub>, was key in balancing the reactivities of many constituent elements, synthesizing not only binary but also ternary NPs (Figure 2.5).<sup>16</sup> In the presence of OLA, the authors speculated that NaBH<sub>4</sub> reduced Se to generate some general alkylammonium selenide species in situ. Although the exact speciation was not well characterized, Se powder was dissolved with ease at RT. In a report from our group by Riha et al., the authors were able to achieve the balanced reactivities of five different constituent elements through the use of NaBH<sub>4</sub> to dissolve both S and Se in OLA which resulted in compositionally controlled CZTS<sub>1-x</sub>Se<sub>x</sub> NPs.<sup>17</sup> Keeping the precursors separate in OLA resulted in either a Se-rich composition or phase separation of CZTS and CZTSe NPs, which the authors speculated was due to the variations in relative chalcogenide speciation at nucleation. Despite the lack of true understanding of the actual speciation, the versatility of using NaBH<sub>4</sub> in the presence of OLA to dissolve Se and balance reactivities demonstrates the value of its extrapolated use to other systems.

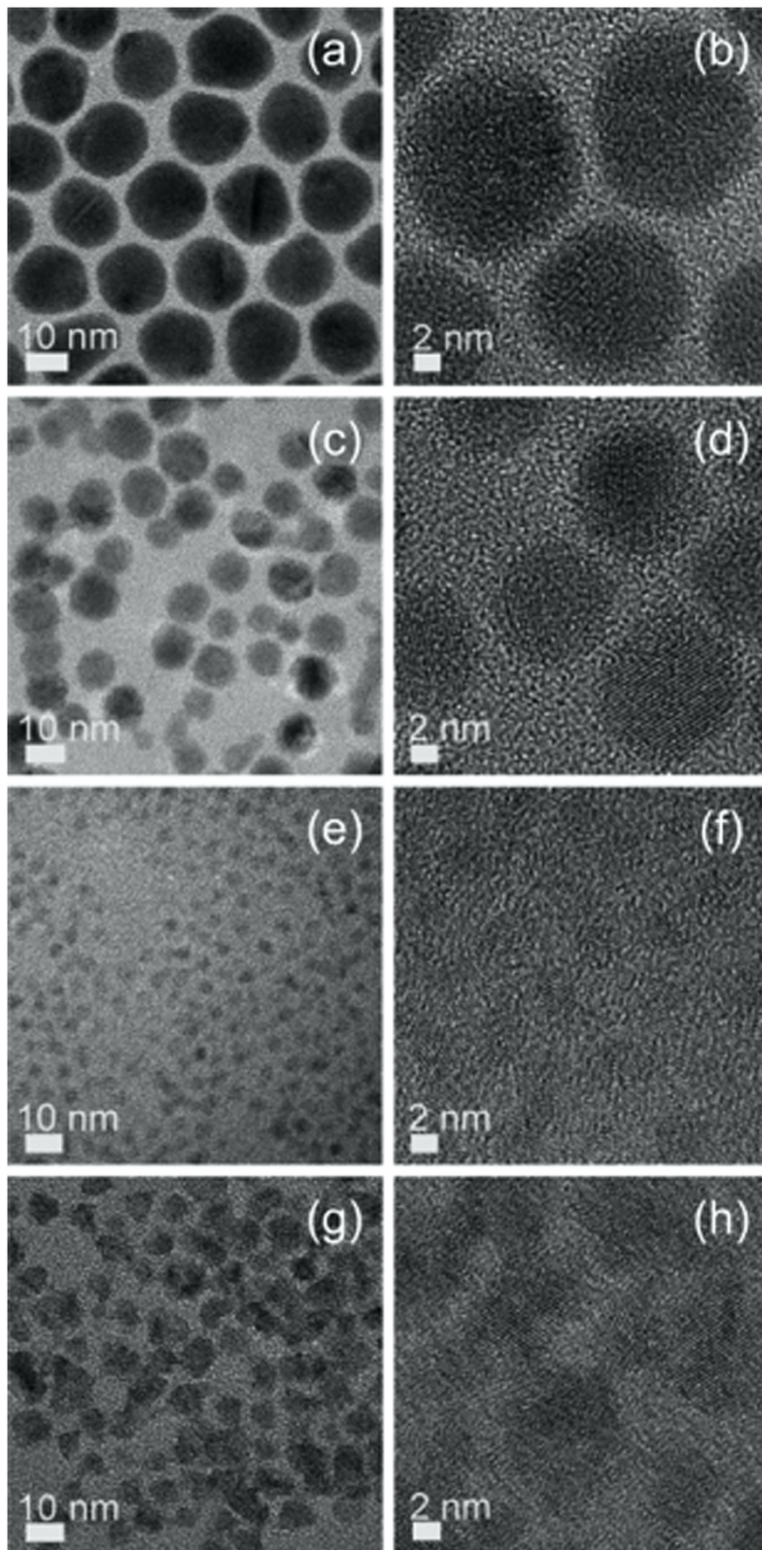


**Figure 2.5.** Versatility of Se-OLA precursor in the presence of NaBH<sub>4</sub>. (a,c,e,g) TEM and (b,d,f,h) HRTEM images of (a,b) Ag<sub>2</sub>Se, (c,d) PbSe, (e, ) ZnSe, and (g,h) CuInSe<sub>2</sub> NPs synthesized with Se-OLA-NaBH<sub>4</sub> precursor. Reprinted with permission from ref 16. Copyright 2010 American Chemical Society.

In summary, while ease of dissolution is motivation for any use of a chalcogen precursor, this rarely results in simplicity of active precursor identity. It is still important to understand the mechanism of chalcogenide precursor evolution and delivery to aid in understanding the reaction pathway. This can be accomplished by careful characterization of all components as exemplified by the Ozin group's detection of H<sub>2</sub>S by reaction of the captured headspace.<sup>14</sup> However, the report highlights the caution necessary to ensure the legitimacy of a control reaction. While it may be tempting to compare OLA by replacing its role with a cleaner alkylamine to narrow the scope of possible reaction mechanisms, care should be taken to truly determine that the final products and reaction pathway are unaffected. Further, unlike tertiary phosphine chalcogenides, S and Se may not possess analogous reactivities to one another in the presence of alkylamines. Further mechanistic insight into the speciation of Se in OLA is required, so it should be treated separately.

#### **2.4. Multiple Roles of 1-Dodecanethiol (DDT): Sulfur Precursor, Stabilizing Ligand, and Solvent**

It is well-reported that DDT can be used not only as a sulfur source via thermal decomposition but also as a stabilizing ligand and/or solvent.<sup>3,18</sup> Thermal decomposition of DDT is reported to be initiated by the formation of a metal thiolate by reaction of the thiol group with the metal of interest and is dependent on the hard-soft acid-base (HSAB) principle.<sup>19–22</sup> Softer Lewis acids interact more strongly with the thiolate group, weakening the adjacent C–S bond, which results in lower temperatures of decomposition as opposed to harder Lewis acids which exhibit the opposite trend. DDT can also influence the reaction pathway as exemplified by Ramasamy et al.<sup>23</sup> The authors synthesized a family of four Cu-Sb-S NPs including CuSbS<sub>2</sub> (chalcostibite), Cu<sub>12</sub>Sb<sub>4</sub>S<sub>13</sub> (tetrahedrite), Cu<sub>3</sub>SbS<sub>3</sub> (skinnerite), and Cu<sub>3</sub>SbS<sub>4</sub> (fematinite) by varying the Cu:Sb ratio, sulfur precursor identity (S/OLA vs 1-DDT/*t*-DDT), and temperature

(Figure 1.8, Chapter 1). The differences in products as a result of sulfur precursor suggests the differences in reaction pathway. Because the authors focused on the characterization of optoelectronic properties such as bandgaps and absorption spectra, there was limited discussion and analysis on the compiled effects of tuning several synthetic knobs for this system. Although how DDT affects the reaction pathway remains unclear, its interactions in the reaction system differ from other sulfur precursors, posing an interesting future study to examine the distinct speciation of the sulfur precursors.

Although DDT can be used as a S source, motivation for its use with elemental Se as a Se source is varied. While TOP readily dissolves Se powder to form TOPSe at RT with sonication or stirring, OLA requires heating to effectively dissolve Se powder. However, by including DDT with OLA, Se can be readily dissolved at RT.<sup>24</sup> Walker et al. proposed that this dissolution happens through a thiol-disulfide redox couple, formed by the reaction of two thiol molecules, that consequently reduces Se and protonates the amine, resulting in a  $(\text{Se}_8^{2-})(\text{R}_2\text{-NH}_3^+)_2$  complex. After the solution was formed, the authors demonstrated the ability to remove the thiol and disulfide compounds under vacuum, forming a selenide precursor free of other chalcogenides. This required the use of the short-chain ethylthiol for its difference in volatility relative to OLA. However, the sulfur compounds can be left in solution with the aim of forming mixed chalcogenide compounds.

## **2.5. Thiourea and Selenourea: Chemical Decomposition**

The use of thiourea and selenourea decomposition products as chalcogen precursors for NP syntheses is covered comprehensively in several reviews<sup>2,3</sup> as well as reports from the Owen group on a library of substituted thiourea and selenourea compounds.<sup>25,26</sup> The Owen group was able to achieve a wide range of reactivities and conversion rates by adjusting the organic substituents, thereby contributing to a continuous reactivity scale of quantifiable assignments as

opposed to step-wise. We highlight one specific use of thiourea in the formation of ternary NPs. In work from Sheets et al.,  $\text{Cu}_3\text{PS}_4$  NPs were prepared by reacting  $\text{Cu}_3\text{P}$  NPs with decomposed thiourea.<sup>27</sup> The authors suggested that thiourea isomerized to ammonium thiocyanate followed by decomposition into gaseous products, including  $\text{H}_2\text{S}$  and  $\text{CS}_2$ . The success of this synthesis is curious because of the necessity for complete rearrangement of all Cu-P bonds to form the Cu-S bonds and S-P bonds that exist exclusively in the ternary material. While the paper does not describe any failed synthetic attempts or mechanistic insights, which would be useful for extrapolation to other systems, it stands as a relatively unique example of using an ex situ prepared binary NP as a precursor to form a ternary compound.

## **2.6. In situ Evolution of Gaseous Chalcogenide Species from Elemental Chalcogen Interaction with 1-Octadecene (ODE)**

Several studies outline the dissolution of chalcogen (S or Se) powder in ODE as an in situ source of hydrogen chalcogenide,  $\text{H}_2\text{E}$ , which is hypothesized to be the active precursor in these NP syntheses.<sup>1,28-31</sup> Generally, the generation of  $\text{H}_2\text{E}$  has been characterized indirectly via two methods: (1) by bubbling the reaction flask headspace into a metal cation solution in which subsequent observation of  $\text{M}_x\text{E}_y$  precipitate indicated transfer of a gaseous chalcogenide species and (2) by the identification of a transformed ODE solvent (i.e. oxidization products, isomerization, etc.) as a result of its interaction with a chalcogen. While general mechanisms for the evolution of gaseous  $\text{H}_2\text{E}$  and expected byproducts have been proposed, there is still some uncertainty in pinpointing an exact reaction mechanism. These indirect characterization methods confirm the presence of a reactive gaseous chalcogenide species, but they are unable to conclusively confirm that the species is  $\text{H}_2\text{E}$  and/or that this gaseous species is the active monomer for NP production. These attempts have been further complicated by the observation of different

interactions of S and Se with ODE.<sup>1,29</sup> While many efforts have been made in utilizing complementary techniques, ideally, we would be able to directly characterize gaseous species in situ simultaneously with the reaction solvent for a complete understanding of the interaction. Moreover, there exists a lack of understanding in the subsequent influence of the chalcogen-ODE precursor and byproducts on the reaction pathway for NP formation. This is likely due to the fact that these studies focus on the syntheses of binaries, which usually are thermodynamically favorable products and less frequently encounter some of the compositional and phase control difficulties of many multinary NP systems. Beyond a more direct observation of the active chalcogenide species, mechanistic exploration of the interactions between these species and metal cations is required. For example, in the case of H<sub>2</sub>E truly being the resultant active chalcogenide species for both S- and Se-ODE systems, these compounds are not guaranteed to react to form NPs equivalently. Hopefully, through discussion of these results, we hope to emphasize the importance of understanding chalcogen powder dissolution in a presumably non-coordinating, “innocent” solvent and studying all interactions, especially among overlooked gaseous species and within the reaction headspace. Further, we hope to highlight that S and Se in ODE do not undergo analogous reaction mechanisms and, thus, do not provide the same reaction pathways when interacting with cationic species in a reaction system. Careful characterization is required to understand all the participants in a specific system without bias.

Yordanov et al. expanded the library of potential solvents that could be used to produce both H<sub>2</sub>S and H<sub>2</sub>Se.<sup>28</sup> However, only Se powder in paraffin was reported whereas S powder was studied in paraffin, hexadecylamine (HDA), stearic acid, trioctylphosphine oxide (TOPO), oleic acid (OA), sunflower-seed oil, and ODE. The effectiveness of a solvent was ordered by H<sub>2</sub>S yield which was determined by gravimetric analysis of CdS precipitate (Table 2.1).

**Table 2.1.** Yield of H<sub>2</sub>S from reaction between sulfur and various organic solvents at 250 °C for 1 h. Reprinted with permission from ref 28. Copyright 2008 Springer Nature.

<b>Compound</b>	<b>Yield, %</b>
Liquid paraffin	79
Hexadecylamine	73
Stearic acid	64
Trioctylphosphine oxide	54
Oleic acid	10
Sunflower-seed oil	9
1-Octadecene	6

The precipitate was generated by cannula transfer of the gaseous species into a solution of Cd (Figure 2.6). While this study stands as a diverse list for choosing chalcogen-solvent systems that yield different concentrations of gaseous chalcogen species, it would be strengthened by further characterization. Drawing conclusions from a single metric ignores the possibility of the explored systems exhibiting chemical differences in the composition of the gaseous chalcogenide species. Additionally, variations in the solvent systems explored (in terms of starting compounds, impurities, and transformed products) could likely affect subsequent NP formation. Thus, for greater understanding of the role of chalcogen-ODE solutions in NP syntheses and extension to more complicated, multinary systems, more detailed studies of the reaction mechanisms and pathways would be beneficial. This would involve characterization of monomer speciation and the influence on end products. From empirical evidence of attempts to synthesize ternary NPs, we observed that Se dissolved in HDA, TOPO, or ODE under the same reaction conditions (1 h at 250 °C) all resulted in different reaction products. This suggests that perhaps the dominant factor may not be the quantity of an active precursor but how the speciation of this precursor influences

the reaction pathway, although we acknowledge that our results are not the most comparable because solvent interactions with Se may not be analogous to those of S.

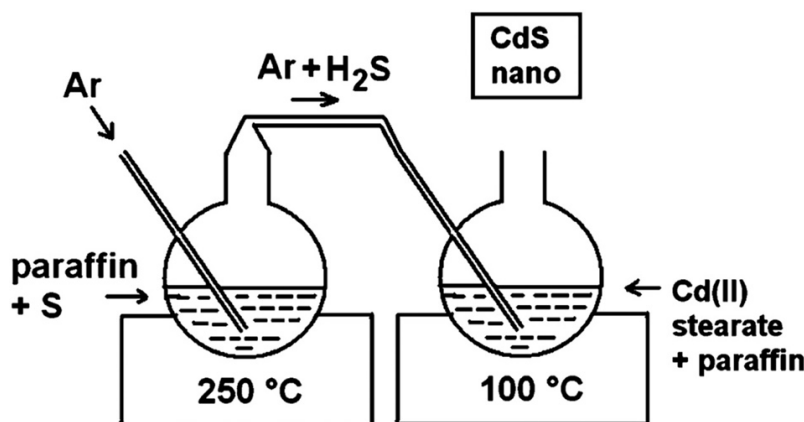


**Figure 2.6.** Schematic representation of CdS NP synthesis by cannula transfer of gaseous headspace of S-paraffin flask to Cd stearate. Reprinted with permission from ref<sup>28</sup>. Copyright 2008 Springer Nature.

A 2011 report from Li et al. attempted to understand the reaction products of sulfur and ODE and how the sulfur precursor is formed and delivered in ODE.<sup>29</sup> In the Peng group's previous study, published in 2009, Xie et al. studied the formation of CdS and discovered that it required a low activation energy, hinting that the reaction temperature could be lowered below typical reaction temperatures (>250 °C) and that the rate-limiting step was the activation of a S-containing precursor.<sup>32</sup> In their 2011 study, Li et al. tested this hypothesis by performing the CdS reaction (cadmium octanoate/S = 2:1 in excess ODE) at the thermally activated reaction temperature (180 °C) or, more specifically, the lowest temperature at which H<sub>2</sub>S generation and corresponding CdS formation were detected in control experiments.<sup>29</sup> While no precursors self-reacted in control reactions at elevated temperatures (100–220 °C), ODE oxidized upon addition of S to form H<sub>2</sub>S and byproducts. The detection of H<sub>2</sub>S was performed by two tests: introduction of Pb(Ac)<sub>2</sub> testing paper to the S-ODE solution headspace and cannula transfer of the reaction gas phase bubbled into silver nitrate and zinc acetate solutions separately which formed black silver sulfide and white zinc

sulfide, respectively. Although unable to directly detect H<sub>2</sub>S gas by these outlined methods, the group further rationalized its presence by the identification of the expected fatty acid side product by Fourier transform infrared spectroscopy (FTIR) and the oxidation of ODE by an  $\alpha$ -H NMR peak of its alkene group. The ultimate yield of S in the form of CdS only accounted for  $\frac{2}{3}$  of the initial elemental sulfur, indicating the likely formation of side products. The authors detected that the oxidation product of ODE in the organic phase consisted of 2-tetradecylthiophene and an unidentifiable, insoluble black mass. The exact structure was identified by NMR (Figure 2.7), gas chromatography-mass spectrometry (GC-MS), and 2D-correlated NMR. Interestingly, these techniques did not show any sign of thiol or disulfide during the synthesis of CdS although the Se-containing counterparts were observed in the formation of analogous CdSe using a similar reaction system by Bullen et al.<sup>1</sup> discussed below. This further suggests the different speciation of S and Se dissolved in ODE. More so than other studies, this work by the Peng group extensively characterized all interactions of the reaction system in the formation of CdS binary NPs.

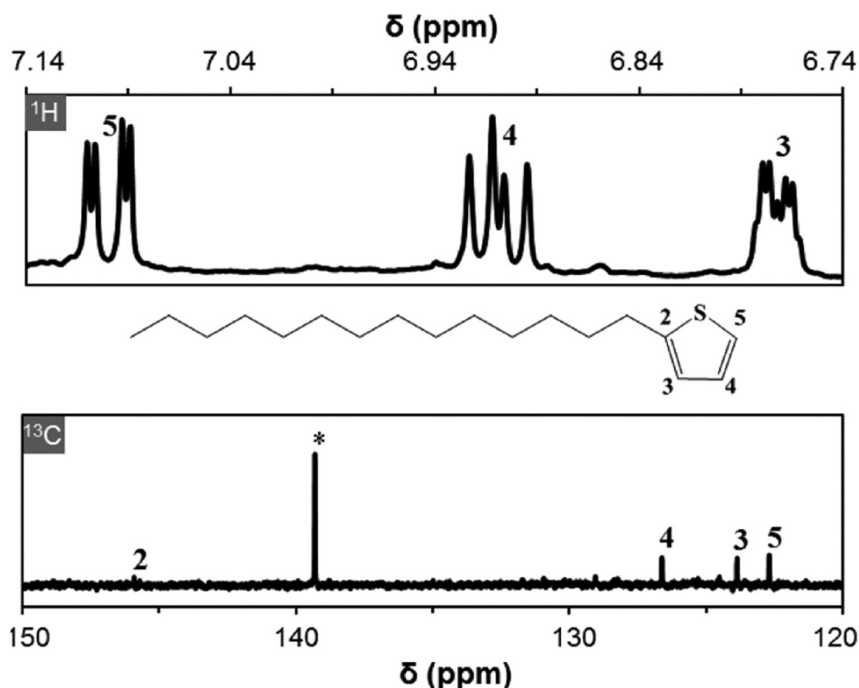


**Figure 2.7.**  $^1\text{H}$  and  $^{13}\text{C}$  NMR detection of the ODE oxidation byproduct, 2-tetradecylthiophene, in the presence of sulfur. The  $^{13}\text{C}$  NMR peak marked by an asterisk comes from C-2 of ODE. Reprinted with permission from ref 29. Copyright 2011 American Chemical Society.

Alternatively, the interactions of Se powder in alkane solution were studied by Deng et al.<sup>30</sup> The authors proposed that *n*-hexadecane oxidizes to an alkene in the presence of Se powder via a dehydrogenation mechanism which was rationalized by the detection of  $\text{H}_2\text{Se}$  through cannula transfer of the reaction headspace into a solution of  $\text{Cd}(\text{NO}_3)_2$  and the detection of an alkene via FTIR. Discussion of the FTIR data is in Chapter 3.

Inspiration was drawn by Bullen et al. who extensively characterized Se as a chalcogen source in ODE to standardize and optimize its use.<sup>1</sup> Some broad comparisons can be drawn to the reaction studied by Deng et al.<sup>30</sup> However, we caution that the systems are not directly comparable because Deng et al. synthesized CdSe in *n*-hexadecane while Bullen et al. used ODE. The reaction mechanism of Se monomer(s) generation could be sensitive to the interaction differences between a primary alkene versus an alkane. The preparation of Se-ODE has varied through the literature in terms of time and temperature. Studies with its use have lacked close monitoring of the evolution

of Se species, its mode of delivery in NP formation, and its efficacy as a Se precursor. The Bullen et al. report exhaustively measured efficacy by ultraviolet-visible (UV-Vis) spectroscopy, reaction yields of CdSe, inductively coupled plasma atomic emission spectroscopy (ICP-AES), photoluminescence excitation (PLE), X-ray absorption spectroscopy (XAS), NMR, and mass spectrometry (MS) (refer to Chapter 3 for an overview of characterization methods).<sup>1</sup> These techniques demonstrated that the most effective use of Se-ODE required heating for 5 h at 180 °C as these were the minimum conditions required for complete Se dissolution. PLE was especially useful, in which the deepest color indicated the highest percentage of Se dissolution in ODE and thus activation. Prolonged heating at higher temperatures and/or longer times resulted in significant loss of Se in solution, hypothesized to be a competitive reaction forming gaseous H<sub>2</sub>Se. ICP-AES on active (5 h at 180 °C) and aged (48 h at 180 °C) samples confirmed some loss of solubilized Se. However, the authors had expected a greater decrease in Se concentration if H<sub>2</sub>Se was the sole deactivation pathway due to literature precedence.<sup>28</sup> Complementary techniques including PLE and reaction yield for CdSe growth were therefore used. Changes in the absorbance profile at increased times or elevated temperature as well as a greatly reduced CdSe yield compared to Se concentration lost in solution suggested to the authors that loss in Se-ODE precursor efficacy could additionally be a result of a Se speciation change to a less active form.

Of note, 1-octadecene can isomerize over time to 2-octadecene in the presence of Se but not otherwise when applied to the same conditions (>5 h at 180 °C) as observed by 2D correlated NMR <sup>1</sup>H-<sup>13</sup>C heteronuclear single quantum coherence (HSQC). While not directly comparable systems, we recall reaction mechanisms proposed from previous studies involving related components. In the combination of S and ODE, Li et al. also observed that precursors and solvents did not autonomously react, and the transformation of ODE required the presence of the

chalcogen.<sup>29</sup> In contrast, the oxidation of ODE resulted in 2-tetradecylthiophene accompanied by an unidentifiable black substance. Deng et al. reported the production of H<sub>2</sub>Se and a dehydrogenated alkene group from the combination of Se powder and long alkyl hydrocarbons (*n*-hexadecane and paraffin), reiterating the different speciations of long-chain alkyl hydrocarbons versus long-chain monoolefins.<sup>30</sup> Beyond the observation of this isomerization, the authors were unable to identify the role of H<sub>2</sub>Se in its production.

Regarding the effects on CdSe NP formation, Bullen et al. observed many different Se species in the reaction system but admitted the inability to differentiate between active and inactive Se species.<sup>1</sup> While the potential Se precursor structures of the Bullen study are detailed in Chapter 3, we would like to highlight the group's restraint in not speculating beyond what any of the data indicated. Interaction between Se and ODE was detected by a varied C-1 signal in <sup>1</sup>H-<sup>13</sup>C HSQC, indicative of Se bonding to C-1 in a variety of ways. No interaction would have, instead, been characterized by a uniform chemical environment. Positive electron ionization mass spectrometry (EI MS) of active (1 h at 200 °C) and inactive (48 h at 200 °C) Se-ODE samples were also studied. Five singly charged species were detected for the active sample, where *m/z* is mass-to-charge ratio: ODE (*m/z* = 252), ODE+Se (*m/z* = 331), ODE+ 2Se (*m/z* = 410), 2ODE+Se (*m/z* = 586), and 2ODE+ 2Se (*m/z* = 664). The same species with the exception of ODE+ 2Se and 2ODE+ 2Se were observed in the inactive sample. While these results neither elucidated the mechanism in which H<sub>2</sub>Se was generated nor suggested how these species contributed to the overall reaction pathway, the detection of these species does support the existence of multiple Se species and the difficulty in deconvolution between active and inactive precursors in the formation of CdSe. Another H<sub>2</sub>Se study by Pu et al. acknowledged similar issues in identifying the exact reaction pathway in the formation of CdSe by Se-ODE.<sup>31</sup> Although the formation of H<sub>2</sub>Se was supported by similar

techniques mentioned above, it was difficult to determine whether H<sub>2</sub>Se played a role in the formation of CdSe. Overall, this report suggests the importance of carefully considering the reaction precursor interactions with all solvents.

The literature for the colloidal nanoparticle community has typically cited ODE as a non-coordinating and innocent bystander in NP reactions as a motivation for its use. However, this is not the case in the presence of a chalcogen and may not be the case with other reaction components as well. This is true in cases outside of the scope of chalcogenide precursors. For example, a contradicting and surprising discovery is the coordination of ODE on synthesized phases of the Li-Zn-Sb family, specifically cubic MgAgAs-type and CaZn<sub>2</sub>Sb-type LiZnSb crystallites.<sup>33</sup>

## **2.7. Evolution of Dialkyl Selenide Species from Elemental Selenium Reaction with 1-Octadecene (ODE)**

Atomic Se reacts with terminal olefins/primary alkenes in a diversity of mechanisms which leads to the formation of Se monomers with correspondingly diverse roles. Proposed are some Se species that could occur as a result of Se radical and terminal alkene interactions (Figure 2.8).<sup>34</sup> In the presence of Se, the alkene can isomerize from the 1—2 to 2—3 position to form Se<sub>n</sub>R<sub>2</sub> species in which an isomerized ODE moiety bonds to a Se-R moiety through the 1-carbon by a 2-electron oxidation generating H<sub>2</sub>Se. This process was observed by Bullen et al. via 2D correlated NMR <sup>1</sup>H-<sup>13</sup>C heteronuclear single quantum coherence (HSQC).<sup>1</sup> The authors proposed that Se bonds to the 1-carbon in a variety of ways, suggesting this might also be occurring with other alkenes of various lengths present in tech. grade ODE and that other reactions between Se and ODE are concurrently occurring. The isomerization mechanism to form Se<sub>n</sub>R<sub>2</sub> should also yield HSeR. Another viable form of Se insertion in olefins is via the Dewar-Chatt-Duncanson orbital model which yields a

seloxide-containing long-chain alkane at the olefin site.<sup>1,35</sup> All in all, these reactions have several terminal steps that could describe a convoluted spectrum.

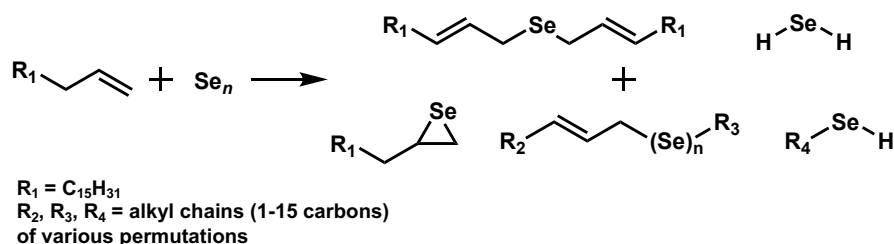


**Figure 2.8.** Potential Se monomers as a result of Se radical and terminal alkene interactions.

## 2.8. Perspective

While we cannot expect that these chalcogenide precursors in a binary nanoparticle system will behave in an extrapolated manner to more complicated multinary systems, the body of literature demonstrates that the field is trending toward identifying reactivity trends of related chalcogenide precursors and that these scales can help direct NP synthesis and serve as strategies for rational precursor selection. Ideally, we would like to make direct, quantifiable reactivity comparisons between the different types of chalcogen precursors and between different solvent systems. Unfortunately, the property trends would be hard to define because there are often many processes occurring that involve transformations of both the chalcogen and solvent system into different and hard to identify species. While it could be argued that Se-ODE and Se-OLA are more reactive precursors than phosphine chalcogenides in terms of BDE ( $P=Se = 364 \text{ kJ mol}^{-1}$  versus  $Se-Se = 172 \text{ kJ mol}^{-1}$  and  $Se=Se = 272 \text{ kJ mol}^{-1}$ , for fragmentation of cyclooctaselenium rings or selenium chains),<sup>1</sup> we see through the literature that the speciation is different for these chalcogen precursors. Thus, the use of BDE to singly assign reactivity for more complicated dissolution mechanism products would be severely overlooking the true interactions between chalcogen and solvent.

However, more broad generalizations could be made. Precursors such as DDT and thiourea are motivated by decomposition mechanisms and easy handling. If interested in control and tunability, tertiary phosphine chalcogenides are well-understood in the literature and therefore result in more rational predictions on potential reaction outcomes. Moreover, there appears to still be a need for understanding the true active chalcogen species in E-ODE as characterizations have shown that the combination produces several Se species with possible additional undetected ones. Interesting observations in the case of phosphine chalcogenides are that S and Se precursor series will generally follow analogous reactivity trends respective to one another and that the reaction pathways of NP formation were also found to be similar. However, this does not appear to be the case for chalcogen powder dissolved in ODE or other long chain alkyl hydrocarbons compounds wherein the speciation of S and Se are different and therefore could result in different reaction pathways of NP formation. This emphasizes the importance of understanding these studies in order to provide careful considerations when designing one's own experimental methods.

Ultimately, described reports in which the speciation and reactivity of chalcogen precursors for NP synthesis were examined, highlighting those with careful analysis in order to test the reaction mechanisms proposed. While describing NP reaction systems is difficult and designing a synthesis for one even more so, we hope to have described some useful methods in understanding the identities of active chalcogen precursors alongside mindful characterization in the mechanism of chalcogen precursor delivery and subsequent formation of byproducts in a variety of solvent systems. Robust studies recognize unexpected interactions of the chalcogen precursor with reaction components and the resultant effects on the NP reaction pathway.

## REFERENCES

- (1) Bullen, C.; van Embden, J.; Jasieniak, J.; Cosgriff, J. E.; Mulder, R. J.; Rizzardo, E.; Gu, M.; Raston, C. L. High Activity Phosphine-Free Selenium Precursor Solution for Semiconductor Nanocrystal Growth. *Chem. Mater.* **2010**, *22* (14), 4135–4143.
- (2) Reiss, P.; Carrière, M.; Lincheneau, C.; Vaure, L.; Tamang, S. Synthesis of Semiconductor Nanocrystals, Focusing on Nontoxic and Earth-Abundant Materials. *Chem. Rev.* **2016**, *116* (18), 10731–10819.
- (3) Alvarado, S. R.; Guo, Y.; Ruberu, T. P. A.; Tavasoli, E.; Vela, J. Inorganic Chemistry Solutions to Semiconductor Nanocrystal Problems. *Coord. Chem. Rev.* **2014**, *263–264*, 182–196.
- (4) García-Rodríguez, R.; Hendricks, M. P.; Cossairt, B. M.; Liu, H.; Owen, J. S. Conversion Reactions of Cadmium Chalcogenide Nanocrystal Precursors. *Chem. Mater.* **2013**, *25* (8), 1233–1249.
- (5) Steckel, J. S.; Yen, B. K. H.; Oertel, D. C.; Bawendi, M. G. On the Mechanism of Lead Chalcogenide Nanocrystal Formation. *J. Am. Chem. Soc.* **2006**, *128* (40), 13032–13033.
- (6) Liu, H.; Owen, J. S.; Alivisatos, A. P. Mechanistic Study of Precursor Evolution in Colloidal Group II-VI Semiconductor Nanocrystal Synthesis. *J. Am. Chem. Soc.* **2007**, *129* (2), 305–312.
- (7) Frenette, L. C.; Krauss, T. D. Uncovering Active Precursors in Colloidal Quantum Dot Synthesis. *Nat. Commun.* **2017**, *8* (1), 2082.
- (8) Ruberu, T. P. A.; Albright, H. R.; Callis, B.; Ward, B.; Cisneros, J.; Fan, H.-J.; Vela, J. Molecular Control of the Nanoscale: Effect of Phosphine–Chalcogenide Reactivity on CdS–CdSe Nanocrystal Composition and Morphology. *ACS Nano* **2012**, *6* (6), 5348–5359.
- (9) Guo, Y.; Alvarado, S. R.; Barclay, J. D.; Vela, J. Shape-Programmed Nanofabrication: Understanding the Reactivity of Dichalcogenide Precursors. *ACS Nano* **2013**, *7* (4), 3616–3626.
- (10) Tappan, B. A.; Barim, G.; Kwok, J. C.; Brutchey, R. L. Utilizing Diselenide Precursors toward Rationally Controlled Synthesis of Metastable CuInSe<sub>2</sub> Nanocrystals. *Chem. Mater.* **2018**, *30* (16), 5704–5713.
- (11) Rhodes, J. M.; Jones, C. A.; Thal, L. B.; MacDonald, J. E. Phase-Controlled Colloidal Syntheses of Iron Sulfide Nanocrystals via Sulfur Precursor Reactivity and Direct Pyrite Precipitation. *Chem. Mater.* **2017**, *29* (19), 8521–8530.
- (12) Mourdikoudis, S.; Liz-Marzán, L. M. Oleylamine in Nanoparticle Synthesis. *Chem. Mater.* **2013**, *25* (9), 1465–1476.
- (13) Thomson, J. W.; Nagashima, K.; Macdonald, P. M.; Ozin, G. A. From Sulfur–Amine Solutions to Metal Sulfide Nanocrystals: Peering into the Oleylamine–Sulfur Black Box. *J. Am. Chem. Soc.* **2011**, *133* (13), 5036–5041.
- (14) Liu, Y.; Yao, D.; Shen, L.; Zhang, H.; Zhang, X.; Yang, B. Alkylthiol-Enabled Se Powder Dissolution in Oleylamine at Room Temperature for the Phosphine-Free Synthesis of Copper-Based Quaternary Selenide Nanocrystals. *J. Am. Chem. Soc.* **2012**, *134* (17), 7207–7210.
- (15) Wei, Y.; Yang, J.; Lin, A. W. H.; Ying, J. Y. Highly Reactive Se Precursor for the

- Phosphine-Free Synthesis of Metal Selenide Nanocrystals. *Chem. Mater.* **2010**, *22* (20), 5672–5677.
- (16) Riha, S. C.; Parkinson, B. A.; Prieto, A. L. Compositionally Tunable  $\text{Cu}_2\text{ZnSn}(\text{S}_{1-x}\text{Se}_x)_4$  Nanocrystals: Probing the Effect of Se-Inclusion in Mixed Chalcogenide Thin Films. *J. Am. Chem. Soc.* **2011**, *133* (39), 15272–15275.
- (17) Aldakov, D.; Lefrançois, A.; Reiss, P. Ternary and Quaternary Metal Chalcogenide Nanocrystals: Synthesis, Properties and Applications. *J. Mater. Chem. C* **2013**, *1* (24), 3756.
- (18) Yarema, O.; Yarema, M.; Wood, V. Tuning the Composition of Multicomponent Semiconductor Nanocrystals: The Case of I–III–VI Materials. *Chem. Mater.* **2018**, *30* (5), 1446–1461.
- (19) Pearson, R. G. Hard and Soft Acids and Bases. *J. Am. Chem. Soc.* **1963**, *85* (22), 3533–3539.
- (20) Parr, R. G.; Pearson, R. G. Absolute Hardness: Companion Parameter to Absolute Electronegativity. *J. Am. Chem. Soc.* **1983**, *105* (26), 7512–7516.
- (21) Pearson, R. G. *Chemical Hardness*; Wiley-VCH Verlag GmbH: Weinheim, Germany, 1997.
- (22) Ramasamy, K.; Sims, H.; Butler, W. H.; Gupta, A. Selective Nanocrystal Synthesis and Calculated Electronic Structure of All Four Phases of Copper–Antimony–Sulfide. *Chem. Mater.* **2014**, *26* (9), 2891–2899.
- (23) Walker, B. C.; Agrawal, R. Contamination-Free Solutions of Selenium in Amines for Nanoparticle Synthesis. *Chem. Commun.* **2014**, *50* (61), 8331.
- (24) Hendricks, M. P.; Campos, M. P.; Cleveland, G. T.; Jen-La Plante, I.; Owen, J. S. A Tunable Library of Substituted Thiourea Precursors to Metal Sulfide Nanocrystals. *Science* **2015**, *348* (6240), 1226–1230.
- (25) Campos, M. P.; Hendricks, M. P.; Beecher, A. N.; Walravens, W.; Swain, R. A.; Cleveland, G. T.; Hens, Z.; Sfeir, M. Y.; Owen, J. S. A Library of Selenourea Precursors to PbSe Nanocrystals with Size Distributions near the Homogeneous Limit. *J. Am. Chem. Soc.* **2017**, *139* (6), 2296–2305.
- (26) Sheets, E. J.; Yang, W.-C.; Balow, R. B.; Wang, Y.; Walker, B. C.; Stach, E. A.; Agrawal, R. An in Situ Phosphorus Source for the Synthesis of  $\text{Cu}_3\text{P}$  and the Subsequent Conversion to  $\text{Cu}_3\text{PS}_4$  Nanoparticle Clusters. *J. Mater. Res.* **2015**, *30* (23), 3710–3716.
- (27) Yordanov, G. G.; Yoshimura, H.; Dushkin, C. D. Phosphine-Free Synthesis of Metal Chalcogenide Quantum Dots by Means of in Situ-Generated Hydrogen Chalcogenides. *Colloid Polym. Sci.* **2008**, *286* (6–7), 813–817.
- (28) Li, Z.; Ji, Y.; Xie, R.; Grisham, S. Y.; Peng, X. Correlation of CdS Nanocrystal Formation with Elemental Sulfur Activation and Its Implication in Synthetic Development. *J. Am. Chem. Soc.* **2011**, *133* (43), 17248–17256.
- (29) Deng, Z.; Cao, L.; Tang, F.; Zou, B. A New Route to Zinc-Blende CdSe Nanocrystals: Mechanism and Synthesis. *J. Phys. Chem. B* **2005**, *109* (35), 16671–16675.
- (30) Pu, C.; Zhou, J.; Lai, R.; Niu, Y.; Nan, W.; Peng, X. Highly Reactive, Flexible yet Green Se Precursor for Metal Selenide Nanocrystals: Se-Octadecene Suspension (Se-SUS). *Nano Res.* **2013**, *6* (9), 652–670.
- (31) Xie, R.; Li, Z.; Peng, X. Nucleation Kinetics vs Chemical Kinetics in the Initial Formation of Semiconductor Nanocrystals. *J. Am. Chem. Soc.* **2009**, *131* (42), 15457–15466.
- (32) White, M. A.; Baumler, K. J.; Chen, Y.; Venkatesh, A.; Medina-Gonzalez, A. M.; Rossini,

- A. J.; Zaikina, J. V.; Chan, E. M.; Vela, J. Expanding the I–II–V Phase Space: Soft Synthesis of Polytypic Ternary and Binary Zinc Antimonides. *Chem. Mater.* **2018**, *30* (17), 6173–6182.
- (33) Dénès, F.; Pichowicz, M.; Povie, G.; Renaud, P. Thiyl Radicals in Organic Synthesis. *Chem. Rev.* **2014**, *114* (5), 2587–2693.
- (34) Shen, H.; Wang, H.; Li, X.; Niu, J. Z.; Wang, H.; Chen, X.; Li, L. S. Phosphine-Free Synthesis of High Quality ZnSe, ZnSe/ZnS, and Cu-, Mn-Doped ZnSe Nanocrystals. *Dalt. Trans.* **2009**, *0* (47), 10534.

## CHAPTER 3

### CHARACTERIZATION OF NANOPARTICLE (NP) SYNTHESSES<sup>3</sup>

This chapter is focused on characterization techniques used to gain insight on NP reaction mechanisms and pathways. Murphy and Buriak outlined a standard of best practices for reporting NP syntheses to which we refer the reader.<sup>1</sup> Beyond the careful characterization of end products, we also discuss methods aimed at identifying all components of the reaction systems before, during, and after NP nucleation and growth. We hope to show exemplary uses of different analytical techniques, including what they offer for insight and their limitations, and we hope to suggest possible complementary tools.

This section is divided into two parts: characterization focused on understanding reaction mechanisms (often reactions involving organic species and precursors that lead to NP formation) and, secondly, characterization focused on understanding the reaction pathway (evolution of solid-phase components including phase, composition, and morphology of solid-state intermediates and NPs formed). At the end, some prospective NP characterization techniques and strategies for elucidating reaction mechanisms and pathways are highlighted.

#### **3.1. Characterization for Elucidating Reaction Mechanisms**

A layer of complexity in NP systems lies in understanding the significant and multifaceted roles of the solvent. It is commonly understood that solvents frequently double as bound ligands

---

<sup>3</sup> This chapter was adapted or excerpted from an invited review for the journal's 50<sup>th</sup> anniversary in *J. Solid State Chem.* **2019**, 273, 243-286 by Jennifer M. Lee, Rebecca C. Miller, Lily J. Moloney, and Amy L. Prieto with Jennifer M. Lee and Rebecca C. Miller as equal contribution first authors. Sections 3.1, 3.2.4, 3.2.5, and 3.3 from the review were written by Jennifer M. Lee with insights and edits from all authors. All other sections were expertly crafted and written collaboratively by all authors and were adapted or rewritten into this chapter to encompass ideas presented in this dissertation.

but their possible role in chemical transformations such as redox or coordination reactions is often overlooked, leaving the full mechanistic picture unknown. The main techniques currently utilized for unveiling the solvent role in NP syntheses are NMR, FTIR, UV–Vis, and mass spectrometry.

### **3.1.1. NMR Spectroscopy: Solution-based, 2D, and Solid-state Techniques**

Solution-based NMR techniques are powerful for describing the organic portion of colloidal NP reaction systems. Often studies focus on the identity of the starting solvents and ligands coordinated to the surface of the NPs as well as their transformations as a result of temperature or interactions with precursors.<sup>2–7</sup> In particular, the value of <sup>1</sup>H NMR is not only the identification of these species but also their quantification by use of an internal standard as well as the nature of their possible coordination to the NP surface. In many of these solution-based experiments, NMR preparation is done with care to avoid the introduction of a compound (i.e. standard deuterated solvent) that may cause an altered reaction mechanism. Some studies measure the neat reaction solution<sup>8</sup> while others add deuterated chloroform (CDCl<sub>3</sub>) only after the reaction has taken place.<sup>9</sup> Alternatively, Liu et al. took precaution by storing CDCl<sub>3</sub> with relevant precursors at RT.<sup>10</sup> The solutions were subsequently studied after prolonged air exposure to ensure not only stability over time but to also ensure any instability phenomenon was deconvoluted from acquired NMR spectra. Although the reports described in this section are by no means an exhaustive list of every NMR study to characterize the organic portion of NP reaction systems, we simply wish to highlight some seminal examples.

Using solution-based NMR spectroscopies, Steckel et al. and Liu et al. proposed reaction mechanisms for Se delivery from a tertiary phosphine selenide to a metal precursor, Pb and Cd, respectively.<sup>9,10</sup> Steckel et al. made four equivalent reaction samples directly in NMR tubes and quenched the reaction progress at different times for ex situ <sup>31</sup>P NMR and other complementary

techniques; Liu et al. ran in situ NMR ( $^1\text{H}$ ,  $^{13}\text{C}$ , and  $^{31}\text{P}$ ) in flame-sealed NMR tubes under vacuum. Despite the different sample preparations, both proposed that the cleavage of the P=Se bond in tertiary phosphine selenides occurred by an acid/base reaction with metal oleates in which Se transferred as  $\text{Se}^{2-}$ , resulting in metal selenide monomer, tertiary phosphine oxide, and an anhydride. To elucidate the mechanism involved, monitoring the growth of the oxidized tertiary phosphine and consumption of the tertiary phosphine selenide precursor by  $^{31}\text{P}$  NMR was key for both studies. Data from the study by Liu et al. is shown in Figure 3.1.<sup>10</sup>

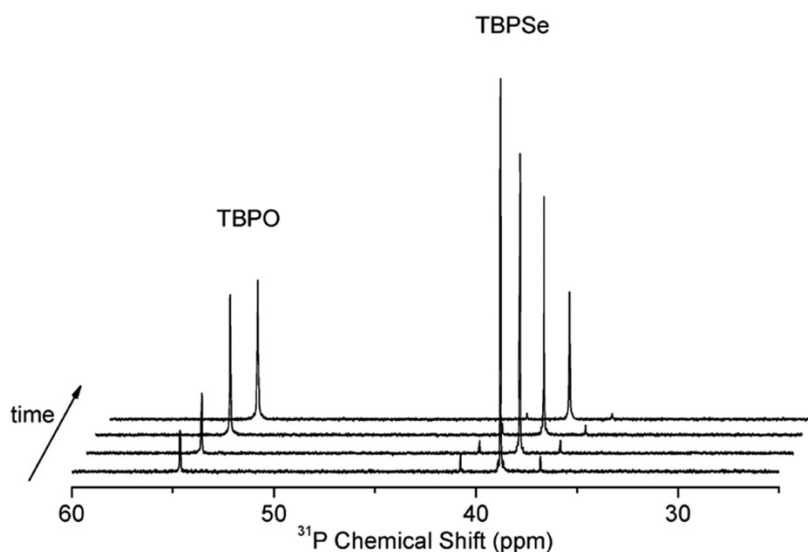


**Figure 3.1.** Conversion of tertiary phosphine selenide (tri-*n*-butylphosphine selenide, TBPSe) and the subsequent growth of tertiary phosphine oxide (tri-*n*-butylphosphine oxide, TBPO) observed by  $^{31}\text{P}$  NMR. Reprinted with permission from ref 10. Copyright 2007 American Chemical Society.

The Owen group has made significant contributions in the characterization of NP surface ligands by solution and solid-state NMR spectroscopies in order to ultimately tune the surface ligands for optoelectronic properties.<sup>11,12</sup> The work described here is significant because of the extensive experimental NMR spectroscopy protocols and thoughtful analysis of the resulting data. For example, Anderson et al. investigated the displacement of Z-type metal carboxylate ligands with various L-type Lewis base ligands (Figure 3.2).<sup>12</sup>

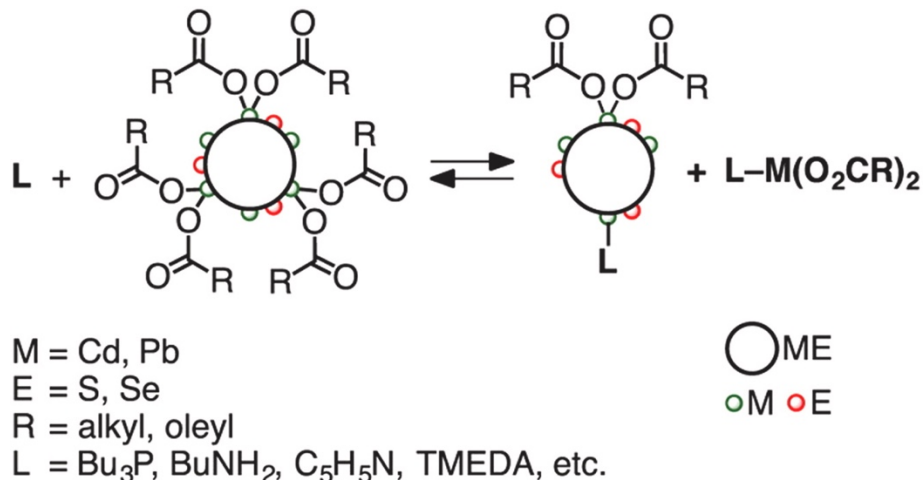


**Figure 3.2.** Displacement of metal carboxylate ligands,  $L\text{-M}(\text{O}_2\text{CR})_2$ , by L-type ligands on metal chalcogenide NPs. Reprinted with permission from ref 12. Copyright 2013 American Chemical Society.

In situ  $^1\text{H}$  NMR spectroscopy was used to monitor the bound and free ligands from CdSe NPs by distinguishing NMR line widths as well as the concentration of free carboxylate ligands to measure relative displacement (Figure 3.3a). Bound ligands tumble slowly causing broad signals while free ligands move freely in solution resulting in sharp signals. The authors targeted an isolated ppm range indicative of the vinylic hydrogens of oleyl chains and separate from the peaks of other solvent species. By increasing the concentration of L-type ligand *N,N,N',N'*-tetramethylethylene-1,2-diamine (TMEDA),  $\text{Cd}(\text{O}_2\text{CR})_2$  was displaced from CdSe NPs, represented by the growth of a sharp peak and consequent decrease in the broad peak (Figure 3.3).

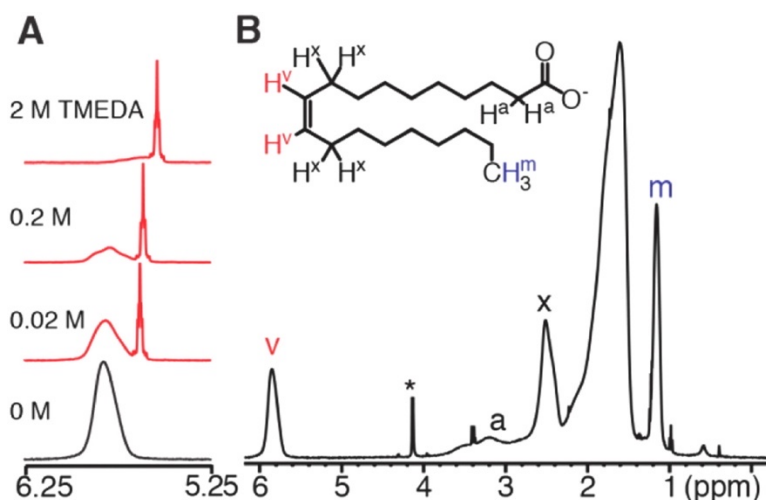


**Figure 3.3.** (A) Vinyl region of oleic chain depicting NMR line widths of bound vs. free ligands. Bound ligands are observed through a broad peak while free ligands are observed through a sharp peak. The authors hypothesized that the changes to the chemical shifts with increasing TMEDA concentration were due to a change in dielectric of the solvent medium. (B)  $^1\text{H}$  NMR spectrum of purified CdSe NPs. The (\*) ferrocene standard ( $\delta = 4.1$  ppm) used to measure oleyl concentrations. Reprinted with permission from ref 12. Copyright 2013 American Chemical Society.

Unfortunately, many NMR studies are limited to binary systems in which a reduced metal or metal cation directly reacts with the delivered chalcogenide. These systems are also typically focused on TOP-related surface compounds, probing common NMR-active nuclei such as  $^1\text{H}$  and  $^{31}\text{P}$ . Because phosphorus species can be directly observed by NMR, gaining insight into the system is less prohibitive than, for example, amine-based systems.<sup>13</sup> Although  $^{15}\text{N}$  NMR does exist, it has low sensitivity as the natural abundance of  $^{15}\text{N}$  is 33% of  $^{13}\text{C}$ . García-Rodríguez et al. tried to rectify this problem by utilizing 2D correlated NMR  $^1\text{H}$ - $^{15}\text{N}$  heteronuclear multiple bond correlation (HMBC) to investigate the role of alkylamine on the synthesis of CdSe NPs.<sup>14</sup> Another hurdle in NMR is that samples must be suspended for homogenous tumbling therefore limiting the types of samples to well-passivated NPs forming solutions without significant aggregation.

Examples of atoms other than  $^1\text{H}$  and  $^{31}\text{P}$  that could be investigated in NP syntheses are  $^{13}\text{C}$ ,  $^{19}\text{F}$ ,  $^{29}\text{Si}$ ,  $^{77}\text{Se}$ ,  $^{113}\text{Cd}$ ,  $^{119}\text{Sn}$ , and  $^{125}\text{Te}$  but are discussed elsewhere.<sup>15</sup> For example,  $^{13}\text{C}$  NMR

is useful in describing organic species when coupled with  $^1\text{H}$  NMR as is the case in a report by Bullen et al.<sup>16</sup> The use of  $^{77}\text{Se}$  is common in identifying chalcogenide species albeit prohibitively expensive to carry out numerous measurements.<sup>17</sup>

Additionally, one of the limitations of common NMR techniques is the inability to probe paramagnetic species. Electron paramagnetic resonance (EPR) has been used to characterize these species, especially targeting point defects in bulk and nanoparticle semiconductors. For example, this has been used to identify  $\text{Mn}^{2+}$  dopants in NP systems via hyperfine interactions of the  $^{55}\text{Mn}$  nuclear spin ( $I = 5/2$ ).<sup>19</sup>

We have split up these characterization techniques and are discussing them individually, but often data from different techniques are understood in conjunction to get a full picture of what transformations may be occurring. Thus, it is important to be careful in consideration of how reaction or sample conditions for one technique (NMR) might affect the material being studied for another technique. From a report by Anderson et al.,  $^1\text{H}$  NMR was used to elucidate bound ligand concentration which subsequently informed understanding on ligand exchange processes.<sup>12</sup> From these results, an important conclusion drawn was the contribution of ligand exchange processes on stoichiometry of the core NPs, an important factor in optoelectronic properties. While surface passivation and the identity of surface ligands to reduce recombination and boost quantum yield (QY) are important, optoelectronic properties are also sensitive to the concentration of free ligands in solution. This factor can affect the core NP stoichiometry because displacement or addition of ligands can remove or add core NP constituent atoms, respectively. For example, if the  $\text{Cd}(\text{O}_2\text{CR})_2$  ligand binds to the surface of the core NP, the Cd concentration would increase. Many reports prior to this one had focused solely on the identity of the bound ligands, unaware of stoichiometry changes consequently concluding in conflicting results. Instead, Anderson et al. made a direct

correlation of PLQY measurements and  $\text{Cd}(\text{O}_2\text{CR})_2$  surface coverage to understand stoichiometry effects. Careful measurements such as these lead not only to deeper understanding of a system, compared to conventional hypotheses of prior literature, but can also provide standard practices for the use of NMR spectroscopy in investigating other NP systems.

Other examples of NMR spectroscopies include 2D NMR and solid-state NMR spectroscopies. While these characterization techniques are already well established in other areas of chemistry, they are gaining more widespread and advanced use in the NP community, often providing unexpected insight. A 2018 paper from the Vela group used a combination of these techniques to characterize a series of Li-Zn-Sb phases that were synthesized via a high-throughput system, WANDA.<sup>20,21</sup> The compounds ODE and triphenylstibine ( $\text{Ph}_3\text{Sb}$ ) were detected as surface passivating ligands by solid-state NMR spectroscopy and confirmed with 2D coupled NMR spectroscopy DQ-SQ which was used to study the spatial relationship of the surface ligands. Separately, Bullen et al. used 2D  $^1\text{H}$ - $^{13}\text{C}$  HSQC NMR spectroscopy to enable the correlation and appropriate peak assignment of the different Se and ODE chemical environments, elucidating the isomerization of 1-ODE to 2-ODE in the presence of Se at prolonged reaction temperature (Figure 3.4).<sup>16</sup> These results challenge the commonly held classification of ODE as a non-coordinating, innocent solvent. We believe mechanistic insight is strengthened by the use of NMR and further supported by the use of complementary techniques.

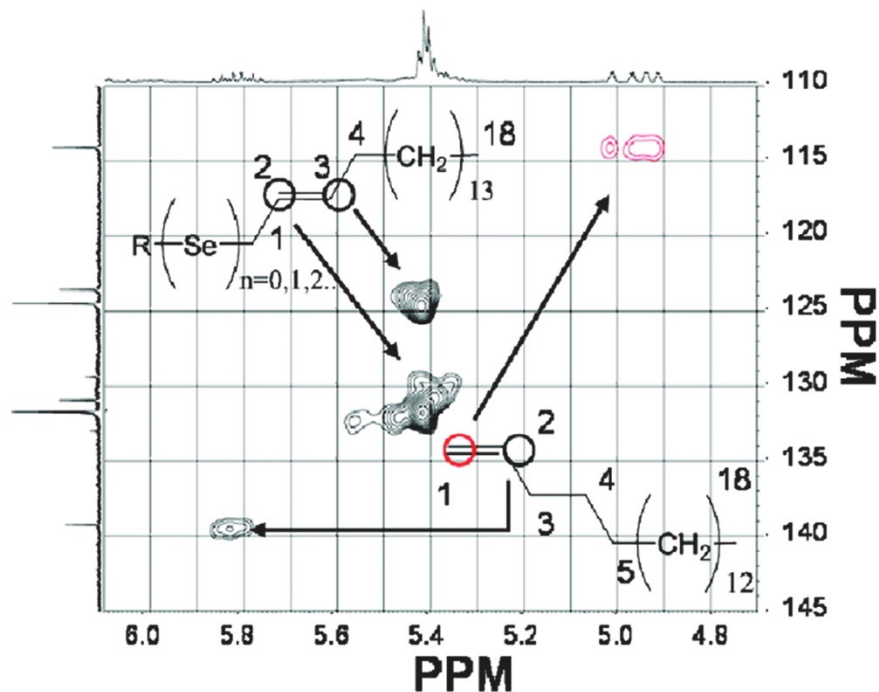


**Figure 3.4.** Isomerization of 1-ODE to 2-ODE (here, a 48 h sample) observed by peak assignment of the alkene region in  $^1\text{H}$ - $^{13}\text{C}$  HSQC. Adapted with permission from ref 16. Copyright 2010 American Chemical Society.

Further challenging convention, De Keukeleere et al. used  $^{31}\text{P}$  solid-state cross-polarization magic angle spinning (CP-MAS) NMR and solid-state  $^1\text{H}$ - $^{31}\text{P}$  heteronuclear correlation spectroscopy to study the surface of TOPO-functionalized  $\text{ZrO}_2$  NPs.<sup>13</sup> Literature prior to 2008 assumed TOPO alone was bound to NPs as L-type ligands, but findings by Wang et al.<sup>22</sup> in 2008 and Kopping et al.<sup>23</sup> discovered NPs, specifically CdSe NPs, were stabilized by phosphinic and/or phosphonic acid impurities in TOPO. In 2017, De Keukeleere et al. demonstrated that pure TOPO is neither inert nor a simple L-type ligand on  $\text{ZrO}_2$  NPs.<sup>13</sup> Under the acidic conditions used to synthesize  $\text{ZrO}_2$ , pure TOPO underwent decomposition. Their results from both liquid and solid-state NMR corroborated the identification of three phosphorus-containing surface ligands, di-*n*-octylphosphinic acid (DOPA), *P,P'*-(di-*n*-octyl) pyrophosphonate (PPA), and hydroxyl-tri-*n*-octylphosphonium ( $[\text{HO-PR}_3]^+$  where  $\text{R} = n\text{-octyl}$ ), which were initially assigned by solution-based  $^{31}\text{P}$  NMR. The solid-state NMR techniques were further used to identify the extent to which

the P-containing ligands were protonated. The authors found that DOPA adsorbed on the oxide surface and formed a hydrogen bond with surface hydroxyls, while PPA ligands did not participate in hydrogen bonding. The protonated TOPO,  $[\text{HO-PR}_3]^+$ , was explained to be tightly associated with the NP surface due to electrostatic interactions and hydrogen bonding. Due to the high affinities of the byproducts for the NP surface, this potential speciation should be considered when using TOPO in other systems as it could likely occur undetected without careful characterization.

The ability of these studies to challenge conventional understanding (i.e. non-participating behavior of ODE) with the use of careful control experiments and considerable attention to the molecular portion of the NP demonstrates the viability of NMR methodologies for characterization of NP syntheses. Some of the explored portions of the NP synthesis include solvent transformations, the NP surface and its interactions with the reaction system, etc. However, in order to directly extrapolate these methods to multinary NP systems, the syntheses of more complicated systems should ideally be well-controlled (i.e. exhibiting suspension in solution) in order to minimize variables. The goal is to develop these characterization methods to inform and evolve multinary NP synthesis toward higher understanding and, thus, higher control.

### **3.1.2. Infrared (IR) Spectroscopy for Solution Composition and NP Ligand Identification**

Fourier transform infrared spectroscopy (FTIR) is a simple technique that can answer similar questions to those answered by solution-based NMR techniques, especially in probing the composition of surface-bound ligands on NPs and the range of organic byproducts remaining in the supernatant. However, unlike NMR, FTIR is not used as a quantitative technique for NP studies; therefore, it is unable to provide the concentrations of species present. This does not discount FTIR from being a valuable technique because information about the reaction mechanism can be suggested. Deng et al. used FTIR to compare *n*-hexadecane before and after heating in the

presence of Se powder.<sup>24</sup> The two spectra were the same with the exception of an absorption band at  $1650\text{ cm}^{-1}$  (Figure 3.5), characteristic of C=C stretching.

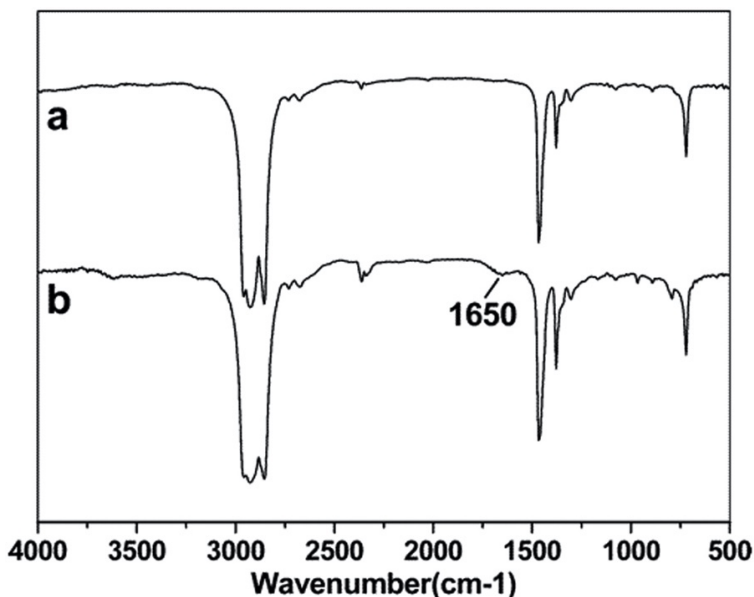


**Figure 3.5.** FTIR spectrum of *n*-hexadecane (a) before and (b) after heating in the presence of Se. The presence of the stretch at  $1650\text{ cm}^{-1}$  indicated alkane dehydrogenation to an alkene. Reprinted with permission from ref 24. Copyright 2005 American Chemical Society.

The observation of this peak suggested to the authors the dehydrogenation of the long chain alkane to alkene and indirect confirmation of  $\text{H}_2\text{Se}$  evolution. While not an unreasonable conclusion, the authors largely based these hypotheses on a broad shoulder absorption peak. Standard IR spectrum tables suggest a medium intensity for a C=C  $\text{sp}^2$  stretch.<sup>25</sup> We offer the following reasons further supporting the existence of the low intensity peak. Weaker signals could likely appear due to an embedded *trans*-disubstituted alkene, but this would appear at slightly higher wavenumbers ( $1678\text{--}1668\text{ cm}^{-1}$ ). While it could be that the broad shoulder peak at  $1650\text{ cm}^{-1}$  was due to an alkene stretch within a long hydrocarbon chain, effectively weakening the alkene stretch and shifting the corresponding peaks toward lower wavenumbers than predicted, the lack of this discussion and complementary characterizations weaken their hypotheses. Another reason that could have resulted in the same FTIR spectrum would have been the low concentration of alkene



observed in FTIR the proposed ammonium fragment ( $[\text{H}_3\text{N}]^+$ ) via a broad N–H stretching band, highlighted by the light blue band ( $\nu(\text{N–H}) = 2700\text{--}3100\text{ cm}^{-1}$ ) in Figure 3.7. This was separate from the expected surface bound amine ( $\nu(\text{N–H}) = 3000\text{--}3400\text{ cm}^{-1}$ ) and alkyl chains ( $\nu(\text{C–H}) = 2700\text{--}3000\text{ cm}^{-1}$ ). This is significant as the stretch was only visible after subtracting the spectrum of the control  $\text{CdSe-NH}_2\text{R}'$  from the spectrum of the complexed ligand ( $\text{CdSe-NH}_2\text{R}'/[\text{O}_2\text{CR}]^-[\text{H}_3\text{NR}'^+]$ ). The predicted carboxylate ion was observed through a carboxylate ( $\text{C–O–O–R}$ ) stretching band distinct from the expected bands of OA, a mixture of OA and  $\text{CdSe-Cd}(\text{O}_2\text{CR})_2$ , and  $\text{CdSe-NH}_2\text{R}'$ . These two key observations supported the formation and tight binding of ammonium oleate to the NP surface which was formed by the addition of acidic molecules to  $\text{CdSe-NH}_2\text{R}'$ . This finding is noteworthy as the subtlety of the FTIR signature for  $[\text{H}_3\text{N}]^+$  could have been overlooked at first glance because the broad N–H band overlapped the alkyl chain stretching band.

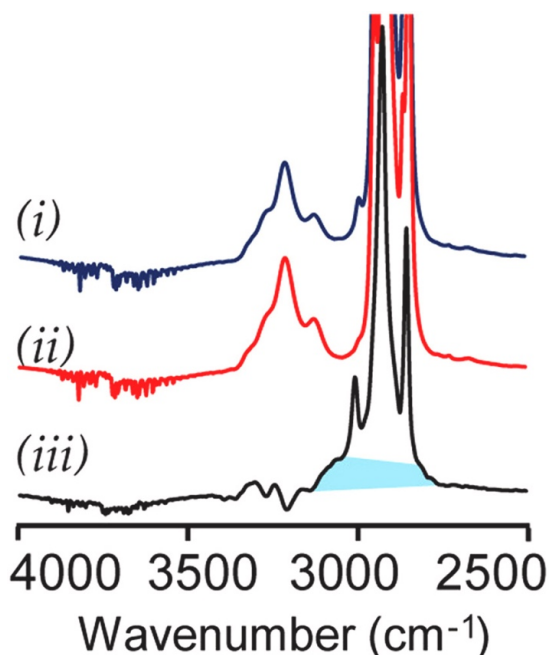


**Figure 3.7.** FTIR spectrum of (i)  $\text{CdSe-NH}_2\text{R}'/[\text{O}_2\text{CR}]^-[\text{H}_3\text{NR}'^+]$  ( $\text{R} = \text{oleyl}$ ,  $\text{R}' = \text{n-octyl}$ ) prepared from anhydrous oleic acid, (ii)  $\text{CdSe-NH}_2\text{R}'$  ( $\text{R}' = \text{n-octyl}$ ), and (iii) their difference spectrum. Stretch characterizing  $[\text{H}_3\text{N}]^+$  ( $\nu(\text{N–H})$ ) is highlighted in light blue. Adapted with permission from ref 26. Copyright 2017 American Chemical Society.

Ultimately, these examples highlight the usefulness of FTIR as a qualitative technique. Extrapolating this characterization method to understand ternaries and other multinary systems would be straightforward as the method does not require the samples to be well-suspended, like in NMR, to gain qualitative information such as the possible identity of ligands or solvent species. Characterization of ligand identity and speciation could then inform on reaction mechanisms such as solvent (i.e. Deng et al.<sup>24</sup>) or ligand (i.e. Chen et al.<sup>26</sup>) transformations.

### 3.1.3. Mass Spectrometry to Support the Presence of Reaction Species Interactions

Mass spectrometry (MS) is a valuable technique to separate the organic speciation of NP syntheses. On its own, however, the data analysis poses difficulty due to the breadth of possible species that could be identified, as demonstrated in a report by Bullen et al.<sup>16</sup> This posits MS as a good complementary technique in which the data could be used as evidence to support hypothesized chemical processes but does not necessarily distinguish between active and inactive components for NP formation. Specific to this study, the interaction of Se and ODE was uncovered via <sup>1</sup>H–<sup>13</sup>C HSQC NMR; thus, EI MS and <sup>77</sup>Se NMR were used to identify possible chalcogen species. When monoolefins are heated in the presence of sulfur or selenium, a diversity of transformations can occur by vulcanization, 2-electron oxidation, and radicals. Thus, in assigning MS data, it was worth considering all possible Se-ODE interactions. Positive EI mass spectra of Se-ODE samples were studied. Five singly charged species were detected: ODE ( $m/z = 252$ ), ODE+Se ( $m/z = 331$ ), ODE+ 2Se ( $m/z = 410$ ), 2ODE+Se ( $m/z = 586$ ), and 2ODE+ 2Se ( $m/z = 664$ ). Moreover, a control reaction using gel permeation chromatography was performed to ensure that the individual contributions to the mass spectra were not arising purely from fragmentation. As the authors noted, only broad conclusions on the reaction mechanism of Se with ODE could be gathered because both reactive and unreactive species are likely produced concurrently.

Mass spectrometry is a powerful technique in identifying a plethora of organic species because it is based on  $m/z$  ratio and samples are not restricted in requiring specific labeling of certain nuclei, as is the case for solution-based NMR. Moreover, sampling for MS is particularly facile and does not have too many constraints as both gas and liquid phases can be probed which could be advantageous for understanding the composition of the reaction headspace. However, MS is better suited as a complementary technique because its advantages present practical dilemmas. Because of the sensitivity of MS for nominal identification of all the species in the sample, analysis and labeling of the peaks are often difficult without adequate knowledge of what could exist in the sample. The high quantity of  $m/z$  peaks observed could pose difficulty in identifying key species relevant for the reaction mechanism. This can be overcome as compounds typically have unique fragmentation patterns which can be matched with files in the standard NIST database. This is unfortunately limited to common compounds and does not contain all species of interest for the NP community. Further, it is difficult to discern whether detected species are evolved due to the harshness of the ion source or as a possible reaction intermediate. Therefore, MS can be used to support findings from other techniques, or the use of it could be strengthened when alternative hypotheses are also proposed and confirmation bias is avoided.

#### **3.1.4. UV–Vis Spectroscopy**

UV–Vis spectroscopy is typically used to characterize optical properties of NPs and reaction solutions. This technique allows access to characterization of both reaction mechanisms and pathways, and its use demonstrates the difficulty in differentiating between the two processes. An example in which UV–Vis was used to understand reaction mechanism kinetics lies in the work of Srivastava et al.<sup>27</sup> The authors were able to experimentally rank reducing agents in order of reducing power by collecting the absorption spectra of reaction solutions held at room temperature.

This lower temperature resulted in amorphous InAs clusters instead of QDs but was key in slowing down the reaction kinetics sufficiently for distinguishing the relative reaction rates.

One example expanding the use of UV–Vis to investigate the reaction pathway of InP was reported by Gary et al., described in Chapter 1.<sup>28</sup> A lowest energy electronic transition (LEET) UV–Vis technique allowed the authors to observe the existence of magic-sized cluster (MSC) intermediates and led them to propose a two-step nucleation and growth reaction of InP QDs. The technique allowed further investigation of the thermodynamic stability of InP MSCs, enabling the elucidation of different reaction pathways depending on the capping ligand, either carboxylate-terminated or phosphonate-terminated. The authors observed different UV–Vis spectra for the differently-capped MSCs; carboxylate-termination gave rise to one peak while phosphonate-termination showed four. In order to test the thermal stability of MSCs based on capping, the MSCs were isolated and exposed to air over 24 h. This resulted in the observation of absorption broadening for the carboxylate clusters and an unchanged absorption profile for the phosphonate clusters. Thus, a higher stability of the phosphonate-terminated MSCs was rationalized which is reflected in the resultant reaction coordinate plot in Figure 3.8.

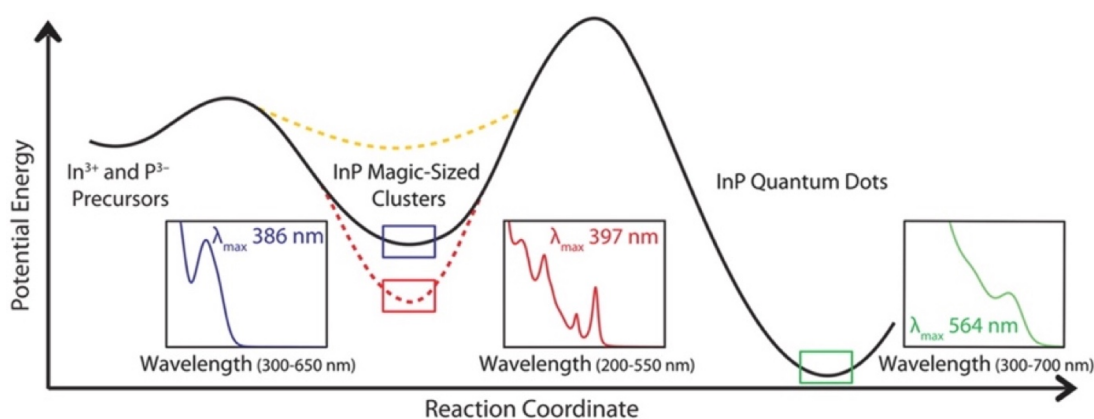


**Figure 3.8.** Reaction coordinate plot of InP QD formation rationalized by UV–Vis LEET data. In violet, carboxylate-terminated InP MSCs; in red, phosphonate-terminated InP MSCs; in green, InP QDs. Yellow dashed path indicates the direct formation of QDs and red dashed route indicates no QD formation. Reprinted with permission from ref 28. Copyright 2015 American Chemical Society.

In the field of quantum-confined NPs or quantum dots (QDs), the phenomenon of quantum confinement extends the use of UV–Vis spectroscopy to the characterization of physical properties. When the spatial dimensions of a material are confined to less than that of the material's Bohr exciton radius, the frontier electron orbitals exist at energy levels within the bands of the bulk semiconductor.<sup>29–31</sup> This ties the size of QDs directly to the magnitude of the optical gap. Thus, UV–Vis spectroscopy is often used for size evaluation of well-known QDs. In conjunction, photoluminescence (PL) spectroscopy is used as a handle for understanding properties such as size dispersion because the PL spectral width is dictated by the size, shape, and composition distribution of a QD ensemble.<sup>29</sup> Measuring these properties can be accomplished both *ex situ* and *in situ*, discussed in the study of CdSe growth kinetics in a review by Kovalenko et al.<sup>5</sup>

The use of this technique continues to advance exemplified by combinatorial *in situ* methods. In a 2018 report, Li et al. gathered IR and UV–Vis spectra to follow the growth mechanisms of QDs by mass conservation.<sup>32</sup> UV–Vis was used specifically to track QD size and concentration. Additionally, we propose this technique could progress understanding on NP reaction syntheses by the development of *in situ* fiber optic methods in which the color of reaction solutions might inform the dynamic inorganic molecular speciation. By understanding the speciation of monomers, advances could be made in understanding NP reaction mechanisms.

### **3.2. Characterization for Elucidating Reaction Pathway**

The techniques mainly used for the characterization, identification, and evaluation of solid phase species (crystalline or amorphous) and their properties include XRD, thermal analysis, XPS, and TEM. We hope the following studies demonstrate sophisticated uses of the techniques to not only characterize final products and starting materials, but also the diverse and complex reaction landscape that exist between these two points.

### **3.2.1. X-ray Diffraction (XRD)**

Powder X-ray diffraction is a common characterization for nanoscale materials to identify the crystalline phases in reaction products, sample purity, crystallite size, and morphology. These features are incredibly useful in gaining insight into the reaction pathway. Beyond examining end products, aliquots at various growth times may also be examined *ex situ*. However, each time an aliquot is taken, the reaction conditions are changed and may possibly affect the reaction pathway. Experimental NP syntheses are normally done on a relatively small scale; thus, the reaction concentrations may be altered even when small volumes are removed. These could lead to abnormal shifts in equilibria and generate misleading or incorrect identification of specific pathways. To ensure that the results of *ex situ* XRD are representative of the reaction conditions, we suggest that the aliquots removed are compared to individual reactions where the entirety of the flask is quenched at matching aliquot time intervals. Best practices for the use of XRD on nanoparticles is described by Holder et al. who describes key aspects in diffraction data analysis with an emphasis on inorganic nanoparticles of various sizes, shapes, and dimensionalities.<sup>33</sup> Greater insight into phase purity, crystal structure morphology, and anisotropic growth mechanisms can be rationalized by the Rietveld method in which parameters such as size, strain, preferential orientation, and sample compositions can be fitted to the raw diffraction pattern.<sup>34-38</sup>

### **3.2.3. Thermal Analysis**

Thermal analysis presents simple techniques useful for probing the phase-purity of NP products. Further, the decomposition of a material can be profiled, offering information on whether the material is a thermodynamic or kinetic product.<sup>39</sup> Employing methods such as thermogravimetric analysis (TGA), differential thermal analysis (DTA), or differential scanning calorimetry (DSC) may provide an indication of the number of phases present in a NP powder

based on the number of transition temperatures observed upon heating. Specifically, Riha et al. from our group employed thermal analysis in the characterization of the first solution-based synthesis for  $\text{Cu}_2\text{ZnSnS}_4$  (CZTS) NPs.<sup>40</sup> The melting points and phase transitions of potential impurities were characterized and compared to that of CZTS samples. Because transitions for the possible impurity phases were detected at lower temperatures than that observed for the CZTS samples, it was inferred that there was a lack of these byproducts in the CZTS samples.<sup>40</sup> These methods can be powerful when complemented with other elemental, phase, and imaging techniques. Due to the possible limitations of these standard methods, thermal analysis may provide purity evidence but does not yield specific compositional or phase evidence alone.

#### **3.2.4. X-ray Photoelectron Spectroscopy and X-ray Absorption Spectroscopy**

X-ray photoelectron spectroscopy (XPS) is a semi-quantitative, surface-sensitive technique that identifies the elemental composition of a sample and the elemental binding environments. This technique can be particularly useful for characterizing solid-phase intermediates and final products of NP syntheses especially for amorphous solids as long-range order is not required. For example, in the work by White et al., XPS on samples from the formation of  $h^*\text{-LiZnSb}$  indicated the presence of an amorphous  $\text{Sb}^0$  intermediate.<sup>20</sup> This was suspected by PXRD because a very broad peak corresponding to the most intense reflection for elemental Sb was observed. XPS on early reaction samples showed three Sb 3d binding environments:  $\text{Sb}(0)$ ,  $\text{Sb}(\text{III})$ , and  $\text{Sb}(\text{V})$ . The +3 and +5 oxidation states were suggested to correspond to free (unreacted) and surface-bound forms of Sb precursor (triphenylstibine,  $\text{Ph}_3\text{Sb}$ ), and the zero-valent species confirmed the amorphous  $\text{Sb}^0$  phase. The identification of elemental oxidation states highlights another advantage of XPS which exists as a complementary handle for characterizing solid-state intermediates in the pursuit of understanding reaction pathways.

Our group has used XPS to study the structure and the stability of NPs under air exposure.<sup>41-43</sup> For example, Riha et al. quantified the oxidation of Cu<sub>2</sub>Se by tracking the Cu:Se ratio.<sup>41</sup> The ratio increased from 2:1–5.2:1 and complementary XRD data indicated the transformation of Cu<sub>2</sub>Se to Cu<sub>1.8</sub>Se. Both data sets suggested the solid-state diffusion of cationic Cu from the particle core to the surface. This finding was particularly useful for Korala et al. in a later study of CZTS NPs synthesized with a Cu<sub>2-x</sub>Se shell.<sup>42</sup> Copper(I) cations in stoichiometric Cu<sub>2</sub>Se NPs generated Cu vacancies in the valence band (“self-doping” of Cu<sub>2</sub>Se to Cu<sub>2-x</sub>Se), increasing the mobile carrier concentration.<sup>41,44</sup> Thus, the authors hypothesized that a conductive shell of Cu<sub>2</sub>Se grown on CZTS would induce self-doping and improve the conductivity of NP thin films upon exposure to air. XPS was used as a complementary technique to confirm the oxidation states of Cu in Cu<sub>2-x</sub>Se. Finally, another oxidation study was done by Fredrick et al. on the surface reactivity of Fe<sub>2</sub>GeS<sub>4</sub>.<sup>43</sup> As-synthesized NPs were studied with XPS, and oxidation of the surface was observed between 0 (several seconds of air exposure) and 24 h. The oxidation of Fe(II) to Fe(III) was observed alongside the transformation of the dominant Ge binding environment from that characteristic of Ge(IV) disulfide to that of GeO<sub>2</sub>. Because these changes are amorphous and could not be detected by PXRD, XPS gave unique information on this process. To alleviate the instability of the particles, ligand exchange was performed to cap the surface with S<sup>2-</sup>. Subsequent XPS spectra demonstrated the slowed oxidation of the Ge species.

XPS is a valuable resource for characterizing the intermediates and end products through the course of a reaction by elucidating elemental binding environments. Beyond identification of amorphous intermediate phases and characterization of NP oxidation, we also believe XPS could be valuable for other investigations. For example, if crystalline and amorphous phases had distinct oxidation states of the same element, they could be identified simultaneously. Additionally, the

measurement of elemental binding environments could inform bond transformations in the study of reaction mechanisms and pathways. However, XPS is limited to solids or samples that are not vulnerable to evacuation of the instrument. Further, due to the surface sensitivity of XPS, the binding environments are more representative of the surface rather than the ensemble. This can be used advantageously but must be kept in mind for all studies.

Another X-ray technique that provides similarly elemental-specific information but is more representative of the bulk of the sample is X-ray absorption spectroscopy. In particular, extended X-ray absorption fine structure (EXAFS) is used to analyze an element's specific local structure and gives a one-dimensional partial pair distribution function. Espinosa-Faller et al. used EXAFS to analyze the local structures of Cu, Zn, and Sn in CZTS NPs.<sup>45</sup> The authors discovered the presence of an aperiodic disorder on the cation sites that diminished with annealing. Liakakos et al. studied the formation of various Co particle morphologies and used EXAFS as a complementary technique to PXRD and TEM.<sup>46</sup> The data confirmed the metallic nature of Co in all of the samples and provided evidence for well-defined local order despite variations in long-range order among the samples.

### **3.2.5. Ex situ Transmission Electron Microscopy (TEM)**

Imaging NP systems by transmission electron microscopy (TEM) is advantageous compared to other techniques because it reveals physical properties in high resolution at the atomic level (Å to nm). While inherently limited by the small sample size observed, it may provide highly detailed structural, morphological, and compositional information including but not limited to structure and defect properties as well as elemental analysis with use of STEM EDS. The combinatorial nature of the properties TEM can probe comes to great use in examining heterostructured NPs in which the spatial orientation of multiple phases is investigated. For

example, core/shell NP syntheses benefit from elemental mapping by STEM EDS, identifying deposition of the shell material on the core rather than nucleation of the shell as NPs on its own.

Here, we highlight this methodology through work by De Trizio et al. in understanding the reaction pathway of  $\text{Cu}_3\text{P}$  NP formation.<sup>47</sup> Images of reaction aliquots sampled throughout the reaction progress revealed two different reaction pathways depending on the TOP:Cu precursor ratio (Figure 3.9): (1) Cu nucleation and subsequent phosphorization, termed a conversion pathway from Cu to  $\text{Cu}_3\text{P}$  NPs or (2) direct  $\text{Cu}_3\text{P}$  nucleation followed by growth, termed a consumption pathway by the authors. These conclusions were drawn by initially probing the roles and functions of the phosphorus precursor, TOP, and suggested capping ligand, TOPO. The concentrations of each were systematically changed and studied over time.

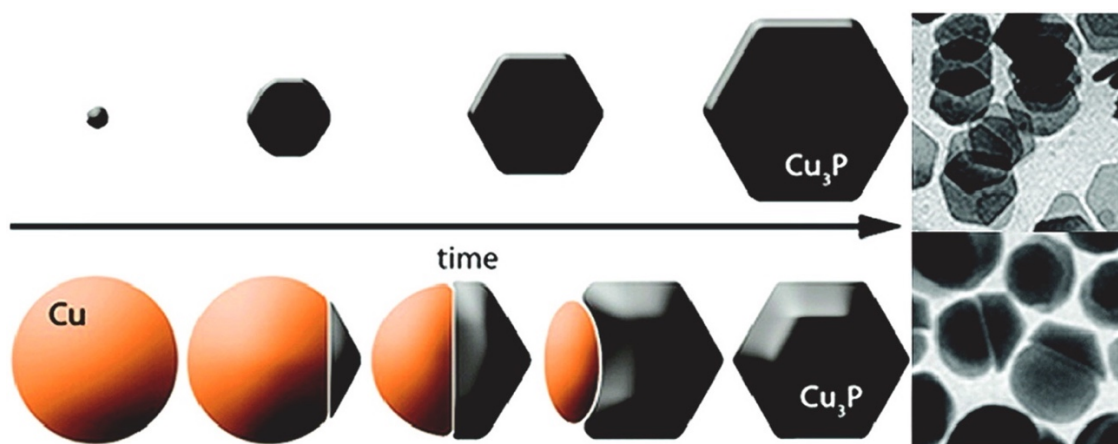


**Figure 3.9.** Reaction pathway to  $\text{Cu}_3\text{P}$  by direct nucleation synthesized with the TOP:Cu molar ratio = 11:1 (top). Reaction pathway to  $\text{Cu}_3\text{P}$  by phosphorization of Cu particles synthesized with the TOP:Cu molar ratio = 5.6:1 (bottom). Reprinted with permission from ref 47. Copyright 2012 American Chemical Society.

When the TOP:Cu molar ratio started at 5.6:1, Janus-type particles were synthesized in which a spherical *fcc*-Cu domain and a hexagonal *hcp*- $\text{Cu}_3\text{P}$  domain co-existed (Figure 3.10). Earlier reaction times revealed isolated Cu particles, and longer reaction times showed fully converted  $\text{Cu}_3\text{P}$  NPs. Thus, the authors hypothesized that phosphorization proceeded from a single site on the Cu particles which then extended into the whole NP. The possibility of inhomogeneous

ligand coverage of the particles was offered due to the following hypothesis. If all sites were homogeneously available, the reaction likely would have proceeded more centrosymmetrically, leading to core-shell type structures.

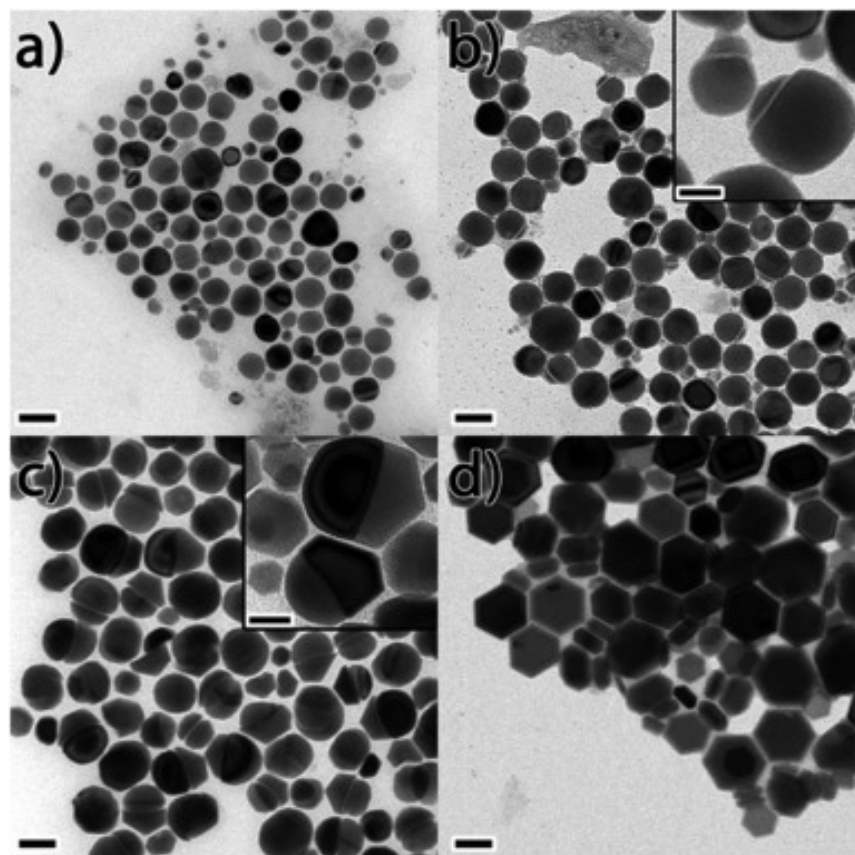


**Figure 3.10.** TEM images documenting the formation of Cu particles and subsequent phosphorization (TOP:Cu molar ratio = 5.6:1). Aliquots collected after (a) 4 min, (b) 10 min, (c) 25 min, (d) 45 min reaction times. The scale bar is 50 nm for the panels and 20 nm for the insets. Reprinted with permission from ref 47. Copyright 2012 American Chemical Society.

When the TOP:Cu molar ratio was 11:1 or greater, the reaction pathway switched to direct  $\text{Cu}_3\text{P}$  nucleation as observed by ex situ TEM (Figure 3.11). Although it was difficult to discern by an ex situ method whether this was a difference in reaction pathway or a result of faster nucleation and growth, the authors observed large differences in the morphologies and phases detected at various reaction times for the two synthetic conditions. Here, the 11:1 TOP:Cu molar ratio resulted in hexagonal plates comprised of only  $\text{Cu}_3\text{P}$  over the whole reaction time length.

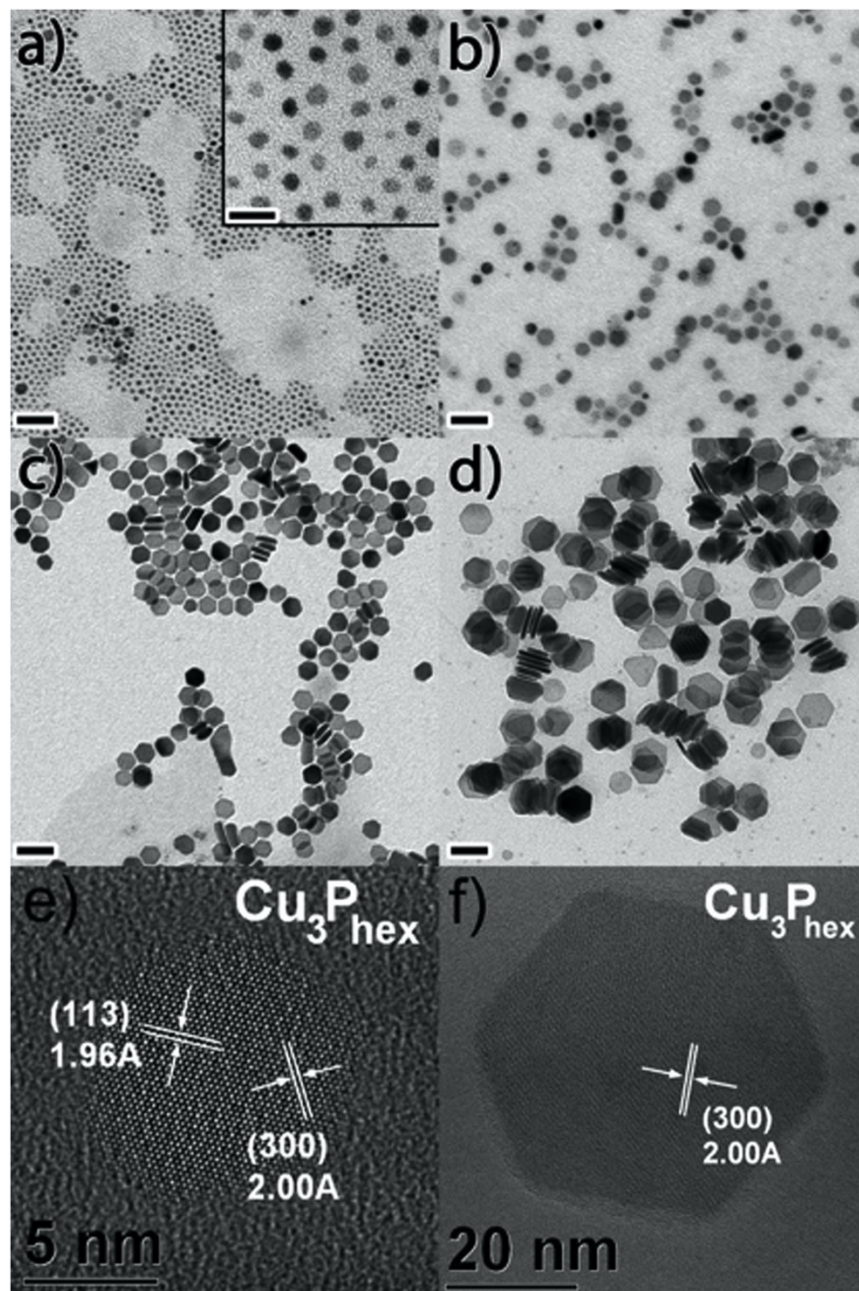


**Figure 3.11.** TEM images tracking the direct formation of  $\text{Cu}_3\text{P}$  nanoplates (TOP:Cu molar ratio = 11:1). Aliquots collected after (a) 10 s, (b) 2 min, (c) 15 min, and (d) 25 min of reaction. The scale bar is 50 nm for the panels and 20 nm for the inset. (e,f) HRTEM images of  $\text{Cu}_3\text{P}$  nanoplates after 10 s and 25 min of reaction, respectively. Adapted with permission from ref 47. Copyright 2012 American Chemical Society.

In situ TEM could have provided higher temporal resolution of the reaction mechanism when compared to ex situ aliquots; however, it is limited by the difficulty in accurately replicating in-flask conditions. De Trizio et al. effectively depicted snapshots of the reaction progress through

the use of ex situ aliquots. The reaction pathway interpretations were strengthened by the use of complementary techniques. In general, while electron microscopy (EM) has the benefits of elemental analysis by STEM EDS and identification of crystalline solids by SAED or HRTEM, it lacks the ability to inform on the organic portion of nanoparticles such as surface ligands or unreacted monomers. EDS could give qualitative insight on whether NP surfaces exhibit a constituent element-rich or -deficient composition, such as the P-rich Cu<sub>3</sub>P NP surfaces reported by Sheets et al.,<sup>16</sup> but more quantitative and accurate techniques describing the identity of these organic ligands such as NMR and IR are available.

### **3.3. Prospects in NP Reaction Characterization: Understanding the Complexity of NP Syntheses**

Nanoparticle synthesis is an interdisciplinary field and involves a wide variety of important components. Referencing Figure 1.2, syntheses are inherently complex with pathways and mechanisms that could simultaneously occur. Many characterization methods are required to probe unique aspects such as molecular interactions or solid phase evolution. Traditionally this has been done through the use of ex situ complementary techniques. In this section, we describe studies that advance NP synthetic characterization through the development of in situ methods which provide temporal observations of processes. Refinement of these techniques require balancing the limitations of the characterization technique while accurately representing the NP reaction in the sample holder. The NP materials employed in these studies are highly studied and well-behaved (i.e. Cd chalcogenides). These act as proof-of-concept systems, and development of their use should lead to progress in a wider range of NP materials.

### 3.3.1. Using Mass Conservation to Rationalize NC Growth via In situ FTIR and UV-Vis Spectroscopies

Li et al. developed a model based on mass conservation to rationalize growth mechanisms of CdS quantum dots (QDs).<sup>32</sup> The model defined the existence of CdS units to exist either as unreacted precursors, NCs, or clusters. Nanocrystals were defined as CdS species with defined crystal structures and lattice parameters corresponding to that of bulk CdS, while clusters encompassed CdS species generally less than 1.5 nm in diameter and potentially lacking periodic crystallinity. Three distinct NC growth channels were identified, all of which involved monomer incorporation in NCs but differed with regard to the origin of the monomer (Figure 3.12).

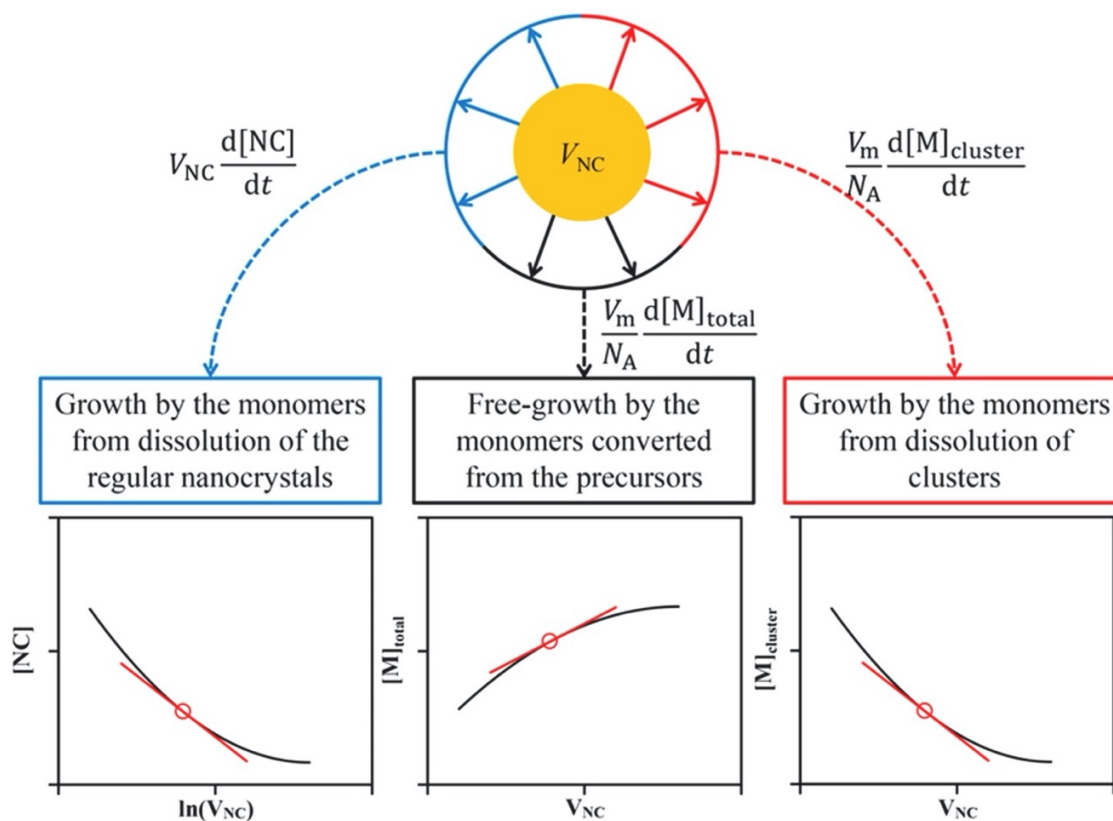


**Figure 3.12.** Three basic reaction channels for CdS growth and their mathematical models. The following terms are defined as: ( $V_{NC}$ ) average volume of monodisperse NCs, ( $[NC]$ ) concentration of nanocrystals, ( $t$ ) time, ( $V_m$ ) molar volume of nanocrystals, ( $[M]_{total}$ ) total concentration of CdS composition units converted from precursors, ( $N_A$ ) Avogadro's number, and ( $[M]_{cluster}$ ) total concentration of composition unit in the form of clusters. Reprinted with permission from ref 32. Copyright 2018 American Chemical Society.

The first channel was defined as incorporation of monomers converted directly from precursors and was termed “focusing of size distribution”. The second and third channels described monomers originating from the dissolution of NCs and clusters, respectively. These channels were associated with the process of “self-focusing of size distribution”. Experimentally, precursor conversion was tracked by liquid-phase Fourier transform infrared (FTIR) spectroscopy, and the NC size and concentration was measured by UV–Vis spectroscopy.

A major discovery from this work was the identification of multiple, simultaneous NC growth channels. This challenged the conventional understanding for NC size-focusing directly after a short burst of nucleation. Due to the inverse relationship of NC growth rate with its diameter, the size distribution of the NC ensemble should narrow. However, this assumes NCs do not dissolve back into solution once formed. Li et al. accounted for multiple monomer dissolution paths in the three growth channels identified and described the contribution of each channel to the total NC volume growth rate at any given time in the calculations depicted in Figure 3.12. Under typical synthetic conditions for CdS, none of the three channels were observed to be dominant. Further, synthetic parameters ([Cd], [OA], [S], [Cd(oleate)<sub>2</sub>], and temperature) were systematically probed in a high-throughput examination of their effect on the growth channels.

In order to track these processes, an automated microreactor system was designed (Figure 3.13). This improved reproducibility, accuracy, and time resolution relative to standard solution-based NP synthetic characterization methods. The CdS synthesis had to be adapted for capillaries, but the reduced volume increased heat transfer rates, eliminating some inherent irreproducibility of typical hot injection syntheses due to temperature variability upon injection of cold precursors. Additionally, NP growth studies typically require removing aliquots to study *ex situ*, which introduces variability by exposure of the reaction to a syringe and the washing of aliquots with

cold solvents. Instead, simultaneous FTIR and UV–Vis spectroscopy measurements were collected in situ, achieving a time resolution on the order of milliseconds between data points. This provided a more accurate view of the reaction components.

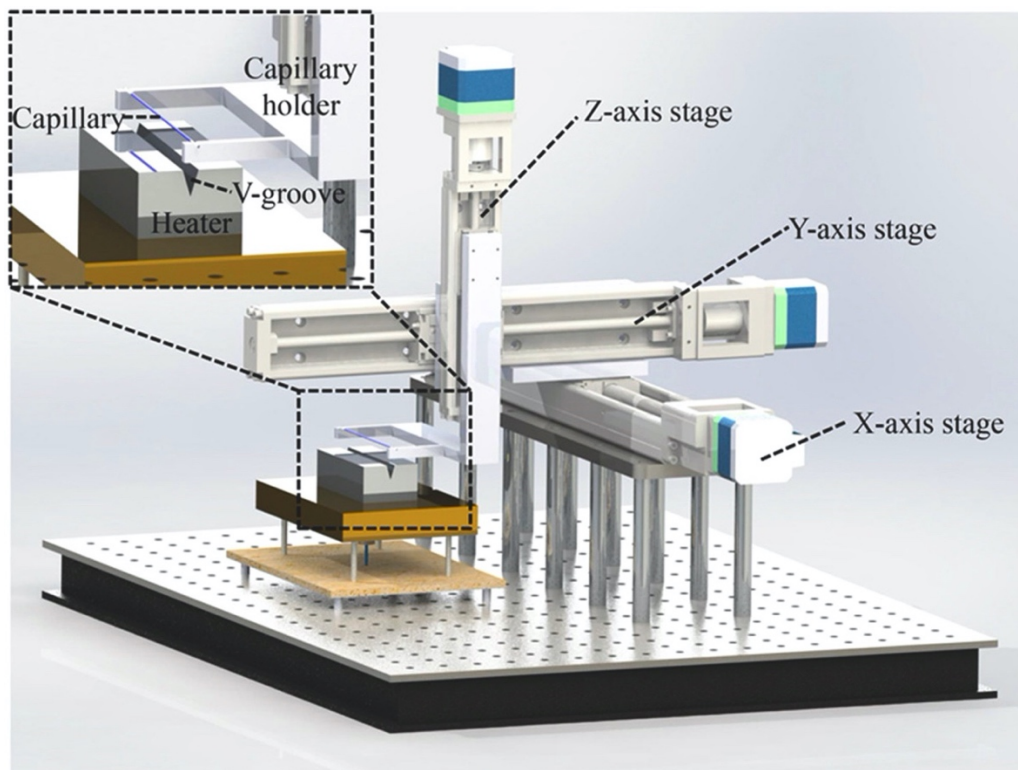


**Figure 3.13.** Schematic of the microreactor system without instrumentation for clarity. Reprinted with permission from ref 32. Copyright 2018 American Chemical Society.

Currently, this method is limited to the characterization of QDs of a sufficiently narrow size distribution. The synthesis of CdS QDs from Cd(oleate)<sub>2</sub> and elemental S in ODE was studied because it is well reported and results in a well-defined growth stage with monodisperse QDs. The authors stated that these theoretical and experimental methods could be extended to polydisperse QD material systems should an experimental descriptor for size distribution be identified. Further extension of this methodology to other NP materials would present other limitations. First, Li et al. relied on the quantum-confinement of CdS NCs to measure their concentration and size by UV–Vis. Extension to non-quantum-confined NPs would require identification of a rapid measurement

for their detection in solution. Second, it would be difficult to study a more complex, multinary system that could possibly undergo a higher number of simultaneous reaction channels due to a larger range of unique intermediates. Identification of spectroscopic signatures for the conversion of precursors, the formation of all intermediates, and the growth of the end products would stand as a major challenge. However, this study has demonstrated an advancement in the in situ detection of concurrent reaction pathways and intermediates for a highly-studied CdS QD synthesis.

An example for a future direction of this instrumental technique could be in gaining insight on III-V InAs QDs. Although we recognize there are plenty of systems that are eligible to be studied by this microreactor system, the synthesis from Srivastava et al.<sup>27</sup> could be a significant next step. The properties of these InAs QDs meet the criteria of the microreactor system but also present an example from a class of materials that is often not considered as well-behaved as II-VI NC systems. Typical syntheses of III-V materials have resulted in broad size distributions due to the small library of pnictide precursors, many of which are highly reactive and exhibit uncontrolled formations of NPs. Srivastava et al. identified a reaction route to small, monodisperse InAs QDs.<sup>27</sup> The authors reported absorption spectra of InAs could be collected on dilute aliquots taken directly from the reaction solution, and well-resolved excitonic features could be observed for all sizes, allowing for the system to be probed by UV-Vis. Additionally, the authors reported the ability to translate the hot injection synthesis to the heat-up method without sacrificing size distribution, encouraging for the potential adaption to capillary use. However, Li et al. argued that a “well-defined” growth stage was required to actually detect these different growth channels.<sup>32</sup> The QD formation of InAs is reported to follow the LaMer model,<sup>48</sup> but it would be interesting to test the sensitivity and capability of the microreactor methodology in this less-explored system.

### 3.3.2. In situ Synchrotron X-ray Scattering Studies

Another prospective method is the use of synchrotron-based in situ small- and wide-angle X-ray scattering (SAXS and WAXS, respectively) to probe the formation of NPs. These methods provide insight into the mechanistic pathway of a reaction by examining the rate-limiting step as well as the reaction pathway by time-resolved identification of formed species. Preliminarily, well-behaved, well-understood CdSe NPs were examined by Abécassis et al. to differentiate between different growth pathways of the NPs (Figure 3.14).<sup>49</sup> The advantage of in situ measurements is the ability to have continuous data feedback and a consistent sample throughout the reaction. Removal of aliquots for ex situ studies may unexpectedly affect the concentration of reactants and species present in the reaction flask. Although the use of a capillary system raises concern on the accurate representation of a typical reaction volume, Abécassis et al. described how the in situ system can characterize on the order of  $10^{17}$  NPs simultaneously.

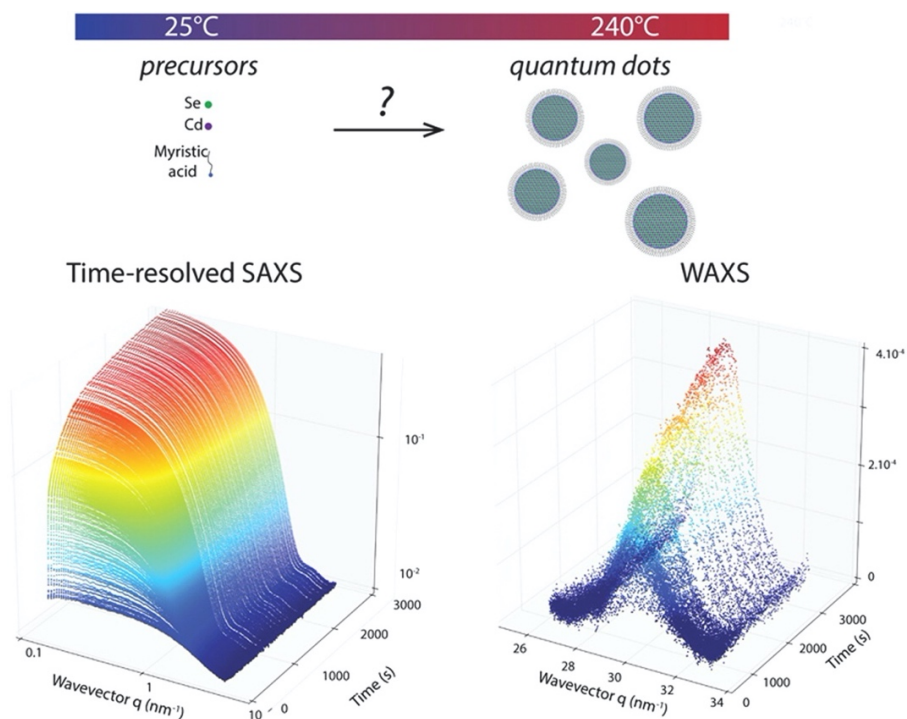


**Figure 3.14.** Time-resolved SAXS and WAXS data used to elucidate the reaction steps from precursors to QDs. Reprinted with permission from ref 49. Copyright 2015 American Chemical Society.

The SAXS signal is sensitive to the size of NPs and its magnitude is directly proportional to the concentration. The complementary WAXS technique characterizes the phase and degree of crystallinity of a crystalline sample. By juxtaposing the data of temperature of the reaction system, mean radius, polydispersity, yield, and concentration of the NPs as a function of time, the authors were able to describe the nucleation and growth pathways for CdSe NPs synthesized with cadmium myristate (CdMyr), Se powder, and ODE (Figure 3.15).

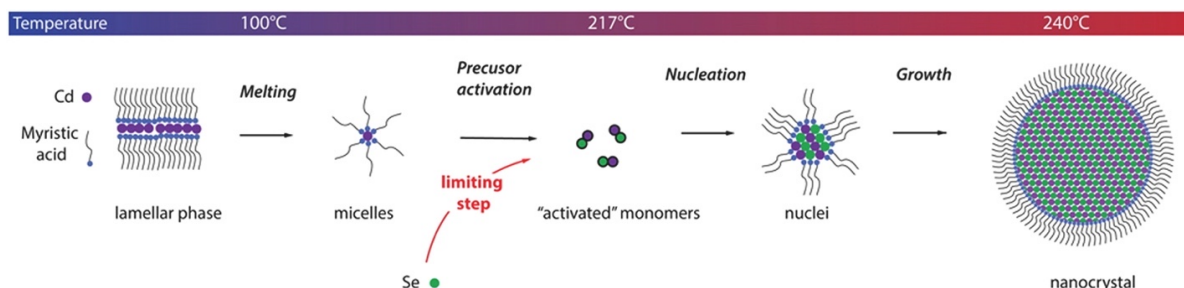


**Figure 3.15.** Reaction pathway scheme to CdSe NPs enabled by in situ SAXS and WAXS. The authors hypothesized that the rate-limiting step was the generation of activated monomers. Reprinted with permission from ref 49. Copyright 2015 American Chemical Society.

The strength of this protocol was the ability to track the nucleation event as a function of temperature, often a highly challenging step to observe and characterize due to its rapid occurrence. As the temperature ramped, the intensity of the low  $q$  profile in SAXS (corresponding to the dispersed CdMyr precursor in ODE) decreased. It was determined that Se powder dispersed in ODE did not have a measurable contribution, so this signified the dissolution of the Cd precursor into molecular monomers. After the SAXS profile briefly remained unchanged, the intensity of the low  $q$  scattering increased when the temperature was raised from 205 to 215 °C which the authors hypothesized to be the onset of NP formation. Nucleation stopped at the maximum reaction temperature of 240 °C. Moreover, the authors considered three different growth-limiting mechanisms: (1) diffusion-limited growth, (2) NP surface limited growth, and (3) precursor to monomer conversion limited growth. The observed growth rate was eight orders of magnitude

lower than the expected theoretical diffusion-limited growth, and the experimental data did not fit calculations for growth limitation by reaction at the NP interface. Therefore, the authors suggested that monomer generation limited the NP growth and hypothesized this was due to the required reduction of Se in order to react with the Cd precursor.

### **3.3.3. Outlook of In situ X-ray Diffraction for NP Synthesis**

Often, the difficulty in establishing in situ techniques is the robustness required from the method to accommodate the harsh environments at which many of these NP syntheses operate, such as chemically reducing environments, high temperature, and/or high pressure. Several in situ techniques for monitoring NP growth as well as chemical and structural transformations are reviewed by Kovalenko et al.<sup>5</sup> Other in situ techniques for studying the surface of NPs in reactive and corrosive environments (i.e. humid air, acidic solutions, etc.) are highlighted by Tao et al.<sup>50</sup>

A method for in situ PXRD study of hydrothermal nanoparticle formation was developed by Andersen et al. (Figure 3.16).<sup>51</sup> Specifically, a hydrothermal synthesis of  $\gamma$ -Fe<sub>2</sub>O<sub>3</sub> was adapted for capillaries allowing second-scale time-resolved observation of the materials' crystallization and growth. The work provides an in-depth experimental approach highlighting the considerations necessary to conduct in situ PXRD experiments at a synchrotron beam source. For example, the group suggested maximizing precursor concentration to provide more diffracting material, resulting in better counting statistics. However, they cautioned this unavoidably sacrifices how the reaction is represented because precursor concentrations affect reaction mechanisms and pathways. Additionally, the authors examined the reproducibility of data collection and analysis by measuring 10 equivalent samples. Ultimately, the report reads as a standard operating procedure and is a unique compendium of detailed, practical experimental information.

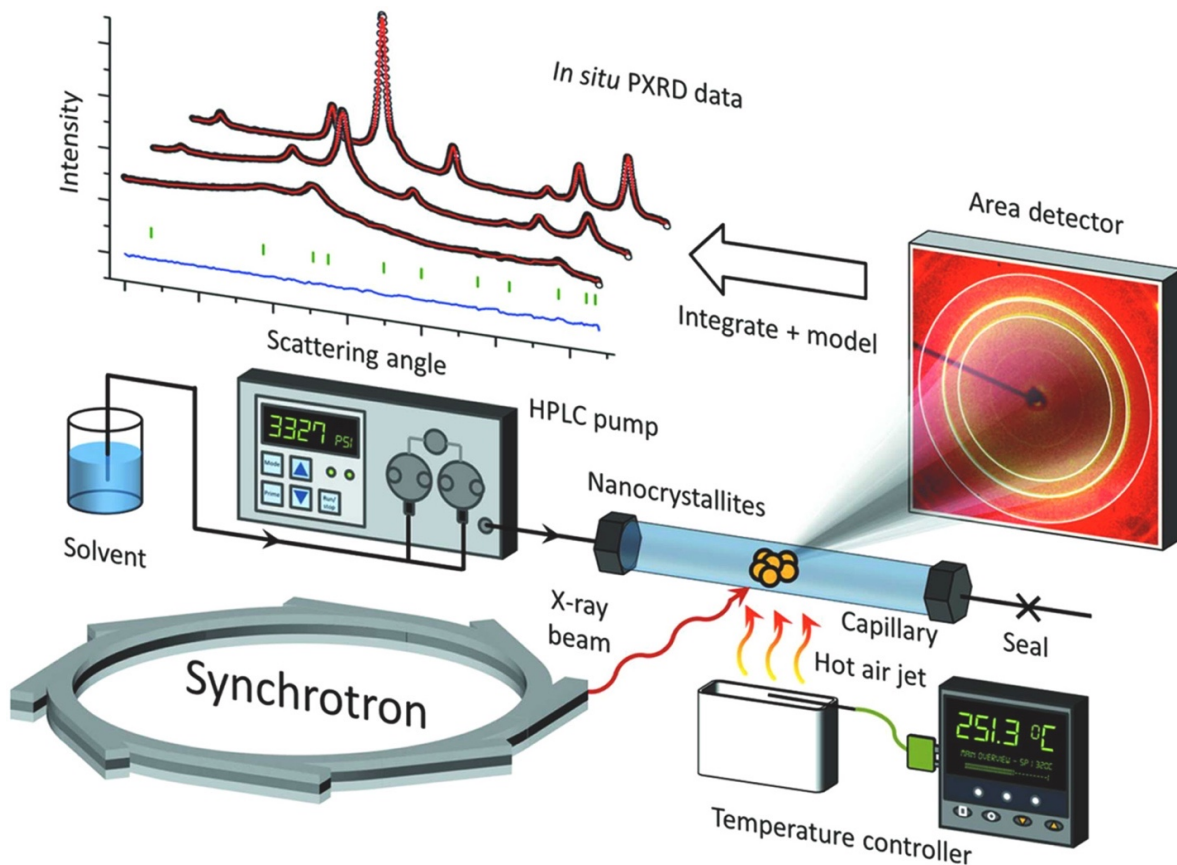


**Figure 3.16.** Graphic representation of in situ synchrotron XRD methodology. Reproduced with permission of the International Union of Crystallography from ref 51.

These techniques, while innovative and pioneering for the field, still required complementary techniques to describe and support conclusions for well-behaved, well-characterized systems. The increased use of in situ characterization methods will require the development of standard techniques in the examination of more complex NP systems which involve unique considerations. More complex reaction mixtures may present species without straightforward, signatory properties for detection, and the addition of competing reaction pathways adds difficulty in deconvoluting the effects of various important parameters. Considering the often observed variability in size dispersion of more complex NP materials, this nonuniformity would open further variables in terms of possible reaction mechanisms and pathways.

### 3.4. Characterization Summary and Perspective

Represented in Figure 3.17 are the techniques commonly utilized for characterization of solution-based NP syntheses. This is by no means an exhaustive list as new advancements and clever strategies can target characterization in unexpected ways. The components in the flask depict possible steps from precursors to end products, represented similarly in Figure 1.2. The green arrows represent possible reaction mechanism transformations, and the black arrows are steps of reaction pathways. Many of these processes occur simultaneously, underscoring the inherent complexity of NP syntheses. However, characterization is commonly carried out on individual components and transformations, which are grouped by relevant techniques and are circled within the flask.

Reaction mechanism processes are typically described by NMR, IR, UV–Vis, and MS. These techniques are particularly useful in describing molecular species and are highly developed for describing the transformation of monomers and ligand coordination. However, their use does not typically extend to the solid-state components which are commonly characterized by XRD, TEM, Raman, thermal analysis, UV–Vis, and XPS. While traditional characterization is performed on isolated components of NP syntheses, ongoing research includes the development and advancement of multidisciplinary characterization methods to observe speciation changes and to elucidate and deconvolute complex reaction schemes and landscapes in solution-based reactions with the goals of enabling and rapidly expanding NP synthesis and architecture control.

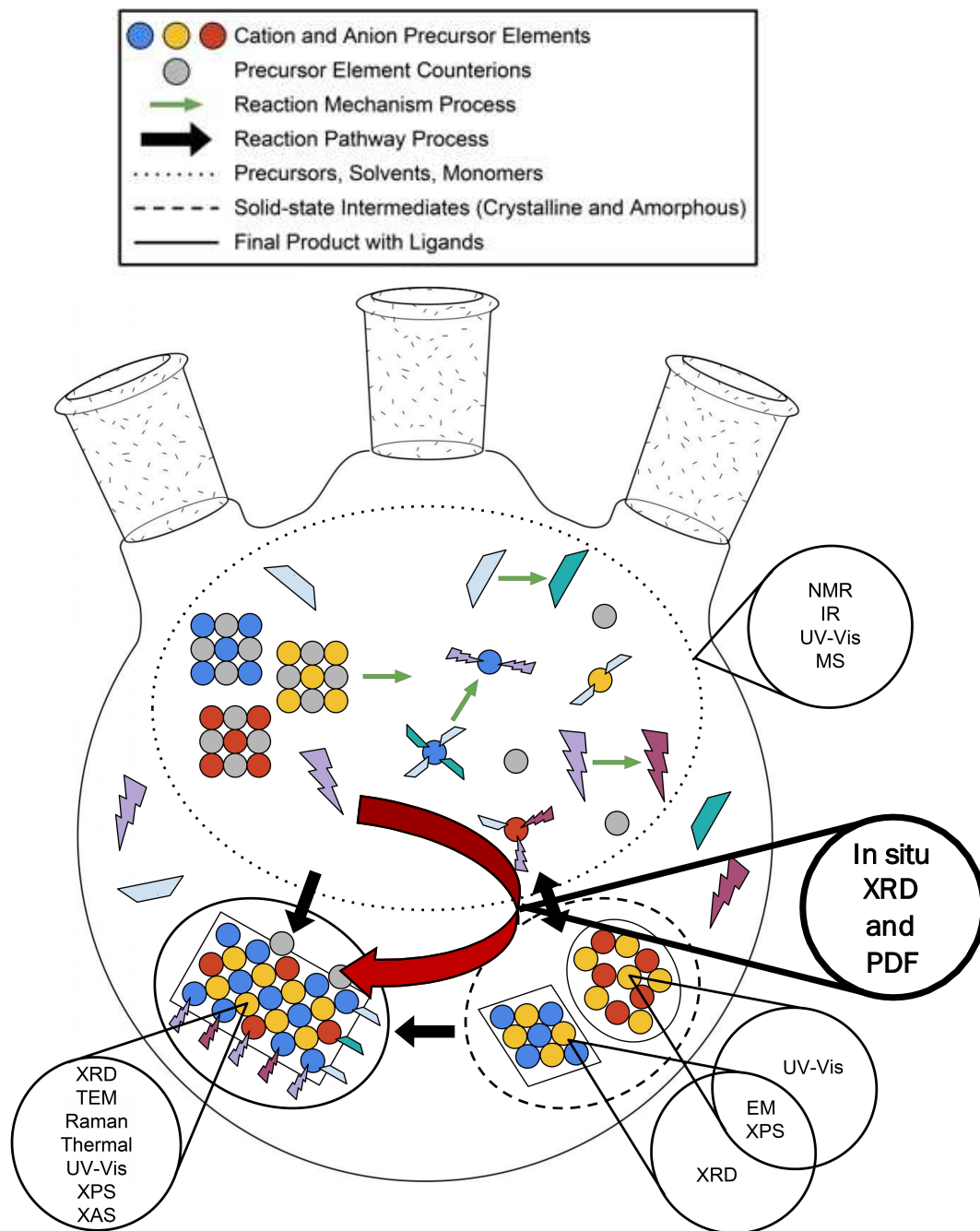


**Figure 3.17.** A cartoon representation of a dynamic NP synthesis labeled with characterization methods to identify specified reaction species. For example, precursors, solvents, and monomers (encompassed within a dotted circle) can be characterized by NMR, IR, UV–Vis, and MS. Solvent molecules are represented with purple lightning bolts and light blue trapezoids. Subsequent transformations of these species are represented with a color hue change (i.e. purple to magenta and light blue to teal). Amorphous intermediate species can be characterized by UV-Vis and crystalline intermediate species can be characterized by XRD although both species could be characterized by electron microscopy and XPS. In situ methods mark an opportunity to capture some of these processes as they are occurring and could capture more than one process with one technique (denoted by a red arrow).

## REFERENCES

- (1) Murphy, C. J.; Buriak, J. M. Best Practices for the Reporting of Colloidal Inorganic Nanomaterials. *Chem. Mater.* **2015**, *27* (14), 4911–4913.
- (2) García-Rodríguez, R.; Hendricks, M. P.; Cossairt, B. M.; Liu, H.; Owen, J. S. Conversion Reactions of Cadmium Chalcogenide Nanocrystal Precursors. *Chem. Mater.* **2013**, *25* (8), 1233–1249.
- (3) Reiss, P.; Carrière, M.; Lincheneau, C.; Vaure, L.; Tamang, S. Synthesis of Semiconductor Nanocrystals, Focusing on Nontoxic and Earth-Abundant Materials. *Chem. Rev.* **2016**, *116* (18), 10731–10819.
- (4) Sowers, K. L.; Swartz, B.; Krauss, T. D. Chemical Mechanisms of Semiconductor Nanocrystal Synthesis. *Chem. Mater.* **2013**, *25* (8), 1351–1362.
- (5) Kovalenko, M. V.; Manna, L.; Cabot, A.; Hens, Z.; Talapin, D. V.; Kagan, C. R.; Klimov, V. I.; Rogach, A. L.; Reiss, P.; Milliron, D. J.; et al. Prospects of Nanoscience with Nanocrystals. *ACS Nano* **2015**, *9* (2), 1012–1057.
- (6) Hens, Z.; Martins, J. C. A Solution NMR Toolbox for Characterizing the Surface Chemistry of Colloidal Nanocrystals. *Chem. Mater.* **2013**, *25* (8), 1211–1221.
- (7) Boles, M. A.; Ling, D.; Hyeon, T.; Talapin, D. V. The Surface Science of Nanocrystals. *Nat. Mater.* **2016**, *15* (2), 141–153.
- (8) Thomson, J. W.; Nagashima, K.; Macdonald, P. M.; Ozin, G. A. From Sulfur–Amine Solutions to Metal Sulfide Nanocrystals: Peering into the Oleylamine–Sulfur Black Box. *J. Am. Chem. Soc.* **2011**, *133* (13), 5036–5041.
- (9) Steckel, J. S.; Yen, B. K. H.; Oertel, D. C.; Bawendi, M. G. On the Mechanism of Lead Chalcogenide Nanocrystal Formation. *J. Am. Chem. Soc.* **2006**, *128* (40), 13032–13033.
- (10) Liu, H.; Owen, J. S.; Alivisatos, A. P. Mechanistic Study of Precursor Evolution in Colloidal Group II–VI Semiconductor Nanocrystal Synthesis. *J. Am. Chem. Soc.* **2007**, *129* (2), 305–312.
- (11) Anderson, N. C.; Owen, J. S. Soluble, Chloride-Terminated CdSe Nanocrystals: Ligand Exchange Monitored by  $^1\text{H}$  and  $^{31}\text{P}$  NMR Spectroscopy. *Chem. Mater.* **2013**, *25* (1), 69–76.
- (12) Anderson, N. C.; Hendricks, M. P.; Choi, J. J.; Owen, J. S. Ligand Exchange and the Stoichiometry of Metal Chalcogenide Nanocrystals: Spectroscopic Observation of Facile Metal-Carboxylate Displacement and Binding. *J. Am. Chem. Soc.* **2013**, *135* (49), 18536–18548.
- (13) De Keukeleere, K.; Coucke, S.; De Canck, E.; Van Der Voort, P.; Delpech, F.; Coppel, Y.; Hens, Z.; Van Driessche, I.; Owen, J. S.; De Roo, J. Stabilization of Colloidal Ti, Zr, and Hf Oxide Nanocrystals by Protonated Tri-*n*-Octylphosphine Oxide (TOPO) and Its Decomposition Products. *Chem. Mater.* **2017**, *acs.chemmater.7b04580*.
- (14) García-Rodríguez, R.; Liu, H. Solution Structure of Cadmium Carboxylate and Its Implications for the Synthesis of Cadmium Chalcogenide Nanocrystals. *Chem. Commun.* **2013**, *49* (71), 7857.
- (15) Schoefberger, W.; Schlagnitweit, J.; Müller, N. Recent Developments in Heteronuclear Multiple-Bond Correlation Experiments. *Annu. Reports NMR Spectrosc.* **2011**, *72*, 1–60.
- (16) Bullen, C.; van Embden, J.; Jasieniak, J.; Cosgriff, J. E.; Mulder, R. J.; Rizzardo, E.; Gu,

- M.; Raston, C. L. High Activity Phosphine-Free Selenium Precursor Solution for Semiconductor Nanocrystal Growth. *Chem. Mater.* **2010**, *22* (14), 4135–4143.
- (17) Frenette, L. C.; Krauss, T. D. Uncovering Active Precursors in Colloidal Quantum Dot Synthesis. *Nat. Commun.* **2017**, *8* (1), 2082.
- (18) Kravchyk, K.; Protesescu, L.; Bodnarchuk, M. I.; Krumeich, F.; Yarema, M.; Walter, M.; Guntlin, C.; Kovalenko, M. V. Monodisperse and Inorganically Capped Sn and Sn/SnO<sub>2</sub> Nanocrystals for High-Performance Li-Ion Battery Anodes. *J. Am. Chem. Soc.* **2013**, *135* (11), 4199–4202.
- (19) Norris, D. J.; Yao, N.; Charnock, F. T.; Kennedy, T. A. High-Quality Manganese-Doped ZnSe Nanocrystals. *Nano Lett.* **2001**, *1* (1), 3–7.
- (20) White, M. A.; Baumler, K. J.; Chen, Y.; Venkatesh, A.; Medina-Gonzalez, A. M.; Rossini, A. J.; Zaikina, J. V.; Chan, E. M.; Vela, J. Expanding the I–II–V Phase Space: Soft Synthesis of Polytropic Ternary and Binary Zinc Antimonides. *Chem. Mater.* **2018**, *30* (17), 6173–6182.
- (21) Chan, E. M.; Xu, C.; Mao, A. W.; Han, G.; Owen, J. S.; Cohen, B. E.; Milliron, D. J. Reproducible, High-Throughput Synthesis of Colloidal Nanocrystals for Optimization in Multidimensional Parameter Space. *Nano Lett.* **2010**, *10* (5), 1874–1885.
- (22) Wang, F.; Tang, R.; Buhro, W. E. The Trouble with TOPO; Identification of Adventitious Impurities Beneficial to the Growth of Cadmium Selenide Quantum Dots, Rods, and Wires. *Nano Lett.* **2008**, *8* (10), 3521–3524.
- (23) Kopping, J. T.; Patten, T. E. Identification of Acidic Phosphorus-Containing Ligands Involved in the Surface Chemistry of CdSe Nanoparticles Prepared in Tri-N-Octylphosphine Oxide Solvents. *J. Am. Chem. Soc.* **2008**, *130* (17), 5689–5698.
- (24) Deng, Z.; Cao, L.; Tang, F.; Zou, B. A New Route to Zinc-Blende CdSe Nanocrystals: Mechanism and Synthesis. *J. Phys. Chem. B* **2005**, *109* (35), 16671–16675.
- (25) Socrates, G. *Infrared and Raman Characteristic Group Frequencies: Tables and Charts*; John Wiley & Sons, 2004.
- (26) Chen, P. E.; Anderson, N. C.; Norman, Z. M.; Owen, J. S. Tight Binding of Carboxylate, Phosphonate, and Carbamate Anions to Stoichiometric CdSe Nanocrystals. *J. Am. Chem. Soc.* **2017**, *139* (8), 3227–3236.
- (27) Srivastava, V.; Dunietz, E.; Kamysbayev, V.; Anderson, J. S.; Talapin, D. V. Monodisperse InAs Quantum Dots from Aminoarsine Precursors: Understanding the Role of Reducing Agent. *Chem. Mater.* **2018**, *30* (11), 3623–3627.
- (28) Gary, D. C.; Terban, M. W.; Billinge, S. J. L.; Cossairt, B. M. Two-Step Nucleation and Growth of InP Quantum Dots via Magic-Sized Cluster Intermediates. *Chem. Mater.* **2015**, *27* (4), 1432–1441.
- (29) Pietryga, J. M.; Park, Y.-S.; Lim, J.; Fidler, A. F.; Bae, W. K.; Brovelli, S.; Klimov, V. I. Spectroscopic and Device Aspects of Nanocrystal Quantum Dots. *Chem. Rev.* **2016**, *116* (18), 10513–10622.
- (30) Smith, A. M.; Nie, S. Semiconductor Nanocrystals: Structure, Properties, and Band Gap Engineering. *Acc. Chem. Res.* **2010**, *43* (2), 190–200.
- (31) Carey, G. H.; Abdelhady, A. L.; Ning, Z.; Thon, S. M.; Bakr, O. M.; Sargent, E. H. Colloidal Quantum Dot Solar Cells. *Chem. Rev.* **2015**, *115* (23), 12732–12763.
- (32) Li, J.; Wang, H.; Lin, L.; Fang, Q.; Peng, X. Quantitative Identification of Basic Growth Channels for Formation of Monodisperse Nanocrystals. *J. Am. Chem. Soc.* **2018**, *140* (16), 5474–5484.

- (33) Holder, C. F.; Schaak, R. E. Tutorial on Powder X-Ray Diffraction for Characterizing Nanoscale Materials. *ACS Nano* **2019**, *13* (7), 7359–7365.
- (34) A. Martinez. Quantitative Phase Analysis from Powder Diffraction Using de Rietveld Method in Hydrogen Storage Alloys Based on TiCr. *J. Phys. Conf. Ser.*
- (35) Wang, Y.; Lap, S.; Chan, I.; Amal, R.; Shen, Y. R.; Kiatkittipong, K. XRD Anisotropic Broadening of Nano-Crystallites. *Adv. X-ray Anal.* **2011**, *54*, 92–100.
- (36) Girgsdies, F.; Fritz-Haber-Institut der Max-Planck-Gesellschaft. Powder X-Ray Diffraction: Phase Analysis and Pattern Fitting.
- (37) León-Reina, L.; García-Maté, M.; Álvarez-Pinazo, G.; Santacruz, I.; Vallcorba, O.; Torre, A. G. D. la; Aranda, M. A. G. Accuracy in Rietveld Quantitative Phase Analysis: A Comparative Study of Strictly Monochromatic Mo and Cu Radiations. *J. Appl. Crystallogr.* **2016**, *49* (Pt 3), 722.
- (38) Ungár, T. The Meaning of Size Obtained from Broadened X-Ray Diffraction Peaks. *Adv. Eng. Mater.* **2003**, *5* (5), 323–329.
- (39) Chamorro, J. R.; McQueen, T. M. Progress toward Solid State Synthesis by Design. *Acc. Chem. Res.* **2018**, acs.accounts.8b00382.
- (40) Riha, S. C.; Parkinson, B. A.; Prieto, A. L. Solution-Based Synthesis and Characterization of Cu<sub>2</sub>ZnSnS<sub>4</sub> Nanocrystals. *J. Am. Chem. Soc.* **2009**, *131* (34), 12054–12055.
- (41) Riha, S. C.; Johnson, D. C.; Prieto, A. L. Cu<sub>2</sub>Se Nanoparticles with Tunable Electronic Properties Due to a Controlled Solid-State Phase Transition Driven by Copper Oxidation and Cationic Conduction. *J. Am. Chem. Soc.* **2011**, *133* (5), 1383–1390.
- (42) Korala, L.; McGoffin, J. T.; Prieto, A. L. Enhanced Conductivity in CZTS/Cu<sub>2-x</sub>Se Nanocrystal Thin Films: Growth of a Conductive Shell. *ACS Appl. Mater. Interfaces* **2016**, *8* (7), 4911–4917.
- (43) Fredrick, S. J.; Prieto, A. L. Solution Synthesis and Reactivity of Colloidal Fe<sub>2</sub>GeS<sub>4</sub>: A Potential Candidate for Earth Abundant, Nanostructured Photovoltaics. *J. Am. Chem. Soc.* **2013**, *135* (49), 18256–18259.
- (44) Kriegel, I.; Jiang, C.; Rodríguez-Fernández, J.; Schaller, R. D.; Talapin, D. V.; da Como, E.; Feldmann, J. Tuning the Excitonic and Plasmonic Properties of Copper Chalcogenide Nanocrystals. *J. Am. Chem. Soc.* **2012**, *134* (3), 1583–1590.
- (45) Espinosa-Faller, F. J.; Conradson, D. R.; Riha, S. C.; Martucci, M. B.; Fredrick, S. J.; Vogel, S.; Prieto, A. L.; Conradson, S. D. Neutron Diffraction and X-Ray Absorption Fine Structure Evidence for Local Lattice Distortions and Aperiodic Antisite Substitution in Cu<sub>2</sub>ZnSnS<sub>4</sub> Nanoparticles. *J. Phys. Chem. C* **2014**, *118* (45), 26292–26303.
- (46) Liakakos, N.; Cormary, B.; Li, X.; Lecante, P.; Respaud, M.; Maron, L.; Falqui, A.; Genovese, A.; Vendier, L.; Koïnis, S.; et al. The Big Impact of a Small Detail: Cobalt Nanocrystal Polymorphism as a Result of Precursor Addition Rate during Stock Solution Preparation. *J. Am. Chem. Soc.* **2012**, *134* (43), 17922–17931.
- (47) De Trizio, L.; Figuerola, A.; Manna, L.; Genovese, A.; George, C.; Brescia, R.; Saghi, Z.; Simonutti, R.; Van Huis, M.; Falqui, A. Size-Tunable, Hexagonal Plate-like Cu<sub>3</sub>P and Janus-like Cu-Cu<sub>3</sub>P Nanocrystals. *ACS Nano* **2012**, *6* (1), 32–41.
- (48) Finney, E. E.; Finke, R. G. Nanocluster Nucleation and Growth Kinetic and Mechanistic Studies: A Review Emphasizing Transition-Metal Nanoclusters. *J. Colloid Interface Sci.* **2008**, *317* (2), 351–374.
- (49) Abécassis, B.; Bouet, C.; Garnero, C.; Constantin, D.; Lequeux, N.; Ithurria, S.; Dubertret, B.; Pauw, B. R.; Pontoni, D. Real-Time in Situ Probing of High-Temperature Quantum

- Dots Solution Synthesis. *Nano Lett.* **2015**, *15* (4), 2620–2626.
- (50) Tao, F. F.; Salmeron, M. In Situ Studies of Chemistry and Structure of Materials in Reactive Environments. *Science* **2011**, *331* (6014), 171–174.
- (51) Andersen, H. L.; Bøjesen, E. D.; Birgisson, S.; Christensen, M.; Iversen, B. B. Pitfalls and Reproducibility of in Situ Synchrotron Powder X-Ray Diffraction Studies of Solvothermal Nanoparticle Formation. *J. Appl. Crystallogr.* **2018**, *51* (2), 526–540.

## CHAPTER 4

### A DIRECTED ROUTE TO COLLOIDAL NANOPARTICLE SYNTHESIS OF THE COPPER SELENOPHOSPHATE $\text{Cu}_3\text{PSe}_4$ <sup>4</sup>

#### 4.1. Overview

The first colloidal nanoparticle synthesis of the copper selenophosphate  $\text{Cu}_3\text{PSe}_4$ , a promising new material for photovoltaics, is reported. Because the formation of binary copper selenide impurities seemed to form more readily, two approaches were developed to install phosphorus bonds directly: (1) the synthesis of molecular tetraphosphorus triselenide,  $\text{P}_4\text{Se}_3$ , and subsequent reaction with a copper precursor,  $(\text{P-Se}) + \text{Cu}$ , and (2) the synthesis of copper phosphide,  $\text{Cu}_3\text{P}$ , nanoparticles and subsequent reaction with a selenium precursor,  $(\text{Cu-P}) + \text{Se}$ . The isolation and purification of  $\text{Cu}_3\text{P}$  nanoparticles and subsequent selenization yielded phase-pure  $\text{Cu}_3\text{PSe}_4$ . Solvent effects and Se precursor reactivities were elucidated and were key to understanding the final reaction conditions.

#### 4.2. Introduction

Ternary copper-based semiconductor nanoparticles (NPs) have emerged as promising materials for photovoltaic absorbers because they are composed of nontoxic, earth-abundant elements and potentially offer tunable optoelectronic properties.<sup>1-5</sup> The copper selenophosphate  $\text{Cu}_3\text{PSe}_4$  is of significant interest as a p-type absorber, motivated by theory predicting a competitive

---

<sup>4</sup> This chapter was published as a communication in *Angewandte Chemie Int. Ed.* **2020**, *59*, 3038-3042 by Jennifer M. Lee, Leslie A. Kraynak, and Amy L. Prieto. The experimental was developed and performed by Jennifer M. Lee with the guidance of Prof. Amy L. Prieto. Leslie A. Kraynak collected the XPS data and provided expertise in the XPS discussion. The manuscript was initially prepared by Jennifer M. Lee with insights by Prof. Amy L. Prieto. All authors contributed to the final edits of the manuscript. The authors would like to thank Eve Mozur for her help with the Rietveld refinement and Nathan Gimble for his thoughtful discussions of Cu XPS. The authors would also like to thank Jacob Schneider for building a custom air-free XPS sample holder, which proved integral for these studies, and to the Miyake group for access to their diffuse reflectance UV/Vis spectrometer.

efficiency of 24 % and a direct band gap.<sup>6</sup> The material crystallizes as the enargite structure type (orthorhombic space group  $Pmn2_1$ ) in which Cu and Se are tetrahedrally coordinated to P. However, little is known about  $\text{Cu}_3\text{PSe}_4$  other than from DFT calculations<sup>6-8</sup> and basic characterization of bulk samples<sup>9,10</sup> (see the Supporting Information, Tables S4.1 and S4.2 for full literature collection). Herein we report a new solution-based NP synthesis of  $\text{Cu}_3\text{PSe}_4$ . Nanoparticle syntheses aim for synthetic control of both thermodynamic and kinetic phases exhibiting interesting physical properties.<sup>2,11-13</sup> To enable access to a wide phase space, control over the synthesis of increasingly complex NPs is required because changes in composition, stoichiometry, and morphology impact optoelectronic properties. While the accessible complexity of NPs is increasing, a significant challenge in the field is the design of new reactions to produce high quality NPs, especially when the roles of the reactants are not well understood. The development of controlled synthetic strategies for compositionally complex NPs, in particular those that combine transition metals and light main-group elements, remains a significant challenge because of the diversity of interactions between different species. Furthermore, the chemical potentials of the precursors must be balanced to prevent the formation of species more thermodynamically favorable than the target compound.

While certain reaction parameters may not contribute directly to the targeted material synthesis, they could inform rational planning and aid the synthesis of other material systems. Here, we describe failed reactions as case studies, wherein the nanoparticle synthesis of phase-pure  $\text{Cu}_3\text{PSe}_4$  was rationalized. Ultimately, the successful route involved the synthesis of directly nucleated copper phosphide,  $\text{Cu}_3\text{P}$ , NPs which were consumed in a selenization step to form  $\text{Cu}_3\text{PSe}_4$  NPs. Strategies that can be extrapolated to other materials composed of these elements are also described.

### 4.3. Results and Discussion

Considering the hard-soft acid-base (HSAB) principle,<sup>13</sup> we anticipated that balancing precursor reactivity would pose a significant challenge. In the case of  $\text{Cu}_3\text{PSe}_4$ , the +5 oxidation state of P makes it a considerably hard acid in relation to the softer  $\text{Cu}^+$  and  $\text{Se}^{2-}$  species. Thus, the incorporation of the main group element could be a potential bottleneck because  $\text{Cu}^+$  and  $\text{Se}^{2-}$  are a compatible HSAB pair. Phosphorus bonds were installed directly by synthesizing P-containing binaries before the introduction of the third element. In this way, different reaction pathways were explored. Here, the (P-Se) + Cu route was explored via molecular and cage-like  $\text{P}_4\text{Se}_3$ , and the (Cu-P) + Se route was explored via  $\text{Cu}_3\text{P}$  NPs (Figure 4.1).

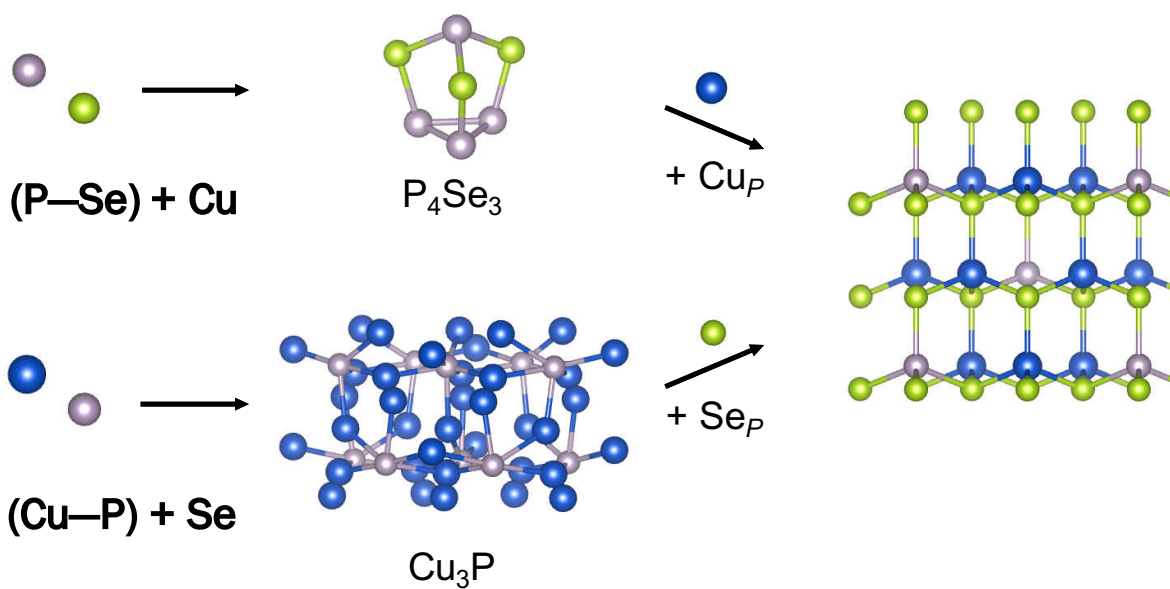


**Figure 4.1.** Reaction pathways explored for the synthesis of  $\text{Cu}_3\text{PSe}_4$ . Cu blue, P silver, Se green. *P* stands for precursor.

The reactivities of the precursors were qualitatively gauged via the analysis of the reaction products. Solvent selections were guided by literature but were ultimately optimized based on empirical evidence. Further detail of these reactions and corresponding figures can be found in the Supporting Information.

#### 4.3.1. Investigation of Pathway Route (P–Se) + Cu

Because Cu is a fast solid-state diffuser, we hypothesized that it could be added to binary compounds of phosphorous selenides. Tetraphosphorus triselenide,  $P_4Se_3$ ,<sup>14</sup> was investigated in this report (Supporting Information, Figure S4.1) because it possesses a cage-like structure with alternating P–Se bonds. Initial results were promising; XRD of the final product suggested the formation of  $Cu_3PSe_4$  (Supporting Information, Figure S4.2a), but those results were difficult to reproduce (Supporting Information, Figure S4.2b). One of the challenges posed by this precursor was its lack of solubility in a wide range of solvents. Moreover, many experiments yielded amorphous products, which is perhaps due to  $P_4Se_3$  having a fairly low glass transition temperature.<sup>15</sup> The P–Se bond is fairly stable considering its minimal electronegativity difference, so while further investigations could be done with other P–Se compounds, we observed minimal bond breaking despite reactions run at elevated temperatures.

#### 4.3.2. Investigation of Pathway Route (Cu–P) + Se

Nanoparticles of  $Cu_3P$  were synthesized through an established hot injection method in which a solution of Cu precursor in oleylamine (OLA)/octylamine was injected into trioctylphosphine (TOP)/trioctylphosphine oxide (TOPO) at elevated temperature.<sup>16</sup> This approach was initially explored because it allows for the control of precursor addition order. This was a particularly important consideration because Cu and Se preferentially form copper selenide binary products.

A swift injection of Se powder in OLA (Se/OLA) into the reaction flask followed immediately, but the reaction mainly yielded Cu–Se binaries (Supporting Information, Figure S4.3). A series of Se precursors with divergent reactivities were selected based on their bond dissociation enthalpies (BDEs, Figure 4.2): diphenyl diselenide in OLA ( $Ph_2Se_2/OLA$ ) and

trioctylphosphine selenide (TOPSe). The BDEs associated with Se powder are  $\text{BDE}(\text{Se}-\text{Se}) = 172 \text{ kJ mol}^{-1}$  and  $\text{BDE}(\text{Se}=\text{Se}) = 272 \text{ kJ mol}^{-1}$ , for  $\text{Se}_n$  chains and rings.<sup>17</sup> Using nominally less reactive  $\text{Ph}_2\text{Se}_2$  ( $\text{BDE}(\text{Se}-\text{Se}) = 182.55 \text{ kJ mol}^{-1}$ )<sup>18</sup> was motivated by the appropriate rate of Se transfer in directing wurtzite- $\text{CuInSe}_2$  syntheses.<sup>19,20</sup> Norako et al.<sup>19</sup> also proposed that OLA influences the phase determination of the wurtzite phase. The precursor TOPSe ( $\text{BDE}(\text{P}=\text{Se}) = 305.35 \text{ kJ mol}^{-1}$ ),<sup>21</sup> formed by reacting stoichiometric amounts of Se powder with TOP, was also investigated because it exhibits further reduced reactivity.

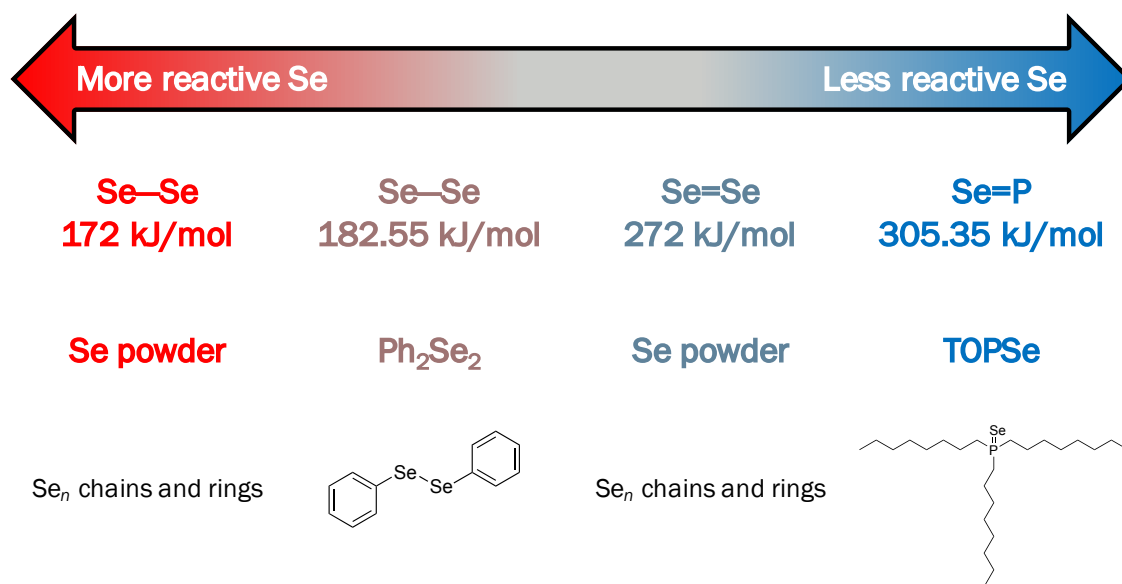


**Figure 4.2.** Series of Se precursors and associated BDEs of relevant Se bonds.

A range of products corresponding to the various Se precursor reactivities were observed although the target ternary material was not, indicating the balance of precursors was not met (Supporting Information, Figures S4.3–S4.5). Under similar reaction conditions, the injection of  $\text{Ph}_2\text{Se}_2/\text{OLA}$  or TOPSe resulted in the formation of Cu-Se (Supporting Information, Figure S4.4) or Cu-P binaries (Supporting Information, Figure S4.5), respectively. Despite the injection order of the precursors, Cu-Se binaries were the common product. In the case of TOPSe, which yielded

Cu-P binaries, the P=Se bond could be too stable to actually contribute Se monomers based on the lack of Se in the final product.

The formation of binary Cu-Se products could be due to the use of OLA, which is known to form Cu(I) complexes. These species could be reactive toward Se monomers. In order to understand the role of OLA, an indication experiment varying the temperature parameter was performed with Cu<sub>3</sub>P. A dispersion of Cu<sub>3</sub>P is black, but a solution of activated Cu(I) in OLA is yellow. Nanoparticles of Cu<sub>3</sub>P were synthesized then dispersed in OLA. Starting at 100 °C, the flask was heated in 25 °C increments. At 225 °C, the solution immediately turned pale yellow, indicating the complexation of OLA to Cu. Therefore, the coordinating ability of OLA could contribute to the favored reaction between Cu(I) complexes and Se<sup>2-</sup> anions. To avoid this pathway, a nominally non-coordinating solvent, ODE, was used. In ODE, Cu<sub>3</sub>P NPs remained dispersed when subjected to the same conditions.

To direct the reaction pathway away from Cu-Se impurities, Cu<sub>3</sub>P NPs were instead treated as a starting material in which P incorporation into the ternary products was encouraged through direct installation of P bonds in the starting reagent. After the isolation and purification of Cu<sub>3</sub>P, a separate selenization step was performed through a heat-up synthesis (Figure 4.1). This strategy of using ex situ prepared binary NPs as a precursor was inspired from a report by Sheets et al. in which Cu<sub>3</sub>P was successfully transformed into analogous copper thiophosphate, Cu<sub>3</sub>PS<sub>4</sub>, NPs by the decomposition of thiourea.<sup>22</sup> While selenourea would be the most direct comparison for Cu<sub>3</sub>PSe<sub>4</sub>, the species of interest in the case of Cu<sub>3</sub>PS<sub>4</sub> NPs were hypothesized to be the gaseous decomposition products of thiourea, mainly H<sub>2</sub>S and CS<sub>2</sub>. Therefore, Se powder in ODE was considered due to the reported in situ formation of H<sub>2</sub>Se.<sup>17,23–26</sup>

A one-pot, heat-up synthesis with Cu<sub>3</sub>P NPs, Se powder, and ODE successfully yielded crude Cu<sub>3</sub>PSe<sub>4</sub>, albeit with Cu-Se impurities as observed by XRD (Supporting Information, Figure S4.6). The oxidation state of Cu in both Cu<sub>3</sub>P and Cu<sub>3</sub>PSe<sub>4</sub> is +1. However, the Cu in the Cu-Se binaries were a mixture of +1 and +2, consistent with Cu<sub>2-x</sub>Se of varying composition.

X-ray photoelectron spectroscopy (XPS) studies were conducted to identify the chemical environments of Cu in the starting material, Cu<sub>3</sub>P NPs, and subsequently elucidate if the Cu(II) impurities were a result of mixed Cu valencies potentially present in the starting material. Although XPS is commonly used as a semi-quantitative surface technique, the penetration depth of about 10 nm is appropriate to probe both the surface and inorganic core of the NPs.<sup>27</sup>

For the Cu 2p spectrum, binding energies (BE) for Cu(I) in Cu<sub>3</sub>P NPs and higher BE satellite peaks corresponding to Cu(II) species<sup>28</sup> were observed (Figure 4.3a; Supporting Information, Table S4.3). The Cu(II) species presumably exist as copper oxide species. Working up these NPs under an inert atmosphere did eliminate the presence of Cu(II) species, but ultimately did not improve the quality of the product of the selenization reaction (Figure 4.3b).

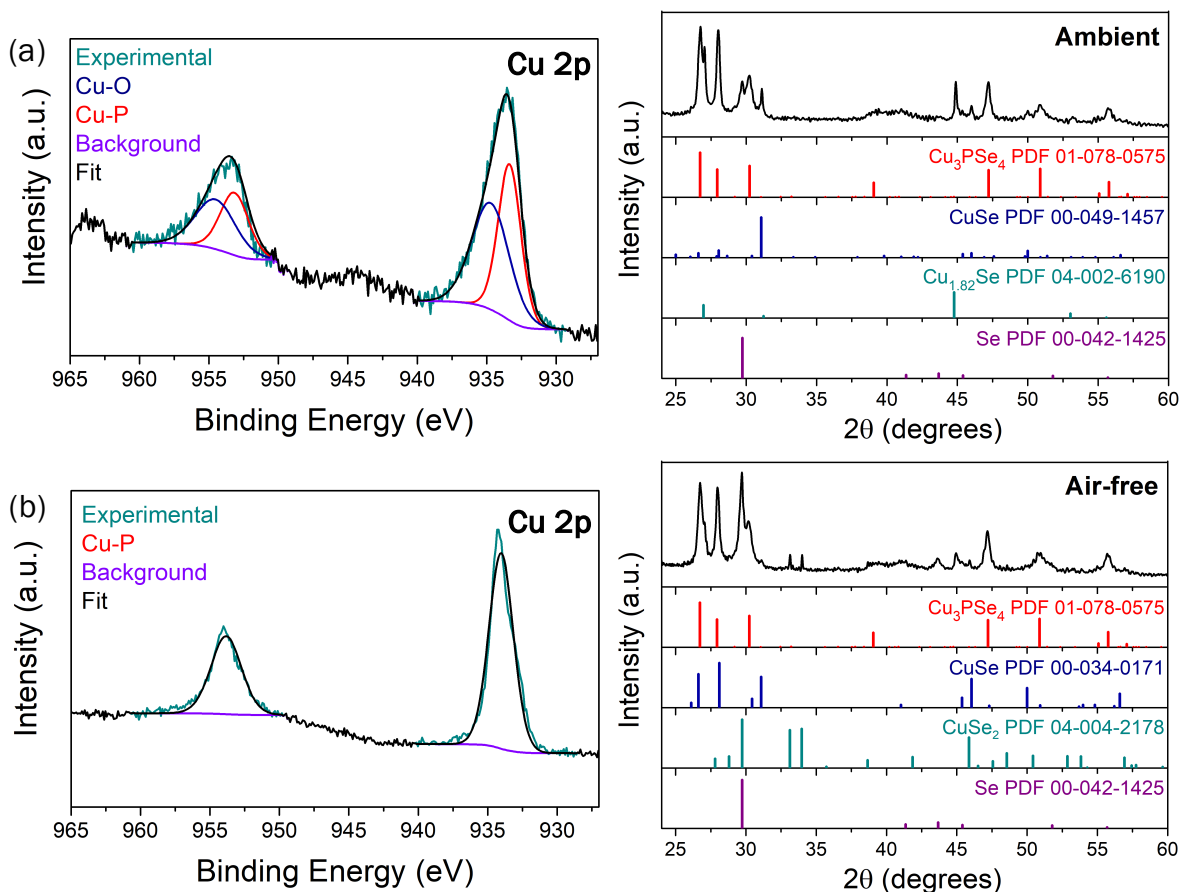


**Figure 4.3.** Cu 2p XPS spectra of Cu<sub>3</sub>P NPs washed in (a) ambient or (b) air-free conditions and corresponding XRD patterns of selenization products made with respective Cu<sub>3</sub>P NPs.

Therefore, the impact of the Cu<sub>3</sub>P NPs quality on the selenization reaction was investigated. In synthetic molecular reactions, starting and intermediate reagents are typically rigorously purified to prevent side reactions. Transitioning from the molecular to nanoparticle regime, considerable care should also be placed in the purity of NPs as intermediates. Although the XRD patterns of the starting material suggest the sole presence of Cu<sub>3</sub>P (Supporting Information, Figure S4.11), Cu-rich pockets were observed upon closer examination by STEM/EDS (Supporting Information, Figure S4.12). To test if these compositions affected the formation of binary impurities, the synthesis of Cu<sub>3</sub>P was manipulated by the TOP/Cu molar ratio.<sup>16</sup> When the molar ratio is 5.6:1, Cu NPs nucleate then are consumed by the P precursor to form Cu<sub>3</sub>P. This results in

Janus-type particles, which could describe the Cu-rich phases that were observed. Increasing the TOP molar ratio to 11:1 results in the direct nucleation of  $\text{Cu}_3\text{P}$ .

Following this TOP-rich protocol, phase-pure  $\text{Cu}_3\text{PSe}_4$  NPs were successfully synthesized when directly nucleated, phase-pure  $\text{Cu}_3\text{P}$  NPs underwent selenization (Figure 4.4a,b). Phase purity was further confirmed by STEM/EDS (Supporting Information, Figures S4.13, S4.14). The success of this reaction could be attributed to the correct local concentration of Cu and P at the nucleation sites or the balanced reactivity of the Se precursor. Further, the reaction pathway could have been directed away from the commonly observed Cu-Se binaries due to the incorporation of a Cu-P bond-breaking step. A similar observation was also noted by Jiang et al. in which the reaction pathway to bulk  $\text{Fe}_2\text{SiS}_4$  was altered when the starting coordinate was Fe-Si binaries instead of the elements.<sup>29</sup> Because  $\text{Cu}_3\text{PSe}_4$  is composed of Cu-Se and P-Se bonds, the Cu-P bonds in the  $\text{Cu}_3\text{P}$  starting material must be broken, enabling an alternative route to the targeted ternary. This step was not required by the hot injection of Se precursor into  $\text{Cu}_3\text{P}$  NPs formed in situ because of the role of OLA in coordinating to Cu(I).

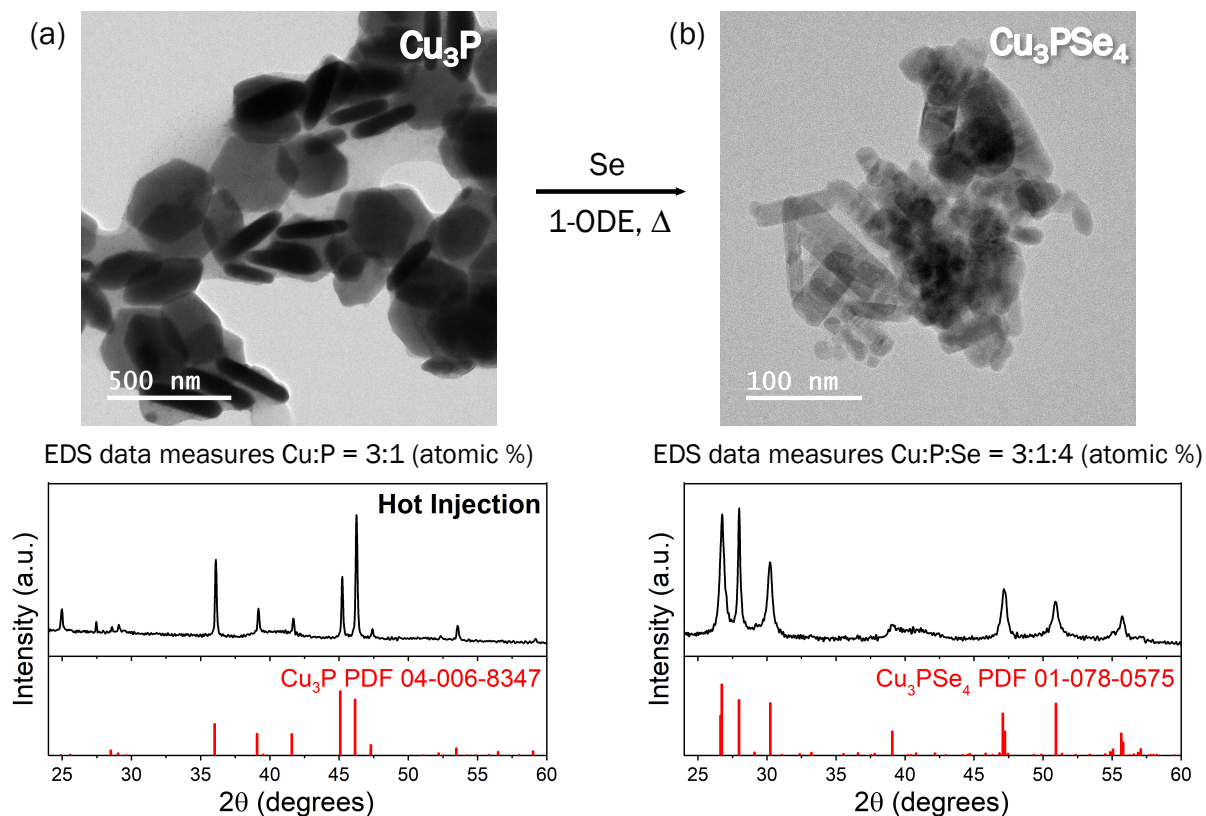


**Figure 4.4.** TEM images and corresponding XRD patterns of (a)  $\text{Cu}_3\text{P}$  made by hot injection synthesis with TOP/Cu molar ratio = 11:1 and transformation to (b) phase-pure  $\text{Cu}_3\text{PSe}_4$ .

Hot injection synthesis still has its inconsistencies owing to the inherent wide variability that arises from the relevant parameters. In our synthesis of  $\text{Cu}_3\text{P}$ , inhomogeneity in morphology and size were observed, potentially leading to the variable sizes and uneven morphologies observed for  $\text{Cu}_3\text{PSe}_4$  NPs. To improve the synthesis of  $\text{Cu}_3\text{P}$  NPs, a heat-up synthesis for  $\text{Cu}_3\text{P}$  NPs was used.<sup>30</sup> The heat-up synthesis resulted in more uniform particles (Figure 4.5a) with phase purity further confirmed by STEM/EDS (Supporting Information, Figure S4.15). When subjecting the particles to selenization by Se in ODE, phase-pure  $\text{Cu}_3\text{PSe}_4$  by XRD (Figure 4.5b) and STEM/EDS (Figure S4.16 in the Supporting Information) was formed.

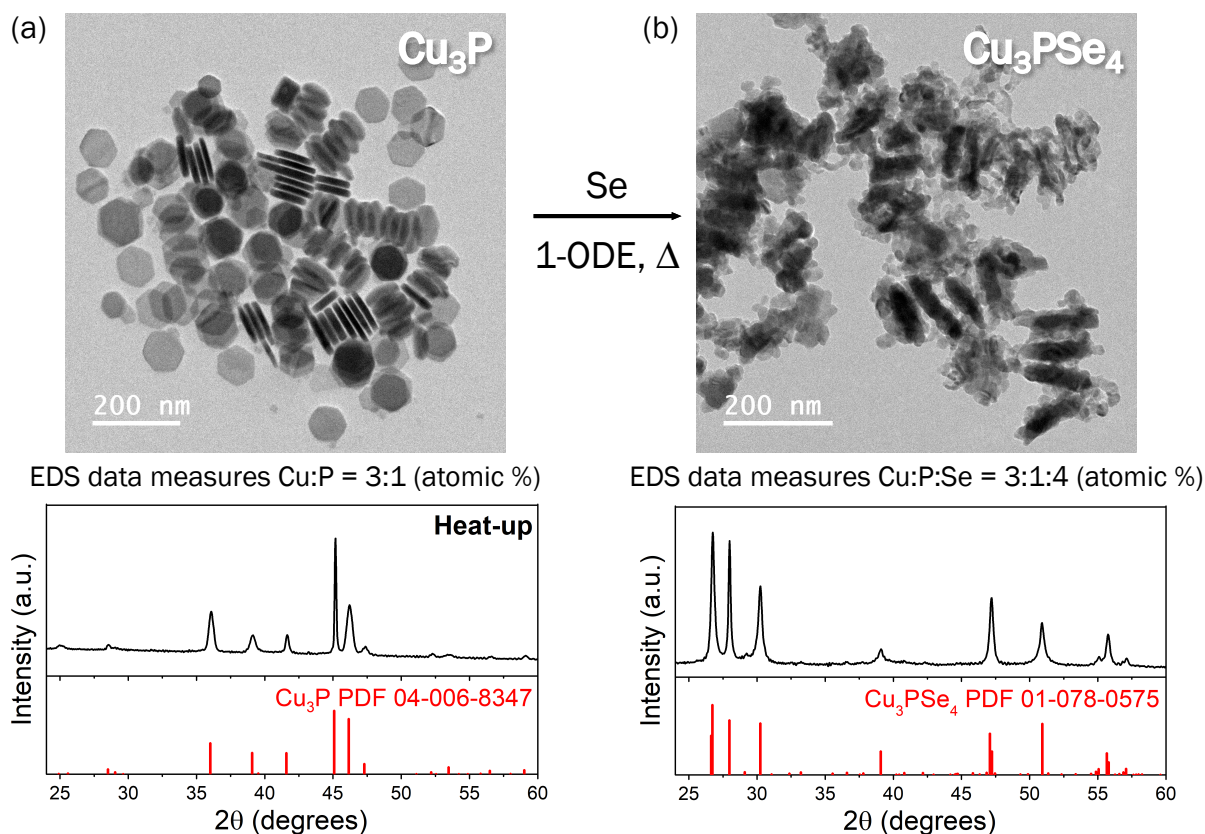


**Figure 4.5.** TEM images and corresponding XRD patterns of (a)  $\text{Cu}_3\text{P}$  synthesized by heat-up and transformation to (b) phase-pure  $\text{Cu}_3\text{PSe}_4$ .

To confirm phase purity, the XRD data of  $\text{Cu}_3\text{PSe}_4$  NPs transformed from heat-up synthesized  $\text{Cu}_3\text{P}$  was analyzed by Rietveld refinement implemented in TOPAS v6 (Bruker AXS; Figure 4.6). The fitted parameters were limited to profile terms, background terms, and unit cell descriptions. Refinements indicated a preferred orientation along the (002) and (022) planes. Improvements in the fits of peak intensity could be made, but these samples are typical of nanoparticle systems which exhibit anisotropic broadening that is due to, for example, stacking of particles or particle morphology.<sup>31</sup> All peaks were indexed to a  $\text{Cu}_3\text{PSe}_4$  reference (ICSD Coll. Code 2856), and a good fit was observed (Figure 4.6). Further refinement details can be found in the Supporting Information, Table S4.4.

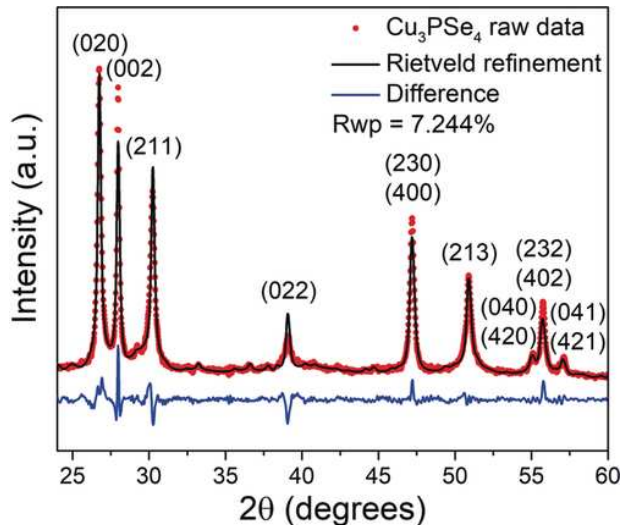


**Figure 4.6.** XRD pattern of  $\text{Cu}_3\text{PSe}_4$  (from heat-up synthesized  $\text{Cu}_3\text{P}$  NPs) analyzed using the Rietveld method to confirm phase purity.

#### 4.4. Conclusion and Outlook

The strategies outlined herein include the investigation of failed reactions to understand precursor roles, the prevention of impurity formation by examination of their origins, and the exploration of potential reaction pathways to the final product. The success of the  $\text{Cu}_3\text{P}$  NPs transformation into  $\text{Cu}_3\text{PSe}_4$  NPs is somewhat surprising considering their individual crystal structures (Figure 4.1). No Cu–P bonds exist in the enargite crystal structure of  $\text{Cu}_3\text{PSe}_4$ . All Cu–P bonds in the binary must be broken and rearranged to Cu–Se and P–Se bonds that exist exclusively in the ternary material. While it remains unclear what the molecular level active participants in this reaction are, the choice of solvents was critical to the success of the reaction. The Cu in  $\text{Cu}_3\text{P}$  nanoparticles is complexed in OLA but not ODE at the reaction conditions. However, the addition of Se to  $\text{Cu}_3\text{P}$  and ODE induces bond rearrangement, perhaps suggesting some transformation of the ODE. While the right balance of precursors was struck for the synthesis of  $\text{Cu}_3\text{PSe}_4$ , a more robust understanding of the mechanism of this reaction would require rigorous characterization of all species (including the reaction flask headspace), effective control reactions that isolate the role(s) of each reaction component, and in situ characterization methods.

## REFERENCES

- (1) Aldakov, D.; Lefrançois, A.; Reiss, P. Ternary and Quaternary Metal Chalcogenide Nanocrystals: Synthesis, Properties and Applications. *J. Mater. Chem. C* **2013**, *1* (24), 3756.
- (2) Reiss, P.; Carrière, M.; Lincheneau, C.; Vaure, L.; Tamang, S. Synthesis of Semiconductor Nanocrystals, Focusing on Nontoxic and Earth-Abundant Materials. *Chem. Rev.* **2016**, *116* (18), 10731–10819.
- (3) Fu, H. Environmentally Friendly and Earth-Abundant Colloidal Chalcogenide Nanocrystals for Photovoltaic Applications. *J. Mater. Chem. C* **2018**, *6* (3), 414–445.
- (4) Fan, F.-J.; Wu, L.; Yu, S.-H. Energetic I–III–VI<sub>2</sub> and I<sub>2</sub>–II–IV–VI<sub>4</sub> Nanocrystals: Synthesis, Photovoltaic and Thermoelectric Applications. *Energy Environ. Sci.* **2014**, *7* (1), 190–208.
- (5) Yarema, O.; Yarema, M.; Wood, V. Tuning the Composition of Multicomponent Semiconductor Nanocrystals: The Case of I–III–VI Materials. *Chem. Mater.* **2018**, *30* (5), 1446–1461.
- (6) Yu, L.; Kokenyesi, R. S.; Keszler, D. A.; Zunger, A. Inverse Design of High Absorption Thin-Film Photovoltaic Materials. *Adv. Energy Mater.* **2013**, *3* (1), 43–48.
- (7) Foster, D. H.; Jieratum, V.; Kykyneshi, R.; Keszler, D. A.; Schneider, G. Electronic and Optical Properties of Potential Solar Absorber Cu<sub>3</sub>PSe<sub>4</sub>. *Appl. Phys. Lett.* **2011**, *99* (18), 181903.
- (8) Foster, D. H.; Barras, F. L.; Vielma, J. M.; Schneider, G. Defect Physics and Electronic Properties of Cu<sub>3</sub>PSe<sub>4</sub> from First Principles. *Phys. Rev. B* **2013**, *88* (19), 195201.
- (9) Garin, J.; Parthé, E. The Crystal Structure of Cu<sub>3</sub>PSe<sub>4</sub> and Other Ternary Normal Tetrahedral Structure Compounds with Composition 1<sub>3</sub>56<sub>4</sub>. *Acta Crystallogr. Sect. B Struct. Crystallogr. Cryst. Chem.* **1972**, *28* (12), 3672–3674.
- (10) Itthibenchapong, V.; Kokenyesi, R. S.; Ritenour, A. J.; Zakharov, L. N.; Boettcher, S. W.; Wager, J. F.; Keszler, D. A. Earth-Abundant Cu-Based Chalcogenide Semiconductors as Photovoltaic Absorbers. *J. Mater. Chem. C* **2013**, *1* (4), 657–662.
- (11) Yin, Y.; Alivisatos, A. P. Colloidal Nanocrystal Synthesis and the Organic-Inorganic Interface. *Nature* **2005**, *437* (7059), 664–670.
- (12) Kovalenko, M. V.; Manna, L.; Cabot, A.; Hens, Z.; Talapin, D. V.; Kagan, C. R.; Klimov, V. I.; Rogach, A. L.; Reiss, P.; Milliron, D. J.; et al. Prospects of Nanoscience with Nanocrystals. *ACS Nano* **2015**, *9* (2), 1012–1057.
- (13) Lee, J. M.; Miller, R. C.; Moloney, L. J.; Prieto, A. L. The Development of Strategies for Nanoparticle Synthesis: Considerations for Deepening Understanding of Inherently Complex Systems. *J. Solid State Chem.* **2019**, *273*, 243–286.
- (14) Irgolic, K.; Zingaro, R. A.; Kudchadker, M. The Synthesis of Tetrphosphorus Triselenide: Preliminary Infrared, Nuclear Magnetic Resonance, and Raman Studies. *Inorg. Chem.* **1965**, *4* (10), 1421–1423.
- (15) Bytchkov, A.; Fayon, F.; Massiot, D.; Hennet, L.; Price, D. L. <sup>31</sup>P Solid-State NMR Studies of the Short-Range Order in Phosphorus–Selenium Glasses. *Phys. Chem. Chem. Phys.* **2010**, *12* (7), 1535.
- (16) De Trizio, L.; Figuerola, A.; Manna, L.; Genovese, A.; George, C.; Brescia, R.; Saghi, Z.;

- Simonutti, R.; Van Huis, M.; Falqui, A. Size-Tunable, Hexagonal Plate-like Cu<sub>3</sub>P and Janus-like Cu–Cu<sub>3</sub>P Nanocrystals. *ACS Nano* **2012**, *6* (1), 32–41.
- (17) Bullen, C.; van Embden, J.; Jasieniak, J.; Cosgriff, J. E.; Mulder, R. J.; Rizzardo, E.; Gu, M.; Raston, C. L. High Activity Phosphine-Free Selenium Precursor Solution for Semiconductor Nanocrystal Growth. *Chem. Mater.* **2010**, *22* (14), 4135–4143.
- (18) Guo, Y.; Alvarado, S. R.; Barclay, J. D.; Vela, J. Shape-Programmed Nanofabrication: Understanding the Reactivity of Dichalcogenide Precursors. *ACS Nano* **2013**, *7* (4), 3616–3626.
- (19) Norako, M. E.; Brutchey, R. L. Synthesis of Metastable Wurtzite CuInSe<sub>2</sub> Nanocrystals. *Chem. Mater.* **2010**, *22* (5), 1613–1615.
- (20) Wang, J.-J.; Wang, Y.-Q.; Cao, F.-F.; Guo, Y.-G.; Wan, L.-J. Synthesis of Monodispersed Wurtzite Structure CuInSe<sub>2</sub> Nanocrystals and Their Application in High-Performance Organic–Inorganic Hybrid Photodetectors. *J. Am. Chem. Soc.* **2010**, *132* (35), 12218–12221.
- (21) Ruberu, T. P. A.; Albright, H. R.; Callis, B.; Ward, B.; Cisneros, J.; Fan, H.-J.; Vela, J. Molecular Control of the Nanoscale: Effect of Phosphine–Chalcogenide Reactivity on CdS–CdSe Nanocrystal Composition and Morphology. *ACS Nano* **2012**, *6* (6), 5348–5359.
- (22) Sheets, E. J.; Yang, W.-C.; Balow, R. B.; Wang, Y.; Walker, B. C.; Stach, E. A.; Agrawal, R. An in Situ Phosphorus Source for the Synthesis of Cu<sub>3</sub>P and the Subsequent Conversion to Cu<sub>3</sub>PS<sub>4</sub> Nanoparticle Clusters. *J. Mater. Res.* **2015**, *30* (23), 3710–3716.
- (23) Deng, Z.; Cao, L.; Tang, F.; Zou, B. A New Route to Zinc-Blende CdSe Nanocrystals: Mechanism and Synthesis. *J. Phys. Chem. B* **2005**, *109* (35), 16671–16675.
- (24) Yordanov, G. G.; Yoshimura, H.; Dushkin, C. D. Phosphine-Free Synthesis of Metal Chalcogenide Quantum Dots by Means of in Situ-Generated Hydrogen Chalcogenides. *Colloid Polym. Sci.* **2008**, *286* (6–7), 813–817.
- (25) Li, Z.; Ji, Y.; Xie, R.; Grisham, S. Y.; Peng, X. Correlation of CdS Nanocrystal Formation with Elemental Sulfur Activation and Its Implication in Synthetic Development. *J. Am. Chem. Soc.* **2011**, *133* (43), 17248–17256.
- (26) Pu, C.; Zhou, J.; Lai, R.; Niu, Y.; Nan, W.; Peng, X. Highly Reactive, Flexible yet Green Se Precursor for Metal Selenide Nanocrystals: Se-Octadecene Suspension (Se-SUS). *Nano Res.* **2013**, *6* (9), 652–670.
- (27) Baer, D. R.; Engelhard, M. H. XPS Analysis of Nanostructured Materials and Biological Surfaces. *J. Electron Spectros. Relat. Phenomena* **2010**, *178–179*, 415–432.
- (28) Biesinger, M. C.; Lau, L. W. M.; Gerson, A. R.; Smart, R. S. C. Resolving Surface Chemical States in XPS Analysis of First Row Transition Metals, Oxides and Hydroxides: Sc, Ti, V, Cu and Zn. *Appl. Surf. Sci.* **2010**, *257* (3), 887–898.
- (29) Jiang, Z.; Ramanathan, A.; Shoemaker, D. P. In Situ Identification of Kinetic Factors That Expedite Inorganic Crystal Formation and Discovery. *J. Mater. Chem. C* **2017**, *5* (23), 5709–5717.
- (30) Liu, J.; Meyns, M.; Zhang, T.; Arbiol, J.; Cabot, A.; Shavel, A. Triphenyl Phosphite as the Phosphorus Source for the Scalable and Cost-Effective Production of Transition Metal Phosphides. *Chem. Mater.* **2018**, *30* (5), 1799–1807.
- (31) Ungár, T. The Meaning of Size Obtained from Broadened X-Ray Diffraction Peaks. *Adv. Eng. Mater.* **2003**, *5* (5), 323–329.

## CHAPTER 5

### MOLECULAR-LEVEL DESIGN PRINCIPLES FOR THE COLLOIDAL NANOPARTICLE SYNTHESIS OF COPPER SELENOPHOSPHATE, $\text{Cu}_3\text{PSe}_4$ : PROBING SELENIUM PRECURSOR EVOLUTION AND DELIVERY<sup>5</sup>

#### 5.1. Overview

Nanoparticle syntheses are inherently complex, especially those that are anomalous to hard-soft acid-base (HSAB) principles, and require reaction pathway elucidation to guide rational syntheses. We have previously shown that the solution-based synthesis of  $\text{Cu}_3\text{PSe}_4$  is acutely sensitive to the Se precursors and solvents. Here, we direct our focus to the Se precursor to monomer transformation, specifically selenium powder in 1-octadecene (ODE), and the role its molecular transformation has on the assembly of P-Se bonds and on the material's synthesis. We build upon our previous work and investigate the impact that Se sources of contrasting electronic properties have on the  $\text{Cu}_3\text{PSe}_4$  reaction pathway. We consider experimentally identified hydrogen selenide ( $\text{H}_2\text{Se}$ ) and dialkyl selenide ( $\text{SeR}_2$ ) whose respective hydrogen and chalcogen bonding properties are natural foils of each other. The application of chalcogen bonding in selenide reagents and their delivery in supramolecular assembly alludes to a synthetic strategy that intersects molecular and materials mindsets as well as computational methods to complement experimental strategies to expand HSAB principles in relation to the reactivity of precursor, or more aptly

---

<sup>5</sup> This chapter was prepared for submission to *Chemical Science* by Jennifer M. Lee, Justin P. Joyce, Nathan Neissius, Devon Leimkuhl, Matthew P. Shores, Anthony K. Rappé, and Amy L. Prieto. The experimental was largely developed and performed by Jennifer M. Lee with the guidance of Prof. Amy L. Prieto. Justin P. Joyce, under the guidance of Prof. Anthony K. Rappé and Prof. Matthew P. Shores, performed all computation and provided expertise on theory and chalcogen bonding. Nathan Neissius performed the solution-based GC-MS and provided insight on its limitations. Devon Leimkuhl made most of the  $\text{Cu}_3\text{P}$  starting material that made the manipulation of reaction conditions and solvent role studies possible, and she performed many of the  $\text{Cu}_3\text{PSe}_4$  reactions (i.e. solvent roles and overnight studies). The manuscript was initially prepared by Jennifer M. Lee with insights by Prof. Amy L. Prieto with the exception of the computational sections which were expertly crafted by Justin P. Joyce. All authors contributed to the final edits of the manuscript. The authors would like to thank Jacob Schneider for help in collecting SEM images, and Dr. Karolien Deneff for her expertise in GC-MS.

monomer due to the interaction of non-innocent solvent, and demonstrate that specific bond formations can be assembled through planned reaction pathways to enable controlled synthesis of a compositionally complex material.

## 5.2. Introduction

Colloidal nanoparticle (NP) synthesis is a toolkit to expand the accessible phase space of semiconductor materials.<sup>1-4</sup> As the demand for materials with coveted physical properties for diverse applications<sup>5-8</sup> such as energy conversion<sup>9-11</sup> and storage<sup>11,12</sup> increases, the diversity of materials to meet these applications is required. Strategies to tune the complexity of the material include composition, stoichiometry, morphology, etc.<sup>1,2,13-16</sup> Ternary copper-based chalcogenide nanoparticles have been an area of intense focus due to their application as photovoltaic absorbers and their non-toxic and earth-abundant composition.<sup>17-20</sup> By virtue of its solution-based regime, colloidal NP synthesis provides a method to expand the phase space accessible to semiconductor materials.<sup>14,21,22</sup> However, refinement of this technique is currently limited by the difficulty in assigning mechanistic details to known reactions, which limits the development of new reactions.

Increasing the complexity of nanoparticle composition inherently introduces synthetic challenges. Contrary to the classical nucleation theory in which nanoparticles nucleate and grow by monomer additions, nanoparticles can also be formed through dynamic chemical processes in which molecular rearrangements occur at very short time scales.<sup>23,24</sup> Elucidation of reaction pathways, let alone mechanisms, is non-trivial due to the speciation that arises from diverse processes such as interactions, transformations, or reactions before and/or after the nucleation event of the desired phase.<sup>25-28</sup> Thus it is imperative to investigate these molecular-level transformations to gain a global understanding of the reaction and meet the goals of composition and phase control.<sup>29-34</sup>

We previously reported the solution-phase synthesis of copper selenophosphate,  $\text{Cu}_3\text{PSe}_4$ , an earth abundant alternative to other PV-related materials.<sup>35</sup> The synthesis of  $\text{Cu}_3\text{PSe}_4$  was particularly curious as its identity is incompatible with principles of hard-soft acid-base (HSAB) theory: the incorporation of P, a light main group element, must simultaneously overcome the formation of HSAB compatible copper-selenide binary impurities. To incorporate P and direct the reaction pathway toward the formation of ternary Cu-P-Se, P-bonds were installed into the starting reagents to yield P-containing binary precursors. We also found that product formation was acutely sensitive to the Se precursor and solvents used. Successful synthesis of  $\text{Cu}_3\text{PSe}_4$  NPs involved the selenization of phase-pure  $\text{Cu}_3\text{P}$  NPs with Se powder in 1-octadecene (ODE). Ultimately, our focus was to target specific bond formations through planned reaction pathways which enabled controlled synthesis of the ternary.

Despite there only being three reagents, an expansive nanoparticle synthetic landscape with several steps and intermediates was revealed. We realized that the reactivity of the Se with the solvent used in the reaction was complex, and a deeper understanding of that chemistry would be widely applicable for the synthesis of selenide-based semiconducting nanoparticles. Here, our scope focuses on the selenium precursor to monomer transformation, delving deeper into the complexities uncovered from the original synthesis of  $\text{Cu}_3\text{PSe}_4$  NPs. Precursors are defined as the starting compounds for the constituent elements of the final NP and monomers (or species) are defined as complexes of the solvated precursor that undergo nucleation such as ions and molecular organometallic complexes.<sup>25</sup> Insight gained could provide general strategies for other colloidal nanoparticle syntheses of complex compositions that require the same constituent elements or use similar starting reagents. Specifically, our focus is on the molecular-level transformations of the Se precursor and the solvent 1-octadecene (ODE) interaction and reaction.

Speciation characterization of Se powder in long chain hydrocarbon solvents was initially reported through work on prototypical Cd chalcogenide binaries.<sup>36-41</sup> Of note, Bullen et al. were motivated to evaluate the efficacy of Se powder in 1-octadecene (ODE) over time and temperature and demonstrated that the most effective use of Se/ODE was heating for 5 h at 180 °C as these were the minimum conditions for complete Se dissolution.<sup>38</sup> The chalcogenide species of interest in this case were dialkyl selenides,  $\text{SeR}_2$  ( $\text{R} = 2,3\text{-alkene}$ ). Prolonged heating at higher temperatures and/or longer times resulted in significant loss of Se in solution, hypothesized to be a competitive reaction forming gaseous hydrogen selenide,  $\text{H}_2\text{Se}$ .

The evolution of gaseous chalcogenide species, namely hydrogen chalcogenide,  $\text{H}_2\text{E}$  ( $\text{E} = \text{S}, \text{Se}$ ), from chalcogen and hydrocarbon interactions is often reported to be the active species of interest for formation of metal chalcogenide NPs.<sup>36,37,39,42</sup> Generally, the generation of  $\text{H}_2\text{E}$  has been indirectly characterized via two methods: (1) by bubbling the reaction flask headspace into a metal cation solution in which formation of chalcogenide precipitate indicates transfer of a reactive gaseous chalcogenide species although it does not identify the species as  $\text{H}_2\text{E}$  nor that this gaseous species is the active monomer for NP production and (2) by identification of a transformed solvent as a result of its interaction with chalcogen precursor which does not necessarily confirm the formation or identity of gaseous  $\text{H}_2\text{E}$ .

Transitioning from what is known experimentally to theory, rapid development in the field of chalcogen bonding has established the dual classification of selenium-containing compounds as both Lewis acidic (LA) and Lewis basic (LB) due to the directional dependence of orbitals that results from a non-uniform electronic distribution. While nanoparticle synthesis is routinely guided by HSAB principles, it serves as a first order approximation for reactivity in terms of materials development and overlooks this directional dependence.

We direct our attention to the noncovalent interactions that form as a result of chalcogen bonding between selenium-containing compounds and nucleophilic  $\text{Cu}_3\text{P}$ , specifically probing the schematic detail of charge transfer in P-Se bond formation. We propose two chalcogenide species of interest based on opposing hydrogen and chalcogen bonding properties to evaluate and characterize toward the synthesis of  $\text{Cu}_3\text{PSe}_4$  NPs (Figure 5.1): hydrogen selenide,  $\text{H}_2\text{Se}$  (Lewis basic along Se-H bond axis), and dialkyl selenide,  $\text{SeR}_2$ , (Lewis acidic along Se-R bond axis). The role of chalcogen bonding is also extended to the non-innocent role of the ODE solvent in the generation of reaction intermediates. Ultimately, the application of chalcogen bonding in supramolecular assembly and selenization reagents for organic transformations alludes to a synthetic strategy for extended materials of unique chemical compositions.

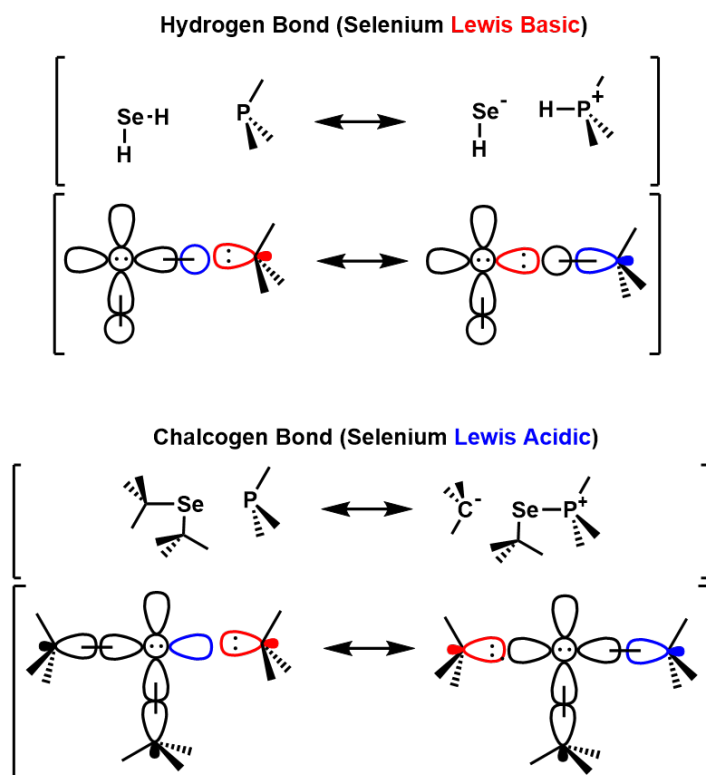


**Figure 5.1.** Directional Lewis acidic and basic properties in  $\text{H}_2\text{Se}$  and  $\text{SeR}_2$  in comparison to nucleophilic  $\text{Cu}_3\text{P}$ , modeled as trimethyl phosphine. Highlighted in blue are Lewis acidic (LA) orbitals and in red are Lewis basic (LB) orbitals. Se-H bonds are LA based on its resonance, i.e. the proton orbital interacts with the nucleophile to give an overall LA bond. Se-R bonds are LB and can directly interact with nucleophile.

## 5.3. Results and Discussion

### 5.3.1. Experimentally Characterized Active Monomer(s) or Species

Our total reaction is the following: Cu<sub>3</sub>P nanoparticles in 1-octadecene ramped to 300 °C and held for 20 mins to yield Cu<sub>3</sub>PSe<sub>4</sub>.<sup>35</sup> Indirect characterization of H<sub>2</sub>Se monomer, as exemplified by the CdE reports, was implemented for our total reaction.<sup>36,37,39,40</sup> Two methods were explored: cannula transfer of the Se/ODE headspace to a dispersion of Cu<sub>3</sub>P NPs in ODE (*Indirect A*) and the direct addition of H<sub>2</sub>Se to Cu<sub>3</sub>P NPs in ODE (*Indirect B*). To deconvolute the inherent diversity of interactions between different species (i.e. molecular vs. bulk, organic vs. inorganic, etc), the methodology was supplemented with a suite of characterization methods of the reaction progress through ex situ time aliquots. To get an overview of the organic species in solution (molecular regime), <sup>1</sup>H NMR and IR were used. To get an overview of the crystalline phases (bulk regime), XRD was used.

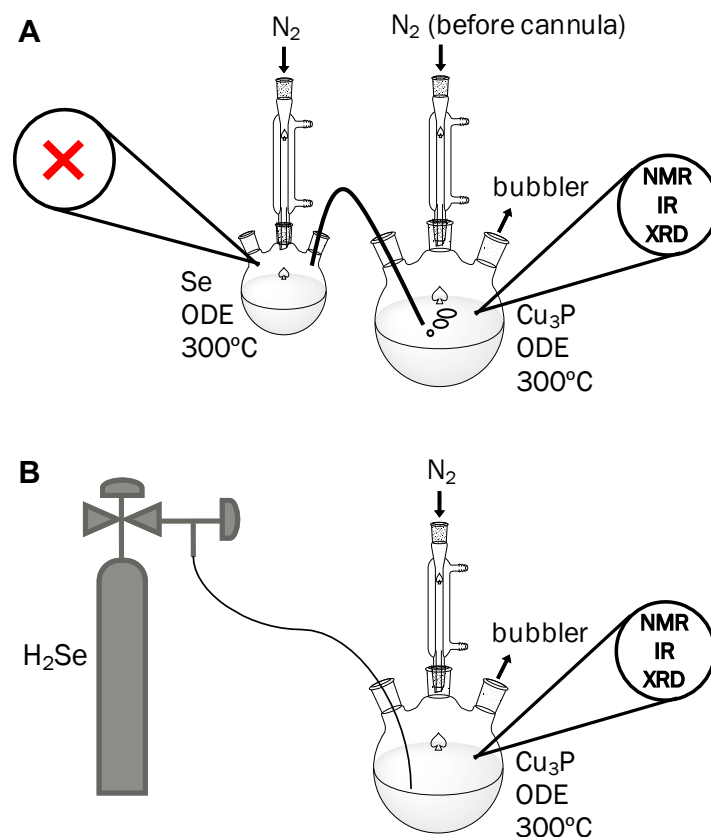


**Figure 5.2.** Cartoon diagrams illustrating two methods for identifying the active Se precursor: (*Indirect A*) cannula transfer of the Se/ODE headspace to a flask of Cu<sub>3</sub>P NPs in ODE and (*Indirect B*) the direct addition of H<sub>2</sub>Se to a flask of Cu<sub>3</sub>P in ODE. Highlighted are appropriate characterization methods for describing specific areas of the reaction flask. Complementary techniques are important to gain a broad perspective of multiple, simultaneous phases and to prevent speculation of processes beyond the data that one technique suggests.

Control experiments of individual reagent behaviour in ODE under reaction conditions (20 min at 300 °C) were characterized via <sup>1</sup>H NMR, IR, and XRD (if applicable) then compared to the total reaction solution (Figures 5.3 and S5.1). The experiments included the solutions of *ODE* (tech grade), *ODE+Se*, and *ODE+Cu<sub>3</sub>P*. Potential convolutions include the ability of ODE to autopolymerize at elevated temperatures and extended periods of time,<sup>43</sup> the vulcanization of ODE in the presence of Se at elevated temperatures,<sup>38</sup> and the potential ability of Cu<sub>3</sub>P NPs to catalyze organic reactions.<sup>44–47</sup> Because it is visually impossible to distinguish the distinct <sup>1</sup>H signals between poly(ODE) and ODE due to overlap (1.19 ppm and 1.26 ppm, respectively) and potential

signal swamping by the majority species, all samples were probed for poly(ODE) by purification of the reaction solution upon reaction completion which isolates the poly(ODE) product. All samples exhibited some extent of ODE autopolymerization (Figure S5.2).

Control *ODE* resulted in no visual transformation in either the  $^1\text{H}$  NMR spectrum (Figure 5.3C) or IR spectrum (Figure S5.1C). Control *ODE*+ $\text{Cu}_3\text{P}$  resulted in some transformations in the  $^1\text{H}$  NMR (Figure 5.3E) and IR (Figure S5.1E) spectra, thus changes in the solution-phase, but there was no transformation in the crystalline phase  $\text{Cu}_3\text{P}$  via XRD. Asterisked in Figure 5.3E are peaks observed as a result of heating. These could be attributed to trace  $\text{H}_2\text{O}$  (1.57 ppm) and hexadecylamine ( $\sim 1.7$  ppm), a labile L-type surface ligand used in the synthesis of the  $\text{Cu}_3\text{P}$  starting reagent that is freed upon heating in solution.<sup>43</sup> Neither transformation changes the fundamental identity of the organic ODE solvent species.

Of note, Control *ODE*+*Se* resulted in the growth of peaks at 1.61 ppm and 5.40 ppm in the  $^1\text{H}$  NMR spectra (Figure 5.3D). This indicates the isomerization of the alkene from the 1—2 to 2—3 position (Figures 5.3A) to form  $\text{SeR}_2$  ( $\text{R} = 2,3\text{-alkene}$ ) species in which an isomerized ODE moiety bonds to a Se-R moiety through the 1-carbon by a 2-electron oxidation generating  $\text{H}_2\text{Se}$ . The isomerization is further corroborated by the growth of an intense peak at  $976\text{ cm}^{-1}$  in the IR spectra which corresponds to a C-H alkene bend, unique from the primary alkene on 1-ODE (Figure S5.1D).<sup>37</sup>

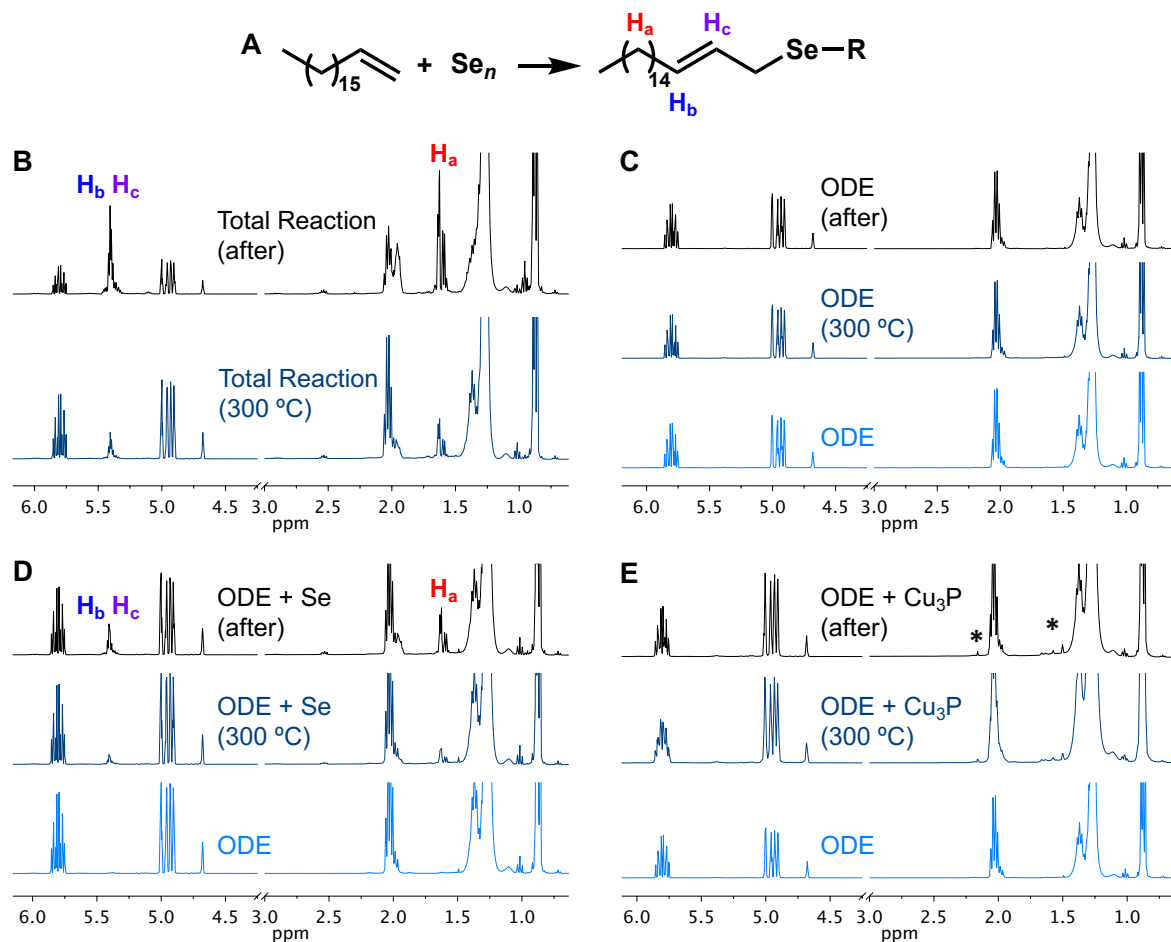


**Figure 5.3.** (A) Reaction of Se with ODE at elevated temperatures resulted in the isomerization of the alkene from the 1—2 to the 2—3 position and the reduction of Se into SeR<sub>2</sub>, H<sub>2</sub>Se, and other Se monomers. This occurs by Se bonding through the 1-carbon. The protons responsible for changes observed in <sup>1</sup>H NMR are labeled. (B) <sup>1</sup>H NMR spectra of the total reaction solution at 300 °C and after cooling. Solutions of the controls (C) *ODE*, (D) *ODE and Se powder*, and (E) *ODE and Cu<sub>3</sub>P NPs*, were characterized via <sup>1</sup>H NMR at room temperature, at 300 °C, and after cooling to room temperature. Asterisked in (E) are peaks observed as a result of heating. These could be attributed to trace H<sub>2</sub>O (1.57 ppm) and hexadecylamine (~1.7 ppm).

This process was previously observed by Bullen et al. via 2D correlated NMR <sup>1</sup>H-<sup>13</sup>C heteronuclear single quantum coherence (HSQC) spectroscopy.<sup>38</sup> The authors proposed that Se bonds to the 1-carbon in a variety of ways, suggesting this might also be occurring with other alkenes of various lengths present in tech. grade ODE and that other reactions between Se and ODE are happening concurrently. We propose a potential reaction scheme for the Se precursor to monomer transformation based on analogous thiyl radical and terminal alkene reactions (Figure

5.4). The isomerization mechanism to form  $\text{SeR}_2$  should also yield  $\text{HSeR}$ . Another viable form of Se insertion in olefins is via the Dewar-Chatt-Duncanson orbital model which yields a selenoxide at the olefin site.<sup>38,48</sup> Although these reactions have several terminal steps that could describe a convoluted spectrum, we are specifically interested in the Lewis acidity of Se-R bonds and Lewis basicity of Se-H bonds. We, thus, direct our focus to  $\text{SeR}_2$  and  $\text{H}_2\text{Se}$  because their respective Lewis acidic and Lewis basic properties are natural foils of each other.

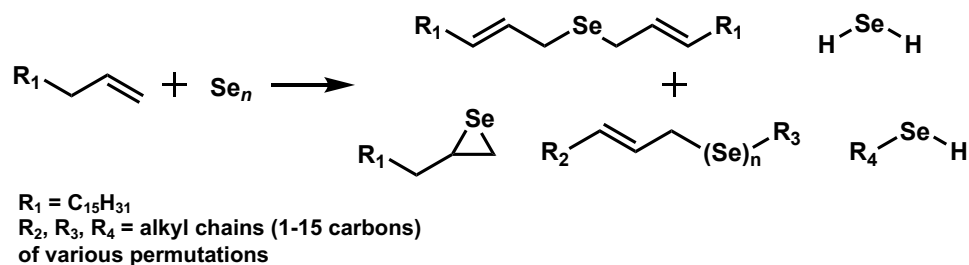


**Figure 5.4.** Potential Se monomers as a result of Se radical and terminal alkene interactions.

In summary, ODE was significantly impacted under the reaction conditions when Se was added, suggesting a significant role by ODE, and can also be impacted by the addition of  $\text{Cu}_3\text{P}$  NPs under reaction conditions as a result of its ligand coverage of labile species. Ultimately, the important processes from the controls as compared to the total reaction were the simultaneous ODE isomerization and Se reduction observed via  $^1\text{H}$  NMR and IR compared against the crystalline phase changes observed via XRD, and these processes were monitored for.

If  $\text{H}_2\text{Se}$ , formed from Se/ODE, was the active chalcogenide species in the transformation of  $\text{Cu}_3\text{P}$  NPs to  $\text{Cu}_3\text{PSe}_4$  NPs, then cannula transfer of the gaseous species from a chalcogenide precursor flask (Se and ODE only) to a dispersion of  $\text{Cu}_3\text{P}$  NPs in ODE should yield  $\text{Cu}_3\text{PSe}_4$  (*Indirect A*). For standard reaction conditions (20 min at  $300\text{ }^\circ\text{C}$ ), no transformation of the starting reagent,  $\text{Cu}_3\text{P}$  NPs, was observed via XRD (Figure 5.5A). Similarly, no changes were observed in either the  $^1\text{H}$  NMR or IR spectra (Figures 5.5A and S5.3A) suggesting no transformation in the solution system as well.

The first noted changes were observed at 1 h. Changes in the  $^1\text{H}$  NMR and IR spectra corresponded to what was expected for the isomerization of ODE and  $\text{Cu}_3\text{P}/\text{ODE}$  interactions (Figures 5.5A and S5.3A, respectively). It is interesting that ODE does not isomerize at the first time aliquot although the reaction is at typical reaction conditions in the presence of chalcogenide species. Temporally, this was also the first indication of new crystalline phases in which there is growth of Cu-Se binaries alongside unidentifiable shoulders at 45 and 47 degrees  $2\theta$ , the highest intensity peaks, in the XRD pattern (Figure 5.5A). Ultimately, no ternary product was observed let alone any reactivity under standard reaction conditions. This is notable as the results suggest that the reaction progress towards the synthesis of ternary  $\text{Cu}_3\text{PSe}_4$  NPs from  $\text{Cu}_3\text{P}$  NPs is not as straightforward as the synthesis of binary Cd chalcogenide NPs, which is often used as a prototypical model for nanoparticle syntheses.<sup>36,49</sup> A solution of Cd cations can directly react with chalcogenide species available in the appropriate oxidation state. The ternary case would require all Cu-P bonds to be broken and rearranged into Cu-Se and Se-P bonds.<sup>35</sup> However, perhaps the concentration of  $\text{H}_2\text{Se}$  released to the headspace was not sufficient for reaction.

If the success of the ternary reaction was indeed due to a specific species,  $\text{H}_2\text{Se}$ , it could be directly added to a dispersion of  $\text{Cu}_3\text{P}$  and ODE to form  $\text{Cu}_3\text{PSe}_4$  (*Indirect B*). Even before the completion of the standard reaction conditions, rapid reactivity was observed. At 1 min, the crystalline species underwent transformation to  $\text{Cu}_{2-x}\text{Se}$  observed via XRD (Figure 5.5C), but there was no evidence of ODE isomerization via  $^1\text{H}$  NMR (Figure 5.5D) or IR (Figure S5.3B). This suggests that  $\text{H}_2\text{Se}$  was not responsible for the ODE isomerization that simultaneously corresponded to the  $\text{Cu}_3\text{P}$  transformation to  $\text{Cu}_3\text{PSe}_4$ . Instead, it was simply a byproduct of Se reduction by ODE.

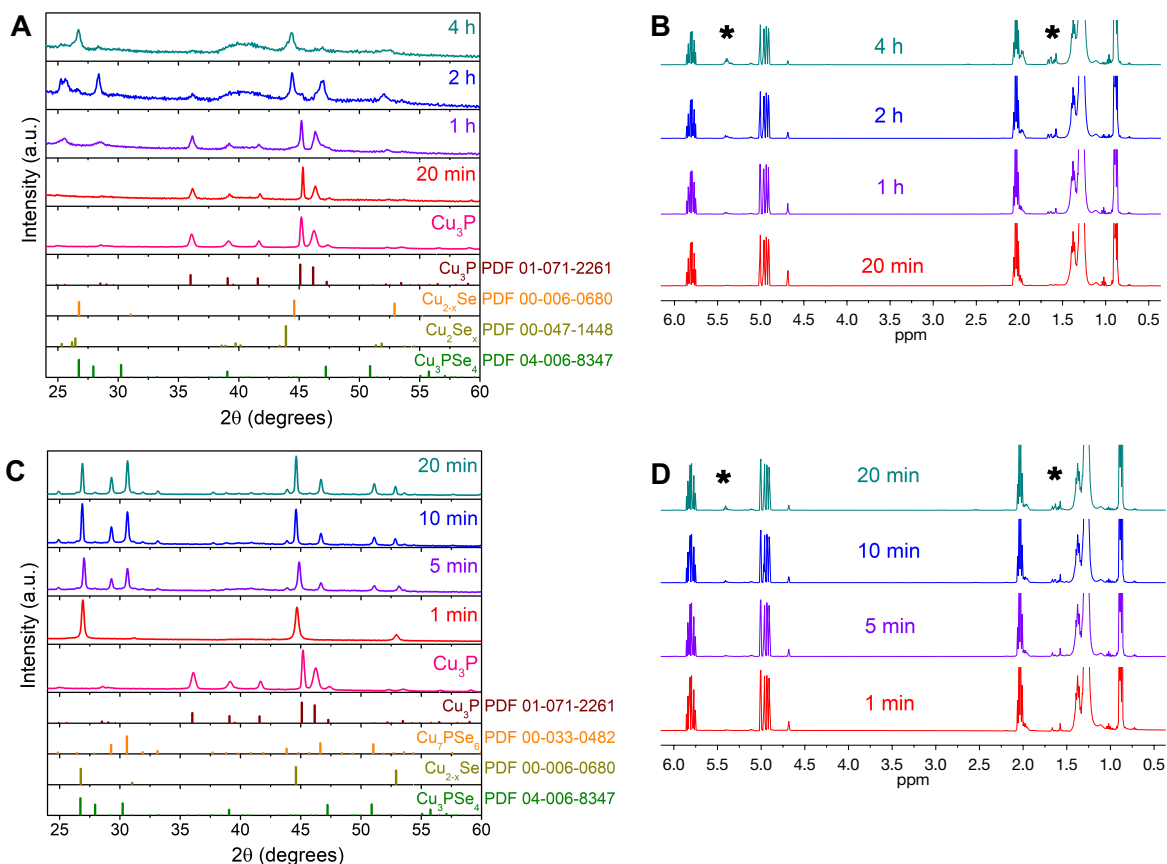


**Figure 5.5.** *Indirect A* ( $\text{Cu}_3\text{P} + \text{Se}/\text{ODE}$  headspace) temporal aliquot characterization of the (A) crystalline materials via XRD and (B) the reaction solutions via  $^1\text{H}$  NMR. Broad amorphous peaks centred around 40 degrees  $2\theta$  are a result of the PMMA puck on the PXRD sample stage. *Indirect B* ( $\text{Cu}_3\text{P} + \text{H}_2\text{Se}$ ) temporal aliquot characterization of the (C) crystalline materials via XRD and the (D) reaction solutions via  $^1\text{H}$  NMR.

Shifts in the  $\text{Cu}_{2-x}\text{Se}$  peaks were observed at 5 mins. This is likely due to the contraction and expansion of the crystal structure as a result of changes in composition due to the fast diffusivity of Cu in the solid-state, confirmed by Rietveld refinements of the diffraction patterns to determine lattice parameters (Figure S5.4). With increasing time, the formation of  $\text{Cu}_7\text{PSe}_6$ , a relatively phosphorus-deficient ternary phase compared to  $\text{Cu}_3\text{PSe}_4$ , was observed with some ODE isomerization. Thus, the direct addition of  $\text{H}_2\text{Se}$  does not make the right product, suggesting that  $\text{H}_2\text{Se}$  is not the sole participant, if at all, in the total synthesis of  $\text{Cu}_3\text{PSe}_4$  NPs.

Between the results of both studies, the headspace of the original reaction may not be merely H<sub>2</sub>Se. Likely, the success of the phase-pure Cu<sub>3</sub>PSe<sub>4</sub> reaction is not dependent on a single component of the reaction system such as gaseous chalcogenide species or H<sub>2</sub>Se but dependent on the reaction system as a whole. While H<sub>2</sub>Se is capable of reacting directly with Cu<sub>3</sub>P, this particular species directs a different route as compared to the route that forms Cu<sub>3</sub>PSe<sub>4</sub>. Instead, SeR<sub>2</sub> is hypothesized to have a much more significant role in the total reaction. This posits the necessity to characterize all species to characterize the chalcogenide species in the gaseous headspace as well as the reaction solution.

### 5.3.2. Role of Chalcogen Bonding

We pivoted our strategy toward direct identification of specific active monomers. The use of <sup>1</sup>H NMR and GC-MS (Figures S5.6-S5.11) alone yielded characterization of a multitude of species (discussion of GC-MS can be found in the Supplementary). Of excitement was the direct characterization of H<sub>2</sub>Se and Se(C<sub>18</sub>H<sub>36</sub>)<sub>2</sub>, the two monomers of interest (Figure S5.6 and S5.9, respectively). However, while our preliminary results seemed to be consistent with the diversity and complexity of Se speciation one might expect at elevated temperatures and in an organic solvent, the characterization of these species did not necessarily reveal their roles as pertinent participants or innocuous bystanders to direct the reaction pathway toward Cu<sub>3</sub>PSe<sub>4</sub>. To deconvolute Se monomer characterization and identify the roles of the different Se monomers, computational methods were used as a bridge.

Dialkyl selenides, like those observed experimentally, can exhibit close, nonbonding contacts with Lewis bases oriented along their bond axis. Referred to as chalcogen bonding, it is traditionally conceptualized in the framework of the  $\sigma$ -hole model where polarizable chalcogen groups can display an electropositive region oriented along their covalent bond.<sup>52–56</sup> We note that

this interpretation has been recently challenged with respect to a charge transfer or sterics based model.<sup>57</sup> In the current reaction system, a molecular unit of Cu<sub>3</sub>P can be nucleophilic through the P to interact with the SeR<sub>2</sub>  $\sigma$ -hole. Thus, we were motivated to understand the impact of chalcogen bonding by simulating the interaction between SeMe<sub>2</sub> (a model chalcogen bond donor) and a molecular PCu<sub>3</sub> unit (not to be confused with the unit cell) as a model system for the interaction between SeR<sub>2</sub> and Cu<sub>3</sub>P NPs, respectively.

We first probed SeMe<sub>2</sub> and its interaction with an inert gas, argon, with a procedure analogous to that of halogen bonding interactions.<sup>58</sup> The Local Energy Decomposition (LED) method was used which assigns the constituents of electrostatics, dispersion, and exchange repulsion from the interaction energy obtained at the DLPNO-CCSD(T) level-of-theory. Diagnostic of SeMe<sub>2</sub> possessing a  $\sigma$ -hole, the equilibrium separation is less than the sum of their van der Waals radii ( $0.985 R_{\Sigma vdW}^{-1}$ ) and parallel to an alkyl-selenide bond. Electrostatics is the dominant attractive force that would seemingly endorse the  $\sigma$ -hole model. However, the angular dependence illustrates that electrostatics preferentially stabilize the perpendicular arrangement where the model system, Ar, intersects the lone pair of Se (Figure 5.6).

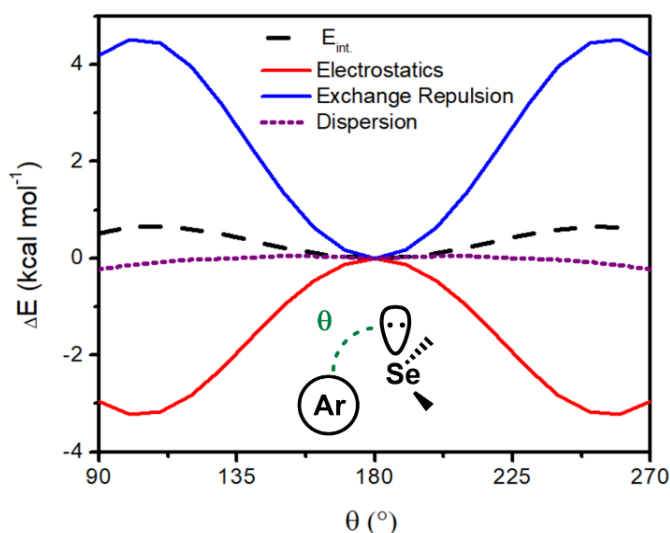


**Figure 5.6.** Angular dependence of the SeMe<sub>2</sub> and Ar interaction in kcal mol<sup>-1</sup>. The interaction is maximized at 180° when the Se  $\sigma$ -hole is in linear contact with Ar.

While dispersion is an isotropic force, exchange repulsion rapidly increases with deviation from a linear geometry. This suggests that exchange repulsion is the defining interaction to chalcogen bonding where its reduction optimizes the impact of dispersion on the total interaction energy ( $E_{\text{int}}$ ). Although counterintuitive, there has been a recent series of independent reports that highlight the decisive contribution of repulsive forces to molecular stability, of which chalcogen bonding is representative.<sup>57,59</sup>

Electrostatic potential (ESP) plots are generated from the potential between a positive point charge and a molecule's electron density. While they accurately depict the electrostatics of an isolated molecule, they do not address electron-electron interactions between fragments. Since there is significant overlap between electron densities for chalcogen bond pairs, their nuclear shielding decreases. Because of electrostatic penetration, the perpendicular orientation of the chalcogen bond is stabilized by electrostatics due in part to the greater electron-nuclear attraction experienced by the Se lone pair. Instead, the system specific impact of electrostatic penetration can be addressed by multiplying the electron density of molecule A ( $\rho_A$ ) by the potential of its adjacent fragment ( $V_B$ ). The associated  $\rho V$  plots for the equilibrium geometry of  $\text{SeMe}_2 - \text{PCu}_3$  are presented below in Figure 5.7. We are surprised to report that the  $\sigma$ -hole of  $\text{SeMe}_2$  is electronegative, contrary to the electropositive region shown in ESP plots. Rather than a source of stability, the electrostatic interaction oriented along the chalcogen covalent bond is repulsive.

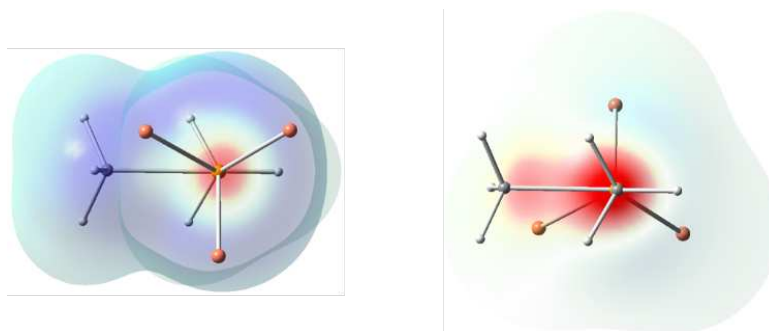


**Figure 5.7.** Electrostatic penetration plot. The plot is oriented along the Se-C bond.

Exchange repulsion results from the orthogonalization of electrons of parallel spin due to the antisymmetry principle. Some of us have recently detailed a procedure to visualize both exchange repulsion ( $\Delta\rho_{\text{SCF}}$ ) and dispersion ( $\Delta\Delta\rho$ ) as perturbations in electron density. Figure 5.8 depicts the reallocation of electron density from the area of overlap (*green*) to their respective fragments (*blue*). Exchange repulsion and electrostatic penetration are inseparable terms since both derive from overlapping electron densities. We report that the LED assignment of electrostatics scales linearly with respect to exchange repulsion by a factor of 0.70. Exchange repulsion is largely compensated for by electrostatic penetration.

Dispersion exerts an inverse effect on electron density where polarization of their excited states accumulates electron density in their bonding region. While the interplay between exchange repulsion and electrostatics is net-repulsive, dispersion provides a final source of stabilization that holds the chalcogen bond together. We have previously referred to the complementarity between exchange repulsion and dispersion as a Gestalt interaction.<sup>59</sup>

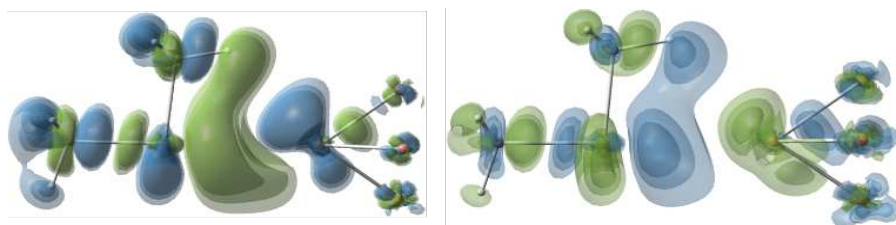


**Figure 5.8.** Reallocation of electron density from the area of overlap (*green*) to their respective fragments (*blue*).

A General Valence Bond (GVB) description of the chalcogen bond interaction is presented in Figure 5.9. The system experiences the least amount of exchange repulsion along the bond axis due to a lesser electron population and its allocation to the bonding region. Natural Resonance Theory (NRT) assigns a charge transfer interaction that contributes approximately 15% to the total resonance form. We are surprised to report that its contribution increases to 45% in the

perpendicular arrangement that suggests charge transfer does not contribute to the directionality of chalcogen bonding.

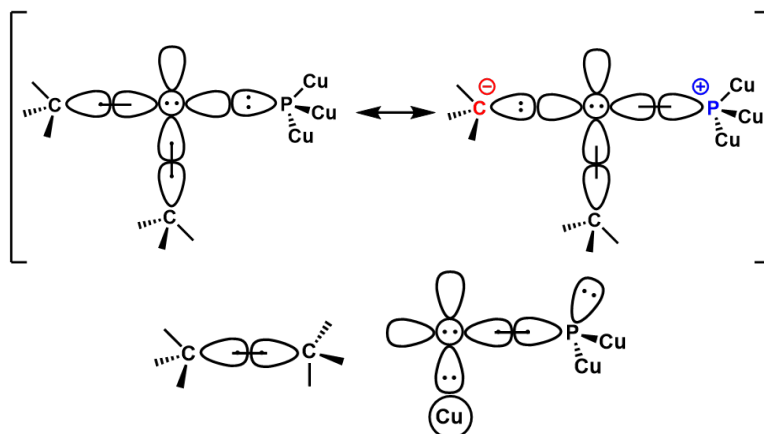


**Figure 5.9.** GVB scheme of the chalcogen bond interaction. Reductive elimination occurs at the Se, resulting in a C(sp<sup>3</sup>)-C(sp<sup>3</sup>) cross-coupling of the adjacent alkyl groups.

The component of charge transfer hints at a reaction pathway where reductive elimination occurs at the Se center, resulting in a C(sp<sup>3</sup>)-C(sp<sup>3</sup>) cross-coupling of the adjacent alkyl groups. More importantly, the proposed mechanism provides a pathway that forms Se-P and Se-Cu bonds in the context of an extended material of tetrahedral geometry.

To indicate any solvent dimerization, <sup>1</sup>H NMR spectra of various reaction solutions were reinvestigated including that of the controls (*ODE*, *ODE+Se*, *ODE+Cu<sub>3</sub>P*), indirect studies, and the total reaction solution (Figure 5.10). All samples were collected after the completion of the respective experiments. For *Indirect A*, both the Se/*ODE* and Cu<sub>3</sub>P/*ODE* flasks were considered.

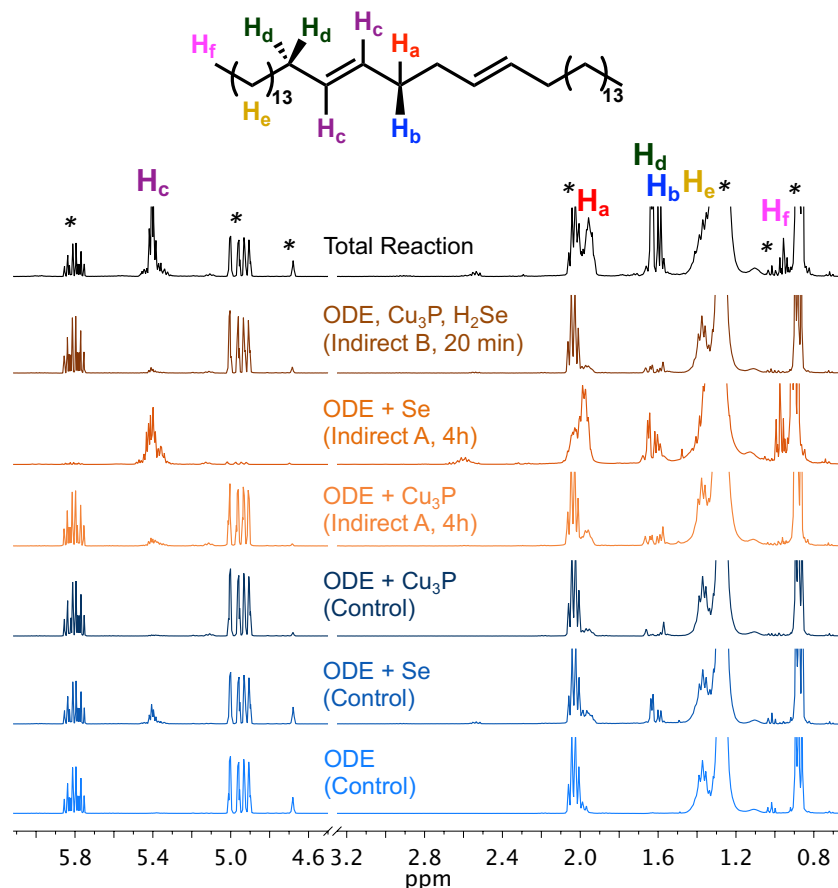


**Figure 5.10.**  $^1\text{H}$  NMR spectra investigating ODE dimerization. All samples were heated to  $300^\circ\text{C}$  and held for 20 mins unless otherwise noted. Protons associated with an ODE dimer species are lettered. Red asterisks indicate signals associated with tech grade ODE. Zoomed in  $^1\text{H}$  NMR spectra investigating ODE dimerization.

Previously for these studies, potential convolutions such as the ability of ODE to autopolymerize at elevated temperatures and extended periods of time and the isomerization of ODE by Se were identified, but these nuances were not necessarily deconvoluted. With the complementary use of theory, we have now enabled a clearer interpretation of our collected data. The spectrum from the total reaction solution matches a mixture of the expected spectrum for tech grade ODE in excess, isomerized ODE via Se coordination to 1-carbon, and the simulated spectrum of the predicted ODE dimer, indicating its potential formation through the proposed chalcogen bonding schematic. The multiplets at 1.59, 1.64, and 1.96 ppm that would arise from the protons adjacent to the dimer's alkenes are broadened; the signal associated with the long

hydrocarbon chain at 1.38 ppm is also broadened. The broadened multiplets are consistent with the broadened resonances of polymers that result from poor molecular rotation and repeating units situated in marginally different chemical environments,<sup>22</sup> suggesting these signals are associated with dimerized ODE as opposed to isomerized ODE.

The only other instances in which the R<sub>2</sub> dimer could be present were in the *ODE + Se* control and the *ODE + Se Indirect A* solutions although this could simply be the isomerization of ODE as exemplified in our earlier controls. Based on the lack of peak broadness for the proton signal H<sub>e</sub> (1.38 ppm), the *ODE + Se* control seemed more characteristic of ODE isomerization (no broad peaks corroborated by lack of growth of the 1.96 ppm multiplet) as opposed to ODE dimerization. On the other hand, the broad peaks of the *ODE + Se Indirect A* spectra appeared to be more characteristic of oligomeric ODE chains. Oligomeric chains such as the ODE dimer are possible in the Se/ODE samples because dialkyl selenides can display the ability to chalcogen bond with itself due to the direction dependence of its orbitals giving both electrophilic and nucleophilic character based on alignment. This process is distinct from SeR<sub>2</sub> vulcanization or ODE autopolymerization. However, both processes could simultaneously be occurring because the majority of the peaks associated with the different species overlap in their <sup>1</sup>H NMR spectra, making deconvolution of the spectra extremely difficult. For example, the broad peaks and multiplet splitting at 1.61 ppm can be associated with the protons adjacent to Se but is convoluted by the potential presence of an ODE dimer.

### 5.3.3. Role of Solvent

To prevent convoluted characterization of the ODE dimerization versus potential ODE autopolymerization (poly(ODE)), the use of squalane was substituted for ODE as a control reaction.<sup>43</sup> Squalane does not autopolymerize which was confirmed (Figure S5.12). Although we

have confirmed the presence of poly(ODE) for our standard reactions, the dimer proton signals are likely not convoluted by the presence of poly(ODE) because poly(ODE) is a saturated alkane and would not exhibit alkene signals that are distinct for the dimer. Nonetheless, the ability of ODE to autopolymerize at elevated temperature could reveal unexpected complexities.

The formation of  $\text{Cu}_3\text{PSe}_4$  from squalane was observed via XRD (Figure 5.11A), but the peak widths were quite narrow, indicating larger crystallite sizes than typically synthesized from ODE. This hinted at a diffusion-limited pathway from  $\text{Cu}_3\text{P}$  to  $\text{Cu}_3\text{PSe}_4$ , independent from the pathway identified for the reaction with ODE where Se speciation played a key role. By  $^1\text{H}$  NMR, no transformations in the reaction solution were observed (Figures 5.11B-C).

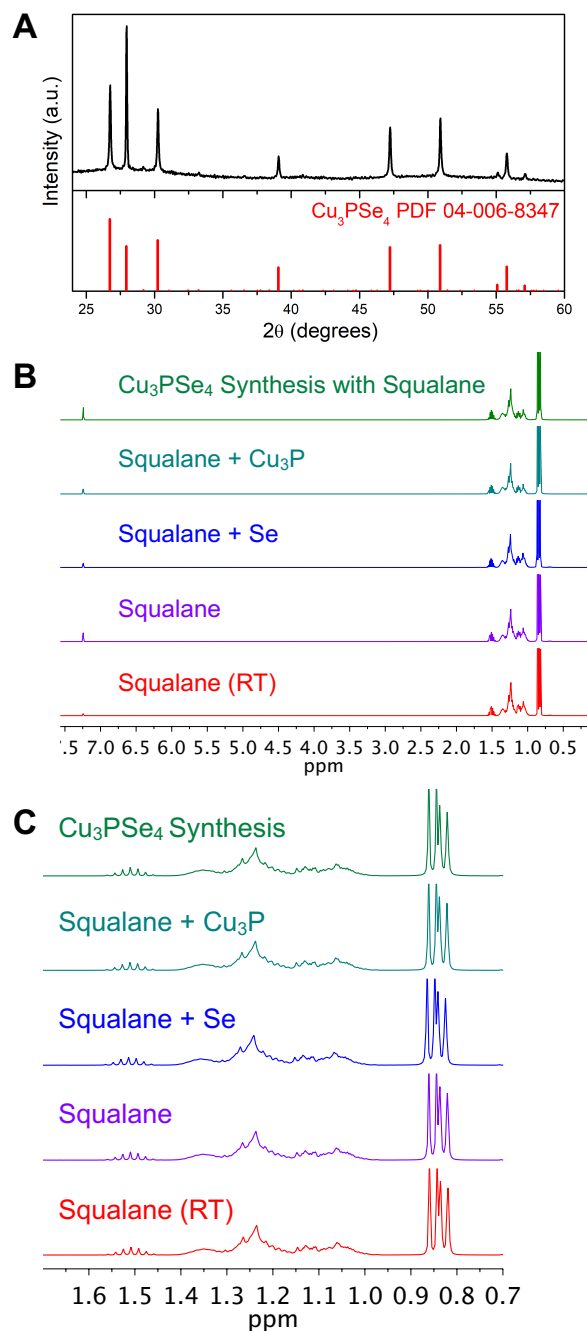


**Figure 5.11.** (A) XRD pattern of the squalane reaction product. (B) <sup>1</sup>H NMR spectrum and (C) zoomed in spectrum of the squalane reaction product.

The speciation of squalane is unchanged when heated to standard reaction conditions (300 °C for 20 min) with individual reagents or on its own (Figures S5.12-S5.14). This contrasts what we see for ODE in which ODE is transformed due to a large breadth of parameters including temperature and addition of Se. This suggests that Se simply melts in squalane, further noted by a solution

colour change to orange-red at elevated temperatures but back to nearly colourless when cooled to room temperature contrasting a persistent yellow solution when Se is dissolved in ODE. Squalane behaves more as a heat-transfer medium as opposed to an active reagent in the reaction. TEM and STEM/EDS were used to probe this pathway and the role of squalane as a heat-transfer medium. Amorphous Se globules were observed to extend into crystalline and agglomerated  $\text{Cu}_3\text{PSe}_4$  (Figures 5.12 and S5.15). We turned to theory to understand the Se monomer responsible for the success of this reaction.

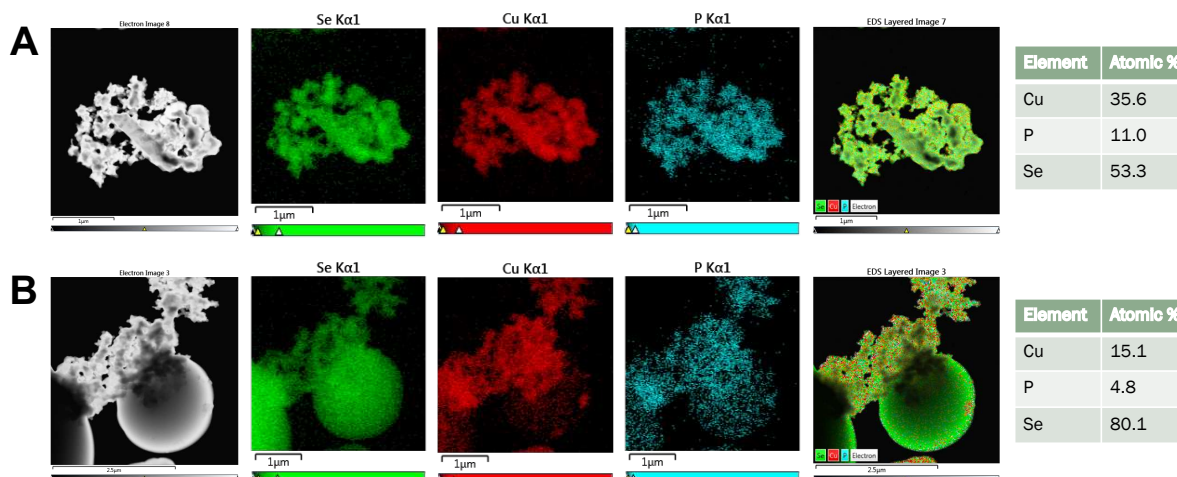


**Figure 5.12.** STEM/EDS of the squalane reaction product. (a) Agglomerated phase-pure  $\text{Cu}_3\text{PSe}_4$ . (b) Diffusion of Se to form reaction products. Spheres are large amorphous Se and the crystallites adjacent to the spheres are  $\text{Cu}_3\text{PSe}_4$  agglomerations.

Defining chalcogen bonding in terms of exchange repulsion expands the scope of the noncovalent interaction between the Se monomer and  $\text{PCu}_3$  molecular unit. Atomic Se has an anisotropic electron distribution: *chalcogen bonding should occur irrespective of the chalcogen group possessing a covalent bond*. We performed a series of multireference calculations to investigate the distance dependence of the Se and  $\text{PCu}_3$  interaction while accounting for the singlet and triplet character of the system. The GVB diagrams show the chalcogen bonding of their triplet state and the formation of three dative bonds of the singlet excited state (Figure 5.13).

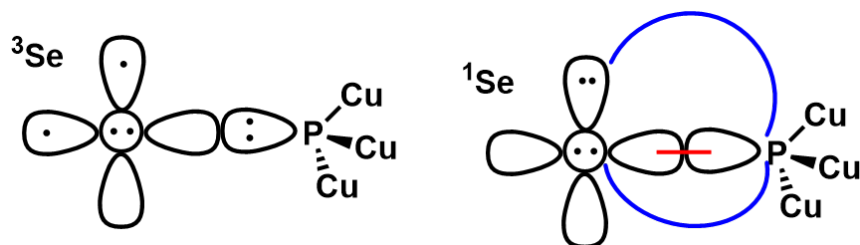


**Figure 5.13.** GVB scheme which shows the chalcogen bonding of the Se triplet state ( $^3\text{Se}$ ), and the formation of three dative bonds of the Se singlet state ( $^1\text{Se}$ ). These states are accessible by both atomic Se and  $\text{SeR}_2$ , thus chalcogen bonding occurs irrespective of the chalcogen group possessing a covalent bond.

The CAS wavefunction assigns their interaction as weakly repulsive at distances intermediate of a noncovalent interaction and a covalent bond. Its maximum is at 3.23 Å that is near equivalent to the equilibrium separation reported for  $\text{SeMe}_2 - \text{PCu}_3$  that is suggestive of the relationship between strain and stability. The perturbation to the CAS wavefunction performed by NEVPT2 accounts for dynamic correlation that is descriptive of dispersion (Figure 5.14). The NEVPT2 potential energy surface is strictly attractive until its equilibrium separation of 2.09 Å that agrees with the crystallographic structure. While dispersion is traditionally approximated as a long-range interaction, it accounts for 60% of the total bond dissociation energy as dynamic correlation persists at distances on the order of a covalent bond.

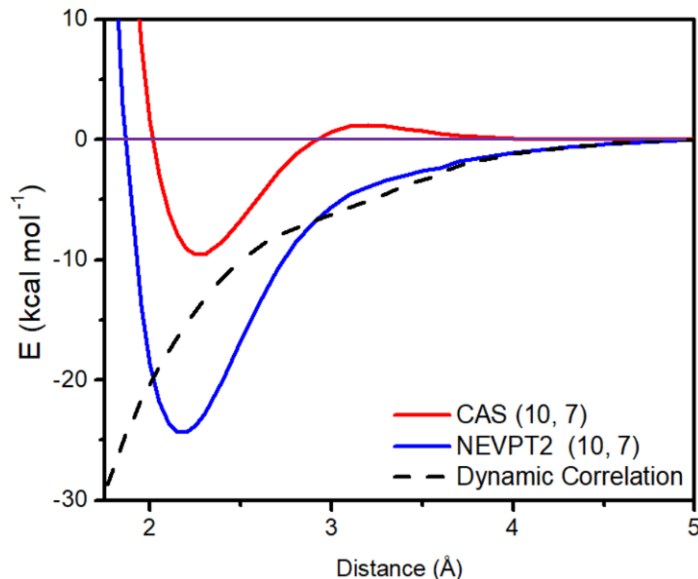


**Figure 5.14.** Comparison of CAS wavefunction versus NEVPT2 in assigning  $\text{SeMe}_2 - \text{PCu}_3$  interaction. NEVPT2 account for dynamic correlation such as dispersion.

The reaction was completed neat (without solvent) to confirm atomic Se's ability to chalcogen bond and further elucidate the role of the solvent. The solid-state reaction was completed with the same molar equivalencies and same reaction conditions. The neat reaction resulted in the synthesis of  $\text{Cu}_3\text{PSe}_4$  although excess Se and perhaps a trace amount of Cu-Se impurity were also present (Figure 5.15). Attempts to vaporize the excess Se were unsuccessful because the  $\text{Cu}_3\text{PSe}_4$  NP product decomposes at the temperatures required to boil Se (b.p.  $685\text{ }^\circ\text{C}$ ) (Figure S5.16).<sup>61</sup> Nonetheless, the successful synthesis of  $\text{Cu}_3\text{PSe}_4$  under solid-state reaction conditions is intriguing because the reaction was performed under significantly milder conditions as compared to literature prep from the elements (20 min at  $300\text{ }^\circ\text{C}$  vs. 10 days at  $800\text{ }^\circ\text{C}$ ).<sup>62</sup>

Our studies exploited two different methods toward the same global minimum for the synthesis of  $\text{Cu}_3\text{PSe}_4$ . Mainly, the use of ODE reduced Se at elevated temperatures, resulting in highly reactive  $\text{Se}_n\text{R}_2$  monomers which directed a pathway in which the solvent was a starting reagent. Alternatively, the pathway can be accessed by diffusion in which a solvent behaves simply as a heat-transfer medium, such as squalane. In this case, no solvent is required either to form

$\text{Cu}_3\text{PSe}_4$ . Access to the Se singlet state links the two different Se species, and the Lewis acidic character that arises enables nucleophilic attack by molecular unit  $\text{PCu}_3$ .

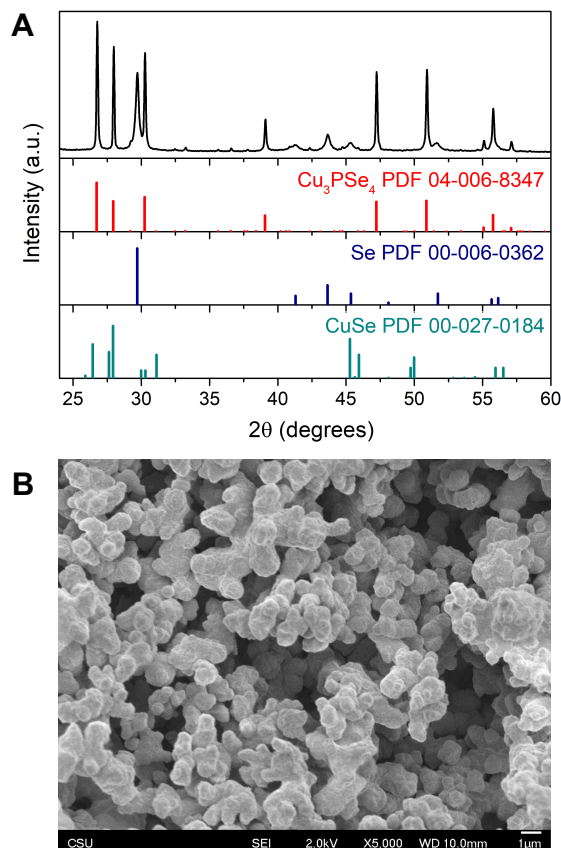


**Figure 5.15.** (A) XRD pattern and (B) SEM image of the neat reaction product.

The choice of ODE as the solvent in this system impacts the chalcogenide speciation, thus the reaction pathway to  $\text{Cu}_3\text{PSe}_4$ . To further investigate the impact of solvent on speciation, ODE was replaced with other solvents suggested by the Yordanov et al. report for the synthesis of CdS nanoparticles.<sup>36</sup> The report quantified the % yield of active species by gravimetric analysis of the resulting CdS precipitate. However, this assumed that the active specie was  $\text{H}_2\text{S}$  and that the monomer quantity was the dominant role on the reaction pathway as opposed to the identity of the solvent and resulting speciation. Because ODE was reported to yield the lowest % yield of monomer, solvents with diverse % yields such as hexadecylamine, HDA, (high % monomer yield) and trioctylphosphine oxide, TOPO, (medium % monomer yield) were chosen.

The use of HDA instead of ODE resulted in Cu-Se binaries (Figure 5.16A). Similarly, replacing ODE with TOPO resulted in Cu-Se binaries but with some formation of  $\text{Cu}_3\text{PSe}_4$  (Figure 5.16B). No observation of the ternary in the HDA synthesis could be due to coordination of amines to Cu(I), which preferentially reacts with Se to form Cu-Se binaries, consistent with our empirical observations in our initial attempts to synthesize  $\text{Cu}_3\text{PSe}_4$  with oleylamine.<sup>35</sup> The mild success of TOPO could be due to the long chain octyl functional groups which are oxidized to alkenes by Se to yield  $\text{H}_2\text{Se}$  and potentially some form of  $\text{SeR}_2$ .<sup>49</sup> However, the diversity of products highlights the uncontrolled reactivities of Se which perhaps interacts with TOPO in some way.

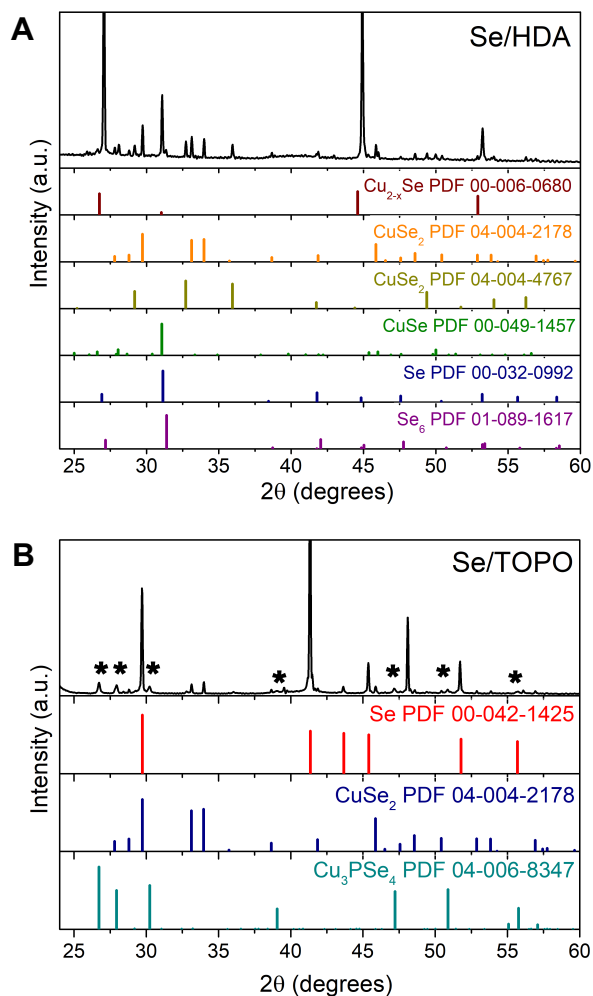


**Figure 5.16.** XRD patterns of the (A)  $\text{Cu}_3\text{P} + \text{Se}/\text{HDA}$  and (B)  $\text{Cu}_3\text{P} + \text{Se}/\text{TOPO}$  reaction products. Asterisked are the peaks associated with  $\text{Cu}_3\text{PSe}_4$ . The same conditions from the  $\text{Cu}_3\text{P} + \text{Se}/\text{ODE}$  were used for both reactions with the sole exception of the solvent.

Overall, the observation of a diversity of products other than the targeted  $\text{Cu}_3\text{PSe}_4$  demonstrates the dynamic role of different solvents on the Se precursor to generate monomers with diverse synthetic roles. Thus, different reaction pathways were revealed. Although the literature presumption that the monomer quantity was solely correlated to product yield was sufficiently evidenced for the Cd chalcogenide system, it does not necessarily consider the bigger picture of the  $\text{Cu}_3\text{PSe}_4$  reaction system as a whole. This again underscores the solvent role in solution-based NP syntheses beyond a heat-transfer medium or a non-participating, innocent bystander but an active and dynamic component that can impact the reaction pathway.<sup>43</sup>

#### **5.4. Conclusion and Outlook**

We exploit a rich chemistry by probing one transformation, the Se precursor to monomer transformation in the presence of ODE and  $\text{Cu}_3\text{P}$ . Nanoparticle syntheses are inherently complex, and processes beyond nucleation and growth such as the dissolution of nucleated species, nucleation of multiple phases, etc. can also occur, sometimes linearly and sometimes simultaneously. Studies to describe these processes start with the characterization of the reaction speciation and the mindfulness that these species can exist beyond what is in solution such as in the headspace of the reaction flask. However, this is non-trivial considering the diverse speciation of the entire reaction flask and limitations in characterization although complementary techniques can help gain a broad perspective of multiple, simultaneous components. First steps to elucidate some of this complexity for the  $\text{Cu}_3\text{PSe}_4$  NP system was to focus solely on the chalcogenide precursor to monomer transformation of Se/ODE. The interaction of Se in ODE leads to a diversity of Se species with correspondingly diverse roles. We specifically directed our attention to the isomerization of ODE by Se reduction to yield  $\text{Se}_n\text{R}_2$  and  $\text{H}_2\text{Se}$  monomers because of their opposing Lewis acidity and basicity character (Figure 5.1). This resulted in the iterative

experimental and computational investigations of three chalcogenide species with varying Lewis acidity/basicity:  $\text{SeR}_2$ , elemental Se, and  $\text{H}_2\text{Se}$ . Additionally elucidated were their interactions with nucleophilic  $\text{Cu}_3\text{P}$ .

Indirect studies initially afforded us a platform of comparison to gain understanding of our own system. Reaction pathway speciation and the solvent roles were probed by ex situ characterization of both solid- and solution-phase temporal aliquots. Although the identities of the Se monomers were not fully confirmed, the Se/ODE precursor generates gaseous Se species which are reactive toward the  $\text{Cu}_3\text{P}$  NPs as confirmed by the copper-selenide precipitate formed from cannula transfer, but they are not solely responsible for the successful synthesis of  $\text{Cu}_3\text{PSe}_4$ , if at all. While some reports suggest that the identity of this gaseous species is  $\text{H}_2\text{Se}$ , direct addition of  $\text{H}_2\text{Se}$  to  $\text{Cu}_3\text{P}$  accessed the P-deficient ternary  $\text{Cu}_7\text{PSe}_6$ . This suggests that the headspace is not solely  $\text{H}_2\text{Se}$ . Through computation, we noted that  $\text{H}_2\text{Se}$  displays the opposite of chalcogen bonding due to its ionic character from  $\text{HSe}^-$  resonance structure.

We then aimed to directly characterize the Se monomers in various ways with  $^1\text{H}$  NMR and GC-MS. Without much context on potential processes in the molecular regime, the identification of Se monomers by GC-MS was extremely difficult considering the complexities of the total reaction. Instead, the combination of these studies in tandem with computational studies enabled the identification of active chalcogenide monomers and the chemical transformations that were undergone by the reaction monomers to direct a pathway toward  $\text{Cu}_3\text{PSe}_4$ , providing a methodology in which characterization of diverse interactions could be deconvoluted. Mainly, in the model system, the  $\text{SeMe}_2$  monomer undergoes reductive elimination at the Se center due to its interaction with nucleophilic  $\text{PCu}_3$  molecular unit to yield P-Se bonds and potentially form an ODE dimer.

Further, our system revealed the use of computation for novel materials development and an advancement in the debate of how chalcogen bonding could be modelled. Small energies matter, and attraction/repulsion interactions are complementary. The consideration of HSAB principles in NP synthesis design was also expanded. Beyond Lewis acidity and basicity character of orbitals, the directional dependence of the orbitals due to anisotropic electron distribution must also be considered for the reactivity of Se monomers. For our system, the Se monomer  $\text{SeR}_2$ , which is Lewis acidic along its Se-R bond axis, contributes largely to the formation of phase-pure  $\text{Cu}_3\text{PSe}_4$  due to its ability to chalcogen bond with  $\text{Cu}_3\text{P}$  to form P-Se bonds, which are anomalous in the context of HSAB. In elucidation of this interaction, we developed a strategy to template Se bonds.

Consideration of the solvent role can be critical in elucidation of the observed reaction pathways. Two reaction pathways toward the target ternary were revealed. One was impacted by speciation to form  $\text{Cu}_3\text{PSe}_4$  as exemplified by the success of ODE and unsuccessful attempts through HDA and TOPO under the same reaction conditions. Each resulted in different reaction products, suggesting altered reaction landscapes. The other pathway was accessed by diffusion in which a solvent behaved simply as a heat-transfer medium, such as squalane or no solvent. By computation we observed that an excited Se singlet state, in which anisotropic electron distribution in the orbitals enabled three dative bonds between the Se monomer and nucleophile, was accessible via  $\text{SeR}_2$  and Se atoms. Thus, while these are two distinct methods (solution-based speciation vs. solid state diffusion), the molecular reaction scheme to form P-Se bonds is similar. All in all, selection of a solvent for colloidal nanoparticle syntheses should be completed mindfully when developing a synthesis. Solvents can undergo transformations themselves in the presence of different reagents, impacting precursor reactivities and the identities of different monomers. This marks their participation in colloidal nanoparticle syntheses beyond surface coordination or heat-

transfer medium and on the reaction pathway itself. Thus, solvents in NP syntheses can serve as reagents and must be mindfully selected in relation to the precursors used for a particular synthesis.

Ultimately, all of these studies pointed to the same conclusion: the reaction system is dependent on the reaction as a whole and not as a summation of individual components. For example, although  $\text{H}_2\text{Se}$  is a reaction component that may, on its own, lead toward a different pathway, it works in tandem with other species to lead toward phase-pure  $\text{Cu}_3\text{PSe}_4$ . With each probe or control, an expansive reaction landscape was revealed for the synthesis of  $\text{Cu}_3\text{PSe}_4$ . Beyond “active chalcogenide monomers” is the importance of *characterizing all species that inform on the molecular-level reactivities and processes*, a strategy that can and should be applied to many nanoparticle systems which use similar P and Se precursors in similar solvents because molecular level processes inform significantly on a material’s synthesis. The nanoparticle community is interdisciplinary, and mature characterization tools, which often only characterize isolated processes (i.e precursor to monomer, final product, etc) or species type (i.e. organics, solids, etc.) in the reaction flask, should be used in a complementary manner to build a multidisciplinary toolkit for NP synthesis characterization. Additionally, computation could complement mature characterization methods to guide rational hypotheses of empirical results or vice versa, be used to guide experimental design.

## REFERENCES

- (1) Kovalenko, M. V.; Manna, L.; Cabot, A.; Hens, Z.; Talapin, D. V.; Kagan, C. R.; Klimov, V. I.; Rogach, A. L.; Reiss, P.; Milliron, D. J.; et al. Prospects of Nanoscience with Nanocrystals. *ACS Nano* **2015**, *9* (2), 1012–1057.
- (2) Aldakov, D.; Lefrançois, A.; Reiss, P. Ternary and Quaternary Metal Chalcogenide Nanocrystals: Synthesis, Properties and Applications. *J. Mater. Chem. C* **2013**, *1* (24), 3756.
- (3) Wang, X.; Zhuang, J.; Peng, Q.; Li, Y. A General Strategy for Nanocrystal Synthesis. *Nature* **2005**, *437* (7055), 121–124.
- (4) Loiudice, A.; Segura Lecina, O.; Buonsanti, R. Atomic Control in Multicomponent Nanomaterials: When Colloidal Chemistry Meets Atomic Layer Deposition. *ACS Mater. Lett.* **2020**, *25*, 14.
- (5) Gao, M. R.; Xu, Y. F.; Jiang, J.; Yu, S. H. Nanostructured Metal Chalcogenides: Synthesis, Modification, and Applications in Energy Conversion and Storage Devices. *Chemical Society Reviews*. The Royal Society of Chemistry March 11, 2013, pp 2986–3017.
- (6) Fan, F.-J.; Wu, L.; Yu, S.-H. Energetic I–III–VI<sub>2</sub> and I<sub>2</sub>–II–IV–VI<sub>4</sub> Nanocrystals: Synthesis, Photovoltaic and Thermoelectric Applications. *Energy Environ. Sci.* **2014**, *7* (1), 190–208.
- (7) Alberi, K.; Nardelli, M. B.; Zakutayev, A.; Mitas, L.; Curtarolo, S.; Jain, A.; Fornari, M.; Marzari, N.; Takeuchi, I.; Green, M. L.; et al. The 2019 Materials by Design Roadmap. *J. Phys. D: Appl. Phys.* **2019**, *52* (1), 013001.
- (8) Talapin, D. V.; Lee, J.-S.; Kovalenko, M. V.; Shevchenko, E. V. Prospects of Colloidal Nanocrystals for Electronic and Optoelectronic Applications. *Chem. Rev.* **2010**, *110* (1), 389–458.
- (9) Tanimoto, T.; Suekuni, K.; Tanishita, T.; Usui, H.; Tadano, T.; Kamei, T.; Saito, H.; Nishiate, H.; Lee, C. H.; Kuroki, K.; et al. Enargite Cu<sub>3</sub>PS<sub>4</sub>: A Cu-S-Based Thermoelectric Material with a Wurtzite-Derivative Structure. *Adv. Funct. Mater.* **2020**, 2000973.
- (10) Deng, T.; Xing, T.; Brod, M. K.; Sheng, Y.; Qiu, P.; Veremchuk, I.; Song, Q.; Wei, T.-R.; Yang, J.; Snyder, G. J.; et al. Discovery of High-Performance Thermoelectric Copper Chalcogenide Using Modified Diffusion-Couple High-Throughput Synthesis and Automated Histogram Analysis Technique. *Energy Environ. Sci.* **2020**.
- (11) Hurst, K. E.; Luther, J. M.; Ban, C.; Christensen, S. T. Nanomaterials for Energy Applications. In *Metrology and Standardization of Nanotechnology*; Wiley-VCH Verlag GmbH & Co. KGaA: Weinheim, Germany, 2017; pp 505–518.
- (12) Brehm, W.; Santhosha, A. L.; Zhang, Z.; Neumann, C.; Turchanin, A.; Martin, A.; Pinna, N.; Seyring, M.; Rettenmayr, M.; Buchheim, J. R.; et al. Copper Thiophosphate (Cu<sub>3</sub>PS<sub>4</sub>) as Electrode for Sodium-Ion Batteries with Ether Electrolyte. *Adv. Funct. Mater.* **2020**, 1910583.
- (13) Costi, R.; Saunders, A. E.; Banin, U. Colloidal Hybrid Nanostructures: A New Type of Functional Materials. *Angewandte Chemie - International Edition*. John Wiley & Sons, Ltd July 5, 2010, pp 4878–4897.
- (14) Yarema, O.; Yarema, M.; Wood, V. Tuning the Composition of Multicomponent

- Semiconductor Nanocrystals: The Case of I–III–VI Materials. *Chem. Mater.* **2018**, *30* (5), 1446–1461.
- (15) Smith, A. M.; Nie, S. Semiconductor Nanocrystals: Structure, Properties, and Band Gap Engineering. *Acc. Chem. Res.* **2010**, *43* (2), 190–200.
  - (16) Buhro, W. E.; Colvin, V. L. Shape Matters. *Nat. Mater.* **2003**, *2* (3), 138–139.
  - (17) van der Stam, W.; Berends, A. C.; de Mello Donega, C. Prospects of Colloidal Copper Chalcogenide Nanocrystals. *ChemPhysChem* **2016**, *17* (5), 559–581.
  - (18) Fu, H. Environmentally Friendly and Earth-Abundant Colloidal Chalcogenide Nanocrystals for Photovoltaic Applications. *J. Mater. Chem. C* **2018**, *6* (3), 414–445.
  - (19) Reiss, P.; Carrière, M.; Lincheneau, C.; Vaure, L.; Tamang, S. Synthesis of Semiconductor Nanocrystals, Focusing on Nontoxic and Earth-Abundant Materials. *Chem. Rev.* **2016**, *116* (18), 10731–10819.
  - (20) Yu, L.; Kokenyesi, R. S.; Keszler, D. A.; Zunger, A. Inverse Design of High Absorption Thin-Film Photovoltaic Materials. *Adv. Energy Mater.* **2013**, *3* (1), 43–48.
  - (21) Boles, M. A.; Engel, M.; Talapin, D. V. Self-Assembly of Colloidal Nanocrystals: From Intricate Structures to Functional Materials. *Chem. Rev.* **2016**, acs.chemrev.6b00196.
  - (22) Mazing, D. S.; Korepanov, O. A.; Aleksandrova, O. A.; Moshnikov, V. A. Synthesis of Ternary Metal Chalcogenide Colloidal Nanocrystals in Aqueous Solutions. *Opt. Spectrosc. (English Transl. Opt. i Spektrosk.* **2018**, *125* (5), 773–776.
  - (23) De Yoreo, J. J.; Gilbert, P. U. P. A.; Sommerdijk, N. A. J. M.; Penn, R. L.; Whitelam, S.; Joester, D.; Zhang, H.; Rimer, J. D.; Navrotsky, A.; Banfield, J. F.; et al. Crystallization by Particle Attachment in Synthetic, Biogenic, and Geologic Environments. *Science* **2015**, *349* (6247), aaa6760–aaa6760.
  - (24) Gebauer, D.; Wolf, S. E. Designing Solid Materials from Their Solute State: A Shift in Paradigms toward a Holistic Approach in Functional Materials Chemistry. *J. Am. Chem. Soc.* **2019**, *141* (11), 4490–4504.
  - (25) Lee, J. M.; Miller, R. C.; Moloney, L. J.; Prieto, A. L. The Development of Strategies for Nanoparticle Synthesis: Considerations for Deepening Understanding of Inherently Complex Systems. *J. Solid State Chem.* **2019**, *273*, 243–286.
  - (26) Friedfeld, M. R.; Stein, J. L.; Cossairt, B. M. Main-Group-Semiconductor Cluster Molecules as Synthetic Intermediates to Nanostructures. *Inorg. Chem.* **2017**, *56* (15), 8689–8697.
  - (27) Mozaffari, S.; Li, W.; Dixit, M.; Seifert, S.; Lee, B.; Kovarik, L.; Mpourmpakis, G.; Karim, A. M. The Role of Nanoparticle Size and Ligand Coverage in Size Focusing of Colloidal Metal Nanoparticles. *Nanoscale Adv.* **2019**, *1* (10), 4052–4066.
  - (28) Whitehead, C. B.; Finke, R. G. Nucleation Kinetics and Molecular Mechanism in Transition-Metal Nanoparticle Formation: The Intriguing, Informative Case of a Bimetallic Precursor,  $\{[(1,5\text{-COD})\text{Ir}^{\text{I}}\cdot\text{HPO}_4]_2\}^{2-}$ . *Chem. Mater.* **2019**, *31* (8), 2848–2862.
  - (29) Soderholm, L.; Mitchell, J. F. Perspective: Toward “Synthesis by Design”: Exploring Atomic Correlations during Inorganic Materials Synthesis. *APL Mater.* **2016**, *4* (5), 053212.
  - (30) Das, A.; Shamirian, A.; Snee, P. T. Arsenic Silylamide: An Effective Precursor for Arsenide Semiconductor Nanocrystal Synthesis. *Chem. Mater.* **2016**, *28* (11), 4058–4064.
  - (31) García-Rodríguez, R.; Hendricks, M. P.; Cossairt, B. M.; Liu, H.; Owen, J. S. Conversion Reactions of Cadmium Chalcogenide Nanocrystal Precursors. *Chem. Mater.* **2013**, *25* (8), 1233–1249.

- (32) Sowers, K. L.; Swartz, B.; Krauss, T. D. Chemical Mechanisms of Semiconductor Nanocrystal Synthesis. *Chem. Mater.* **2013**, *25* (8), 1351–1362.
- (33) Holder, C. F.; Schaak, R. E. Tutorial on Powder X-Ray Diffraction for Characterizing Nanoscale Materials. *ACS Nano* **2019**, *13* (7), 7359–7365.
- (34) Schaak, R. E.; Williams, M. E. Full Disclosure: The Practical Side of Nanoscale Total Synthesis. *ACS Nano* **2012**, *6* (10), 8492–8497.
- (35) Lee, J. M.; Kraynak, L. A.; Prieto, A. L. A Directed Route to Colloidal Nanoparticle Synthesis of the Copper Selenophosphate  $\text{Cu}_3\text{PSe}_4$ . *Angew. Chemie Int. Ed.* **2020**, *59* (8), 3038–3042.
- (36) Yordanov, G. G.; Yoshimura, H.; Dushkin, C. D. Phosphine-Free Synthesis of Metal Chalcogenide Quantum Dots by Means of in Situ-Generated Hydrogen Chalcogenides. *Colloid Polym. Sci.* **2008**, *286* (6–7), 813–817.
- (37) Deng, Z.; Cao, L.; Tang, F.; Zou, B. A New Route to Zinc-Blende CdSe Nanocrystals: Mechanism and Synthesis. *J. Phys. Chem. B* **2005**, *109* (35), 16671–16675.
- (38) Bullen, C.; van Embden, J.; Jasieniak, J.; Cosgriff, J. E.; Mulder, R. J.; Rizzardo, E.; Gu, M.; Raston, C. L. High Activity Phosphine-Free Selenium Precursor Solution for Semiconductor Nanocrystal Growth. *Chem. Mater.* **2010**, *22* (14), 4135–4143.
- (39) Frenette, L. C.; Krauss, T. D. Uncovering Active Precursors in Colloidal Quantum Dot Synthesis. *Nat. Commun.* **2017**, *8* (1), 2082.
- (40) Pu, C.; Zhou, J.; Lai, R.; Niu, Y.; Nan, W.; Peng, X. Highly Reactive, Flexible yet Green Se Precursor for Metal Selenide Nanocrystals: Se-Octadecene Suspension (Se-SUS). *Nano Res.* **2013**, *6* (9), 652–670.
- (41) Li, Z.; Ji, Y.; Xie, R.; Grisham, S. Y.; Peng, X. Correlation of CdS Nanocrystal Formation with Elemental Sulfur Activation and Its Implication in Synthetic Development. *J. Am. Chem. Soc.* **2011**, *133* (43), 17248–17256.
- (42) Sheets, E. J.; Yang, W.-C.; Balow, R. B.; Wang, Y.; Walker, B. C.; Stach, E. A.; Agrawal, R. An in Situ Phosphorus Source for the Synthesis of  $\text{Cu}_3\text{P}$  and the Subsequent Conversion to  $\text{Cu}_3\text{PS}_4$  Nanoparticle Clusters. *J. Mater. Res.* **2015**, *30* (23), 3710–3716.
- (43) Dhaene, E.; Billet, J.; Bennett, E.; Van Driessche, I.; De Roo, J. The Trouble with ODE: Polymerization during Nanocrystal Synthesis. *Nano Lett.* **2019**, *19* (10), 7411–7417.
- (44) Bhattacharyya, K. X.; Pradel, C.; Lecante, P.; Mézailles, N. Mechanistic Investigations of the Synthesis of Size-Tunable Ni Nanoparticles by Reduction of Simple Ni II Diamide Precursors. *Chem. - A Eur. J.* **2017**, *23* (39), 9352–9361.
- (45) Aiken, J. D.; Finke, R. G. A Review of Modern Transition-Metal Nanoclusters: Their Synthesis, Characterization, and Applications in Catalysis. *Journal of Molecular Catalysis A: Chemical*. Elsevier September 8, 1999, pp 1–44.
- (46) Wei, S.; Qi, K.; Jin, Z.; Cao, J.; Zheng, W.; Chen, H.; Cui, X. One-Step Synthesis of a Self-Supported Copper Phosphide Nanobush for Overall Water Splitting. *ACS Omega* **2016**, *1* (6), 1367–1373.
- (47) Li, Z.; Ji, S.; Liu, Y.; Cao, X.; Tian, S.; Chen, Y.; Niu, Z.; Li, Y. Well-Defined Materials for Heterogeneous Catalysis: From Nanoparticles to Isolated Single-Atom Sites. *Chemical Reviews*. American Chemical Society January 22, 2020, pp 623–682.
- (48) Shen, H.; Wang, H.; Li, X.; Niu, J. Z.; Wang, H.; Chen, X.; Li, L. S. Phosphine-Free Synthesis of High Quality ZnSe, ZnSe/ZnS, and Cu-, Mn-Doped ZnSe Nanocrystals. *Dalt. Trans.* **2009**, *0* (47), 10534.
- (49) Deng, Z.; Cao, L.; Tang, F.; Zou, B. A New Route to Zinc-Blende CdSe Nanocrystals:

Mechanism and Synthesis.

- (50) Scilabra, P.; Terraneo, G.; Resnati, G. The Chalcogen Bond in Crystalline Solids: A World Parallel to Halogen Bond. *Acc. Chem. Res.* **2019**, *52*, 59.
- (51) Benz, S.; López-Andarias, J.; Mareda, J.; Sakai, N.; Matile, S. Catalysis with Chalcogen Bonds. *Angew. Chemie Int. Ed.* **2017**, *56* (3), 812–815.
- (52) Wang, W.; Zhu, H.; Feng, L.; Yu, Q.; Hao, J.; Zhu, R.; Wang, Y. Dual Chalcogen–Chalcogen Bonding Catalysis. *J. Am. Chem. Soc.* **2020**, *142* (6), 3117–3124.
- (53) Murray, J. S.; Lane, P.; Politzer, P. Expansion of the  $\sigma$ -Hole Concept. *J. Mol. Model.* **2009**, *15* (6), 723–729.
- (54) Rahman, F.; Tzeli, D.; Petsalakis, I. D.; Ballester, P.; Rebek, J.; Yu, Y.; Jr, J. R.; Yu, Y. Chalcogen Bonding and Hydrophobic Effects Force Molecules into Small Spaces Chalcogen Bonding and Hydrophobic Effects Force Molecules into Small Spaces. *J. Am. Chem. Soc.* **2020**.
- (55) Haberhauer, G.; Gleiter, R. The Nature of Strong Chalcogen Bonds Involving Chalcogen-Containing Heterocycles. *Angew. Chemie Int. Ed.* **2020**, *59* (47), 21236–21243.
- (56) Scholfield, M. R.; Ford, M. C.; Vander Zanden, C. M.; Billman, M. M.; Ho, P. S.; Rappé, A. K. Force Field Model of Periodic Trends in Biomolecular Halogen Bonds. *J. Phys. Chem. B* **2015**, *119* (29), 9140–9149.
- (57) Joyce, J. P.; Shores, M. P.; Rappé, A. K. Protobranching as Repulsion-Induced Attraction: A Prototype for Geminal Stabilization. *Phys. Chem. Chem. Phys.* **2020**, *22* (29), 16998–17006.
- (58) Cudby, M. E. A.; Willis, H. A. The Nuclear Magnetic Resonance Spectra of Polymers. *Annu. Reports NMR Spectrosc.* **1972**, *4* (C), 363–389.
- (59) Schulte-Kellinghaus, M.; Krämer, V. Thermogravimetric Investigations of Some Thioorthophosphates and Thiohypodiphosphates. *Thermochim. Acta* **1978**, *27* (1–3), 141–149.
- (60) Garin, J.; Parthé, E. The Crystal Structure of  $\text{Cu}_3\text{PSe}_4$  and Other Ternary Normal Tetrahedral Structure Compounds with Composition  $1_356_4$ . *Acta Crystallogr. Sect. B Struct. Crystallogr. Cryst. Chem.* **1972**, *28* (12), 3672–3674.

## CHAPTER 6

### IN SITU CHARACTERIZATION SUITE FOR THE REACTION LANDSCAPE ELUCIDATION OF COLLOIDAL COPPER SELENOPHOSPHATE, $\text{Cu}_3\text{PSe}_4$ , NANOPARTICLE (NP) SYNTHESIS<sup>6</sup>

#### 6.1. Introduction

Elucidation of reaction pathways and landscapes are valuable to inform and subsequently guide the rational yet rapid synthesis of colloidal nanoparticles.<sup>1-4</sup> Common characterization methods,<sup>5,6</sup> reviewed in Chapter 3, to characterize reaction mechanism processes include NMR,<sup>7-14</sup> IR,<sup>15-17</sup> UV-Vis,<sup>18,19</sup> and MS.<sup>20,21</sup> These techniques are particularly useful in describing molecular species and are highly developed for describing the transformation of monomers and ligand coordination. However, their use does not typically extend to the solid-state components which are commonly characterized by XRD,<sup>22-25</sup> TEM,<sup>26</sup> Raman,<sup>27-30</sup> thermal analysis,<sup>31-33</sup> and XPS.<sup>34-37</sup> Ultimately, the true pitfall of traditional characterization methods is that they are performed on isolated components of NP syntheses and are, thus, limited to the characterization of specific processes. Further, these methods are often completed on ex situ aliquots in which speciation could be an artifact of quenching.<sup>38,39</sup> What is not well understood is the characterization of overlooked species such as amorphous inorganic, intermediate inorganic, or gaseous species. Unfortunately, these transient species are difficult to capture, and their characterization is limited to a couple of techniques such as electron microscopy (EM) and STEM/EDS, which are quite expensive or inaccessible, limiting the number of alternative options for complementary

---

<sup>6</sup> This chapter was written by Jennifer M. Lee with insights and edits from Amy L. Prieto. All samples and capillaries for in situ were prepared by Jennifer M. Lee. The Epyrean data was collected by Jewels M. Fallon at Colorado State University (Neilson group), and the ssNMR data was collected by Sawankumar V. Patel at Florida State University (Hu group) at the MagLab. The  $\text{Cu}_3\text{PSe}_4$  synthesis with  $\frac{1}{4}$  Se was performed by Devon Leimkuhl at Colorado State University (Prieto group), an undergraduate who I mentored.

techniques. To gain greater spatial resolution of the reaction flask of simultaneous processes and speciation, in situ information about how, when, and what materials form during synthesis is desired.<sup>40-44</sup> This information combined with theory to provide a basis upon which to inform materials design<sup>3,45-48</sup> would provide the foundation necessary to move toward a more expansive synthesis-by-design approach to inorganic materials than is currently available.<sup>45,46,49,50</sup>

The advancements outlined herein provide temporal observations of processes via in situ methodology.<sup>38,39,41,51</sup> We investigate the solution-based synthesis of  $\text{Cu}_3\text{PSe}_4$  as a case study in which a single-pot  $\text{Cu}_3\text{P}$ , Se powder, and 1-octadecene (ODE) precursors are heated to 300 °C and held for 20 min under  $\text{N}_2$  environment.<sup>52</sup> Crystalline or nanoscale species can be monitored by diffraction, and molecular and supramolecular speciation can be monitored by ssNMR. We are currently able to perform in situ diffraction in-house due to a PANalytical Empyrean, which is outfitted with a silver focusing mirror and Ag X-ray source, providing harder and higher energy beams than that of Cu. However, if the signal to noise ratio presents challenges, we will apply for beamtime at Argonne. Both  $^{31}\text{P}$  and  $^{77}\text{Se}$  ssNMRs can be performed through our collaboration with the Hu group at FSU<sup>53,54</sup>

## 6.2. Experimental

*Materials and Methods.* All reactions were performed under inert atmosphere unless otherwise noted. All product workup was done on the benchtop in ambient conditions unless otherwise noted. Copper (II) chloride ( $\text{CuCl}_2$ , Riedel-de Haën, 97%), trioctylphosphine oxide (TOPO, Aldrich, 99%), triphenyl phosphite (TPOP, Oakwood Chemical, 97%), hexadecylamine (HDA, Aldrich, 90%), and selenium powder (Se, Strem Chemicals Inc., 99.99%) were purchased and used as received. Technical grade toluene, hexanes, ethanol, isopropanol, and chloroform were obtained

from Fisher Scientific. The solvent 1-octadecene (ODE, Aldrich, 90%) was sparged with N<sub>2</sub> for 2 h before use.

*Cu<sub>3</sub>P Nanoparticle Heat-up Synthesis.* Literature protocol developed by Liu et al.<sup>55</sup> was adapted for the formation of Cu<sub>3</sub>P by a scalable and cost-effective heat-up method. In a typical synthesis, 0.5 mmol CuCl<sub>2</sub>, 5.0 mmol HDA, 5.0 mmol TPOP (Cu:HDA:TPOP = 1:10:10), and 10 g ODE were added to a 50 mL three-neck round-bottomed flask equipped with glass stir bar, reflux condenser, and thermocouple. The reaction flask was degassed under N<sub>2</sub> at 150°C for 1 h. The solution was then heated to 300°C where it was held for 0.5 h. The reaction was cooled to 200°C before removal of the heating mantle, then further cooled to ~80°C. The particles were collected by dispersion of the reaction mixture in chloroform then flocculation with isopropanol. After 15 min of centrifugation at 5800 rpm, the supernatant was discarded. The washing procedure was repeated with a sonication step to aid dispersion in chloroform before addition of isopropanol. The mixture was centrifuged at 5800 rpm for 8 min, and then the supernatant was discarded. Nanoparticles were stored in hexanes.

*Nanoparticle Synthesis of Cu<sub>3</sub>PSe<sub>4</sub> with Aliquot Removal.* Nanoparticles of Cu<sub>3</sub>P, as synthesized above, were initially dried over N<sub>2</sub> then finished drying under vacuum overnight in a 100 mL 3-neck round-bottom flask equipped with a glass stir bar, Liebig condenser, and thermocouple. Excess Se (1.07 mmol) and ODE (10.7 mL, 0.1 M dispersion Se/ODE) were then added to the flask. For the neat reaction, the solvent was eliminated, but the other quantities and reaction parameters remained the same. The flask was pumped and purged between vacuum and N<sub>2</sub> for three cycles, then heated to 150 °C at a rate of 500 °C/h under vacuum. The flask was switched to positive N<sub>2</sub> pressure and heated to 300 °C where it was held for 20 min. Aliquots of the reaction were removed by a glass Luer-lock syringe at relevant time and temperature points into

scintillation vials. Samples were centrifuged, and the solution was decanted for characterization. The isolated precipitate was dispersed in toluene and flocculated with ethanol similarly to the washing procedure described above for Cu<sub>3</sub>P. After 15 min of centrifugation at 5800 rpm, the supernatant was discarded. The washing procedure was repeated with a sonication step to aid dispersion in toluene before addition of ethanol. The mixture was centrifuged at 5800 rpm for 8 min, and then the supernatant was discarded. Nanoparticles were stored in hexanes. Any remaining reaction mixture in the flask was cooled to ~80°C by removal of the heating mantle and separated into centrifuge tubes. Samples were centrifuged, and the solution was decanted for characterization. The isolated precipitate was washed with toluene and ethanol as previously described. Particles were stored in hexanes.

### **6.3. Materials Characterization**

*Solution-Based Reaction Capillary Preparation.* A scintillation vial of Cu<sub>3</sub>P, Se powder, and ODE was sonicated for 10 min. The reaction mixture was then injected into a borosilicate capillary which was flame-sealed on one end, taking care the solution minimally touched the open end of the capillary. The open end of the capillary was then attached to a sealing line where the mixture was frozen with liquid N<sub>2</sub> then pumped/purged three times between vacuum and N<sub>2</sub>. While the capillary was under N<sub>2</sub>, the capillary was flame-sealed.

*Capillary Preparation of Powders.* A borosilicate capillary was flame-sealed on one end. Powders were tapped into the capillary, and the open end was flame-sealed.

*Diffraction.* Ex situ powder X-ray diffraction (PXRD) was performed on a Bruker D8 Discover DaVinci Powder X-ray Diffractometer equipped with Cu K $\alpha$  radiation ( $\lambda = 1.54 \text{ \AA}$ ). Samples were prepared by dispersing the nanoparticles in hexanes and then drop-casting onto a p-type boron

doped Si Zero Diffraction Plate. The patterns were characterized by matching known PDF patterns in the PDF-4 database installed on the DIFFRAC.EVA software. The data was treated with the subtraction of  $K\alpha$  peaks and the smoothing function of the software. In situ X-ray scattering data was collected on a PANalytical Empyrean Diffractometer with the GaliPIX 2D detector using  $AgK\alpha$  radiation. Samples were packed in a 1.2 mm inner diameter (ID) borosilicate capillary and flame-sealed on both ends by the above methods. Empyrean optics (i.e. slit sizes, soller slits, anti-scattering slits) and the packing fraction of each starting reagent ( $Cu_3P$ , Se, ODE) were optimized to maximize signal-to-noise ratio.

*Magnetic Resonance.* Solution-based  $^1H$  NMR spectroscopy was performed on an Agilent (Varian) 400MR equipped with automated tuning. Samples were dissolved in  $CDCl_3$  as reference. The deuterated solvent  $CDCl_3$  was dried over activated 4Å molecular sieves. The data was processed in MestReNova, and all spectra were shifted to 7.24 ppm for  $CDCl_3$ . Solid-state NMR (ssNMR) was performed in collaboration with the Hu group at Florida State University and the National High Magnetic Field Laboratory (MagLab). Samples were packed in a 3 mm outer diameter (OD) borosilicate capillary and were flame-sealed to be no longer than 15 mm in length.

#### **6.4. Results and Discussion**

Ex situ studies provided a framework in which the reaction pathway could be elucidated. Aliquots of the total reaction were sampled with a Luer-Lock glass syringe at 150 °C, 200 °C, 225 °C, 250 °C, and 300 °C. At 300 °C, additional samples were taken after 5, 10, and 20 min. Through 200 °C, only the starting reagent Se was observed, swamping out signal from  $Cu_3P$ . The first noted transformation is at 225 °C in the XRD (Figure 6.1). This aligns well with the m.p. of Se powder (220 °C). However, there is no change in the  $^1H$  NMR, so the solution presumably remains

unchanged for this process. The formation of  $\text{Cu}_3\text{PSe}_4$  began at 250 °C and was the only crystalline species present instantaneously at 300 °C (Figure 6.1A). At 300 °C was the first transformation in the solution as observed in the  $^1\text{H}$  NMR (Figure 6.1B). This corresponds to the formation of dialkyl selenides,  $\text{SeR}_2$  where R = alkene of various lengths, in which an isomerized ODE reacts with Se-R moiety through the 1-carbon by a 2-electron oxidation.

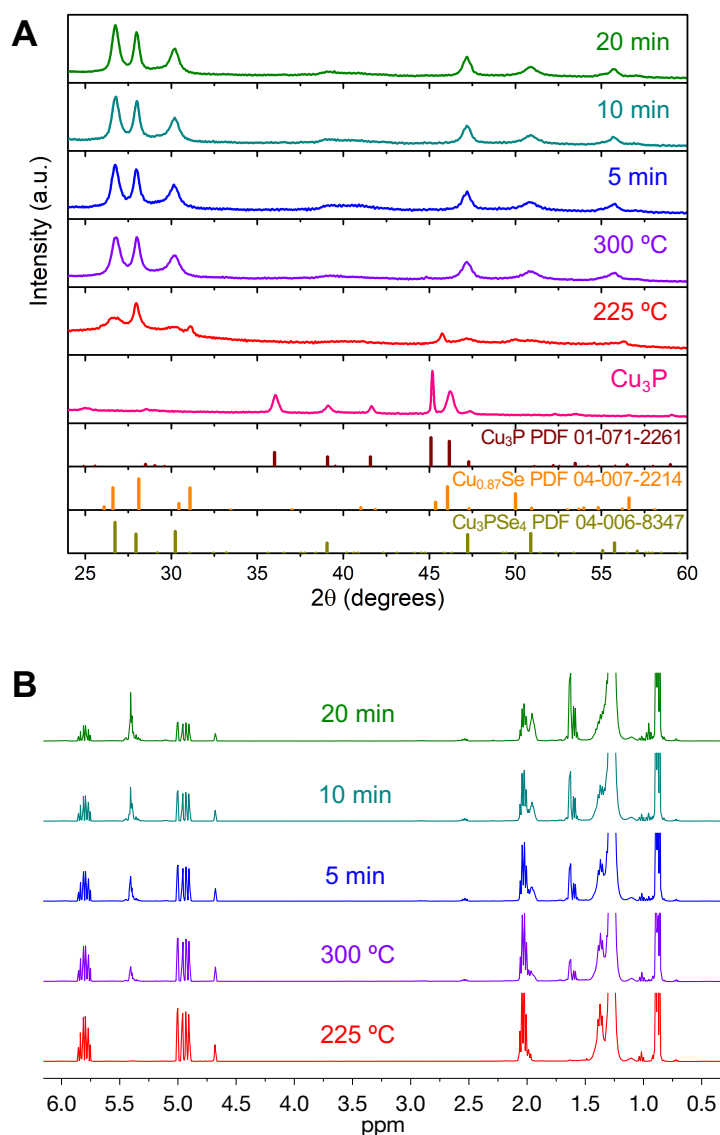


**Figure 6.1.** Ex situ aliquot characterization of  $\text{Cu}_3\text{PSe}_4$  synthesis ( $\text{Cu}_3\text{P} + \text{Se}/\text{ODE}$ , 300 °C for 20 min) via (A) XRD and (B)  $^1\text{H}$  NMR.

The data point at 225 °C is curious due to the crystal structures of the starting material and final product in which all Cu-P bonds are transformed into Cu-Se and Se-P bonds. The existence of the Cu-Se binary suggests that Cu-P bonds are broken to form Cu-Se bonds first, but it is unclear if  $\text{Cu}_{1-x}\text{Se}$  is an artifact of quenching the aliquot sample or an intermediate that participates in the reaction pathway. It is also unclear from these characterization methods how phosphorus is incorporated into the ternary product. Two hypotheses include P insertion into the Cu-Se crystal structure (conversion pathway) or Cu-Se dissolves back into solution before P incorporation (consumption pathway).

Previous computational studies have demonstrated that dative P-Se bonds were driven by chalcogen bonding in which the sigma-hole along the Se-R bond interacted with corresponding nucleophilic  $\text{Cu}_3\text{P}$  upon linear contact (Chapter 5). By computation, we also observed that an excited Se singlet state, in which anisotropic electron distribution in the orbitals enabled three dative bonds between the Se monomer and nucleophile, was accessible via  $\text{SeR}_2$  and Se atoms. Thus, the molecular reaction scheme to form P-Se bonds is accessible by either a solution-mediated pathway (ODE-based) where the solvent is an active participant or by solid-state diffusion (neat) although it is unclear if these overall pathways are the same or distinct. To target these questions, in situ methodologies are crucial to enable spatial resolution of the reaction as it progresses. Further, in situ experiments provide an opportunity to confirm theory. While in situ diffraction can provide information on the crystalline intermediates, techniques such as ssNMR that inform on the molecular regime or local range are also required to elucidate the reaction schemes in which growth of  $\text{Cu}_3\text{PSe}_4$  can occur.

In situ methodologies for solid state reactions have emerged as valuable and powerful techniques to access spatial resolution of the reaction speciation as well as dynamic

structure/materials property relationships.<sup>43,56</sup> Thus, capillary setups for traditional solid-state syntheses and materials are well known. While a capillary preparation for the solution-based synthesis of CdSe exists in which sticky tack was used to seal both ends of the capillary,<sup>38</sup> these methods are not as well recognized nor developed for high temperature ( $>100$  °C), solution-based syntheses. To refine these techniques and overcome these limitations, a capillary preparation that could withstand high temperatures and remain under inert conditions was developed and optimized (Figure 6.2A; see also Section 6.3). Shown in Figure 6.2B is an image of a sealed capillary with solution-based sample and the same capillary upon heating to reaction conditions of 300 °C for 20 min. The capillary remained intact.

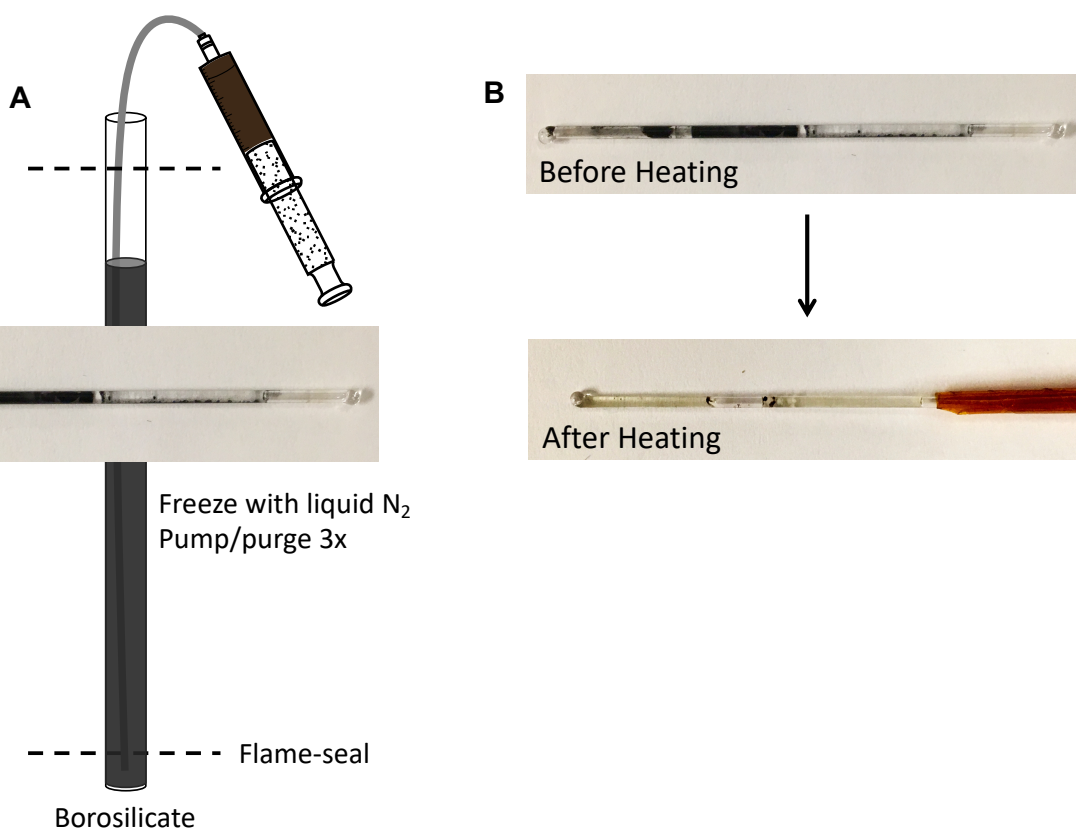


**Figure 6.2.** (A) Capillary preparation for air-sensitive, solution-based reactions that could withstand high temperatures. (B) Images of a 1.2 mm outer diameter borosilicate capillary containing Cu<sub>3</sub>P, Se powder, and ODE before heating and after heating to 300 °C for 1 h in which there is black precipitate for the product and the solution has turned yellow, indicative of Se powder dissolved in ODE.

Through iterative optimizations via the Empyrean optics (i.e. slit sizes, soller slits, anti-scattering slits), X-ray source (Ag, 0.5608 Å, 22.1071 KeV as opposed to lower energy Cu), and packing fraction of each starting reagent (Cu<sub>3</sub>P, Se, ODE), diffraction data was collected on the packed capillaries of both the solution-based and neat reactions at room temperature (Figure 6.3). When the concentration of the precursors (or packing fractions) was not optimized for X-ray absorption on capillary samples, no signal was observed.

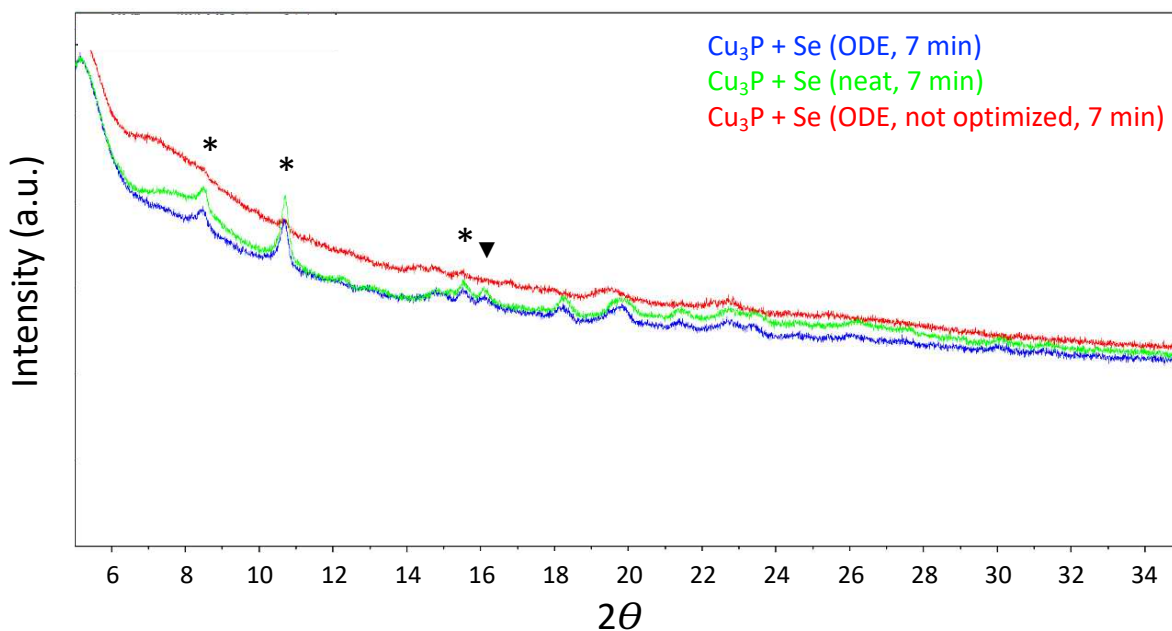


**Figure 6.3.** Room temperature XRD of capillaries containing ODE-based or neat reaction samples. All scans were collected for 7 min on the Empyrean with a silver X-ray source and Ag focusing mirror. Asterisk (\*) are peaks corresponding to Se and one of the peaks corresponding to Cu<sub>3</sub>P is labeled with a triangle (▼).

Sample packing is a crucial parameter to consider due to the capillary sample X-ray absorption that occurs as a result of the transmission geometry (Debye-Scherrer) of the powder X-ray diffraction measurements.<sup>57-59</sup> However, the virtue of this geometry is its ability to offset peak broadening that occurs from small crystallites by simply rotating the capillary on its axis to increase the number of crystallite orientations offered to the incident X-ray beam. To mitigate any sample absorption, especially from Se which strongly absorbs X-rays, the Se content was reduced

in the solution-based sample ( $\text{Cu}_3\text{P}:4 \text{ Se}:2 \text{ ODE}$  weight%) and the neat reaction was diluted with  $\text{SiO}_2$  ( $\text{Cu}_3\text{P}:8 \text{ Se}:72 \text{ SiO}_2$  weight%), but the reaction amount of the starting materials stayed consistent with normal-scale reactions. When the packing fraction was optimized, both samples showed comparable peak intensities in the XRD when collected at 7 min scans, irrespective of the solution-based or neat reaction conditions. In the XRD data, we distinctly observed Se powder and perhaps  $\text{Cu}_3\text{P}$ , which was expected for the RT temp scans due to the higher concentration and crystallinity of Se powder in comparison to  $\text{Cu}_3\text{P}$ . While we could boost the  $\text{Cu}_3\text{P}$  concentration, the reaction pathway was altered when the concentration of Se was decreased to  $\frac{1}{4}$  of its original concentration in a normal scale reaction (Figure 6.4). As opposed to phase-pure  $\text{Cu}_3\text{PSe}_4$ , we also observed the formation of metastable  $\text{Cu}_7\text{PSe}_6$  and  $\text{Cu}_{1.77}\text{Se}$  via XRD.

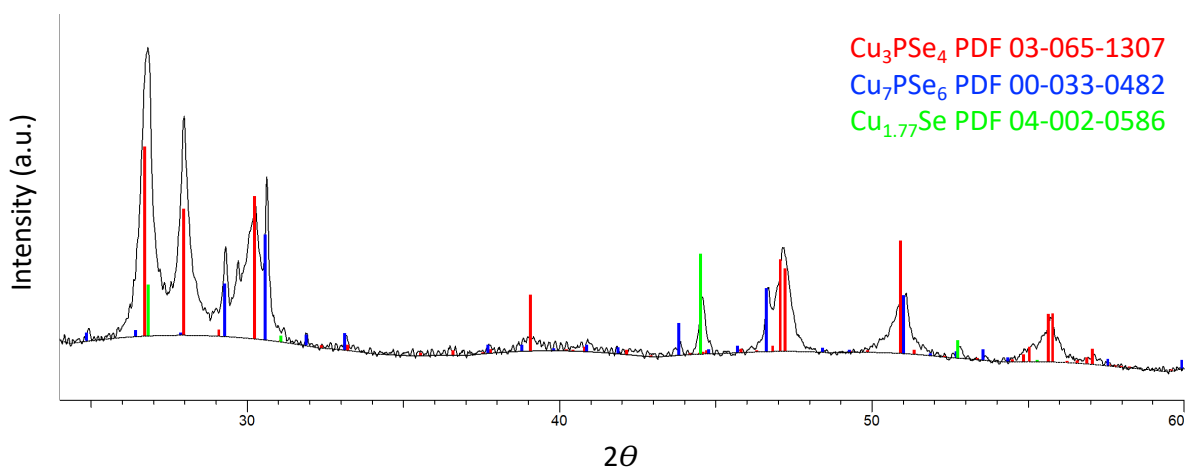


**Figure 6.4.** XRD pattern of the  $\text{Cu}_3\text{PSe}_4$  reaction product in which the content of the Se starting reagent was quartered.

Because the neat reaction was most reflective of the reaction scale in terms of starting reagent quantities, preliminary passes applying heat were implemented for the neat sample (Figure 6.5). Samples were ramped from  $25 \text{ }^\circ\text{C}$  to  $200 \text{ }^\circ\text{C}$  in which a 7 min scan was collected at  $25 \text{ }^\circ\text{C}$  increments. Then, the reaction was ramped from  $200 \text{ }^\circ\text{C}$  to  $300 \text{ }^\circ\text{C}$  in which a 7 min scan was collected at each  $10 \text{ }^\circ\text{C}$  increments. The sample was held at  $300 \text{ }^\circ\text{C}$  for 20 min before collecting

another 7 min scan. The sample was allowed to cool back to 25 °C, at which point a final 7 min scan was collected.

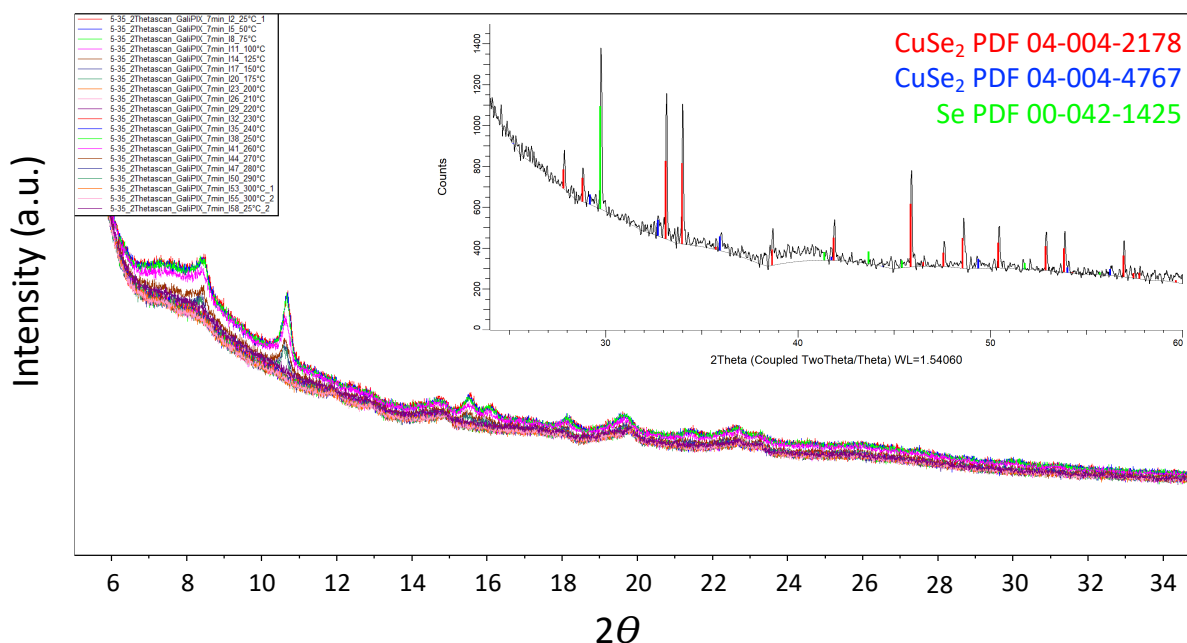


**Figure 6.5.** In situ XRD of capillary containing neat reaction ( $\text{Cu}_3\text{P}:8 \text{ Se}:72 \text{ SiO}_2$  weight%). The heating profile of the reaction was from 25 °C to 300 °C then cooled. All scans were collected for 7 min on the Empyrean with a silver X-ray source and Ag focusing mirror.

Upon heating the samples, the sample signal continued to decrease. Unfortunately, the heating stage impacted how the sample was mounted to the instrument, throwing the capillary off its rotation axis, preventing incident X-rays from irradiating the sample. To examine if our ternary  $\text{Cu}_3\text{PSe}_4$  product was still formed in the capillary despite the lack of collected data, the capillary was cracked, and the powder was examined by PXRD. No ternary product was formed, instead  $\text{CuSe}_2$  binaries and Se were observed. This could be a result of diffusion. Because the powder was diluted so significantly with ground  $\text{SiO}_2$  powder, the  $\text{Cu}_3\text{P}$  and Se powders were not in high surface contact to one another. Instead, to overcome these limitations and probe the neat reaction, a diffractometer outfitted with a HTK high temperature stage in which the powder is not in a capillary but still under flowing  $\text{N}_2$  could prove much more promising. In this case, both diffusion

and sample X-ray absorption would be addressed. While in-house experiments with the Empyrean built a foundation in which future studies could be built, the signal intensities from the capillary samples were too low for our purposes of exploring the reaction pathway. Instead, we motivate the application for beamtime at synchrotron sources such as Argonne to increase the power of the energy source and improve signal collected at the detector.

The goal of ssNMR is to characterize species that are often overlooked by typical characterization methods such as phosphorus-containing compounds or are difficult to characterize due to its complex speciation such as selenium-containing compounds.<sup>60-62</sup> While we have previously attempted solution-based <sup>31</sup>P NMR on our samples, insight was only gained on the ligands or surfactants but not on the inorganic core material.<sup>17,63</sup> While characterization via STEM/EDS allows for elemental analysis of the starting and final crystalline nanoparticles, amorphous (or intermediate) P-containing species are more difficult to monitor due to its small atomic number which can be difficult to detect by electron microscopy techniques.<sup>64,65</sup> Further, these species likely exist as molecular or supramolecular species in solution which could be obliterated by the electron beam. Although we do not see any crystalline phosphorus-containing intermediates via XRD, the presence of crystalline Cu-Se intermediates suggests that phosphorus exists somewhere in our reaction flask. Further, in situ provides an opportunity to confirm theory. We previously collaborated with a computational chemist and hypothesized that compatible Lewis acidic/basic monomer pair, SeR<sub>2</sub> (Lewis basic along the Se-R bond) and nucleophilic Cu<sub>3</sub>P, participate in chalcogen bonding to form dative P-Se bonds in [PSe<sub>4</sub>]<sup>3-</sup> tetrahedra via charge transfer (Chapter 5). Thus, we seek to characterize elusive P-intermediates to elucidate their roles in the Cu<sub>3</sub>PSe<sub>4</sub> synthesis.

Preliminary work in collaboration with the Hu group for  $^{31}\text{P}$  ssNMR on the powders of the starting material ( $\text{Cu}_3\text{P}$ ) and final product ( $\text{Cu}_3\text{PSe}_4$ ) showed that they resonate at very different  $^{31}\text{P}$  NMR shifts, 180 ppm and -83 ppm respectively (Figure 6.6). The very large difference in the chemical shifts provides an opportunity in which phosphorus speciation of the full reaction ( $\text{Cu}_3\text{P} + \text{Se}/\text{ODE}$  at 300 °C for 20 min) can be deconvoluted.

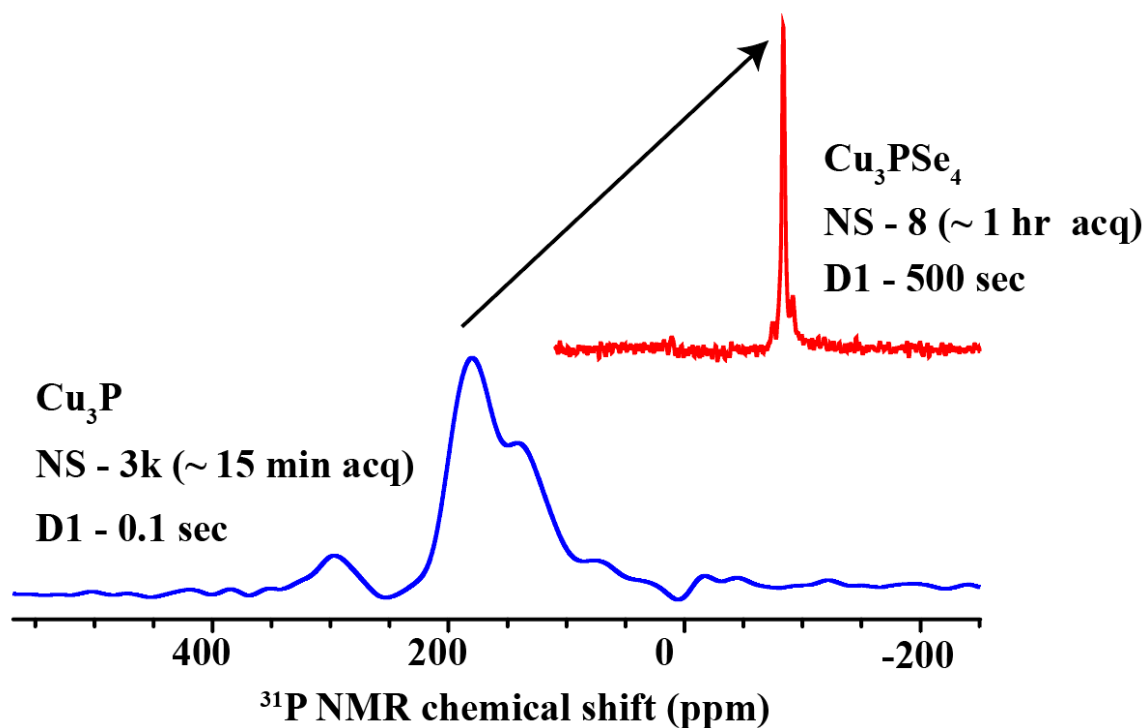


**Figure 6.6.**  $^{31}\text{P}$  ssNMR of  $\text{Cu}_3\text{P}$  and  $\text{Cu}_3\text{PSe}_4$  powders. The  $^{31}\text{P}$  NMR shift for  $\text{Cu}_3\text{P}$  has fast relaxation and the peak resonates around 180 ppm. The final product has a negative shift of around -83 ppm.

However, sensitivity of the probe could present issues in the signal-to-noise ratio of the standard reaction. The powder samples were run at 20 kHz spin rate using the 2.5 mm probe at room temperature. This is incredibly more sensitive than the laser probe that would be used for solution-based samples because the laser probe requires samples to be static (no spinning). The experiments will additionally be coupled with heating and cooling which is generally plagued by convolutions or loss of signal. Further, metallic Se and some metallic character in  $\text{Cu}_3\text{P}$  can

conduct electrons and subsequently generate a local magnetic current when spinning, preventing collection of signal. While the reagent quantities can be balanced to limit the impact of metallic Se, the solvent also dilutes signal from the samples. Ongoing work is focused on optimizing the starting reagent quantities to maximize signal collection while still representing the reaction concentrations. To overcome any of these challenges, the power or the number of scans collected can also be increased.

## 6.5. Conclusion and Outlook

The ability to increase spatial resolution of a reaction is incredibly valuable to elucidate, map, and guide reaction landscapes. While our work only presents preliminary data, it serves as a foundation for solution-based in situ methodology to be built on. A significant challenge that existed for the collection of high-quality data across all techniques was the optimization of the starting reagent amount to balance having enough material to overcome instrumentation limitations (i.e. X-ray or energy absorption, signal dilution, etc) while still being representative of the overall reaction. An additional consideration was the collection time of the samples. The diffraction patterns were collected over 7 min for each temperature step, totaling 140 min in experiment time not including ramp time to each temperature point. First and foremost, sample quantities must be optimized. Then, in both cases, the power of the instrument can be increased to improve the data quality and reduce the time required for each temperature point.

One method we did not explore but could prove quite useful as a complementary technique is in situ PDF. The PDF method probes nearest neighbors around an atom with high energy (short wavelength) X-rays, elucidating local atomic structure. Visualized in Figure 6.7 is the simulated PDF analysis of  $\text{Cu}_3\text{P}$ ,  $\text{Cu}_3\text{PSe}_4$ , and potential intermediate  $\text{Cu}_{1-x}\text{Se}$ . While the bonds in  $\text{Cu}_3\text{PSe}_4$  could be convoluted by the bonds of the starting material and the intermediate, we are interested

in the bonds formed through the progress of a reaction. Thus, we focus our attention to the bonds of the starting material and intermediate which exhibit much more distinct peaks. Further this simulated range is only from 2.3–2.5 Å which is an incredibly narrow window. We expect to take measurements out to at least 10 Å.

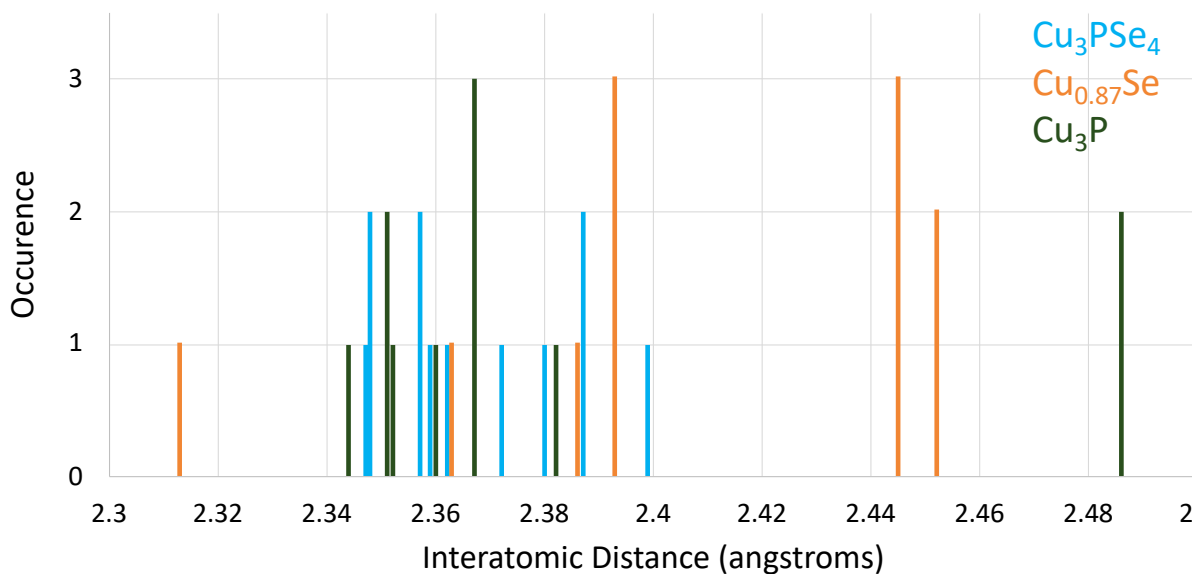


**Figure 6.7.** Simulated and predicted PDF analysis of Cu<sub>3</sub>PSe<sub>4</sub>, Cu<sub>0.87</sub>Se, and Cu<sub>3</sub>P nearest atomic neighbor permutations between the distances of 2.3–2.5 angstroms.

We are currently able to perform in situ diffraction and PDF in-house due to a PANalytical Empyrean, which is outfitted with a silver focusing mirror and Ag X-ray source. However, because the signal-to-noise ratio presented challenges, we can apply for beamtime at Argonne which offers both in-person and mail-in services. Both <sup>31</sup>P and <sup>77</sup>Se ssNMRs can be performed through our collaboration with the Hu group at FSU.

Nanoparticle syntheses are inherently complex, and deconvolution of this complexity requires elucidation of intermediates and amorphous species to control the rational synthesis of phase-pure materials. In situ techniques provide a methodology in which overlooked species that could reveal a lot about a material's reaction pathway are identified because a wide range of

reaction parameters such as time, temperature, and speciation can be rapidly probed. In this way, reaction conditions can be rationally designed as opposed to completed by one-by-one reactions or by continued trial-and-error. A combination of in situ methods and theory can also be used for materials discovery by capturing unusual structures that were calculated to have interesting physical properties but were unable to be previously synthesized because conditions beyond equilibrium were required to stabilize the structures. Ultimately, in situ experiments provide a multidisciplinary toolkit in which a diversity of species ranging from the molecular, supramolecular, macromolecular, and nanocrystalline could be characterized simultaneously as a function of temperature to effectively inform and subsequently guide reaction landscapes. Advancements in this technique can also contribute to materials discovery in which total phase awareness could reveal exciting materials with interesting properties that would otherwise not be seen in traditional NP syntheses.

## REFERENCES

- (1) Chamorro, J. R.; McQueen, T. M. Progress toward Solid State Synthesis by Design. *Acc. Chem. Res.* **2018**, *51* (11), 2918–2925.
- (2) Soderholm, L.; Mitchell, J. F. Perspective: Toward “Synthesis by Design”: Exploring Atomic Correlations during Inorganic Materials Synthesis. *APL Mater.* **2016**, *4* (5), 053212.
- (3) Alberi, K.; Nardelli, M. B.; Zakutayev, A.; Mitas, L.; Curtarolo, S.; Jain, A.; Fornari, M.; Marzari, N.; Takeuchi, I.; Green, M. L.; et al. The 2019 Materials by Design Roadmap. *J. Phys. D. Appl. Phys.* **2019**, *52* (1), 013001.
- (4) Kovalenko, M. V.; Manna, L.; Cabot, A.; Hens, Z.; Talapin, D. V.; Kagan, C. R.; Klimov, V. I.; Rogach, A. L.; Reiss, P.; Milliron, D. J.; et al. Prospects of Nanoscience with Nanocrystals. *ACS Nano* **2015**, *9* (2), 1012–1057.
- (5) Murphy, C. J.; Buriak, J. M. Best Practices for the Reporting of Colloidal Inorganic Nanomaterials. *Chem. Mater.* **2015**, *27* (14), 4911–4913.
- (6) Lee, J. M.; Miller, R. C.; Moloney, L. J.; Prieto, A. L. The Development of Strategies for Nanoparticle Synthesis: Considerations for Deepening Understanding of Inherently Complex Systems. *J. Solid State Chem.* **2019**, *273*, 243–286.
- (7) Liu, H.; Owen, J. S.; Alivisatos, A. P. Mechanistic Study of Precursor Evolution in Colloidal Group II-VI Semiconductor Nanocrystal Synthesis. *J. Am. Chem. Soc.* **2007**, *129* (2), 305–312.
- (8) Steckel, J. S.; Yen, B. K. H.; Oertel, D. C.; Bawendi, M. G. On the Mechanism of Lead Chalcogenide Nanocrystal Formation. *J. Am. Chem. Soc.* **2006**, *128* (40), 13032–13033.
- (9) García-Rodríguez, R.; Hendricks, M. P.; Cossairt, B. M.; Liu, H.; Owen, J. S. Conversion Reactions of Cadmium Chalcogenide Nanocrystal Precursors. *Chem. Mater.* **2013**, *25* (8), 1233–1249.
- (10) Reiss, P.; Carrière, M.; Lincheneau, C.; Vaure, L.; Tamang, S. Synthesis of Semiconductor Nanocrystals, Focusing on Nontoxic and Earth-Abundant Materials. *Chem. Rev.* **2016**, *116* (18), 10731–10819.
- (11) Sowers, K. L.; Swartz, B.; Krauss, T. D. Chemical Mechanisms of Semiconductor Nanocrystal Synthesis. *Chem. Mater.* **2013**, *25* (8), 1351–1362.
- (12) Boles, M. A.; Ling, D.; Hyeon, T.; Talapin, D. V. The Surface Science of Nanocrystals. *Nat. Mater.* **2016**, *15* (2), 141–153.
- (13) Hassinen, A.; Moreels, I.; de Mello Donegá, C.; Martins, J. C.; Hens, Z. Nuclear Magnetic Resonance Spectroscopy Demonstrating Dynamic Stabilization of CdSe Quantum Dots by Alkylamines. *J. Phys. Chem. Lett.* **2010**, *1* (17), 2577–2581.
- (14) Hens, Z.; Martins, J. C. A Solution NMR Toolbox for Characterizing the Surface Chemistry of Colloidal Nanocrystals. *Chem. Mater.* **2013**, *25* (8), 1211–1221.
- (15) Deng, Z.; Cao, L.; Tang, F.; Zou, B. A New Route to Zinc-Blende CdSe Nanocrystals: Mechanism and Synthesis. *J. Phys. Chem. B* **2005**, *109* (35), 16671–16675.
- (16) Socrates, G. *Infrared and Raman Characteristic Group Frequencies: Tables and Charts*; John Wiley & Sons, 2004.
- (17) Chen, P. E.; Anderson, N. C.; Norman, Z. M.; Owen, J. S. Tight Binding of Carboxylate, Phosphonate, and Carbamate Anions to Stoichiometric CdSe Nanocrystals. *J. Am. Chem.*

- Soc.* **2017**, *139* (8), 3227–3236.
- (18) Srivastava, V.; Dunietz, E.; Kamysbayev, V.; Anderson, J. S.; Talapin, D. V. Monodisperse InAs Quantum Dots from Aminoarsine Precursors: Understanding the Role of Reducing Agent. *Chem. Mater.* **2018**, *30* (11), 3623–3627.
  - (19) Gary, D. C.; Terban, M. W.; Billinge, S. J. L.; Cossairt, B. M. Two-Step Nucleation and Growth of InP Quantum Dots via Magic-Sized Cluster Intermediates. *Chem. Mater.* **2015**, *27* (4), 1432–1441.
  - (20) Kar, M.; Agrawal, R.; Hillhouse, H. W. Formation Pathway of CuInSe<sub>2</sub> Nanocrystals for Solar Cells. *J. Am. Chem. Soc.* **2011**, *133* (43), 17239–17247.
  - (21) Bullen, C.; van Embden, J.; Jasieniak, J.; Cosgriff, J. E.; Mulder, R. J.; Rizzardo, E.; Gu, M.; Raston, C. L. High Activity Phosphine-Free Selenium Precursor Solution for Semiconductor Nanocrystal Growth. *Chem. Mater.* **2010**, *22* (14), 4135–4143.
  - (22) Holder, C. F.; Schaak, R. E. Tutorial on Powder X-Ray Diffraction for Characterizing Nanoscale Materials. *ACS Nano* **2019**, *13* (7), 7359–7365.
  - (23) Scherrer, P. Estimation of the Size and Internal Structure of Colloidal Particles by Means of Röntgen Rays. *Nachr. Ges. Wiss. Göttingen* **1918**, 96–100.
  - (24) Ahmadi, M.; Pramana, S. S.; Xi, L.; Boothroyd, C.; Lam, Y. M.; Mhaisalkar, S. Evolution Pathway of CIGSe Nanocrystals for Solar Cell Applications. *J. Phys. Chem. C* **2012**, *116* (14), 8202–8209.
  - (25) Walsh, A.; Chen, S.; Wei, S. H.; Gong, X. G. Kesterite Thin-Film Solar Cells: Advances in Materials Modelling of Cu<sub>2</sub>ZnSnS<sub>4</sub>. *Adv. Energy Mater.* **2012**, *2* (4), 400–409.
  - (26) De Trizio, L.; Figuerola, A.; Manna, L.; Genovese, A.; George, C.; Brescia, R.; Saghi, Z.; Simonutti, R.; Van Huis, M.; Falqui, A. Size-Tunable, Hexagonal Plate-like Cu<sub>3</sub>P and Janus-like Cu-Cu<sub>3</sub>P Nanocrystals. *ACS Nano* **2012**, *6* (1), 32–41.
  - (27) Yu, B.-B.; Zhang, X.; Jiang, Y.; Liu, J.; Gu, L.; Hu, J. S.; Wan, L. J. Solvent-Induced Oriented Attachment Growth of Air-Stable Phase-Pure Pyrite FeS<sub>2</sub> Nanocrystals. *J. Am. Chem. Soc.* **2015**, *137* (6), 2211–2214.
  - (28) Steinhagen, C.; Harvey, T. B.; Stolle, C. J.; Harris, J.; Korgel, B. A. Pyrite Nanocrystal Solar Cells: Promising, or Fool’s Gold? *J. Phys. Chem. Lett.* **2012**, *3* (17), 2352–2356.
  - (29) Tanino, H.; Maeda, T.; Fujikake, H.; Nakanishi, H.; Endo, S.; Irie, T. Raman Spectra of CuInSe<sub>2</sub>. *Phys. Rev. B* **1992**, *45* (23), 13323–13330.
  - (30) Fernandes, P. A.; Salomé, P. M. P.; Da Cunha, A. F. Study of Polycrystalline Cu<sub>2</sub>ZnSnS<sub>4</sub> Films by Raman Scattering. *J. Alloys Compd.* **2011**, *509* (28), 7600–7606.
  - (31) Riha, S. C.; Parkinson, B. A.; Prieto, A. L. Solution-Based Synthesis and Characterization of Cu<sub>2</sub>ZnSnS<sub>4</sub> Nanocrystals. *J. Am. Chem. Soc.* **2009**, *131* (34), 12054–12055.
  - (32) Shin, S. W.; Han, J. H.; Park, C. Y.; Moholkar, A. V.; Lee, J. Y.; Kim, J. H. Quaternary Cu<sub>2</sub>ZnSnS<sub>4</sub> Nanocrystals: Facile and Low Cost Synthesis by Microwave-Assisted Solution Method. *J. Alloys Compd.* **2012**, *516*, 96–101.
  - (33) Chesman, A. S. R.; van Embden, J.; Duffy, N. W.; Webster, N. A. S.; Jasieniak, J. J. In Situ Formation of Reactive Sulfide Precursors in the One-Pot, Multigram Synthesis of Cu<sub>2</sub>ZnSnS<sub>4</sub> Nanocrystals. *Cryst. Growth Des.* **2013**, *13* (4), 1712–1720.
  - (34) White, M. A.; Baumler, K. J.; Chen, Y.; Venkatesh, A.; Medina-Gonzalez, A. M.; Rossini, A. J.; Zaikina, J. V.; Chan, E. M.; Vela, J. Expanding the I–II–V Phase Space: Soft Synthesis of Polytypic Ternary and Binary Zinc Antimonides. *Chem. Mater.* **2018**, *30* (17), 6173–6182.
  - (35) Riha, S. C.; Johnson, D. C.; Prieto, A. L. Cu<sub>2</sub>Se Nanoparticles with Tunable Electronic

- Properties Due to a Controlled Solid-State Phase Transition Driven by Copper Oxidation and Cationic Conduction. *J. Am. Chem. Soc.* **2011**, *133* (5), 1383–1390.
- (36) Korala, L.; McGoffin, J. T.; Prieto, A. L. Enhanced Conductivity in CZTS/Cu<sub>2-x</sub>Se Nanocrystal Thin Films: Growth of a Conductive Shell. *ACS Appl. Mater. Interfaces* **2016**, *8* (7), 4911–4917.
- (37) Fredrick, S. J.; Prieto, A. L. Solution Synthesis and Reactivity of Colloidal Fe<sub>2</sub>GeS<sub>4</sub>: A Potential Candidate for Earth Abundant, Nanostructured Photovoltaics. *J. Am. Chem. Soc.* **2013**, *135* (49), 18256–18259.
- (38) Abécassis, B.; Bouet, C.; Garnero, C.; Constantin, D.; Lequeux, N.; Ithurria, S.; Dubertret, B.; Pauw, B. R.; Pontoni, D. Real-Time in Situ Probing of High-Temperature Quantum Dots Solution Synthesis. *Nano Lett.* **2015**, *15* (4), 2620–2626.
- (39) Andersen, H. L.; Bøjesen, E. D.; Birgisson, S.; Christensen, M.; Iversen, B. B. Pitfalls and Reproducibility of in Situ Synchrotron Powder X-Ray Diffraction Studies of Solvothermal Nanoparticle Formation. *J. Appl. Crystallogr.* **2018**, *51* (2), 526–540.
- (40) Shoemaker, D. P.; Hu, Y.-J.; Chung, D. Y.; Halder, G. J.; Chupas, P. J.; Soderholm, L.; Mitchell, J. F.; Kanatzidis, M. G. In Situ Studies of a Platform for Metastable Inorganic Crystal Growth and Materials Discovery. *Proc. Natl. Acad. Sci.* **2014**, *111* (30), 10922–10927.
- (41) Jiang, Z.; Ramanathan, A.; Shoemaker, D. P. In Situ Identification of Kinetic Factors That Expedite Inorganic Crystal Formation and Discovery. *J. Mater. Chem. C* **2017**, *5* (23), 5709–5717.
- (42) Jiang, Z.; Tian, S.; Lai, S.; McAuliffe, R. D.; Rogers, S. P.; Shim, M.; Shoemaker, D. P. Capturing Phase Evolution during Solvothermal Synthesis of Metastable Cu<sub>4</sub>O<sub>3</sub>. *Chem. Mater.* **2016**, *28* (9), 3080–3089.
- (43) Haynes, A. S.; Stoumpos, C. C.; Chen, H.; Chica, D.; Kanatzidis, M. G. Panoramic Synthesis as an Effective Materials Discovery Tool: The System Cs/Sn/P/Se as a Test Case. *J. Am. Chem. Soc.* **2017**, *139* (31), 10814–10821.
- (44) Li, J.; Wang, H.; Lin, L.; Fang, Q.; Peng, X. Quantitative Identification of Basic Growth Channels for Formation of Monodisperse Nanocrystals. *J. Am. Chem. Soc.* **2018**, *140* (16), 5474–5484.
- (45) Mansouri Tehrani, A.; Oliynyk, A. O.; Parry, M.; Rizvi, Z.; Couper, S.; Lin, F.; Miyagi, L.; Sparks, T. D.; Brgoch, J. Machine Learning Directed Search for Ultraincompressible, Superhard Materials. *J. Am. Chem. Soc.* **2018**, *140* (31), 9844–9853.
- (46) Kononova, O.; Huo, H.; He, T.; Rong, Z.; Botari, T.; Sun, W.; Tshitoyan, V.; Ceder, G. Text-Mined Dataset of Inorganic Materials Synthesis Recipes. *Sci. data* **2019**, *6* (1), 203.
- (47) Aykol, M.; Dwaraknath, S. S.; Sun, W.; Persson, K. A. Thermodynamic Limit for Synthesis of Metastable Inorganic Materials. *Sci. Adv.* **2018**, *4* (4), eaaq0148.
- (48) Sun, W.; Holder, A.; Orvañanos, B.; Arca, E.; Zakutayev, A.; Lany, S.; Ceder, G. Thermodynamic Routes to Novel Metastable Nitrogen-Rich Nitrides. *Chem. Mater.* **2017**, *29* (16), 6936–6946.
- (49) Bhutani, A.; Schiller, J. A.; Zuo, J. L.; Eckstein, J. N.; Greene, L. H.; Chaudhuri, S.; Shoemaker, D. P. Combined Computational and in Situ Experimental Search for Phases in an Open Ternary System, Ba-Ru-S. *Chem. Mater.* **2017**, *29* (14), 5841–5849.
- (50) Das, A.; Shamirian, A.; Snee, P. T. Arsenic Silylamide: An Effective Precursor for Arsenide Semiconductor Nanocrystal Synthesis. *Chem. Mater.* **2016**, *28* (11), 4058–4064.
- (51) Kroupa, D. M.; Anderson, N. C.; Castaneda, C. V.; Nozik, A. J.; Beard, M. C. In Situ

- Spectroscopic Characterization of a Solution-Phase X-Type Ligand Exchange at Colloidal Lead Sulphide Quantum Dot Surfaces. *Chem. Commun.* **2016**, 52 (96), 13893–13896.
- (52) Lee, J. M.; Kraynak, L. A.; Prieto, A. L. A Directed Route to Colloidal Nanoparticle Synthesis of the Copper Selenophosphate  $\text{Cu}_3\text{PSe}_4$ . *Angew. Chemie Int. Ed.* **2020**, 59 (8), 3038–3042.
- (53) Chien, P. H.; Griffith, K. J.; Liu, H.; Gan, Z.; Hu, Y. Y. Recent Advances in Solid-State Nuclear Magnetic Resonance Techniques for Materials Research. In *Annual Review of Materials Research*; Annual Reviews Inc., 2020; Vol. 50, pp 493–520.
- (54) Wang, L. S.; Patel, S. V.; Sanghvi, S. S.; Hu, Y.-Y.; Haile, S. M. Structure and Properties of  $\text{Cs}_7(\text{H}_4\text{PO}_4)(\text{H}_2\text{PO}_4)_8$ : A New Superprotonic Solid Acid Featuring the Unusual Polycation  $(\text{H}_4\text{PO}_4)^+$ . *J. Am. Chem. Soc.* **2020**, jacs.0c08870.
- (55) Liu, J.; Meyns, M.; Zhang, T.; Arbiol, J.; Cabot, A.; Shavel, A. Triphenyl Phosphite as the Phosphorus Source for the Scalable and Cost-Effective Production of Transition Metal Phosphides. *Chem. Mater.* **2018**, 30 (5), 1799–1807.
- (56) Jiang, Z.; Ramanathan, A.; Shoemaker, D. P. In Situ Identification of Kinetic Factors That Expedite Inorganic Crystal Formation and Discovery. *J. Mater. Chem. C* **2017**, 5 (23), 5709–5717.
- (57) Straas, T.; Becker, J.; Iversen, B. B.; Als-Nielsen, J. The Debye-Scherrer Camera at Synchrotron Sources: A Revisit. *J. Synchrotron Radiat.* **2013**, 20 (1), 98–104.
- (58) Cromer, D. T.; Liberman, D. A. Anomalous Dispersion Calculations near to and on the Long-wavelength Side of an Absorption Edge. *Acta Crystallogr. Sect. A* **1981**, 37 (2), 267–268.
- (59) Patterson, A. L. The Scherrer Formula for X-Ray Particle Size Determination. *Phys. Rev.* **1939**, 56 (10), 978–982.
- (60) Francisco, R. H. P.; Eckert, H. Compound Formation and Local Structure in Ternary Metal-Phosphorus-Selenium Systems. *J. Solid State Chem.* **1994**, 112 (2), 270–276.
- (61) Baldus, H.-P.; Blachnik, R.; Loennecke, P.; Tattershall, B. W. Phosphorus-31 and Selenium-77 Nuclear Magnetic Resonance Spectra of Phosphorus-Poor Phosphorous Selenide Compounds. *J. Chem. Soc. Dalton Trans.* **1991**, No. 10, 2643.
- (62) Frenette, L. C.; Krauss, T. D. Uncovering Active Precursors in Colloidal Quantum Dot Synthesis. *Nat. Commun.* **2017**, 8 (1), 2082.
- (63) Anderson, N. C.; Hendricks, M. P.; Choi, J. J.; Owen, J. S. Ligand Exchange and the Stoichiometry of Metal Chalcogenide Nanocrystals: Spectroscopic Observation of Facile Metal-Carboxylate Displacement and Binding. *J. Am. Chem. Soc.* **2013**, 135 (49), 18536–18548.
- (64) *Scanning Transmission Electron Microscopy*; Pennycook, S. J., Nellist, P. D., Eds.; Springer New York: New York, NY, 2011.
- (65) Lugg, N. R.; Kothleitner, G.; Shibata, N.; Ikuhara, Y. On the Quantitativeness of EDS STEM. *Ultramicroscopy* **2015**, 151, 150–159.

## CHAPTER 7

### OUTLOOK ON THE SYNTHETIC AND CHARACTERIZATION TOOLKITS FOR SOLUTION-BASED NANOPARTICLES (NPs) OF COMPOSITIONAL COMPLEXITY: USING COPPER SELENOPHOSPHATE, $\text{Cu}_3\text{PSe}_4$ , AS A CASE STUDY

#### 7.1. Introduction

The successful synthesis of  $\text{Cu}_3\text{PSe}_4$  revealed a complex reaction landscape despite the implementation of only three precursors:  $\text{Cu}_3\text{P}$ , Se, and 1-octadecene (ODE). The following are future directions based on  $\text{Cu}_3\text{PSe}_4$  as a case study for the synthetic control of multinary phase spaces via solution-based nanoparticle syntheses, the assessment of materials properties, and the implementation in devices. The strategies we are interested in developing and advancing include the following: bond formation templating (to potentially control assembly of polyhedra), mapping of synthetic landscape via rigorous/robust interdisciplinary characterization, connecting reaction processes or intermediate/amorphous phases to the crystal structure of the final material, role of solvent, computational methods to bridge experimental data and elucidation of reaction schemes, and crystal structure and materials properties relationships.

#### 7.2. Experimental

*Materials and Methods.* All reactions were performed under inert atmosphere unless otherwise noted. All product workup was done on the benchtop in ambient conditions unless otherwise noted. Copper (II) chloride ( $\text{CuCl}_2$ , Riedel-de Haën, 97%), silver nitrate ( $\text{AgNO}_3$ , Alfa-Aesar, 99.9%), trioctylphosphine oxide (TOPO, Aldrich, 99%), triphenyl phosphite (TPOP, Oakwood Chemical, 97%), hexadecylamine (HDA, Aldrich, 90%), 1,2-hexadecanediol (Aldrich, 90%), and selenium powder (Se, Strem Chemicals Inc., 99.99%) were purchased and used as received. Technical grade toluene, hexanes, ethanol, isopropanol, and chloroform were obtained from Fisher Scientific. The

solvents 1-octadecene (ODE, Aldrich, 90%), oleylamine (OLA, Aldrich, 70%), oleic acid (OA, Aldrich, 90%) and octyl ether (Aldrich, 99%) were sparged with N<sub>2</sub> for 2 h before use.

*Cu<sub>3</sub>P Nanoparticle Heat-up Synthesis.* Literature protocol developed by Liu et al.<sup>1</sup> was adapted for the formation of Cu<sub>3</sub>P by a scalable and cost-effective heat-up method. In a typical synthesis, 0.5 mmol CuCl<sub>2</sub>, 5.0 mmol HDA, 5.0 mmol TPOP (Cu:HDA:TPOP = 1:10:10), and 10 g ODE were added to a 50 mL three-neck round-bottomed flask equipped with glass stir bar, reflux condenser, and thermocouple. The reaction flask was degassed under N<sub>2</sub> at 150°C for 1 h. The solution was then heated to 300°C where it was held for 0.5 h. The reaction was cooled to 200°C before removal of the heating mantle, then further cooled to ~80°C. The particles were collected by dispersion of the reaction mixture in chloroform then flocculation with isopropanol. After 15 min of centrifugation at 5800 rpm, the supernatant was discarded. The washing procedure was repeated with a sonication step to aid dispersion in chloroform before addition of isopropanol. The mixture was centrifuged at 5800 rpm for 8 min, and then the supernatant was discarded. Nanoparticles were stored in hexanes.

*Synthesis of Cu<sub>3</sub>PSe<sub>4</sub> by Irradiation.* Nanoparticles of Cu<sub>3</sub>P were initially dried over N<sub>2</sub> then finished drying under vacuum in a 20 mL scintillation vial. To generate dialkyl selenide, a solution of 0.1 M Se/ODE was heated to 180 °C and held for 5 h under N<sub>2</sub>. The dialkyl selenide solution was allowed to cool to room temperature, then charged to the scintillation vial with Cu<sub>3</sub>P NPs and a Teflon stir bar. The mixture was placed under a shoebox where only a blue LED lamp (350 – 500 nm, λ<sub>max</sub> = 450 nm) could be illuminated onto the sample.

*Synthesis of AgP<sub>2</sub> NPs and subsequent transformation.* The synthesis of AgP<sub>2</sub> NPs was adapted from Henkes et al. in which AgP<sub>2</sub> and impurities were formed by phosphorization of Ag NPs.<sup>2</sup> Nanoparticles of Ag were synthesized by heating a solution of 70.2 g AgNO<sub>3</sub>, 70.9 mg 1,2-

hexadecanediol, 100  $\mu$ L OLA, 100  $\mu$ L OA, and 2.00 mL octyl ether to 100  $^{\circ}$ C for 1 h. The mixture was slowly cooled and saturated with ethanol to crash an orange-brown precipitate which was washed with hexanes. All hexanes washes were reserved, and an equal amount of ethanol was added. The mixture was centrifuged, and the solution was decanted to isolate Ag NPs. The Ag NPs were further washed with ethanol and dried under  $N_2$ . To a scintillation vial, 9.5 mg of Ag NPs and 1.0 mL TOP were added and mixed by sonication. Simultaneously, a reaction flask of 2.0 mL TOP was heated to 370  $^{\circ}$ C, upon which, the Ag/TOP mixture was rapidly injected. The reaction was heated at 370  $^{\circ}$ C for 2 h and then slowly cooled and saturated with ethanol. The  $AgP_2$  and impurities mixture was isolated by centrifugation, washed with ethanol, and dried under  $N_2$  then by vacuum. The  $AgP_2$  and impurities precursor was then charged into a 100 mL 3-neck RBF equipped with a glass stir glass stir bar, Liebig condenser, and thermocouple. Excess Se (1.07 mmol) and ODE (10.7 mL, 0.1 M dispersion Se/ODE) were added to the flask. The flask was pumped and purged between vacuum and  $N_2$  for three cycles, then heated to 150  $^{\circ}$ C at a rate of 500  $^{\circ}$ C/h under vacuum. The flask was switched to positive  $N_2$  pressure and heated to 300  $^{\circ}$ C where it was held for 20 min. The flask was then cooled to  $\sim 80^{\circ}$ C by removal of the heating mantle. The particles were collected by dispersion of the reaction mixture in toluene then flocculation with ethanol. After 15 min of centrifugation at 5800 rpm, the supernatant was discarded. The washing procedure was repeated with a sonication step to aid dispersion in toluene before addition of ethanol. The mixture was centrifuged at 5800 rpm for 8 min, and then the supernatant was discarded. Nanoparticles were stored in hexanes.

### **7.3. Expansion of a Synthetic Toolkit**

Colloidal NP synthesis is an incredibly interdisciplinary field, requiring understanding of all possible interactions between organic, inorganic, organometallic, and solid-state species to

probe and elucidate complex reaction mechanisms and landscapes with the goal to guide synthetic strategies for complex materials.<sup>3-9</sup> To expand the accessible phase space of semiconductor materials, a toolkit to bridge a diverse set of techniques and strategies is critical/crucial. Our contribution involved the development or utilization of the following strategies for the synthesis of compositionally complex  $\text{Cu}_3\text{PSe}_4$  NPs:

- Bond installation of difficult-to-incorporate main group element to yield binary starting materials and to direct reaction pathways.
- Expansion of HSAB principles.
  - Rather than treat Lewis acidity and basicity as global parameters of reactivity, directionality of orbitals due to nonuniform electron distribution must also be considered. This gives rise to bond formation templating.
- Judicious solvent selection by examining its role in NP reactions via speciation characterization. Beyond heat transfer mediums, solvents can also be starting reagents.
- Iterative reaction parameter tuning and subsequent careful characterization to prevent impurity formation.
- Investigation of failed reactions or extreme synthetic conditions to understand precursor roles and reactivity trends.
- Use of bond dissociation enthalpy (BDE) to predict reactivity of the Se precursor.
- Bridging mature characterization methods to build a rigorous and robust multidisciplinary characterization toolkit to study various phases (i.e. solid, liquid, gas) and map synthetic landscapes of nanoparticle syntheses.
  - Imaging nanoparticle formation by TEM
  - Elemental analysis by XPS and STEM/EDS

- In situ (XRD) and ex situ (XRD,  $^1\text{H}$  NMR, and IR) characterization to observe speciation changes and reaction landscape
- Molecular level processes and speciation characterization to inform on materials synthesis (supramolecular assembly).
  - Connecting reaction processes or intermediate/amorphous phases to the crystal structure of the final material.
- Reaction pathway manipulations to elucidate thermodynamic vs. kinetic control.
- Computational methods to bridge experimental data and elucidation of reaction schemes in complex systems where diverse/deconvoluted interactions are characterized.
  - Consideration of chalcogen bonding in Se monomer reactivity towards nucleophiles.

The culmination and combination of these strategies reveal a preliminary toolkit for the synthetic control of a multinary NP phase space and could be extrapolated to the rational synthetic design of diverse and complex materials. To further develop this specific toolkit, we can take inspiration from synthetic molecular chemists who build a criterion for a specific bond formation by testing permutations of reaction conditions (i.e. time, temperature, solvent) and precursors of diverse functionality (i.e. sterics, aromaticity, electron donating/accepting, etc).<sup>10</sup>

We must first build a catalog of materials that are related to  $\text{Cu}_3\text{PSe}_4$  in a diversity of ways such as composition, bonding scheme, crystal structure, and constituent element valences. This could include materials such  $\text{Cu}_7\text{PSe}_6$ ,<sup>11–15</sup>  $\text{Ag}_7\text{PSe}_6$ ,<sup>16,17</sup>  $\text{Cu}_3\text{PS}_4$ ,<sup>13,18</sup>  $\text{Cu}_2\text{SiSe}_3$ ,<sup>19,20</sup> and ternary nitrides.<sup>21–24</sup> We can then use the strategy of bond installation to rationalize a binary precursor in which the main group element is bonded to either the transition metal or the chalcogen constituent elements. Bond installation as a generalizable technique is particularly appealing for the synthesis

of ternary nitrides in which the incorporation of nitrogen is quite difficult due the hardness of  $\text{N}^{3-}$  in the context of HSAB principles.<sup>3,23-25</sup> All in all, any difficult-to-incorporate main group element for multinary NP synthesis would be interesting to explore. Once the binary starting materials are established, precursors that are complementary to the Lewis acidity or basicity of the binary precursor can be judiciously selected. It is crucial to consider that the solvent will impact the precursor to monomer transformation, so the Lewis acidic/basic character of the *monomers* is what we are specifically interested in.

Limiting our initial screening to the synthesis of ternary transition metal-main group element-chalcogenides, which are anomalous to HSAB principles but analogous to the Cu/P/Se system in composition and constituent element valencies, results in a large number of interesting targets. One such material of immediate interest is the  $\text{Ag}_7\text{PSe}_6$  argyrodite compound, in which its solid-state synthesis is reported but a solution-based nanoparticle synthesis has not yet been developed.<sup>17</sup> While both  $\text{Ag}^+$  of  $\text{Ag}_7\text{PSe}_6$  and  $\text{Cu}^+$  of analogous  $\text{Cu}_7\text{PSe}_6$  are similar in terms of softness, the structure of  $\text{Ag}_7\text{PSe}_6$  differs slightly from  $\text{Cu}_7\text{PSe}_6$  due to the ability of  $\text{Ag}^+$  to adopt lower chalcogenide coordination environments as a result of relativistic effects.<sup>26,27</sup> This will inevitably result in different speciation thus different reaction landscapes between the two.

Here, we explored the synthesis of  $\text{Ag}_7\text{PSe}_6$ <sup>17,28</sup> via  $\text{AgP}_2$  NPs and Se/ODE starting materials. Unlike for the syntheses of Cu-P-Se which used  $\text{Cu}_3\text{P}$  as a precursor, no analogous  $\text{Ag}_3\text{P}$  exists,<sup>29</sup> so a different binary precursor in which phosphorus bonds are installed was implemented. We attempted the use of  $\text{AgP}_2$  NPs, but the synthesis by Henkes et al. resulted in a mixture of  $\text{AgP}_2$ ,  $\text{Ag}_3\text{P}_{11}$ , and  $\text{Ag}$ .<sup>2</sup> Regardless, the use of a stoichiometrically different metal phosphide precursor provided a unique opportunity to understand if the reaction pathways of  $\text{Cu}_3\text{PSe}_4$  (synthesized in Chapter 4) and  $\text{Cu}_7\text{PSe}_6$  (synthesized in Chapter 5) by  $\text{Cu}_3\text{P}$  and Se/ODE

precursors were dependent or independent of the precursor constituent element concentrations. While  $\text{Cu}_3\text{P}$  is the correct stoichiometry for  $\text{Cu}_3\text{PSe}_4$ , it is quite phosphorus-rich for the comparably phosphorus-deficient  $\text{Cu}_7\text{PSe}_6$  ternary. Here,  $\text{AgP}_2$  is not the correct stoichiometry but is quite phosphorus-rich compared to the targeted  $\text{Ag}_7\text{PSe}_6$ . Preliminary reactions were run analogously to the synthesis of  $\text{Cu}_3\text{PSe}_4$  NPs.<sup>30</sup> A single reaction flask was charged with  $\text{AgP}_2$  (Figure 7.1A), Se powder, and ODE, then ramped to 300 °C under  $\text{N}_2$  and held for 20 min. While  $\text{Ag}_7\text{PSe}_6$  was successfully synthesized (Figure 7.1B), there were also a slew of impurities which could be a result of the complex phase space for the Ag/P/Se ternary phase diagram<sup>28</sup> or the Ag-P precursor quality (Figure 7.1A).

Upon optimization, if high quality phase-pure  $\text{AgP}_2$  still results in a range of Ag-P-Se phase materials, the components or phases of the Se/ODE precursor with a specific Lewis acidity or basicity can be isolated before transfer into the reaction. We have previously shown that Lewis basic  $\text{H}_2\text{Se}$ , a gaseous species that can be generated as a byproduct of Se and ODE reaction, can access metastable  $\text{Cu}_7\text{PSe}_6$  on its own (Chapter 5). Thus, we can isolate gaseous Se species before transferring it to  $\text{AgP}_2$  NPs to potentially synthesize phase-pure  $\text{Ag}_7\text{PSe}_6$ . Alternatively, if phase-pure  $\text{AgP}_2$  results in the successful synthesis of phase-pure  $\text{Ag}_7\text{PSe}_6$  by the single pot method, the synthesis of other ternary semiconductor nanoparticles of I-V-VI valencies can be attempted to understand how widely these strategies can be extrapolated.

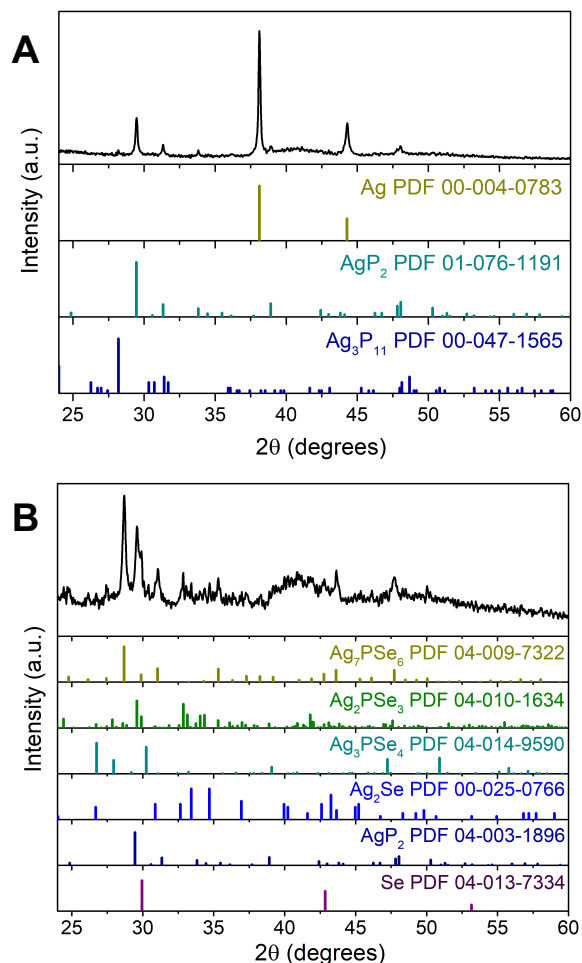


**Figure 7.1.** XRD patterns of the (A) the Ag-P starting material and (B) the Ag-P-Se final products. The synthesis of AgP<sub>2</sub> results in Ag and Ag<sub>3</sub>P<sub>11</sub> impurities and must be optimized before use as a high-quality starting material. The final products indicate that the strategies of P-bond installation and Se/ODE are promising.

Ultimately, it is curious that we can access Ag<sub>7</sub>PSe<sub>6</sub> irrespective of the constituent element concentration within the AgP<sub>2</sub> starting material. We are generally able to access a large phase space, demonstrating that coupling a metal phosphide binary precursor (i.e. installation of main group element bonds) of any constituent element stoichiometry with the Se/ODE precursor shows promise as a general strategy. Gaining the ability to tune this phase space will be particularly exciting because it will require refined strategies that could expand the materials that can be synthesized by this methodology. Independent of successful phase-pure syntheses, the results will

allow us to evaluate our synthetic methods and the differences in the materials that contribute to the differences in reaction landscapes, leading to synthetic control.

Due to the interdisciplinary nature of NP synthesis, the toolkits from molecular and materials synthesis must be bridged to expand the toolkit for NP synthesis.<sup>7,9,10,31</sup> Our work was primarily done by ex situ methods (i.e. temporal aliquots of the reaction flask characterized by XRD, <sup>1</sup>H NMR, IR, and GC-MS) complemented with characterization of different reaction flask components (i.e. gaseous headspace, reaction solution, and powder) to characterize speciation as a function of time and phase (Chapter 5). However, advancements in these characterization methods are required. While complementary methods help elucidate the reaction picture, these pictures remain as independent snapshots that may not be correlated to one another just because they are characterized at the same time. For example, a 10 min sample characterized by <sup>1</sup>H NMR may show transformations in the solution-phase. However, that does not necessarily mean that a crystalline product characterized by XRD for the 10 min sample is correlated to the transformation in solution. Further, temporal aliquots are often taken at elevated temperatures (>150 °C), thus sampling at these high temperatures can quench and crystallize products that don't necessarily exist during the course of a reaction.<sup>32,33</sup> By virtue of this method, it is also difficult to capture transient intermediates. Consequently, characterization of only the final products overlooks the complex processes that occur throughout the reaction which hold a lot of exciting opportunities for materials discovery.<sup>34-38</sup> We are, thus, interested in developing methods to increase our spatial resolution of our reaction flask to simultaneously capture both the molecular and bulk phases as they are being formed, converted, or consumed.<sup>39,40</sup> By providing a reaction landscape, the reaction landscape can then be controlled. In this way, predictive design leads to predictive synthesis.

One tool that was not extensively explored for our work but would be valuable for a NP synthesis toolkit includes in situ characterization methods. A method to prepare samples with solvent and that are robust to high temperatures can be found in Chapter 6. In situ X-ray techniques such as diffraction and PDF (pair distribution function) allow us to see long and local ranges, respectively.<sup>32,33,38,41,42</sup> More aptly, the respective methods show the crystalline materials that are consumed/converted (XRD) as well as amorphous species that are consumed/converted and the bonds that break/form (PDF) as a function of time or temperature. In situ PDF is particularly appealing because the characterization of amorphous species is often overlooked due to the limited number of characterization techniques to effectively identify inorganic, amorphous species. However, the characterization of intermediate, amorphous species is incredibly important to understand nucleation and growth processes, to connect intermediate phases to the crystal structure of the final material, and to provide a robust map of a reaction pathway. In situ solid state NMR (ssNMR) can also be used to probe the molecular- and supramolecular-level processes that occur for a specific nucleus.<sup>43-45</sup>

Preliminary work in collaboration with the Hu group for <sup>31</sup>P NMR on the powders of the starting material (Cu<sub>3</sub>P) and final product (Cu<sub>3</sub>PSe<sub>4</sub>) showed that they resonate at very different <sup>31</sup>P NMR shifts, 180 ppm and -83 ppm respectively (see Chapter 6). The very large difference in the chemical shifts provides an opportunity in which the data of the full reaction (Cu<sub>3</sub>P + Se/ODE at 300 °C for 20 min) can be easily interpreted. However, sensitivity of the probe could present issues. The powder samples were run at 20 kHz spin rate using the 2.5 mm probe at room temperature. This is incredibly more sensitive than the laser probe that would be used for solution-based samples. The laser probe requires samples to be static (no spinning) and are generally plagued by convolutions or loss of signal when coupled with heating and cooling stages.

In both the diffraction and NMR instruments, the solvent dilutes signal from the samples and must be optimized which may not be representative of the reaction concentrations. Further, different reagents can absorb the energy of the source, dramatically reducing the intensity of the signal. In some cases, the absorption of energy can prevent the collection of any signal. For example, Se powder absorbs x-rays strongly, but the power of the energy source can be increased to overcome this limitation (i.e. switching from Cu to Ag X-ray tube or using a synchrotron source). Alternatively, metallic Se and semiconducting  $\text{Cu}_3\text{P}$  can conduct electrons and thus, generate a local magnetic current when spinning, preventing collection of signal. However, the power or the number of scans collected can be increased.

Despite these limitations, even greater are the opportunities. The ability to map reaction landscapes can consequently give us the ability to control and direct reaction pathways, in particular providing a handle to target more difficult to synthesize phases such as metastable phases (Figure 7.2). For the Cu-P-Se system, this phase is  $\text{Cu}_7\text{PSe}_6$ , a phosphorus-deficient phase as compared to  $\text{Cu}_3\text{PSe}_4$ . Kinetic trapping or the ability to predict synthetic conditions for trapping metastable phases is of particular interest in order to expand the phase space of materials that are theorized to have interesting physical properties but often allude synthetic materials chemists.<sup>10,46–53</sup> While theory can predict new materials, it does not yet provide a guiding protocol on how these materials can be made. Gaining the ability to increase spatial resolution of NP reactions allows us to probe under what conditions we can retain metastability and how to start and stop energy landscapes because we can sweep and manipulate through a large continuous range of parameters including time, temperature, and precursor identity. If we can successfully synthesize a metastable phase, we can extrapolate these characterization strategies to the synthesis of analogous materials. Having the ability to “see” reactions as they happen can also further molecular level understanding

on how it connects to materials synthesis. We can, thus, start to target more precise atomic control by the bond assembly or supramolecular assembly. For example, magic-size clusters (MSCs) (see Chapters 1 and 3) were first identified as supramolecular intermediates toward NP synthesis.<sup>8,54</sup> Rather than start syntheses from molecular precursors, the Cossairt group used MSCs as single-source precursors to control the assembly of monodisperse InP NPs. In this way, our goal is to not only control the synthesis of phase-pure materials through reaction landscape elucidation but to narrow syntheses down to a single pot for controlled nucleation and growth of uniformly shaped and sized NPs.

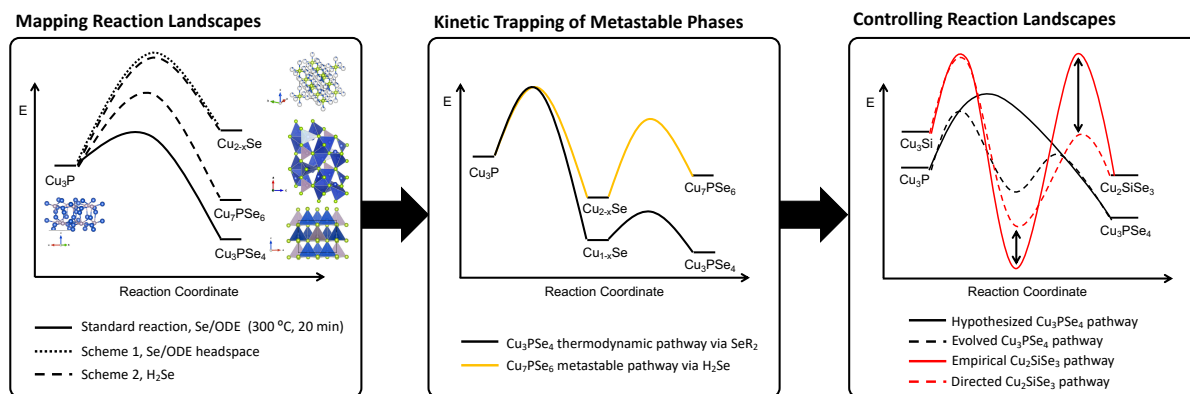


**Figure 7.2.** Reaction pathway schemes in which we describe how robust multidisciplinary characterization of NP reactions can effectively map reaction landscapes with increasing levels of detail. This requires characterization of molecular-level speciation as well as bulk speciation to inform on a material's synthesis.

To further expand the phase space landscape, it is crucial to think about NP synthesis in new ways such as the manifestation of new reaction knobs or synergy between experiment and theory. New knobs of synthesis could be explored in order to add more parameters for control and tunability. For our reaction, the UV-Vis spectrum for the chalcogen-bond interaction between PCu<sub>3</sub> and SeMe<sub>2</sub> was simulated (Figure 7.3). Surprisingly, a fairly intense visible-light absorbance centered around 450 nm (blue light) was observed for the following transition: orbitals associated

with the transition places an electron in the sigma\*-orbital of the dialkyl selenide which would replace the Se-CH<sub>3</sub> bond with an Se-P bond.

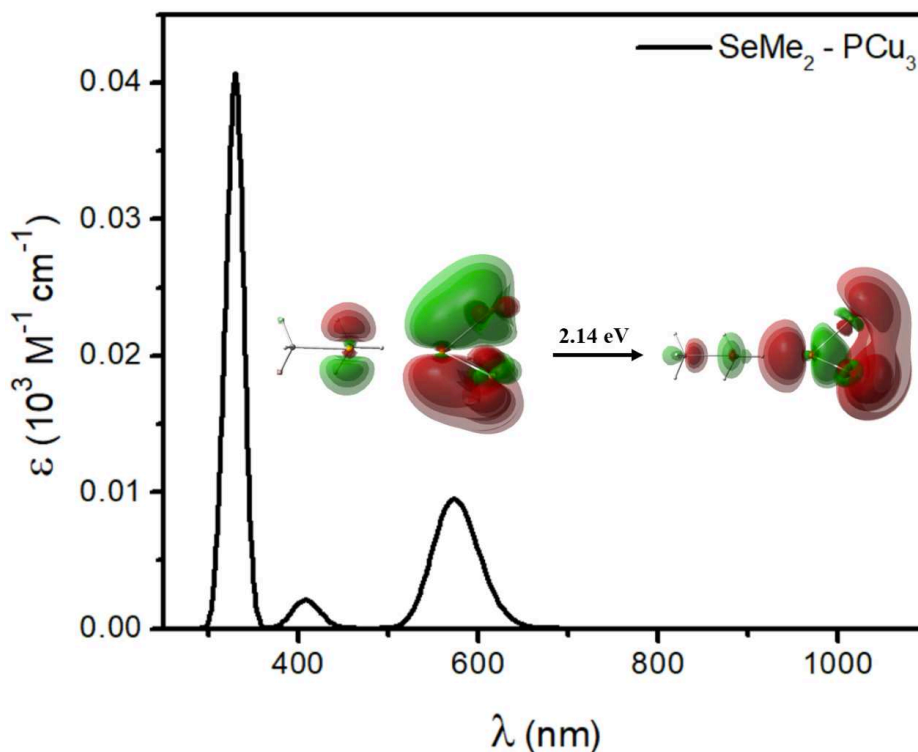


**Figure 7.3.** Simulated UV-Vis spectrum of the chalcogen bond interaction between PCu<sub>3</sub> and SeMe<sub>2</sub> which shows an absorbance centered around 450 nm. The transition energy for this process in which orbitals associated with the transition places an electron in the sigma\*-orbital of the dialkyl selenide corresponds to about 2.14 eV.

Thus, we proposed that Cu<sub>3</sub>PSe<sub>4</sub> could be synthesized by photoinitiation in which a mixture of dialkyl selenide and Cu<sub>3</sub>P under blue LED lamp (350 – 500 nm, λ<sub>max</sub> = 450 nm) illumination could yield Cu<sub>3</sub>PSe<sub>4</sub>. To generate dialkyl selenide, we used a solution of 0.1 M Se/ODE (180 °C for 5 h, N<sub>2</sub>).<sup>55</sup> It is important to note that the Se monomers for the Se/ODE precursor does not solely contain dialkyl selenides but a slew of diverse selenide species including seloxides, dialkyl diselenides, and hydrogen selenides.<sup>56</sup> (See Chapters 2 and 5)

After 1 h of LED irradiation, the reaction mixture turned yellow to dark olive green and brown, the same color change observed for the successful synthesis of Cu<sub>3</sub>PSe<sub>4</sub> NPs. In the UV-

Vis, there is a shoulder peak associated with ODE that disappeared after 1 h irradiation, suggesting transformation in the solution phase. Via XRD, there were  $\text{Cu}_3\text{P}$  and  $\text{Cu}_2\text{Se}$  crystalline products, showing that the  $\text{Cu}_3\text{P}$  starting material was starting its transformation. However, upon longer irradiation (1 week), the XRD showed a slew of Cu-Se binaries including  $\text{CuSe}$ ,  $\text{Cu}_3\text{Se}_2$ , and  $\text{Cu}_{1.82}\text{Se}$ . The varying stoichiometries suggest that Cu is in several different configurations, showing a diversity of reaction pathways. The varied reaction pathways could be a result of the varied Se monomers. Atomic Se reacts with terminal olefins/primary alkenes in a diversity of mechanisms which leads to the formation of Se monomers with correspondingly diverse roles (Figure 2.8, Chapter 2).<sup>56</sup> Depending on the Se bond (atomic Se, Se-H, or Se-R), we see different electron distributions due to the different contributing resonance structures. This gives directional Lewis acidic and basic character to the different Se monomers,<sup>57-60</sup> which gives rise to different Se reactivity toward nucleophilic  $\text{Cu}_3\text{P}$ . Although future investigations to isolate the Se monomers would be required in order to evaluate the success of light as a knob for NP synthesis, the ability to photoinitiate a solid-state reaction<sup>61-63</sup>, where diffusion is often the limiting factor, is an incredible opportunity to use light as opposed to heat to overcome the diffusion barrier to access metastable phases. With the collaboration of a theorist, the energies of different bond formations can be calculated. If they are within the UV-vis range, a LED light can be illuminated on the reactions. Thus, photoinitiated reactions demonstrate the potential synergy between synthetic and computational chemists.

#### **7.4. Computation as a Guide to Navigate the Interdisciplinary Nature of NP Synthesis**

Collaboration with a computational chemist offers the ability to learn something that may be blind to experimentalists. For our own work (Chapter 5), computation was shown to be a powerful tool for modeling molecular level processes that were not directly observed by mature

ex situ characterization methods. While GC-MS and  $^1\text{H}$  NMR characterized a diversity of Se species, the techniques could not confidently ascertain if certain species were pertinent participants or innocuous bystanders let alone describe how they might participate in the formation of Se bonds. Thus, computation was used as a bridge to narrow down the Se monomers that directed the reaction pathway and describe the molecular reaction scheme by which Se bonds are templated.

In doing so, hard-soft acid-base (HSAB) principles were expanded. Nanoparticle synthesis is often guided by how HSAB principles inform on the reactivity and compatibility of different precursors toward the final products.<sup>25,64</sup> However, the interdisciplinary nature of nanoparticle synthesis often convolutes the underlying physical phenomena that contribute towards reactivity and overlooks the complexity of NP syntheses. HSAB principles by Pearson serve as first order approximations for materials development and on its own is not sufficient to predict precursors to use for synthesis. It can retroactively help describe why some reactions work, but it doesn't take into account other factors such as anisotropic electron distribution. Thus, many materials are anomalous to these principles, limiting how precursor reactivities are described, thus rationally selected for new syntheses.

We have previously reported on the solution-based synthesis of  $\text{Cu}_3\text{PSe}_4$  (Chapter 4).<sup>30</sup> Its synthesis is particularly curious as its identity is incompatible with principles of HSAB: the incorporation of P, a light main group element, must simultaneously overcome the formation of HSAB compatible copper-selenide binary impurities. To incorporate phosphorus and direct the reaction pathway toward the formation of ternary Cu-P-Se, P-bonds were installed into P-containing binary starting reagents ( $\text{Cu}_3\text{P}$  and  $\text{P}_4\text{Se}_3$ ). Rapid development in the field of chalcogen bonding has established the dual classification of selenium-containing compounds as both Lewis acidic (LA) and Lewis basic (LB) due to the directional dependence of orbitals that results from a

non-uniform electronic distribution.<sup>57-60</sup> Rather than treat Lewis acidity and basicity as global properties determining reactivity, we additionally considered a directional dependence of orbitals that results from a non-uniform electronic distribution. We, thus, hypothesized that the electrophilic properties of experimentally identified SeR<sub>2</sub> monomer (Lewis basic along Se-R bond) can drive dative P-Se bond formation with the corresponding nucleophile Cu<sub>3</sub>P (nucleophilic through its P atoms). In this way, a methodology merging computation and experimental was developed to correlate selenization reagents to supramolecular assembly in which precursors (or more aptly monomers due to the interaction of solvent) can be judiciously selected via retrosynthesis through these expanded HSAB principles. This alludes to a synthetic strategy in which the intersection of molecular and material mindsets can inform on how extended materials of unique chemical compositions can be made.

In the case study explored, computation complemented mature characterization methods to guide rational hypotheses of empirical results and vice versa, which was used to guide experimental design. Computation can also manifest as a method to direct syntheses via machine-learning in which parameters could be predicted by the input of both successful and failed reactions.<sup>30,47,48,65,66</sup> It can also direct syntheses by reaction landscape elucidation of a system (i.e. reaction mechanisms, schemes, intermediates, interactions between species, etc) and quantification of the energy potentials or stabilities of reactants, intermediates, and products. This would lead to the development of a reaction coordinate plot for that system which could be used to understand how and why a reaction works and be extrapolated to other analogous systems. This work would be useful for the rational synthesis of systems that are far from equilibrium, a challenge which currently alludes synthetic chemists. If reaction mechanisms at high temperatures

or kinetic conditions could be predicted, the strategies developed would open opportunities for materials discovery and syntheses beyond continued trial-and-error.

### 7.5. Material Properties Exploration as a Feedback Loop for Better NP Syntheses

Predictable next steps for the  $\text{Cu}_3\text{PSe}_4$  NP material include exploration of its material properties (i.e. structural, crystallographic, electronic, photoelectrochemical, etc.). The p-type semiconductor is of particular interest as a solar photovoltaic absorber due to a theoretical study reporting its spectroscopic limited maximum efficiency (SLME), or theoretical PCE, at 24% (Figure 7.4).<sup>13</sup> It is a direct band gap material of 1.40 eV,<sup>67</sup> measured experimentally for the bulk, or 1.38 eV,<sup>68</sup> measured experimentally for our NP material, which is within the desired range for solar PV devices (1.0 eV - 1.6 eV). Despite the competitive photovoltaic (PV) properties,  $\text{Cu}_3\text{PSe}_4$  has not received much attention.

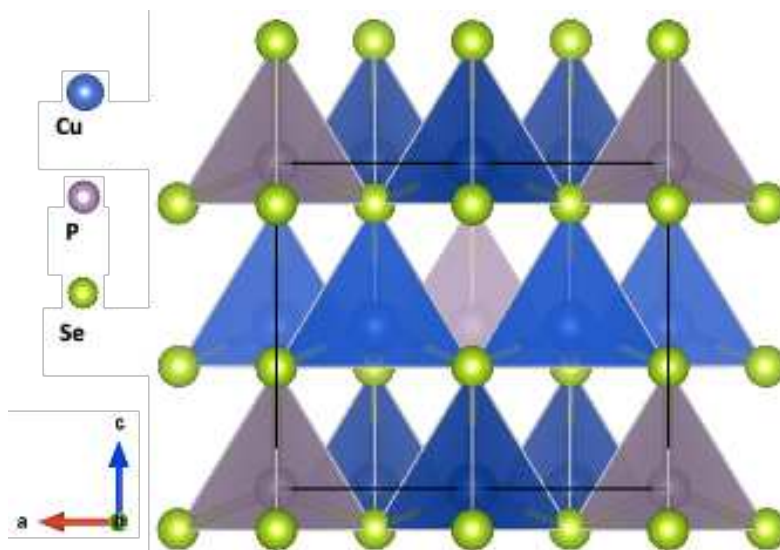


**Figure 7.4.** Enargite crystal structure of  $\text{Cu}_3\text{PSe}_4$  in which Cu (blue) and P (grey) atoms are tetrahedrally coordinated to Se atoms (green). This framework gives rise to long-range channels in which ion can be transported through.

By virtue of the colloidal nanoparticle synthesis, nanoparticles can be suspended and processed/fabricated into thin film PV devices.<sup>69</sup> Thin films can be casted onto substrates via drop-

coating, spin-coating, or dip-coating which can then be annealed to enhance performance despite their nonuniform morphologies.<sup>70-72</sup> Photoelectrochemical (PEC) characterization can be used to measure the photocurrent generated by the material itself and be used to observe trends after each device iteration to optimize thin film fabrication. An alternative knob in optimization is ligand exchange of long organic chains functionalized on the inorganic NP core to short, conductive ligands to increase electron transport efficiency.<sup>73-76</sup> However, the particles are agglomerated as imaged by TEM, in which the morphology of  $\text{Cu}_3\text{PSe}_4$  appears to be templated by the stacked hexagonal plates of the  $\text{Cu}_3\text{P}$  starting material. This could potentially prevent full ligand exchange resulting in poor coverage. On the other hand, the agglomeration could prove advantageous toward particle to particle communication (i.e. electrical contact, conductivity, etc.).<sup>77-81</sup> It would, thus, be curious to probe the material's PEC properties by rethinking the synthesis of  $\text{Cu}_3\text{PSe}_4$  to incorporate control over size and morphology.

Copper selenophosphate also shows promise as a thermoelectric material owing to a low lattice thermal conductivity as a result of compositional complexity.<sup>82,83</sup> Compositional complexity can increase the diversity and potential number of atoms in the compounds, consequently increasing the contribution from acoustic phonons which are mainly responsible for heat transport. Studies for analogous enargite-based structures in the bulk show promise.<sup>67,84</sup> However, its performance is limited by its low electrical conductivity. Zhang et al. demonstrated that thermoelectric properties could be enhanced by controllably introducing Cu vacancies into the lattice to synthesize  $\text{Cu}_{3-x}\text{PSe}_4$  ( $x = 0, 0.03, 0.06, 0.09, 0.12$ ) bulk materials.<sup>83</sup> The authors found that all Cu deficient samples showed increased carrier concentration and improved electrical properties while maintaining the low lattice thermal conductivities. A maximum figure of merit (zT) value of 0.62 was obtained at 727 K for the  $x = 0.12$  sample. NPs provide a unique opportunity

to further probe and improve the thermoelectric properties of  $\text{Cu}_3\text{PSe}_4$  because the small particle sizes can increase acoustic phonon scattering. After base studies, an adapted procedure for Cu defect engineering can then be explored for  $\text{Cu}_3\text{PSe}_4$  NPs.

Analogous copper thiophosphate,  $\text{Cu}_3\text{PS}_4$ , has attracted attention as both a battery electrode and solid electrolyte candidate owing to the cost-effective and abundant constituent elements.<sup>85,86</sup> As an anode material, metal thiophosphates have emerged to show high gravimetric capacity and long cycle life based on conversion reactions for Li- and Na-ion batteries.<sup>87-89</sup> Both P and S can participate in the electrochemical conversion reaction which results in improved storage performance as compared to their metal sulfide counterparts.<sup>86</sup> Lithium and sodium analogues to  $\text{Cu}_3\text{PS}_4$  are of interest as solid electrolyte materials due to their high room temperature ionic conductivity and their high ductility which is particularly important as dynamic structures are required for effective ion transport.<sup>90-93</sup> The tetrahedral  $[\text{PS}_4]^{3-}$  macrostructure also assemble into channels on a long-range order, which is amenable for ion transport (Figure 7.4). Further, the incorporation of Cu into crystal structure can increase the overall conductivity of the material.

To our knowledge, the  $\text{Cu}_3\text{PSe}_4$  material has not been investigated for either application. To study the material in either capacity, slurries of the NP material could be drop-casted onto substrates and assembled into batteries. The Prieto group is proficient in electrodeposition as a synthetic technique, providing a method in which a uniform film of the material can be studied phase-pure in a device without additives and binders.<sup>94-96</sup> Other battery components would be judiciously selected.

Curiously, the ability to study the materials properties of  $\text{Cu}_3\text{PSe}_4$  also enables iterative synthetic optimization in which property and device implementation behaves as a characterization tool and informs on the quality of the material. While engineering the material into the best device

for a desired application is not our goal, if we can connect an underlying physical phenomenon to the *what and why* it improves a material property, we can access predicting ability and ways to optimize syntheses. This is extremely powerful as a materials design function and can have implications in further understanding, for example, multicomponent systems and how interfaces might interact with one another and how we may judiciously select components to function synergistically with one another. Not only can we come up with better ways to understand and characterize materials, we can also come up with better ways to make materials. Essentially, our goals here would be to make materials better and make better materials.

## 7.6. Perspective

All in all, the diversity of these proposals demonstrates the plethora of opportunities inspired from one NP system:  $\text{Cu}_3\text{PSe}_4$ . Options include expansion of a synthetic toolkit that target difficult to synthesize materials such as metastable phases or ternary nitrides, collaboration with a computational chemist to bridge the interdisciplinary nature of NP synthesis and deepen what we understand about the reaction landscapes and phase spaces of these complex systems, and exploration of materials properties.

Extrapolation of these techniques to new systems builds a criterion for which materials could be successfully or unsuccessfully synthesized and evaluated by our strategies. We can use similarities to target the strategies and we can use the results to assess the differences. Further, extrapolation of our methods is one way to evaluate our methodologies to build a toolkit that can additionally screen materials that can be synthesized by those methods. We could initially screen for composition, bonding scheme, crystal structure, constituent element valancies, etc. The more iterations our methods are wrung under, the more robust our method becomes. The more robust the method, the more parameters we elucidate toward controlling reaction pathways, resulting in

more predictive chemistry. Our ultimate goal is to inspire new directions and perspectives on a toolkit for colloidal nanoparticles, and we hope that any of these pursuits challenge and expand the knowledge of the NP community and that these strategies are adapted and extrapolated to other complex and unique NP systems.

## REFERENCES

- (1) Liu, J.; Meyns, M.; Zhang, T.; Arbiol, J.; Cabot, A.; Shavel, A. Triphenyl Phosphite as the Phosphorus Source for the Scalable and Cost-Effective Production of Transition Metal Phosphides. *Chem. Mater.* **2018**, *30* (5), 1799–1807.
- (2) Henkes, A. E.; Schaak, R. E. Trioctylphosphine: A General Phosphorus Source for the Low-Temperature Conversion of Metals into Metal Phosphides. *Chem. Mater.* **2007**, *19* (17), 4234–4242.
- (3) Lee, J. M.; Miller, R. C.; Moloney, L. J.; Prieto, A. L. The Development of Strategies for Nanoparticle Synthesis: Considerations for Deepening Understanding of Inherently Complex Systems. *J. Solid State Chem.* **2019**, *273*, 243–286.
- (4) Wang, X.; Zhuang, J.; Peng, Q.; Li, Y. A General Strategy for Nanocrystal Synthesis. *Nature* **2005**, *437* (7055), 121–124.
- (5) Yarema, O.; Yarema, M.; Wood, V. Tuning the Composition of Multicomponent Semiconductor Nanocrystals: The Case of I–III–VI Materials. *Chem. Mater.* **2018**, *30* (5), 1446–1461.
- (6) Loiudice, A.; Segura Lecina, O.; Buonsanti, R. Atomic Control in Multicomponent Nanomaterials: When Colloidal Chemistry Meets Atomic Layer Deposition. *ACS Mater. Lett.* **2020**, *25*, 14.
- (7) García-Rodríguez, R.; Hendricks, M. P.; Cossairt, B. M.; Liu, H.; Owen, J. S. Conversion Reactions of Cadmium Chalcogenide Nanocrystal Precursors. *Chem. Mater.* **2013**, *25* (8), 1233–1249.
- (8) Friedfeld, M. R.; Stein, J. L.; Cossairt, B. M. Main-Group-Semiconductor Cluster Molecules as Synthetic Intermediates to Nanostructures. *Inorg. Chem.* **2017**, *56* (15), 8689–8697.
- (9) Sowers, K. L.; Swartz, B.; Krauss, T. D. Chemical Mechanisms of Semiconductor Nanocrystal Synthesis. *Chem. Mater.* **2013**, *25* (8), 1351–1362.
- (10) Soderholm, L.; Mitchell, J. F. Perspective: Toward “Synthesis by Design”: Exploring Atomic Correlations during Inorganic Materials Synthesis. *APL Mater.* **2016**, *4* (5), 053212.
- (11) Kuhs, W. F.; Nitsche, R.; Scheunemann, K. The Argyrodites - A New Family of Tetrahedrally Close-Packed Structures. *Mater. Res. Bull.* **1979**, *14* (2), 241–248.
- (12) Weldert, K. S.; Zeier, W. G.; Day, T. W.; Panthöfer, M.; Snyder, G. J.; Tremel, W. Thermoelectric Transport in Cu<sub>7</sub>PSe<sub>6</sub> with High Copper Ionic Mobility. *J. Am. Chem. Soc.* **2014**, *136* (34), 12035–12040.
- (13) Yu, L.; Kokenyesi, R. S.; Keszler, D. A.; Zunger, A. Inverse Design of High Absorption Thin-Film Photovoltaic Materials. *Adv. Energy Mater.* **2013**, *3* (1), 43–48.
- (14) Gaudin, E.; Petricek, V.; Boucher, F.; Taulelle, F.; Evain, M. Structures and Phase Transitions of the A<sub>7</sub>PSe<sub>6</sub> (A = Ag, Cu) Argyrodite-Type Ionic Conductors. III. α-Cu<sub>7</sub>PSe<sub>6</sub>. *Acta Crystallogr. Sect. B Struct. Sci.* **2000**, *56* (6), 972–979.
- (15) Gaudin, E.; Boucher, F.; Petricek, V.; Taulelle, F.; Evain, M. Structures and Phase Transitions of the A<sub>7</sub>PSe<sub>6</sub> (A = Ag, Cu) Argyrodite-Type Ionic Conductors. II. β- and γ-Cu<sub>7</sub>PSe<sub>6</sub>. *Acta Crystallogr. Sect. B Struct. Sci.* **2000**, *56* (3), 402–408.
- (16) Beeken, R. B.; Driessen, C. R.; Hinaus, B. M.; Pawlisch, D. E. Electrical Conductivity of

- Ag<sub>7</sub>PSe<sub>6</sub> and Cu<sub>7</sub>PSe<sub>6</sub>. *Solid State Ionics* **2008**, *179* (21–26), 1058–1060.
- (17) Evain, M.; Gaudin, E.; Boucher, F.; Petricek, V.; Taulelle, F. Structures and Phase Transitions of the Ag<sub>7</sub>PSe<sub>6</sub> (A = Ag, Cu) Argyrodite-Type Ionic Conductors. I. Ag<sub>7</sub>PSe<sub>6</sub>. *Acta Crystallogr. Sect. B Struct. Sci.* **1998**, *54* (4), 376–383.
  - (18) Sheets, E. J.; Yang, W.-C.; Balow, R. B.; Wang, Y.; Walker, B. C.; Stach, E. A.; Agrawal, R. An in Situ Phosphorus Source for the Synthesis of Cu<sub>3</sub>P and the Subsequent Conversion to Cu<sub>3</sub>PS<sub>4</sub> Nanoparticle Clusters. *J. Mater. Res.* **2015**, *30* (23), 3710–3716.
  - (19) Shigemi, A.; Maeda, T.; Wada, T. First-Principles Calculation of Cu<sub>2</sub>SnS<sub>3</sub> and Related Compounds. *Phys. status solidi* **2015**, *252* (6), 1230–1234.
  - (20) Zhang, Y.; Wang, Y.; Zhang, J.; Xi, L.; Zhang, P.; Zhang, W. Pinning down High-Performance Cu-Chalcogenides as Thin-Film Solar Cell Absorbers: A Successive Screening Approach. *J. Chem. Phys.* **2016**, *144* (19), 194706.
  - (21) Niewa, R.; Jacobs, H. Group V and VI Alkali Nitridometalates: A Growing Class of Compounds with Structures Related to Silicate Chemistry. *Chem. Rev.* **1996**, *96* (6), 2053–2062.
  - (22) Tareen, A. K.; Priyanga, G. S.; Behara, S.; Thomas, T.; Yang, M. Mixed Ternary Transition Metal Nitrides: A Comprehensive Review of Synthesis, Electronic Structure, and Properties of Engineering Relevance. *Progress in Solid State Chemistry*. Elsevier Ltd March 1, 2019, pp 1–26.
  - (23) Sun, W.; Bartel, C. J.; Arca, E.; Bauers, S. R.; Matthews, B.; Orvañanos, B.; Chen, B.-R.; Toney, M. F.; Schelhas, L. T.; Tumas, W.; et al. A Map of the Inorganic Ternary Metal Nitrides. *Nat. Mater.* **2019**, *18* (7), 732–739.
  - (24) DiSalvo, F. J.; Clarke, S. J. Ternary Nitrides: A Rapidly Growing Class of New Materials. *Curr. Opin. Solid State Mater. Sci.* **1996**, *1* (2), 241–249.
  - (25) Pearson, R. G. Hard and Soft Acids and Bases. *J. Am. Chem. Soc.* **1963**, *85* (22), 3533–3539.
  - (26) Gaudin, E.; Petricek, V.; Boucher, F.; Taulelle, F.; Evain, M. Structures and Phase Transitions of the A<sub>7</sub>PSe<sub>6</sub> (A = Ag, Cu) Argyrodite-Type Ionic Conductors. a-Cu<sub>7</sub>PSe<sub>6</sub>. *Acta Crystallogr. Sect. B Struct. Sci.* **2000**, No. 856, 972–979.
  - (27) Gaudin, E.; Boucher, F.; Petricek, V.; Taulelle, F.; Evain, M. Structures and Phase Transitions of the A<sub>7</sub>PSe<sub>6</sub> (A = Ag, Cu) Argyrodite-Type Ionic Conductors. II. β- and β-Cu<sub>7</sub>PSe<sub>6</sub>. *Acta Crystallogr. Sect. B Struct. Sci.* **2000**, *56* (3), 402–408.
  - (28) Golovei, M. I.; Voroshilov, Y. V.; Potorii, M. V. ASM Phase Diagrams: Ag/P/Se <https://www.asminternational.org/phase-diagrams>.
  - (29) Karakaya; Thompson. ASM Phase Diagrams: Ag/P <https://www.asminternational.org/phase-diagrams>.
  - (30) Lee, J. M.; Kraynak, L. A.; Prieto, A. L. A Directed Route to Colloidal Nanoparticle Synthesis of the Copper Selenophosphate Cu<sub>3</sub>PSe<sub>4</sub>. *Angew. Chemie Int. Ed.* **2020**, *59* (8), 3038–3042.
  - (31) Coughlan, C.; Ibáñez, M.; Dobrozhan, O.; Singh, A.; Cabot, A.; Ryan, K. M. Compound Copper Chalcogenide Nanocrystals. *Chem. Rev.* **2017**, *117* (9), 5865–6109.
  - (32) Abécassis, B.; Bouet, C.; Garnero, C.; Constantin, D.; Lequeux, N.; Ithurria, S.; Dubertret, B.; Pauw, B. R.; Pontoni, D. Real-Time in Situ Probing of High-Temperature Quantum Dots Solution Synthesis. *Nano Lett.* **2015**, *15* (4), 2620–2626.
  - (33) Andersen, H. L.; Bøjesen, E. D.; Birgisson, S.; Christensen, M.; Iversen, B. B. Pitfalls and Reproducibility of in Situ Synchrotron Powder X-Ray Diffraction Studies of Solvothermal

- Nanoparticle Formation. *J. Appl. Crystallogr.* **2018**, *51* (2), 526–540.
- (34) Haynes, A. S.; Stoumpos, C. C.; Chen, H.; Chica, D.; Kanatzidis, M. G. Panoramic Synthesis as an Effective Materials Discovery Tool: The System Cs/Sn/P/Se as a Test Case. *J. Am. Chem. Soc.* **2017**, *139* (31), 10814–10821.
- (35) Kar, M.; Agrawal, R.; Hillhouse, H. W. Formation Pathway of CuInSe<sub>2</sub> Nanocrystals for Solar Cells. *J. Am. Chem. Soc.* **2011**, *133* (43), 17239–17247.
- (36) Jiang, Z.; Tian, S.; Lai, S.; McAuliffe, R. D.; Rogers, S. P.; Shim, M.; Shoemaker, D. P. Capturing Phase Evolution during Solvothermal Synthesis of Metastable Cu<sub>4</sub>O<sub>3</sub>. *Chem. Mater.* **2016**, *28* (9), 3080–3089.
- (37) Jiang, Z.; Ramanathan, A.; Shoemaker, D. P. In Situ Identification of Kinetic Factors That Expedite Inorganic Crystal Formation and Discovery. *J. Mater. Chem. C* **2017**, *5* (23), 5709–5717.
- (38) Shoemaker, D. P.; Hu, Y.-J.; Chung, D. Y.; Halder, G. J.; Chupas, P. J.; Soderholm, L.; Mitchell, J. F.; Kanatzidis, M. G. In Situ Studies of a Platform for Metastable Inorganic Crystal Growth and Materials Discovery. *Proc. Natl. Acad. Sci.* **2014**, *111* (30), 10922–10927.
- (39) Li, J.; Wang, H.; Lin, L.; Fang, Q.; Peng, X. Quantitative Identification of Basic Growth Channels for Formation of Monodisperse Nanocrystals. *J. Am. Chem. Soc.* **2018**, *140* (16), 5474–5484.
- (40) Bhutani, A.; Schiller, J. A.; Zuo, J. L.; Eckstein, J. N.; Greene, L. H.; Chaudhuri, S.; Shoemaker, D. P. Combined Computational and in Situ Experimental Search for Phases in an Open Ternary System, Ba-Ru-S. *Chem. Mater.* **2017**, *29* (14), 5841–5849.
- (41) Fallon, M. J.; Martinolich, A. J.; Maughan, A. E.; Gallington, L. C.; Neilson, J. R. Low-Temperature Synthesis of Superconducting Iron Selenide Using a Triphenylphosphine Flux. *Dalt. Trans.* **2019**, *48* (43), 16298–16303.
- (42) Martinolich, A. J.; Neilson, J. R. Toward Reaction-by-Design: Achieving Kinetic Control of Solid State Chemistry with Metathesis. *Chem. Mater.* **2017**, *29* (2), 479–489.
- (43) Chien, P. H.; Griffith, K. J.; Liu, H.; Gan, Z.; Hu, Y. Y. Recent Advances in Solid-State Nuclear Magnetic Resonance Techniques for Materials Research. In *Annual Review of Materials Research*; Annual Reviews Inc., 2020; Vol. 50, pp 493–520.
- (44) Wang, L. S.; Patel, S. V.; Sanghvi, S. S.; Hu, Y.-Y.; Haile, S. M. Structure and Properties of Cs<sub>7</sub>(H<sub>4</sub>PO<sub>4</sub>)(H<sub>2</sub>PO<sub>4</sub>)<sub>8</sub>: A New Superprotonic Solid Acid Featuring the Unusual Polycation (H<sub>4</sub>PO<sub>4</sub>)<sup>+</sup>. *J. Am. Chem. Soc.* **2020**, jacs.0c08870.
- (45) Poli, F.; Wong, A.; Kshetrimayum, J. S.; Monconduit, L.; Letellier, M. In Situ NMR Insights into the Electrochemical Reaction of Cu<sub>3</sub>P Electrodes in Lithium Batteries. *Chem. Mater.* **2016**, *28* (6), 1787–1793.
- (46) Chamorro, J. R.; McQueen, T. M. Progress toward Solid State Synthesis by Design. *Acc. Chem. Res.* **2018**, *51* (11), 2918–2925.
- (47) Alberi, K.; Nardelli, M. B.; Zakutayev, A.; Mitas, L.; Curtarolo, S.; Jain, A.; Fornari, M.; Marzari, N.; Takeuchi, I.; Green, M. L.; et al. The 2019 Materials by Design Roadmap. *J. Phys. D: Appl. Phys.* **2019**, *52* (1), 013001.
- (48) Mansouri Tehrani, A.; Oliynyk, A. O.; Parry, M.; Rizvi, Z.; Couper, S.; Lin, F.; Miyagi, L.; Sparks, T. D.; Brgoch, J. Machine Learning Directed Search for Ultraincompressible, Superhard Materials. *J. Am. Chem. Soc.* **2018**, *140* (31), 9844–9853.
- (49) Aykol, M.; Dwaraknath, S. S.; Sun, W.; Persson, K. A. Thermodynamic Limit for Synthesis of Metastable Inorganic Materials. *Sci. Adv.* **2018**, *4* (4), eaaq0148.

- (50) Goldsmith, B. R.; Boley, M.; Vreeken, J.; Scheffler, M.; Ghiringhelli, L. M. Uncovering Structure-Property Relationships of Materials by Subgroup Discovery. *New J. Phys.* **2017**, *19* (1), 013031.
- (51) Butler, K. T.; Davies, D. W.; Cartwright, H.; Isayev, O.; Walsh, A. Machine Learning for Molecular and Materials Science. *Nature*. Nature Publishing Group July 26, 2018, pp 547–555.
- (52) Rickman, J. M.; Lookman, T.; Kalinin, S. V. Materials Informatics: From the Atomic-Level to the Continuum. *Acta Materialia*. Acta Materialia Inc April 15, 2019, pp 473–510.
- (53) Liu, Y.; Zhao, T.; Ju, W.; Shi, S.; Shi, S.; Shi, S. Materials Discovery and Design Using Machine Learning. *Journal of Materiomics*. Chinese Ceramic Society September 1, 2017, pp 159–177.
- (54) Gary, D. C.; Terban, M. W.; Billinge, S. J. L.; Cossairt, B. M. Two-Step Nucleation and Growth of InP Quantum Dots via Magic-Sized Cluster Intermediates. *Chem. Mater.* **2015**, *27* (4), 1432–1441.
- (55) Bullen, C.; van Embden, J.; Jasieniak, J.; Cosgriff, J. E.; Mulder, R. J.; Rizzardo, E.; Gu, M.; Raston, C. L. High Activity Phosphine-Free Selenium Precursor Solution for Semiconductor Nanocrystal Growth. *Chem. Mater.* **2010**, *22* (14), 4135–4143.
- (56) Dénès, F.; Pichowicz, M.; Povie, G.; Renaud, P. Thiyl Radicals in Organic Synthesis. *Chem. Rev.* **2014**, *114* (5), 2587–2693.
- (57) Scilabra, P.; Terraneo, G.; Resnati, G. The Chalcogen Bond in Crystalline Solids: A World Parallel to Halogen Bond. *Acc. Chem. Res.* **2019**, *52*, 59.
- (58) Haberhauer, G.; Gleiter, R. The Nature of Strong Chalcogen Bonds Involving Chalcogen-Containing Heterocycles. *Angew. Chemie Int. Ed.* **2020**, *59* (47), 21236–21243.
- (59) Benz, S.; López-Andarias, J.; Mareda, J.; Sakai, N.; Matile, S. Catalysis with Chalcogen Bonds. *Angew. Chemie Int. Ed.* **2017**, *56* (3), 812–815.
- (60) Wang, W.; Zhu, H.; Feng, L.; Yu, Q.; Hao, J.; Zhu, R.; Wang, Y. Dual Chalcogen–Chalcogen Bonding Catalysis. *J. Am. Chem. Soc.* **2020**, *142* (6), 3117–3124.
- (61) Sakamoto, M.; Fujistuka, M.; Majima, T. Light as a Construction Tool of Metal Nanoparticles: Synthesis and Mechanism. *J. Photochem. Photobiol. C Photochem. Rev.* **2009**, *10* (1), 33–56.
- (62) Costa Bassetto, V.; Oliveira Silva, W.; Pereira, C. M.; Girault, H. H. Flash Light Synthesis of Noble Metal Nanoparticles for Electrochemical Applications: Silver, Gold, and Their Alloys. *J. Solid State Electrochem.* **2020**, *24* (8), 1781–1788.
- (63) Schliebe, C.; Jiang, K.; Schulze, S.; Hietschold, M.; Cai, W. Bin; Lang, H. A Convenient Light Initiated Synthesis of Silver and Gold Nanoparticles Using a Single Source Precursor. *Chem. Commun.* **2013**, *49* (38), 3991–3993.
- (64) Lee, J. M.; Miller, R. C.; Moloney, L. J.; Prieto, A. L. The Development of Strategies for Nanoparticle Synthesis: Considerations for Deepening Understanding of Inherently Complex Systems. *J. Solid State Chem.* **2019**, *273*, 243–286.
- (65) Kononova, O.; Huo, H.; He, T.; Rong, Z.; Botari, T.; Sun, W.; Tshitoyan, V.; Ceder, G. Text-Mined Dataset of Inorganic Materials Synthesis Recipes. *Sci. data* **2019**, *6* (1), 203.
- (66) Cao, B.; Adutwum, L. A.; Oliynyk, A. O.; Lubner, E. J.; Olsen, B. C.; Mar, A.; Buriak, J. M. How To Optimize Materials and Devices *via* Design of Experiments and Machine Learning: Demonstration Using Organic Photovoltaics. *ACS Nano* **2018**, *12* (8), 7434–7444.
- (67) Itthibenchapong, V.; Kokenyesi, R. S.; Ritenour, A. J.; Zakharov, L. N.; Boettcher, S. W.;

- Wager, J. F.; Keszler, D. A. Earth-Abundant Cu-Based Chalcogenide Semiconductors as Photovoltaic Absorbers. *J. Mater. Chem. C* **2013**, *1* (4), 657–662.
- (68) Lee, J. M.; Kraynak, L. A.; Prieto, A. L. A Directed Route to Colloidal Nanoparticle Synthesis of the Copper Selenophosphate  $\text{Cu}_3\text{PSe}_4$ . *Angew. Chemie Int. Ed.* **2020**, *59* (8), 3038–3042.
- (69) Chernomordik, B. D.; Marshall, A. R.; Pach, G. F.; Luther, J. M.; Beard, M. C. Quantum Dot Solar Cell Fabrication Protocols. *Chem. Mater.* **2017**, *29* (1), 189–198.
- (70) Panthani, M. G.; Kurley, J. M.; Crisp, R. W.; Dietz, T. C.; Ezzyat, T.; Luther, J. M.; Talapin, D. V. High Efficiency Solution Processed Sintered CdTe Nanocrystal Solar Cells: The Role of Interfaces. *Nano Lett.* **2014**, *14* (2), 670–675.
- (71) Crisp, R. W.; Panthani, M. G.; Rance, W. L.; Duenow, J. N.; Parilla, P. A.; Callahan, R.; Dabney, M. S.; Berry, J. J.; Talapin, D. V.; Luther, J. M. Nanocrystal Grain Growth and Device Architectures for High-Efficiency CdTe Ink-Based Photovoltaics. *ACS Nano* **2014**, *8* (9), 9063–9072.
- (72) Shaw, S.; Yuan, B.; Tian, X.; Miller, K. J.; Cote, B. M.; Colaux, J. L.; Migliori, A.; Panthani, M. G.; Cademartiri, L. Building Materials from Colloidal Nanocrystal Arrays: Preventing Crack Formation during Ligand Removal by Controlling Structure and Solvation. *Adv. Mater.* **2016**, *28* (40), 8892–8899.
- (73) Marino, E.; Kodger, T. E.; Crisp, R. W.; Timmerman, D.; MacArthur, K. E.; Heggen, M.; Schall, P. Repairing Nanoparticle Surface Defects. *Angew. Chemie Int. Ed.* **2017**.
- (74) Giansante, C. Library Design of Ligands at the Surface of Colloidal Nanocrystals. *Acc. Chem. Res.* **2020**, *53* (8), 1458–1467.
- (75) Owen, J. The Coordination Chemistry of Nanocrystal Surfaces. *Science* **2015**, *347* (6222).
- (76) Kroupa, D. M.; Vörös, M.; Brawand, N. P.; McNichols, B. W.; Miller, E. M.; Gu, J.; Nozik, A. J.; Sellinger, A.; Galli, G.; Beard, M. C. Tuning Colloidal Quantum Dot Band Edge Positions through Solution-Phase Surface Chemistry Modification. *Nat. Commun.* **2017**, *8*, 15257.
- (77) Anderson, N. C.; Hendricks, M. P.; Choi, J. J.; Owen, J. S. Ligand Exchange and the Stoichiometry of Metal Chalcogenide Nanocrystals: Spectroscopic Observation of Facile Metal-Carboxylate Displacement and Binding. *J. Am. Chem. Soc.* **2013**, *135* (49), 18536–18548.
- (78) Chen, P. E.; Anderson, N. C.; Norman, Z. M.; Owen, J. S. Tight Binding of Carboxylate, Phosphonate, and Carbamate Anions to Stoichiometric CdSe Nanocrystals. *J. Am. Chem. Soc.* **2017**, *139* (8), 3227–3236.
- (79) Korala, L.; McGoffin, J. T.; Prieto, A. L. Enhanced Conductivity in CZTS/ $\text{Cu}_{2-x}\text{Se}$  Nanocrystal Thin Films: Growth of a Conductive Shell. *ACS Appl. Mater. Interfaces* **2016**, *8* (7), 4911–4917.
- (80) Agocs, D. B.; Danna, T.; Prieto, A. L. Ambient Surface Stability of Thin Film Nanocrystalline  $\text{Cu}_3\text{SbSe}_4$  and Structure-Property Relationships. *ACS Appl. Energy Mater.* **2019**, *2* (3), 1903–1910.
- (81) Talapin, D. V.; Lee, J.-S.; Kovalenko, M. V.; Shevchenko, E. V. Prospects of Colloidal Nanocrystals for Electronic and Optoelectronic Applications. *Chem. Rev.* **2010**, *110* (1), 389–458.
- (82) Slassi, A.; Hammi, M.; El Rhazouani, O.; Arejdal, M. Ab Initio Study of Thermoelectric Properties of  $\text{Cu}_3\text{PSe}_4$  and  $\text{Cu}_3\text{PS}_4$ : Alternative Materials for Thermoelectric Applications. *Opt. Quantum Electron.* **2017**, *49* (4), 171.

- (83) Zhang, Y. M.; Shen, X. C.; Yan, Y. C.; Wang, G. W.; Wang, G. Y.; Li, J. Y.; Lu, X.; Zhou, X. Y. Enhanced Thermoelectric Performance of Ternary Compound  $\text{Cu}_3\text{PSe}_4$  by Defect Engineering. *Rare Met.* **2020**, 1–6.
- (84) Tanimoto, T.; Suekuni, K.; Tanishita, T.; Usui, H.; Tadano, T.; Kamei, T.; Saito, H.; Nishiate, H.; Lee, C. H.; Kuroki, K.; et al. Enargite  $\text{Cu}_3\text{PS}_4$ : A Cu-S-Based Thermoelectric Material with a Wurtzite-Derivative Structure. *Adv. Funct. Mater.* **2020**, 2000973.
- (85) Brehm, W.; Santhosha, A. L.; Zhang, Z.; Neumann, C.; Turchanin, A.; Martin, A.; Pinna, N.; Seyring, M.; Rettenmayr, M.; Buchheim, J. R.; et al. Copper Thiophosphate ( $\text{Cu}_3\text{PS}_4$ ) as Electrode for Sodium-Ion Batteries with Ether Electrolyte. *Adv. Funct. Mater.* **2020**, 1910583.
- (86) Tripathy, D.; Sampath, S. Understanding the High Capacity Contributions of  $\text{Cu}_3\text{PS}_4$  towards Lithium Storage. *J. Power Sources* **2020**, 478, 378–7753.
- (87) Liang, Q.; Zheng, Y.; Du, C.; Luo, Y.; Zhang, J.; Li, B.; Zong, Y.; Yan, Q. General and Scalable Solid-State Synthesis of 2D  $\text{MPS}_3$  (M = Fe, Co, Ni) Nanosheets and Tuning Their Li/Na Storage Properties. *Small Methods* **2017**, 1 (12), 1700304.
- (88) Edison, E.; Chaturvedi, A.; Ren, H.; Sreejith, S.; Lim, C. T.; Madhavi, S. Route of Irreversible Transformation in Layered Tin Thiophosphite and Enhanced Lithium Storage Performance. *ACS Appl. Energy Mater.* **2018**, 1 (10), 5772–5778.
- (89) Huang, S.; Meng, C.; Xiao, M.; Ren, S.; Wang, S.; Han, D.; Li, Y.; Meng, Y. Pseudocapacitive Sodium Storage by Ferroelectric  $\text{Sn}_2\text{P}_2\text{S}_6$  with Layered Nanostructure. *Small* **2018**, 14 (21), 1704367.
- (90) Famprikis, T.; Dawson, J. A.; Fauth, F.; Clemens, O.; Suard, E.; Fleutot, B.; Courty, M.; Chotard, J.-N.; Islam, M. S.; Masquelier, C. A New Superionic Plastic Polymorph of the  $\text{Na}^+$  Conductor  $\text{Na}_3\text{PS}_4$ . *ACS Mater. Lett.* **2019**, 1 (6), 641–646.
- (91) Kudu, Ö. U.; Famprikis, T.; Fleutot, B.; Braidia, M. D.; Le Mercier, T.; Islam, M. S.; Masquelier, C. A Review of Structural Properties and Synthesis Methods of Solid Electrolyte Materials in the  $\text{Li}_2\text{S} - \text{P}_2\text{S}_5$  Binary System. *J. Power Sources* **2018**, 407, 31–43.
- (92) Ma, Z.; Xue, H. G.; Guo, S. P. Recent Achievements on Sulfide-Type Solid Electrolytes: Crystal Structures and Electrochemical Performance. *Journal of Materials Science*. Springer New York LLC March 1, 2018, pp 3927–3938.
- (93) Xu, K. Electrolytes and Interphases in Li-Ion Batteries and Beyond. *Chemical Reviews*. American Chemical Society December 10, 2014, pp 11503–11618.
- (94) Mosby, J. M.; Prieto, A. L. Direct Electrodeposition of  $\text{Cu}_2\text{Sb}$  for Lithium-Ion Battery Anodes. *J. Am. Chem. Soc.* **2008**, 130 (32), 10656–10661.
- (95) Ma, J.; Prieto, A. L. Electrodeposition of Pure Phase  $\text{SnSb}$  Exhibiting High Stability as a Sodium-Ion Battery Anode. *Chem. Commun.* **2019**, 55 (48), 6938–6941.
- (96) Schulze, M. C.; Belson, R. M.; Kraynak, L. A.; Prieto, A. L. Electrodeposition of  $\text{Sb/CNT}$  Composite Films as Anodes for Li- and Na-Ion Batteries. *Energy Storage Mater.* **2020**, 25, 572–584.

## APPENDIX A

### CHAPTER 4 SUPPORTING INFORMATION

#### **A Directed Route to Colloidal Nanoparticle Synthesis of the Copper Selenophosphate $\text{Cu}_3\text{PSe}_4$ Supplementary**

##### **A.1. Experimental**

*Materials and Methods.* All reactions were performed under inert atmosphere unless otherwise noted. All product workup was done on the benchtop in ambient conditions unless otherwise noted. Copper (I) chloride ( $\text{CuCl}$ , Oakwood Chemical, 98%), copper (II) chloride ( $\text{CuCl}_2$ , Riedel-de Haën, 97%), trioctylphosphine oxide (TOPO, Aldrich, 99%), trioctylphosphine (TOP, Aldrich, 97%), triphenyl phosphite (TPOP, Oakwood Chemical, 97%), octylamine (Aldrich, 99%), hexadecylamine (HDA, Aldrich, 90%), selenium powder (Se, Strem Chemicals Inc., 99.99%), diphenyl diselenide ( $\text{Ph}_2\text{Se}_2$ , Aldrich, 98%), activated carbon (Sigma Aldrich, 20-40 mesh), tetralin (Alfa Aesar, 97%), and benzene (Fischer) were purchased and used as received. Technical grade toluene, hexanes, ethanol, isopropanol, and chloroform were obtained from Fisher Scientific. Oleylamine (OLA, Aldrich, 70%), 1-octadecene (ODE, Aldrich, 90%), and heptane (Mallinckrodt) were sparged with  $\text{N}_2$  for 2 h before use. White phosphorus ( $\text{P}_4$ ) was obtained by the melting and subsequent vapor transport of red phosphorus (P, Alfa Aesar). Elemental P was sealed in an evacuated fused 10 mm x 12 mm silica tube and placed in a tube furnace with one end outside in order to maintain a temperature gradient. The temperature was set to 450°C, and the reaction was run for at least 3 h to condense  $\text{P}_4$  on the cool end of the ampoule. Upon completion, the silica tube was opened and  $\text{P}_4$  was collected in a glovebox and used immediately.

## A.2. Investigation of Pathway Route (P-Se) + Cu

*P<sub>4</sub>Se<sub>3</sub> Synthesis.* Literature procedure developed by Irgolic et al.<sup>1</sup> was used with minor modifications to increase reaction yield. A 500 mL three-neck round-bottom flask equipped with Teflon stir bar, distilling apparatus, and thermocouple was charged with 20.2 mmol P<sub>4</sub>, 63.3 mmol Se, 624.5 mmol C, and 85 mL heptane. The mixture was refluxed for 1.5 h. Afterwards, 38 mL tetralin was added via syringe. The heptane was removed by distillation by slowly raising the temperature to 207°C at a rate of 150°C/h. The hot solution was allowed to settle and was passed through a coarse filter. The residue in the flask containing C, Se, and P<sub>4</sub>Se<sub>3</sub> was extracted with three 15 mL portions of hot tetralin, and the washings were added to the first filtrate. The combined tetralin solutions were cooled in ice, and P<sub>4</sub>Se<sub>3</sub> separated as a fine yellow-orange crystalline powder. The crude product was recrystallized from benzene.

*Cu<sub>3</sub>PSe<sub>4</sub> Nanoparticle Hot Injection Synthesis (Reaction Pathway P<sub>4</sub>Se<sub>3</sub> + Cu precursor).* In a typical synthesis, 0.38 mmol of P<sub>4</sub>Se<sub>3</sub> was mixed with 2 mL OLA in a scintillation vial, which readily dissolves to yield a blood red solution. The Cu flask was prepared by mixing 0.38 mmol CuCl with 1 mL OLA in a 25 mL 3-neck round-bottom flask equipped with a Teflon stir bar, reflux condenser, and thermocouple. The flask was heated under vacuum to 110°C at a rate of 500°C/h, then pumped and purged three times between N<sub>2</sub> and vacuum. It was subsequently heated to 150°C under N<sub>2</sub> where it was held for 2 h. After 0.5 h at 150°C, 0.28 mL octylamine was injected. Simultaneously, 2.14 mmol TOP and 1.19 mmol TOPO were added to a 50 mL three-neck round-bottom flask equipped with glass stir bar, reflux condenser, and thermocouple. The reaction flask was heated to 150°C under vacuum in which it was pumped and purged three times. It was held under vacuum and allowed to degas for 2 h. Afterwards, the reaction flask was switched to positive pressure under N<sub>2</sub> and heated to 370°C until the solution turned a pale greenish-yellow, indicating

decomposition of TOP/TOPO. Upon decomposition, the contents of the Cu flask were rapidly injected via a gastight Luer-Lock syringe. The temperature typically dropped ~50-70°C following injection. The flask was allowed to regain temperature to 370°C, and the particles grew 15 mins. After, the P<sub>4</sub>Se<sub>3</sub>/OLA solution was injected at 370°C and held for 0.5 h. After the growth period, the reaction was quenched by removal of the heating mantle, allowing the mixture to cool to ~80°C. The particles were collected by dispersion of the reaction mixture in toluene then flocculation with ethanol. After 15 min of centrifugation at 5800 rpm, the supernatant was discarded. The washing procedure was repeated with a sonication step to aid dispersion in toluene before addition of ethanol. The mixture was centrifuged at 5800 rpm for 8 min, and then the supernatant was discarded. Nanoparticles were stored in hexanes.

### **A.3. Investigation of Pathway Route (Cu-P) + Se**

*Copper phosphide (Cu<sub>3</sub>P) Hot Injection Nanocrystal Synthesis (Cu<sub>3</sub>P Products A and B).* Literature protocol developed by De Trizio et al.<sup>2</sup> for the formation of colloidal Cu<sub>3</sub>P nanocrystals with hexagonal plate-like morphology was adapted and optimized. The molar ratio of TOP:Cu affects the reaction pathway in the following way: *Cu<sub>3</sub>P Product A* (see below) involves the direct nucleation of Cu<sub>3</sub>P and *Cu<sub>3</sub>P Product B* (see below) involves the nucleation of Cu then transformation to Cu<sub>3</sub>P.

*Cu<sub>3</sub>P Product A (Direct Nucleation of Cu<sub>3</sub>P).* In a typical synthesis, 1.6 mmol CuCl was mixed with 2.4 mL OLA in a 25 mL 3-neck round-bottom flask equipped with a Teflon stir bar, reflux condenser, and thermocouple. The flask was heated under vacuum to 110°C at a rate of 500°C/h, then pumped and purged three times between N<sub>2</sub> and vacuum. It was subsequently heated to 150°C under N<sub>2</sub> where it was held for 2 h. After 0.5 h at 150°C, 1.2 mL octylamine was injected. Simultaneously, 17.9 mmol TOP (TOP:Cu molar ratio = 11:1) and 10.3 mmol TOPO were added

to a 100 mL three-neck round-bottom flask equipped with glass stir bar, reflux condenser, and thermocouple. The reaction flask was heated to 150°C under vacuum in which it was pumped and purged three times. It was held under vacuum and allowed to degas for 2 h. Afterwards, the reaction flask was switched to positive pressure under N<sub>2</sub> and heated to 370°C until the solution turned a pale greenish-yellow, indicating decomposition of TOP/TOPO. Upon decomposition, the contents of the Cu flask were rapidly injected via a gastight Luer-Lock syringe. The temperature typically dropped ~50-70°C following injection. The flask was allowed to regain temperature to 350°C, and the particles grew 1 – 5 mins. After the growth period, the reaction was quenched by removal of the heating mantle, allowing the mixture to cool to ~80°C. For “ambient” washing conditions, the particles were collected by dispersion of the reaction mixture in toluene then flocculation with ethanol. The mixture was centrifuged at 5800 rpm for 8 min, and then the supernatant was discarded. Nanoparticles were stored in hexanes. For “air-free” washing conditions, the same procedure as “ambient” was performed with the exception that the particles were washed and collected in a N<sub>2</sub> glovebox (O<sub>2</sub> < 0.1 ppm).

*Cu<sub>3</sub>P Product B (Phosphorization of Cu to Cu<sub>3</sub>P).* Followed all protocol for product A with the exception of TOP:Cu molar ratio = 5.6:1 (9 mmol TOP:1.6 mmol CuCl) and the TOPO amount was decreased to 5.2 mmol. Particles were washed under ambient conditions.

*Cu<sub>3</sub>P Nanoparticle Heat-up Synthesis.* Literature protocol developed by Liu et al.<sup>3</sup> was adapted for the formation of Cu<sub>3</sub>P by a scalable and cost-effective heat-up method. In a typical synthesis, 0.5 mmol CuCl<sub>2</sub>, 5.0 mmol HDA, 5.0 mmol TPOP (Cu:HDA:TPOP = 1:10:10), and 10 g ODE were added to a 50 mL three-neck round-bottomed flask equipped with glass stir bar, reflux condenser, and thermocouple. The reaction flask was degassed under N<sub>2</sub> at 150°C for 1 h. The solution was then heated to 300°C where it was held for 0.5 h. The reaction was cooled to 200°C

before removal of the heating mantle, then further cooled to  $\sim 80^{\circ}\text{C}$ . The particles were collected by dispersion of the reaction mixture in chloroform then flocculation with isopropanol. After 15 min of centrifugation at 5800 rpm, the supernatant was discarded. The washing procedure was repeated with a sonication step to aid dispersion in chloroform before addition of isopropanol. The mixture was centrifuged at 5800 rpm for 8 min, and then the supernatant was discarded. Nanoparticles were stored in hexanes.

*Cu<sub>3</sub>PSe<sub>4</sub> Nanoparticle Hot-Injection Synthesis (Reaction Pathway Cu<sub>3</sub>P + Se precursor).* The *Copper phosphide (Cu<sub>3</sub>P) Hot Injection Nanocrystal Synthesis* (see above) was appended to include Se injection. A Se precursor flask was prepared simultaneously with the preparation of the Cu flask. The Se precursors investigated were Se powder in OLA, Ph<sub>2</sub>Se<sub>2</sub> in OLA, and TOPSe (see Figure S4.3). The precursor Se powder required heating to  $180^{\circ}\text{C}$  to dissolve in OLA (0.2 M Se in OLA) to yield a clear, dark red solution with a yellowish-orange tint (prepared in 3-neck round-bottom flask equipped with a Teflon stir bar, reflux condenser, and thermocouple). The precursor Ph<sub>2</sub>Se<sub>2</sub> dissolves readily in OLA (0.36 M Ph<sub>2</sub>Se<sub>2</sub> in OLA) to yield a clear, yellow solution (prepared in scintillation vial). Sonication of stoichiometric amounts of Se powder in TOP yields a clear, colorless solution of TOPSe (prepared in scintillation vial). Molar ratios of Cu to Se precursors were stoichiometric. The Se flask was injected via gastight Luer-Lock syringe into the TOP/TOPO reaction flask at  $370^{\circ}\text{C}$  either before or after the injection of the Cu precursor. Growth times were generally between 0.5 – 1.5 h or until the solution turned black, indicating the formation of nanoparticles. After the growth period, the reaction was quenched by removal of the heating mantle, allowing the mixture to cool to  $\sim 80^{\circ}\text{C}$ . The particles were collected by dispersion of the reaction mixture in toluene then flocculation with ethanol. After 15 min of centrifugation at 5800 rpm, the supernatant was discarded. The washing procedure was repeated with a sonication step

to aid dispersion in toluene before addition of ethanol. The mixture was centrifuged at 5800 rpm for 8 min, and then the supernatant was discarded. Nanoparticles were stored in hexanes.

*Transformation of Cu<sub>3</sub>P to Cu<sub>3</sub>PSe<sub>4</sub> One-Pot, Heat-up Nanoparticle Synthesis (Reaction Pathway Cu<sub>3</sub>P + Se precursor).* Nanoparticles of Cu<sub>3</sub>P, as synthesized above, were initially dried over N<sub>2</sub> then finished drying under vacuum overnight in a 100 mL 3-neck round-bottom flask equipped with a glass stir bear, Liebig condenser, and thermocouple. Excess Se (1.07 mmol) and ODE (10.7 mL, 0.1 M dispersion Se/ODE) were then added to the flask. The flask was pumped and purged between vacuum and N<sub>2</sub> for three cycles, then heated to 150°C at a rate of 500°C/h under vacuum. The flask was switched to positive N<sub>2</sub> pressure and heated to 300°C where it was held for 20 min. The flask was then cooled to ~80°C by removal of the heating mantle to aid in the collection of the crude product. The particles were collected by dispersion of the reaction mixture in toluene then flocculation with ethanol. After 15 min of centrifugation at 5800 rpm, the supernatant was discarded. The washing procedure was repeated with a sonication step to aid dispersion in toluene before addition of ethanol. The mixture was centrifuged at 5800 rpm for 8 min, and then the supernatant was discarded. Nanoparticles were stored in hexanes.

#### **A.4. Materials Characterization**

*Diffraction.* Powder X-ray diffraction (PXRD) was performed on a Bruker D8 Discover DaVinci Powder X-ray Diffractometer equipped with Cu K $\alpha$  radiation ( $\lambda = 1.54 \text{ \AA}$ ). Samples were prepared by dispersing the nanoparticles in hexanes and then drop-casting onto a p-type boron doped Si Zero Diffraction Plate. The patterns were characterized by matching known PDF patterns in the PDF-4 database installed on the DIFFRAC.EVA software. The data was treated with the subtraction of K $\alpha$  peaks and the smoothing function of the software.

*Imaging.* High-resolution TEM images were obtained with a JEOL JEM 2100F TEM operated at an acceleration voltage of 200 keV. Semiquantitative elemental analysis of nanoparticles samples were performed with a JEOL JSM 6500F FE-SEM equipped with an EDAX Genesis energy dispersive spectroscopy detector. Samples were prepared by dipping carbon-coated gold TEM grids (200 mesh, Ted Pella) into dilute dispersions of nanoparticles in hexanes.

*X-ray Photoelectron Spectroscopy (XPS).* XPS was performed using a Physical Electronics ESCA 5800 system with a monochromatic Al K $\alpha$  (E = 1486.6 eV) X-ray source. The data was processed in CasaXPS. All spectra were shifted using the Cu 3s peak as the reference at 132.5 eV because it was expected to have minimal binding energy shifts in the presence of both organic and inorganic species. Typical spectra are shifted to adventitious carbon at 284.80 eV. However, the “ambient” and “air-free” carbon spectra showed different binding environments (Figure S8), so referencing adventitious carbon was not reliable for our experiments. “Ambient” samples were prepared by dropcasting directly onto the sample holder and transported to the XPS instrument inside a sealed container and transferred quickly. “Air-free” samples were prepared by drop-casting directly onto a custom-built air-free sample holder.<sup>4</sup> In this way, samples were only exposed to the N<sub>2</sub> glovebox (O<sub>2</sub> < 0.1 ppm, H<sub>2</sub>O < 0.1 ppm) and the XPS instrument vacuum chamber.

*Diffuse Reflectance.* Reflection measurements were performed on a Cary 5000 UV/vis/NIR spectrophotometer equipped with an integrating sphere diffuse reflectance accessory (DRA) (Internal DRA-2500) using the standard wide-open aperture. The samples were scanned at a rate of 10 nm/s with a 1.0 nm data interval, from 1100 to 400 nm, with a detector crossover at 800 nm. Nanoparticle samples were diluted with BaSO<sub>4</sub> and BaSO<sub>4</sub> was used as a reference. The spectra were treated with the Kubelka-Munk model to determine the optical absorption edges.

## A.5. Literature reports of $\text{Cu}_3\text{PSe}_4$

**Table S4.1.** Compilation of all known investigations of  $\text{Cu}_3\text{PSe}_4$  by computation.

<i>Ref.</i>	<i>DOI</i>	<i>Authors</i>	<i>Title</i>	<i>Journal</i>	<i>Year</i>	<i>Overview</i>
5	10.1063/1.3656760	D.H. Foster, V. Jieratum, R. Kykyneshi, D.A. Keszler, G. Schneider	Electronic and optical properties of potential solar absorber $\text{Cu}_3\text{PSe}_4$	Applied Physics Letters	2011	Electronic and optical properties via DFT with hybrid functionals (see below)
6	10.1002/aenm.201200538	L. Yu, R.S. Kokenyesi, D.A. Keszler, A. Zunger	Inverse Design of High Absorption Thin-Film Photovoltaic Materials	Advanced Energy Materials	2013	Materials screening based on intrinsic optoelectronic properties via $G_0W_0$ method on top of Heyd-Scuseria-Ernzerhof hybrid functional ( $G_0W_0@HSE06$ )
7	10.1063/1.4824770	T. Shi, W.-J. Yin, M. Al-Jassim, Y. Yan	Structural, electronic, and optical properties of $\text{Cu}_3\text{-V-VI}_4$ compound semiconductors	Applied Physics Letters	2013	Structural, electronic, and optical properties via DFT with hybrid functional
8	10.1103/PhysRevB.88.195201	D.H. Foster, F.L. Barras, J.M. Vielma, G. Schneider	Defect physics and electronic properties of $\text{Cu}_3\text{PSe}_4$	Physical Review B	2013	Thermodynamic stability, defect energies and concentrations, and material properties via generalized gradient approximation of DFT with Hubbard $U$ term ( $GGA+U$ )
9	10.1016/j.jpccs.2013.12.004	D.T. Do, S.D. Mahanti	Bonds, bands, and band gaps in tetrahedrally bonded ternary compounds: The role of group V lone pairs	Journal of Physics and Chemistry of Solids	2014	Band structures by HSE06, GGA, and $GGA+U$ methods
10	10.1016/j.mssp.2015.05.008	A. Slassi	Electronic structure and optical properties of $\text{Cu}_3\text{PX}_4$ ( $X = \text{S}$ and $\text{Se}$ ): Solar cell made of abundant materials	Materials Science in Semiconductor Processing	2015	Electronic structure and optical properties via full potential linearized augmented plane wave (FP-LAPW)
11	10.1063/1.4950818	Y. Zhang, Y. Wang, J. Zhang, L. Xi, P. Zhang, W. Zhang	Pinning down high-performance Cu-chalcogenides as thin-film solar cell absorbers: A successive screening approach	The Journal of Chemical Physics	2016	Materials screening via modified Becke-Johnson potential with an on-site Coulomb $U$ ( $mBJ+U$ )
12	10.1039/C6TC05510A	Z. Ma, J. Hu, R. Sa, Q. Li, Y. Zhang, K. Wu	Screening novel candidates for mid-IR nonlinear optical materials from $\text{I}_3\text{-V-VI}_4$ compounds	Journal of Materials Chemistry C	2017	Optical properties via projector augmented wave (PAW) method
13	10.1007/s11082-017-1004-9	A. Slassi, M. Hammi, O. El Rhazouani, M. Arejdal	Ab initio study of thermoelectric properties of $\text{Cu}_3\text{PSe}_4$ and $\text{Cu}_3\text{PS}_4$ : alternative materials for thermoelectric applications	Optical Quantum Electronics	2017	Thermoelectric properties via <i>ab initio</i> calculations

**Table S4.2.** Compilation of all known investigations of Cu<sub>3</sub>PSe<sub>4</sub> by traditional solid state.

<i>Ref.</i>	<i>DOI</i>	<i>Authors</i>	<i>Title</i>	<i>Journal</i>	<i>Year</i>	<i>Overview</i>
14	10.1107/S0567740872008568	J. Garin, E. Parthé	The crystal structure of Cu <sub>3</sub> PSe <sub>4</sub> and other ternary normal tetrahedral structure compounds with composition 1 <sub>3</sub> 5 <sub>6</sub> <sub>4</sub>	Acta Crystallographica Section B	1972	Bulk synthesis and crystal structure
15	10.1007/BF00617913	R. Ott, W. Klingen, H. Hahn	Zur Struktur des Cu <sub>3</sub> PSe <sub>4</sub>	Naturwissenschaften	1972	Crystal structure of bulk
16	10.1016/0040-6031(78)85028-X	M. Schulte-Kellinghaus, V. Krämer	Thermogravimetric investigations of some thioorthophosphates and thiohypodiphosphates	Thermochimica Acta	1978	Thermal stability
17	10.1016/0022-4596(83)90214-1	J.V. Marzik, A.K. Hsieh, K. Dwight, A. Wold	Photoelectronic properties of Cu <sub>3</sub> PS <sub>4</sub> and Cu <sub>3</sub> PS <sub>3</sub> Se single crystals	Journal of Solid State Chemistry	1983	Synthesis by chemical vapor transport
18	10.1016/0926-2040(92)90019-6	D. Lathrop, D. Franke, R. Maxwell, T. Tepe, R. Flesher, Z. Zhang, H. Eckert	Dipolar <sup>31</sup> P NMR Spectroscopy of crystalline inorganic phosphorus compounds	Solid State Nuclear Magnetic Resonance	1992	<sup>31</sup> P- <sup>31</sup> P coupling to elucidate distance distributions
19	10.1006/jssc.1994.1303	R.H.P. Francisco, H. Eckert	Compound formation and local structure in ternary metal-phosphorus-selenium systems	Journal of Solid State Chemistry	1994	<sup>31</sup> P MAS-NMR and XRD over compositional range of Cu-P-Se
20	10.1016/S0926-2040(03)00047-X	C.G. Canlas, R.B. Muthukumaran, M.G. Kanatzidis, D.P. Weliky	Investigation of longitudinal <sup>31</sup> P relaxation in metal selenophosphate compounds	Solid State Nuclear Magnetic Resonance	2003	Investigation of [PSe <sub>4</sub> ] <sup>3-</sup> building block
5	10.1063/1.3656760	D.H. Foster, V. Jieratum, R. Kykyneshi, D.A. Keszler, G. Schneider	Electronic and optical properties of potential solar absorber Cu <sub>3</sub> PSe <sub>4</sub>	Applied Physics Letters	2011	E <sub>g</sub> by diffuse reflectance (see above)
21	10.1039/C2TC00106C	V. Itthibenchapong, R.S. Kokenyesi, A.J. Ritenour, L.N. Zakharov, S.W. Boettcher, J.F. Wager, D.A. Keszler	Earth-abundant Cu-based chalcogenide semiconductors as photovoltaic absorbers	Journal of Materials Chemistry C	2013	Optical and electronic properties of pressed pellets, photoelectrochemical measurements of single crystals

## A.6. Investigation of Pathway Route (P-Se) + Cu

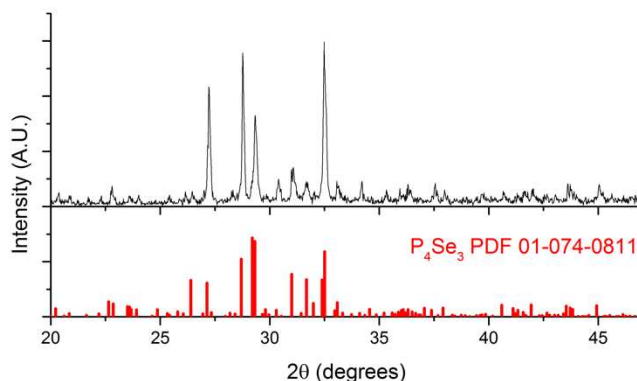


**Figure S4.1.** XRD pattern for  $P_4Se_3$  powder. Peaks were indexed to standard XRD pattern for  $P_4Se_3$ . Although the pattern appears to be of pure  $P_4Se_3$ , it is likely that there are some C and Se impurities. The compound  $P_4Se_3$  was of interest because it could aid in the correct connectivity required for the tetrahedral selenophosphate moiety in the target material. Bulk synthesis of  $Cu_3PSe_4$  was reported by Canlas et al.<sup>20</sup> in which stoichiometric amounts of copper metal,  $P_2Se_5$ , and elemental Se were reacted. The alternating phosphorus and selenium atoms observed in  $P_2Se_5$  is also observed in  $P_4Se_3$ . However, this also results in a high degree of covalency between atoms based on the minimal electronegativity difference between P and Se.

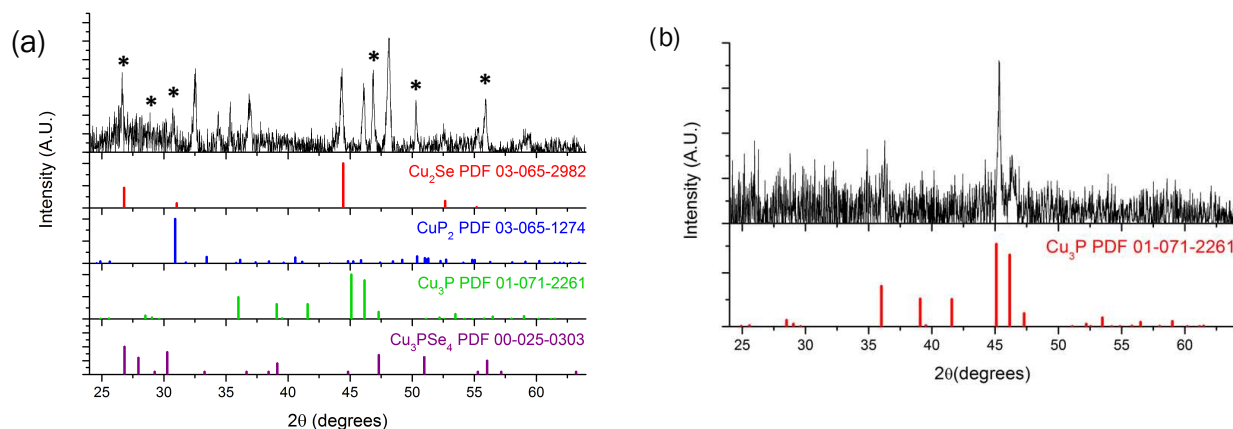


**Figure S4.2.** (a) XRD pattern of product synthesized from following reaction parameters: injection order of Cu precursor then  $P_4Se_3$ /OLA after 15 mins. ( $CuCl:P_4Se_3$  molar ratio = 1:1), injection temperature at  $370^\circ C$ , growth time of 0.5 h. Asterisk (\*) are the peaks that could be assigned to the  $Cu_3PSe_4$  phase. (b) XRD pattern of product from reproduced experiment. Reactions using  $P_4Se_3$  often resulted in amorphous products. Depending on the polymeric morphology  $P_4Se_3$  adopts, the  $T_g$  can range between  $75-190^\circ C$ , well below the temperatures required by these reactions.

## A.7. Investigation of Pathway Route (Cu-P) + Se

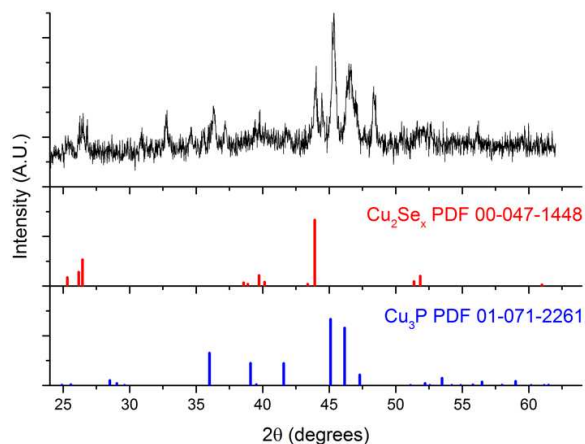


**Figure S4.3.** XRD pattern of the product synthesized from the following reaction parameters: injection order of Se/OLA then Cu precursor (CuCl:Se molar ratio = 3:4), injection temperature at 370°C, and 0.5 h growth time.

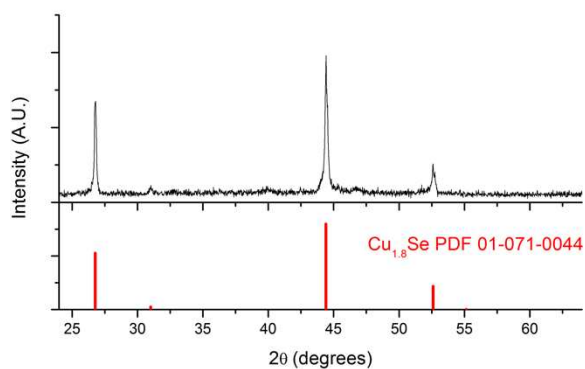


**Figure S4.4.** XRD pattern of the product synthesized from the following reaction parameters: injection order of  $\text{Ph}_2\text{Se}_2$ /OLA then Cu precursor (CuCl: $\text{Ph}_2\text{Se}_2$  molar ratio = 3:2), injection temperature at 370°C, and 0.5 h growth time.

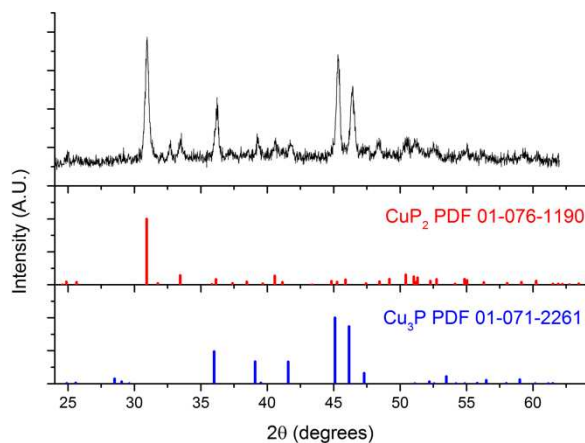


**Figure S4.5.** XRD pattern of the product synthesized from the following reaction parameters: injection order of TOPSe then Cu precursor (CuCl: TOPSe molar ratio = 3:4), injection temperature at 370°C, and 1.5 h growth time.

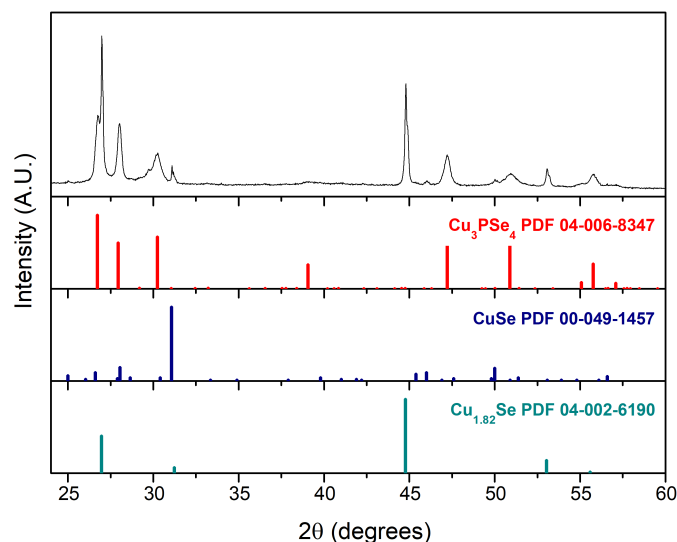


**Figure S4.6.** XRD pattern of  $\text{Cu}_3\text{P} + \text{Se/ODE}$  reaction pathway crude product.

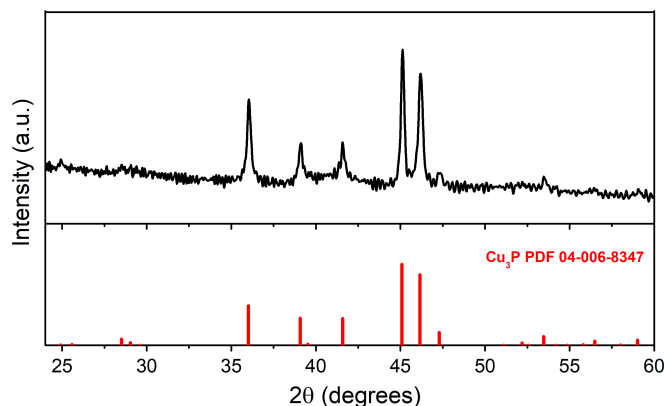


**Figure S4.7.** XRD pattern of  $\text{Cu}_3\text{P}$  NP sample used in both XPS studies (ambient and air-free washing).

**Table S4.3.** Summary of binding energies (BE) for Cu 2p XPS spectra of  $\text{Cu}_3\text{P}$  NPs washed in ambient or air-free conditions. See Figure 2 for Cu 2p XPS spectra.

<i>Conditions</i>	<i>Species</i>	<i>Cu 2p<sub>3/2</sub> (eV)</i>	<i>Cu 2p<sub>1/2</sub> (eV)</i>
Ambient washing	Cu(I) in $\text{Cu}_3\text{P}$	933.4	953.2
Ambient washing	Cu(II) in CuO	934.7	954.5
Ambient washing	Cu(II) satellite peaks	944.4	963.8
Air-free washing	Cu(I) in $\text{Cu}_3\text{P}$	933.9	953.7

To understand if the Cu(II) species in the  $\text{Cu}_3\text{P}$  NP sample washed in ambient conditions were indeed a result of oxidation from exposure to air, the workup of  $\text{Cu}_3\text{P}$  was done under an inert atmosphere ( $\text{O}_2 < 0.1$  ppm). The absence of satellite peaks in the resulting Cu 2p XPS data suggests no Cu(II) species were present (Figure 2b). However, even with the supposed prevention of Cu(II) species formation, the resulting products from this intermediate reagent contained Cu-Se binary impurities albeit with different stoichiometries. This suggests that the presence of Cu(II) species in the  $\text{Cu}_3\text{P}$  NPs worked up by the original “ambient” protocol does not influence the formation of Cu-Se impurities in the final transformation product.

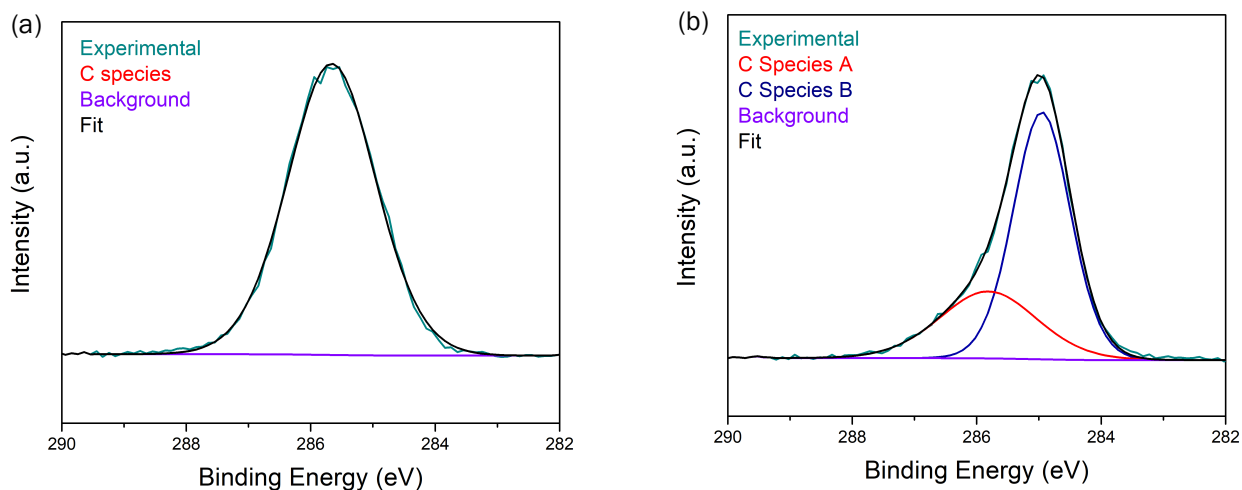


**Figure S4.8.** Carbon 1s XPS data of  $\text{Cu}_3\text{P}$  NP sample washed in (a) ambient and (b) air-free conditions.

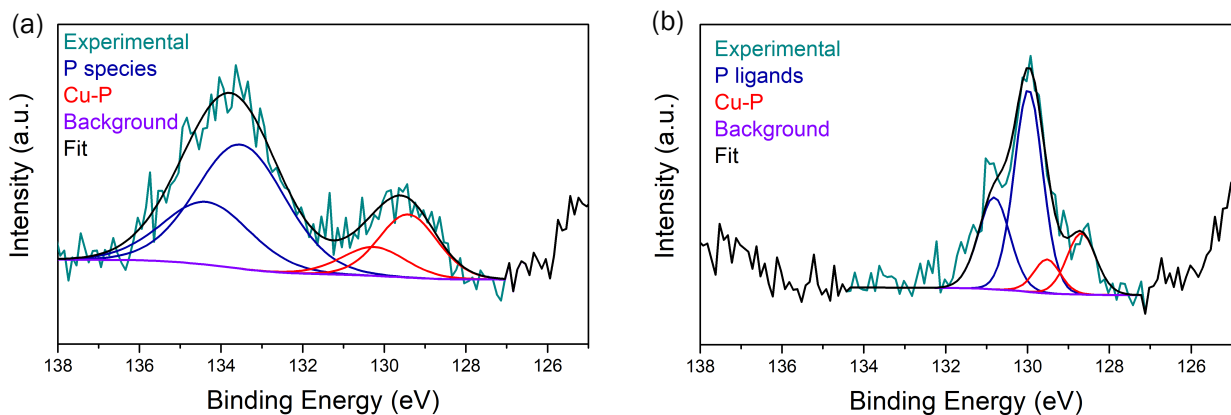


**Figure S4.9.** Phosphorus 2p XPS data of  $\text{Cu}_3\text{P}$  NP sample washed in (a) ambient and (b) air-free conditions. The higher binding environments in both spectra could be due to TOPO or TOP L-type ligands on the surface. The presence of phosphate from air could potentially account for the broadness of the higher binding environment peak observed in (a).

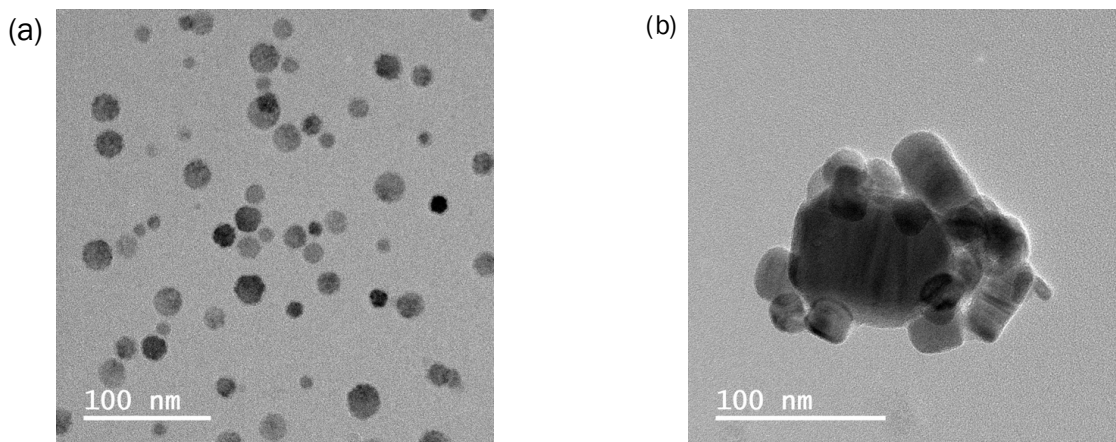


**Figure S4.10.** TEM images of (a)  $\text{Cu}_3\text{P}$  nanoparticles synthesized by hot injection with TOP:Cu molar ratio of 5.6:1 and (b) subsequently transformed  $\text{Cu}_3\text{PSe}_4$  synthesized by heat-up.

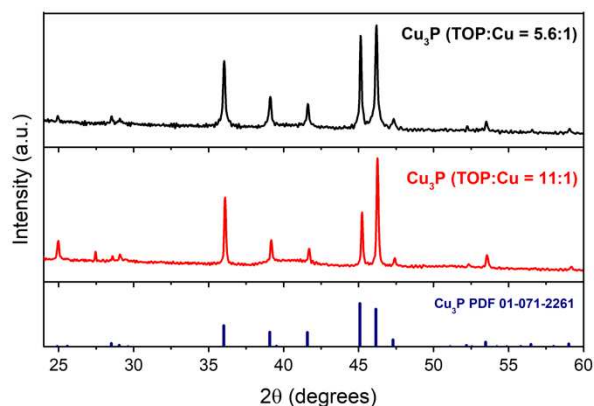
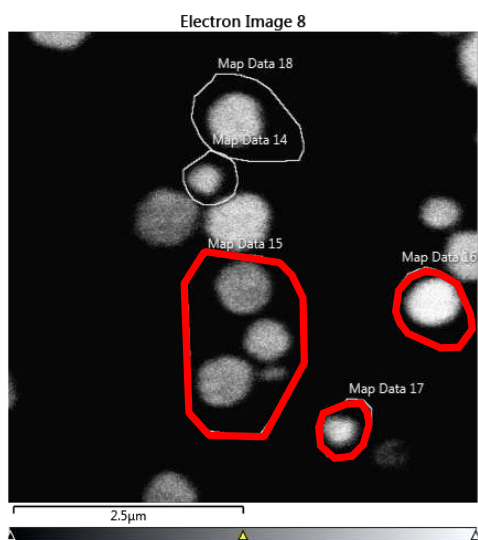


**Figure S4.11.** XRD pattern comparison of  $\text{Cu}_3\text{P}$  nanoparticle hot injection syntheses with different precursor molar ratios.



Map Data	Element	Atomic %
14	Cu	71.9
	P	28.1
15	Cu	86.6
	P	13.4
16	Cu	96.3
	P	3.7
17	Cu	100
	P	0
18	Cu	75.9
	P	24.1

**Figure S4.12.** STEM/EDS data of  $\text{Cu}_3\text{P}$  nanoparticles synthesized by hot injection with TOP:Cu molar ratio of 5.6:1. Highlighted in red are Cu-rich areas.

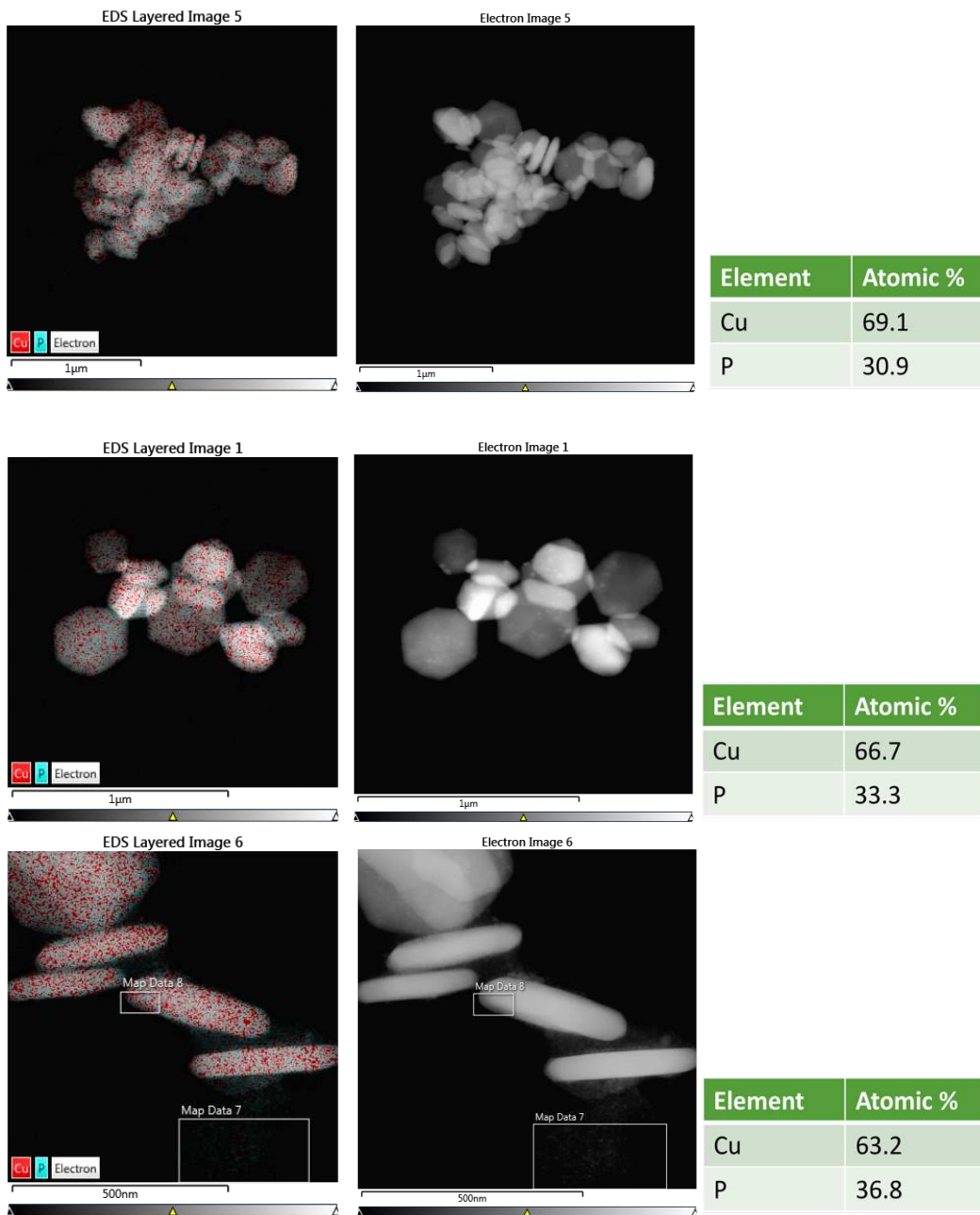


**Figure S4.13.** STEM/EDS data of different areas of Cu<sub>3</sub>P NP sample synthesized by hot injection with TOP:Cu molar ratio of 11:1.

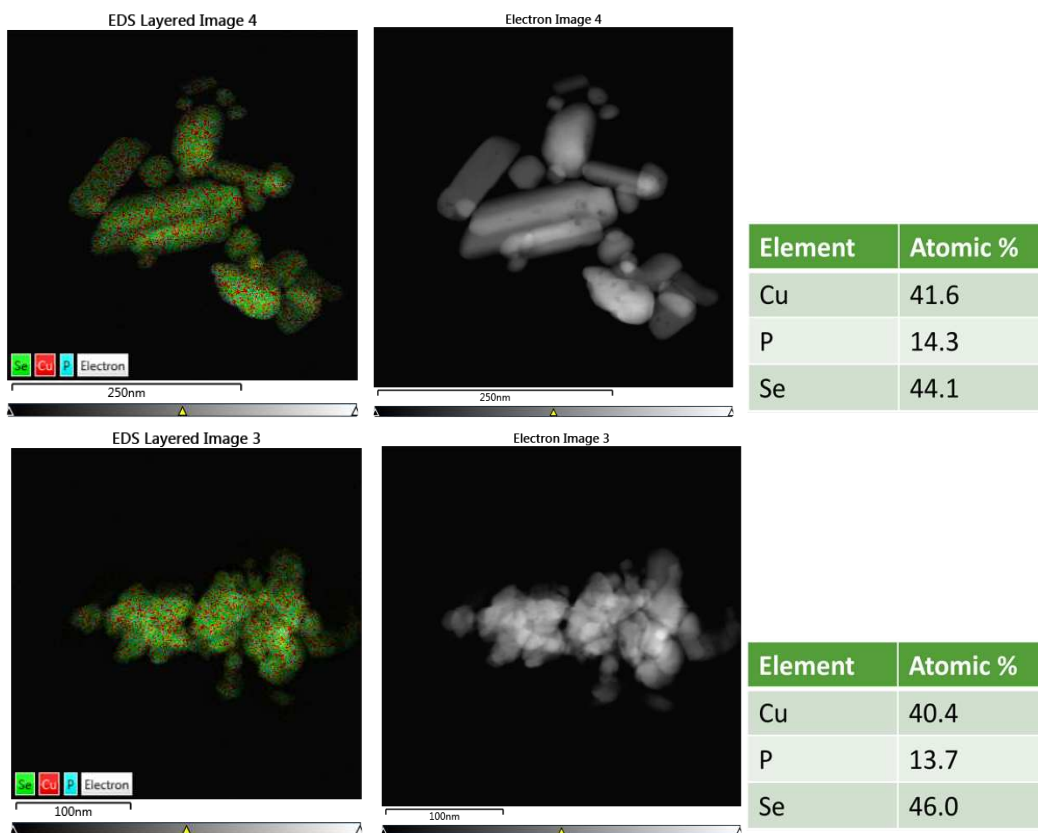


**Figure S4.14.** STEM/EDS data of different areas of  $\text{Cu}_3\text{PSe}_4$  sample made from  $\text{Cu}_3\text{P}$  NPs synthesized by hot injection (TOP:Cu molar ratio of 11:1).

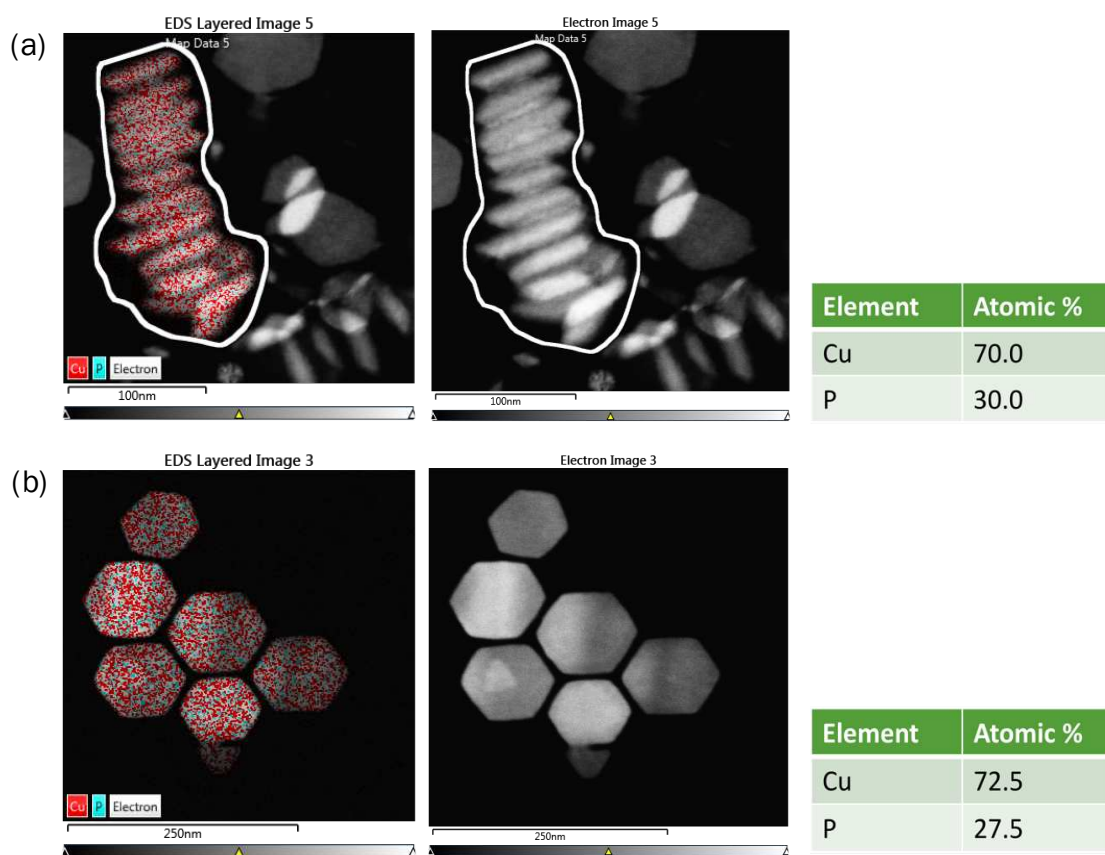


**Figure S4.15.** STEM/EDS data of  $\text{Cu}_3\text{P}$  NP samples synthesized by heat-up synthesis that are (a) stacked and (b) flat.

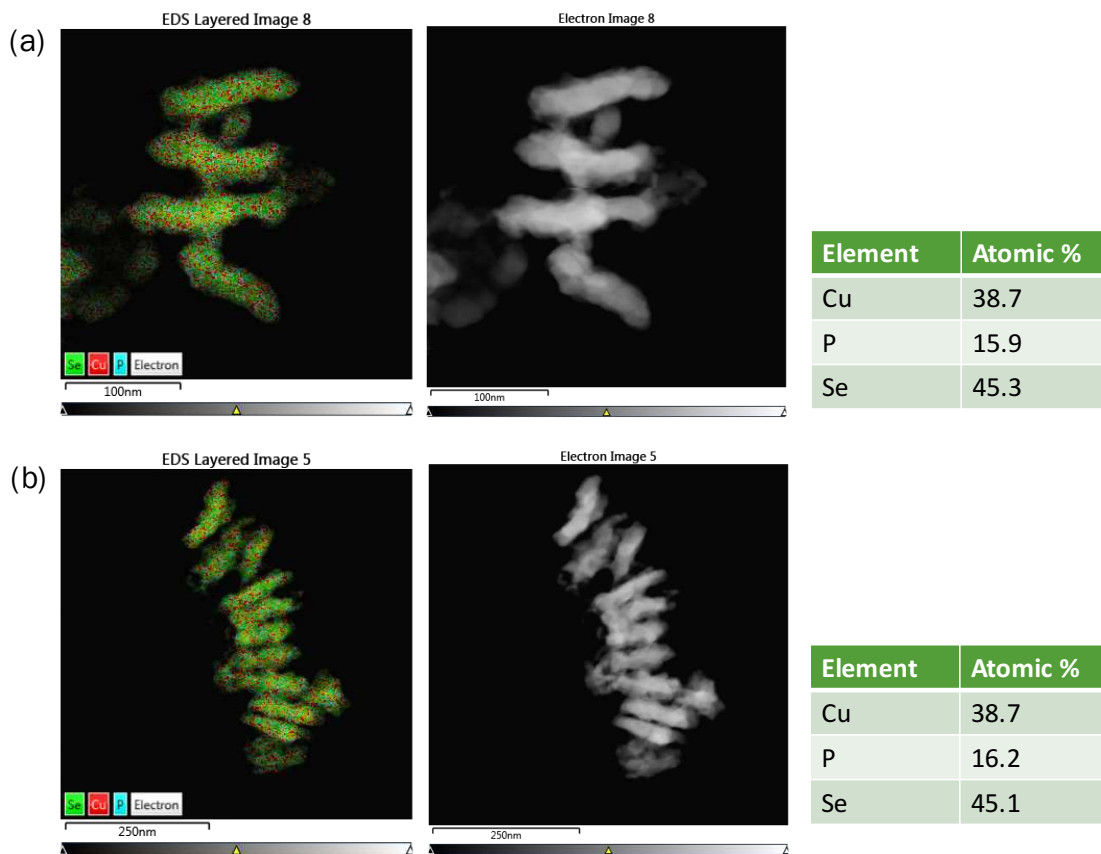


**Figure S4.16.** STEM/EDS data of different areas of Cu<sub>3</sub>PSe<sub>4</sub> sample made from Cu<sub>3</sub>P NPs synthesized by heat-up synthesis.

**Table S4.4.** Crystallographic data extracted from the Rietveld refinement of Cu<sub>3</sub>PSe<sub>4</sub> (space group: Pmn2<sub>1</sub>) NPs synthesized from heat-up Cu<sub>3</sub>P NPs

<i>Parameter</i>	<i>Refinement</i>	<i>Reference (ICSD Coll. Code 2856)</i>
Rwp	7.244%	N/A
Unit cell dimensions (Å)	<i>a</i> = 7.707	<i>a</i> = 7.697(2)
	<i>b</i> = 6.686	<i>b</i> = 6.661(2)
	<i>c</i> = 6.389	<i>c</i> = 6.381(2)
Volume (Å <sup>3</sup> )	329.22	327.15

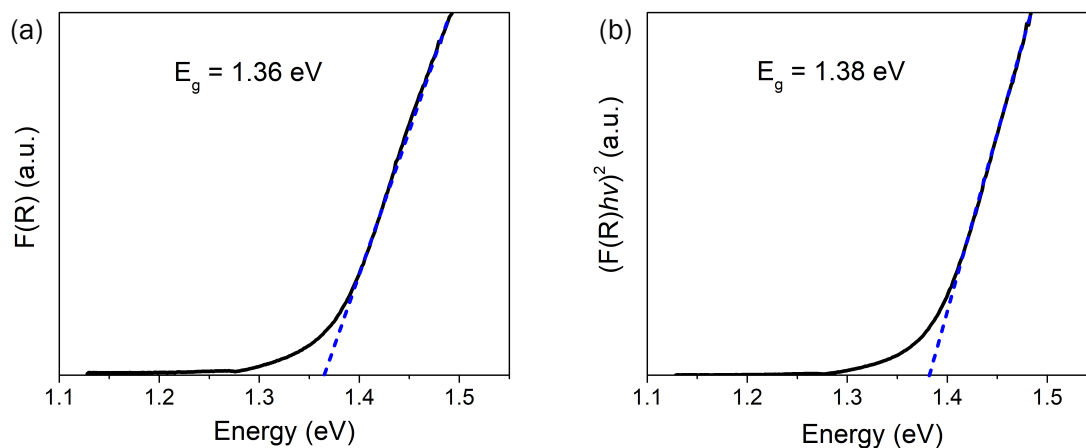


**Figure S4.17.** Diffuse reflectance spectra of  $\text{Cu}_3\text{PSe}_4$  nanoparticles (made from HU  $\text{Cu}_3\text{P}$  NPs) applied with the Kubelka-Munk (K-M) model to determine bandgap ( $E_g$ ) via extrapolation of the flat line (dashed blue line). (a) The raw data was plotted with the K-M function to yield an extrapolated  $E_g$  of 1.36 eV. (b) The data was treated with a modified K-M function to account for a direct allowed transition to yield an extrapolated  $E_g$  of 1.38 eV. Both measured  $E_g$  values are consistent with values found in literature (1.35 eV<sup>21</sup> and 1.40 eV<sup>5</sup>).

## REFERENCES

- (1) Irgolic, K.; Zingaro, R. A.; Kudchadker, M. The Synthesis of Tetraphosphorus Triselenide: Preliminary Infrared, Nuclear Magnetic Resonance, and Raman Studies. *Inorg. Chem.* **1965**, *4* (10), 1421–1423.
- (2) De Trizio, L.; Figuerola, A.; Manna, L.; Genovese, A.; George, C.; Brescia, R.; Saghi, Z.; Simonutti, R.; Van Huis, M.; Falqui, A. Size-Tunable, Hexagonal Plate-like Cu<sub>3</sub>P and Janus-like Cu–Cu<sub>3</sub>P Nanocrystals. *ACS Nano* **2012**, *6* (1), 32–41.
- (3) Liu, J.; Meyns, M.; Zhang, T.; Arbiol, J.; Cabot, A.; Shavel, A. Triphenyl Phosphite as the Phosphorus Source for the Scalable and Cost-Effective Production of Transition Metal Phosphides. *Chem. Mater.* **2018**, *30* (5), 1799–1807.
- (4) Schneider, J. D.; Agocs, D. B.; Prieto, A. L. Design of a Sample Transfer Holder to Enable Air-Free X-Ray Photoelectron Spectroscopy. *Chem. Mater.* **2020**, *32* (19), 8091–8096.
- (5) Foster, D. H.; Jieratum, V.; Kykyneshi, R.; Keszler, D. A.; Schneider, G. Electronic and Optical Properties of Potential Solar Absorber Cu<sub>3</sub>PSe<sub>4</sub>. *Appl. Phys. Lett.* **2011**, *99* (18), 181903.
- (6) Yu, L.; Kokenyesi, R. S.; Keszler, D. A.; Zunger, A. Inverse Design of High Absorption Thin-Film Photovoltaic Materials. *Adv. Energy Mater.* **2013**, *3* (1), 43–48.
- (7) Shi, T.; Yin, W.-J.; Al-Jassim, M.; Yan, Y. Structural, Electronic, and Optical Properties of Cu<sub>3</sub>-V-VI<sub>4</sub> Compound Semiconductors. *Appl. Phys. Lett.* **2013**, *103* (15), 152105.
- (8) Foster, D. H.; Barras, F. L.; Vielma, J. M.; Schneider, G. Defect Physics and Electronic Properties of Cu<sub>3</sub>PSe<sub>4</sub> from First Principles. *Phys. Rev. B* **2013**, *88* (19), 195201.
- (9) Do, D. T.; Mahanti, S. D. Bonds, Bands, and Band Gaps in Tetrahedrally Bonded Ternary Compounds: The Role of Group V Lone Pairs. *J. Phys. Chem. Solids* **2014**, *75* (4), 477–485.
- (10) Slassi, A. Electronic Structure and Optical Properties of Cu<sub>3</sub>PX<sub>4</sub>(X=S and Se): Solar Cell Made of Abundant Materials. *Mater. Sci. Semicond. Process.* **2015**, *39*, 217–222.
- (11) Zhang, Y.; Wang, Y.; Zhang, J.; Xi, L.; Zhang, P.; Zhang, W. Pinning down High-Performance Cu-Chalcogenides as Thin-Film Solar Cell Absorbers: A Successive Screening Approach. *J. Chem. Phys.* **2016**, *144* (19), 194706.
- (12) Ma, Z.; Hu, J.; Sa, R.; Li, Q.; Zhang, Y.; Wu, K. Screening Novel Candidates for Mid-IR Nonlinear Optical Materials from I<sub>3</sub>-V-VI<sub>4</sub> Compounds. *J. Mater. Chem. C* **2017**, *5* (8), 1963–1972.
- (13) Slassi, A.; Hammi, M.; El Rhazouani, O.; Arejda, M. Ab Initio Study of Thermoelectric Properties of Cu<sub>3</sub>PSe<sub>4</sub> and Cu<sub>3</sub>PS<sub>4</sub>: Alternative Materials for Thermoelectric Applications. *Opt. Quantum Electron.* **2017**, *49* (4), 171.
- (14) Garin, J.; Parthé, E. The Crystal Structure of Cu<sub>3</sub>PSe<sub>4</sub> and Other Ternary Normal Tetrahedral Structure Compounds with Composition I<sub>3</sub>S<sub>6</sub>. *Acta Crystallogr. Sect. B Struct. Crystallogr. Cryst. Chem.* **1972**, *28* (12), 3672–3674.
- (15) Ott, R.; Klingen, W.; Hahn, H. Zur Struktur Des Cu<sub>3</sub>PSe<sub>4</sub>. *Naturwissenschaften* **1972**, *59* (8), 364–364.
- (16) Schulte-Kellinghaus, M.; Krämer, V. Thermogravimetric Investigations of Some Thioorthophosphates and Thiohypodiphosphates. *Thermochim. Acta* **1978**, *27* (1–3), 141–

149.

- (17) Marzik, J. V.; Hsieh, A. K.; Dwight, K.; Wold, A. Photoelectronic Properties of  $\text{Cu}_3\text{PS}_4$  and  $\text{Cu}_3\text{PS}_3\text{Se}$  Single Crystals. *J. Solid State Chem.* **1983**, *49* (1), 43–50.
- (18) Lathrop, D.; Franke, D.; Maxwell, R.; Tepe, T.; Flesher, R.; Zhang, Z.; Eckert, H. Dipolar  $^{31}\text{P}$  NMR Spectroscopy of Crystalline Inorganic Phosphorus Compounds. *Solid State Nucl. Magn. Reson.* **1992**, *1* (2), 73–83.
- (19) Francisco, R. H. P.; Eckert, H. Compound Formation and Local Structure in Ternary Metal-Phosphorus-Selenium Systems. *J. Solid State Chem.* **1994**, *112* (2), 270–276.
- (20) Canlas, C. G.; Muthukumaran, R. B.; Kanatzidis, M. G.; Weliky, D. P. Investigation of Longitudinal  $^{31}\text{P}$  Relaxation in Metal Selenophosphate Compounds. *Solid State Nucl. Magn. Reson.* **2003**, *24* (2–3), 110–122.
- (21) Itthibenchapong, V.; Kokenyesi, R. S.; Ritenour, A. J.; Zakharov, L. N.; Boettcher, S. W.; Wager, J. F.; Keszler, D. A. Earth-Abundant Cu-Based Chalcogenide Semiconductors as Photovoltaic Absorbers. *J. Mater. Chem. C* **2013**, *1* (4), 657–662.

## APPENDIX B

### CHAPTER 5 SUPPORTING INFORMATION

#### **Molecular-Level Design Principles for the Colloidal Nanoparticle Synthesis of Copper Selenophosphate, $\text{Cu}_3\text{PSe}_4$ : Probing Selenium Precursor Evolution and Delivery**

##### **B.1. Experimental**

*Materials and Methods.* All reactions were performed under inert atmosphere unless noted. All workup was done on the benchtop in ambient conditions unless noted. Copper (II) chloride ( $\text{CuCl}_2$ , Riedel-de Haën, 97%), trioctylphosphine oxide (TOPO, Aldrich, 99%), triphenyl phosphite (TPOP, Oakwood Chemical, 97%), hexadecylamine (HDA, Aldrich, 90%), and selenium powder (Se, Strem Chemicals Inc., 99.99%) were purchased and used as received. A lecture bottle of hydrogen selenide ( $\text{H}_2\text{Se}$ , Solketric Chemicals Inc., UHP Grade) was used as received. Technical grade toluene, hexanes, ethanol, isopropanol, and chloroform were obtained from Fisher Scientific. 1-Octadecene (ODE, Aldrich, 90%) was sparged with  $\text{N}_2$  for 2 h before use.

*$\text{Cu}_3\text{P}$  Nanoparticle Heat-up Synthesis.* Literature protocol developed by Liu et al.<sup>1</sup> was adapted for the formation of  $\text{Cu}_3\text{P}$ . In a typical synthesis, 0.5 mmol  $\text{CuCl}_2$ , 5.0 mmol HDA, 5.0 mmol TPOP (Cu:HDA:TPOP = 1:10:10), and 10 g ODE were added to a 50 mL three-neck round-bottomed flask equipped with glass stir bar, reflux condenser, and thermocouple. The reaction flask was degassed under  $\text{N}_2$  at 150°C for 1 h. The solution was then heated to 300°C where it was held for 0.5 h. The reaction was cooled to 200°C before removal of the heating mantle, then further cooled to ~80°C. The particles were collected by dispersion of the reaction mixture in chloroform then flocculation with isopropanol. After 15 min of centrifugation at 5800 rpm, the supernatant was discarded. The washing procedure was repeated with a sonication step to aid dispersion in

chloroform before addition of isopropanol. The mixture was centrifuged at 5800 rpm for 8 min, and then the supernatant was discarded. Nanoparticles were stored in hexanes.

*Transformation of Cu<sub>3</sub>P to Cu<sub>3</sub>PSe<sub>4</sub> One-Pot, Heat-up Nanoparticle Synthesis.* Nanoparticles of Cu<sub>3</sub>P, as synthesized above, were initially dried over N<sub>2</sub> then finished drying under vacuum overnight in a 100 mL 3-neck round-bottom flask equipped with a glass stir bar, Liebig condenser, and thermocouple. Excess Se (1.07 mmol) and ODE (10.7 mL, 0.1 M dispersion Se/ODE) were then added to the flask. The flask was pumped and purged between vacuum and N<sub>2</sub> for three cycles, then heated to 150 °C at a rate of 500 °C/h under vacuum. The flask was switched to positive N<sub>2</sub> pressure and heated to 300 °C where it was held for 20 min.\* The flask was then cooled to ~80°C by removal of the heating mantle. The particles were collected by dispersion of the reaction mixture in toluene then flocculation with ethanol. After 15 min of centrifugation at 5800 rpm, the supernatant was discarded. The washing procedure was repeated with a sonication step to aid dispersion in toluene before addition of ethanol. The mixture was centrifuged at 5800 rpm for 8 min, and then the supernatant was discarded. Nanoparticles were stored in hexanes.

\* For the synthesis of Cu<sub>3</sub>PSe<sub>4</sub> by “Bullen et al. conditions”, the flask was instead heated to 180°C at a rate of 500°C/h and held for 5 h or overnight.

*Control Experiments of Individual Reagent Behavior in ODE.* Control experiments included (1) ODE (tech grade), (2) ODE+Se, and (3) ODE+Cu<sub>3</sub>P. All samples were subjected to the reaction conditions for Cu<sub>3</sub>PSe<sub>4</sub> synthesis (see above). Samples collected after the reaction (20 min at 300 °C) and after cooling were characterized by <sup>1</sup>H NMR, IR, and XRD (when applicable). The <sup>1</sup>H NMR signal distinct for poly(ODE) (1.20 ppm) overlaps with that ODE (~1.26 ppm), so it is visually impossible to separate these signals. Upon cooling, all samples were washed with acetone and centrifuged to isolate and detect the possible presence of poly(ODE).<sup>2</sup>

*Solvent Role Investigation on the Reaction Pathway Toward Cu<sub>3</sub>PSe<sub>4</sub>.* Synthesis of the Cu<sub>3</sub>PSe<sub>4</sub> nanoparticles was followed with the exception of the solvent identity (i.e. squalane, HDA, TOPO, neat). The molarity 0.1 M Se/solvent was maintained unless the solvent is a solid at room temperature in which 0.1 mol/g was used.

*Cannula Transfer.* A 100 mL 3-neck round-bottom flask equipped with a glass stir bar, Liebig condenser, and thermocouple was charged with Se (1.07 mmol) and 10.7 mL ODE. Similarly equipped, a 50 mL 3-neck round-bottom flask was charged with Cu<sub>3</sub>P nanoparticles (~20 mg) and 10.7 mL ODE. Both flasks were pumped and purged between vacuum and N<sub>2</sub> for three cycles, then heated to 150°C at a rate of 500°C/h under vacuum. The flasks were switched to positive N<sub>2</sub> pressure and heated to 300°C. At 300°C, a cannula purged with N<sub>2</sub> was connected from the headspace of the Se/ODE flask to the dispersion of the Cu<sub>3</sub>P/ODE flask. A bubbler was attached to the Cu<sub>3</sub>P/ODE flask and the N<sub>2</sub> port to Cu<sub>3</sub>P/ODE was closed. Aliquots of the reaction were removed by a glass Luer-lock syringe at relevant time points into scintillation vials. Samples were centrifuged, and the solution was decanted. The isolated precipitate was washed with toluene and ethanol similarly to the washing procedure described above and stored in hexanes.

*Direct Addition of H<sub>2</sub>Se.* [Caution: The gaseous compound H<sub>2</sub>Se is highly toxic and should be used with proper handling and care.] A 50 mL 3-neck round-bottom flask was charged with Cu<sub>3</sub>P nanoparticles (~20 mg) and 10.7 mL ODE. The flask was pumped and purged between vacuum and N<sub>2</sub> for three cycles, then heated to 150°C at a rate of 500°C/h under vacuum. The flask was switched to positive N<sub>2</sub> pressure and heated to 300°C at which point, the H<sub>2</sub>Se lecture bottle was connected to the reaction flask by needle. The tank was opened for 10 min, then closed, and the reaction was allowed to react for an additional 10 min. Aliquots of the reaction were removed by a glass Luer-lock syringe at relevant time points into scintillation vials. Samples were centrifuged,

and the solution was decanted for characterization. The isolated precipitate was washed with toluene and ethanol similarly to the washing procedure described above and stored in hexanes.

*Synthesis of Ag-P-Se.* The protocol for the transformation of  $\text{Cu}_3\text{P}$  to  $\text{Cu}_3\text{PSe}_4$  and subsequent isolation was adapted for the synthesis of Ag-P-Se NPs. Literature protocol developed by Henkes et al.<sup>3</sup> was adapted for the formation of  $\text{AgP}_2$  NPs.

*Computational Methods.* Computation was completed by Justin P. Joyce of the Shores/Rappé at Colorado State University, and the methods are described in the discussion.

## **B.2. Materials Characterization**

*Diffraction.* Powder X-ray diffraction (PXRD) was performed on a Bruker D8 Discover DaVinci Powder X-ray Diffractometer equipped with  $\text{Cu K}\alpha$  radiation ( $\lambda = 1.54 \text{ \AA}$ ). Samples were prepared by dispersing the nanoparticles in hexanes and then drop-casting onto a p-type boron doped Si Zero Diffraction Plate. The patterns were characterized by matching known PDF patterns in the PDF-4 database installed on the DIFFRAC.EVA software. The data was treated with the subtraction of  $\text{K}\alpha$  peaks and the smoothing function of the software.

*Imaging.* High-resolution TEM images were obtained with a JEOL JEM 2100F TEM operated at an acceleration voltage of 200 keV. Semiquantitative elemental analysis of nanoparticles samples were performed with an Oxford X-Max 80  $\text{mm}^2$  detector and analyzed with AZtecTEM software. Samples were prepared by dipping carbon-coated gold TEM grids (200 mesh, Ted Pella) into dilute dispersions of nanoparticles in hexanes. SEM images were obtained with a JEOL JSM-6500F microscope courtesy of Jacob Schneider from the Prieto group at Colorado State University. Samples were prepared by casting powder onto conductive carbon tape on an aluminum stub.

*Magnetic Resonance.* Solution-based  $^1\text{H}$  NMR spectroscopy was performed on an Agilent (Varian) 400MR equipped with automated tuning. Samples were dissolved in  $\text{CDCl}_3$  as reference. The deuterated solvent  $\text{CDCl}_3$  was dried over activated 4Å molecular sieves. The data was processed in MestReNova, and all spectra were shifted to 7.24 ppm for  $\text{CDCl}_3$ .

*Optical Spectroscopy.* Fourier transform infrared (FTIR) spectra were collected using a Thermo Scientific Nicolet 380 instrument with an attenuated total reflectance (ATR) attachment of ZnSe.

*Mass Spectrometry.* Gas chromatography-mass spectrometry (GC-MS) was performed on an Agilent 5973N Mass Selective Detector interfaced to a 6890 gas chromatograph using a positive electron ionization (EI) source. The GC-MS column used was Stabilwax with a length of 30 m, inner diameter (ID) of 0.25 mm, and film thickness ( $d_f$ ) of 0.25  $\mu\text{m}$ . Solid-phase microextraction (SPME) was performed with a StableFlex fiber (divinylbenzene/Carboxen/polydimethylsiloxane, DVB/CAR/PDMS) to sample the gaseous headspace of the reaction flasks. The fiber was exposed to the samples for 10 min. Liquid samples (1.0  $\mu\text{L}$ ) were collected after reaction completion and were injected directly and heated to a maximum temperature of 325°C before data collection with a flow rate of 1.0 mL/min. All possible judicious permutations of the species were scanned with “combination\_with\_replacement” from “itertools” in Python to identify mass spectrum fragmentations. The considered input values are summarized in the following table.

**Table S5.1.** Potential species that contribute to the mass spectra fragmentations

<i>Species</i>	<i>Molar Mass (g/mol)</i>	<i>Input Value</i>
$\text{H}_2$	2.02	2
1-octadecene (ODE, $\text{C}_{18}\text{H}_{36}$ )	252.49	252
ODE dimer	504.97	504
Se, $\text{Se}_8$	78.97, 631.76	79, 632
Toluene ( $\text{C}_7\text{H}_8$ )	92.14	92
Ethanol ( $\text{C}_2\text{H}_5\text{OH}$ )	46.07	46
$\text{Cu}_3\text{P}$ unit	221.61	221
$\text{Cu}_3\text{PSe}_4$ unit	537.5	537

### B.3. Control Reactions for the Indirect Characterization of Active Se Monomers

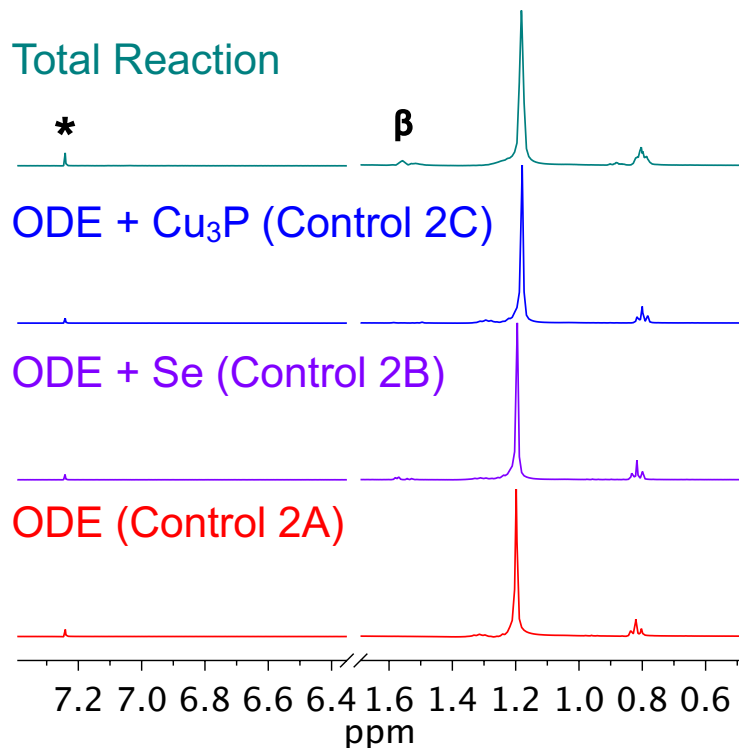


**Figure S5.1.** Poly(ODE) investigation via <sup>1</sup>H NMR spectra of Controls 2A-C and the total reaction solutions. Samples were heated to 300 °C for 20 min and allowed to cool before washing with acetone.<sup>2</sup> The major distinguishing peak for poly(ODE) is at 1.19 ppm which can be difficult to deconvolute from the tech grade ODE distinguishing peaks. Asterisk (\*) is the CDCl<sub>3</sub> reference signal at 7.24 ppm. The peaks labelled with beta (β) denote trace amounts of H<sub>2</sub>O.

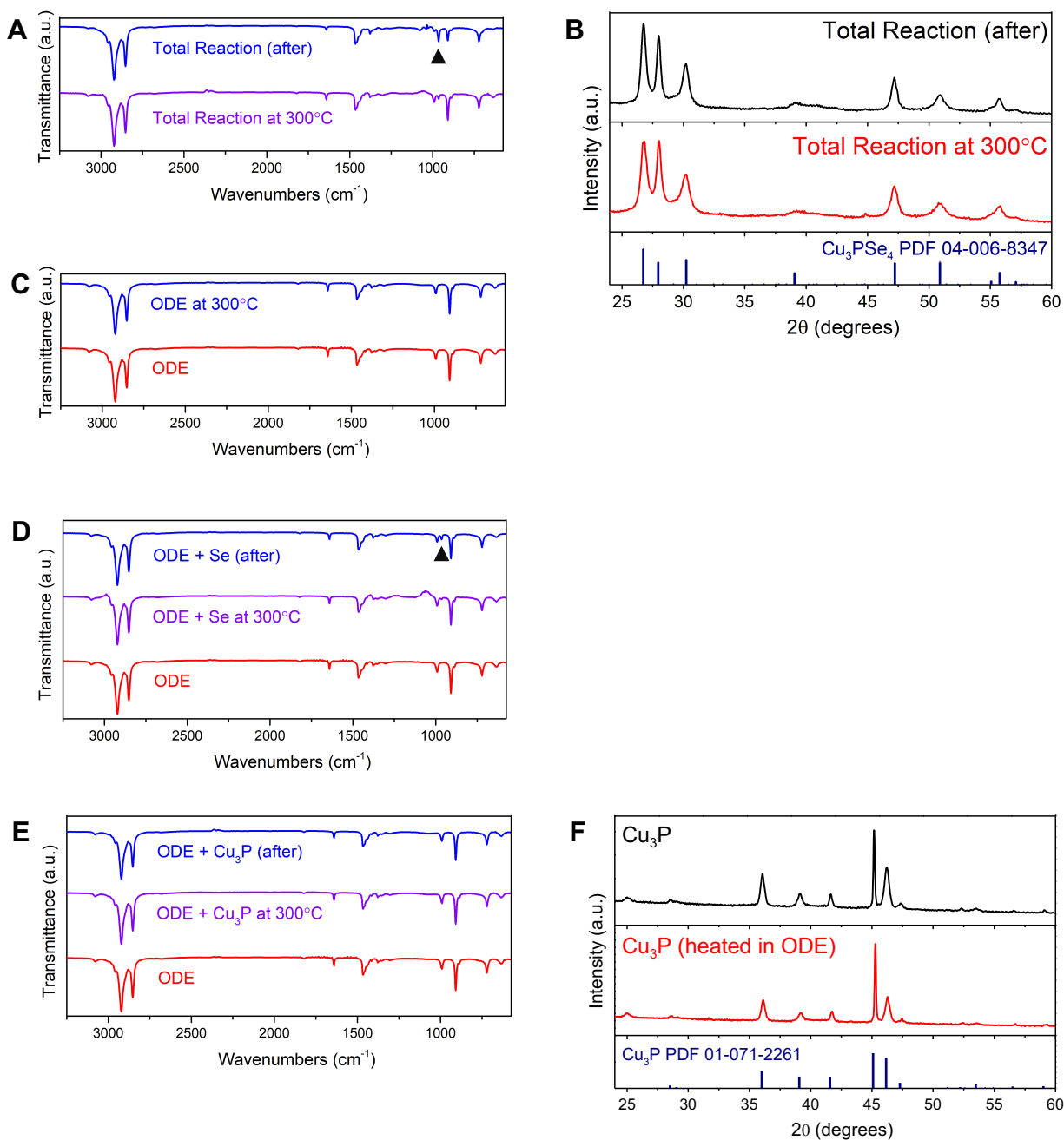


**Figure S5.2.** (A) IR spectra of the total reaction solution at 300 °C and after cooling. Solutions of the controls (C) ODE, Control 2A, (D) ODE and Se powder, Control 2B, and (E) ODE and Cu<sub>3</sub>P NPs, Control 2C, were characterized IR at room temperature, at 300 °C, and after cooling to room temperature. The peaks labelled with a triangle in (A) and (D) represents a strong C-H alkene bend at 976.18 cm<sup>-1</sup>, unique from the primary alkene on 1-ODE. The solid products of (B) the total reaction and (F) Control 2C were characterized by XRD.

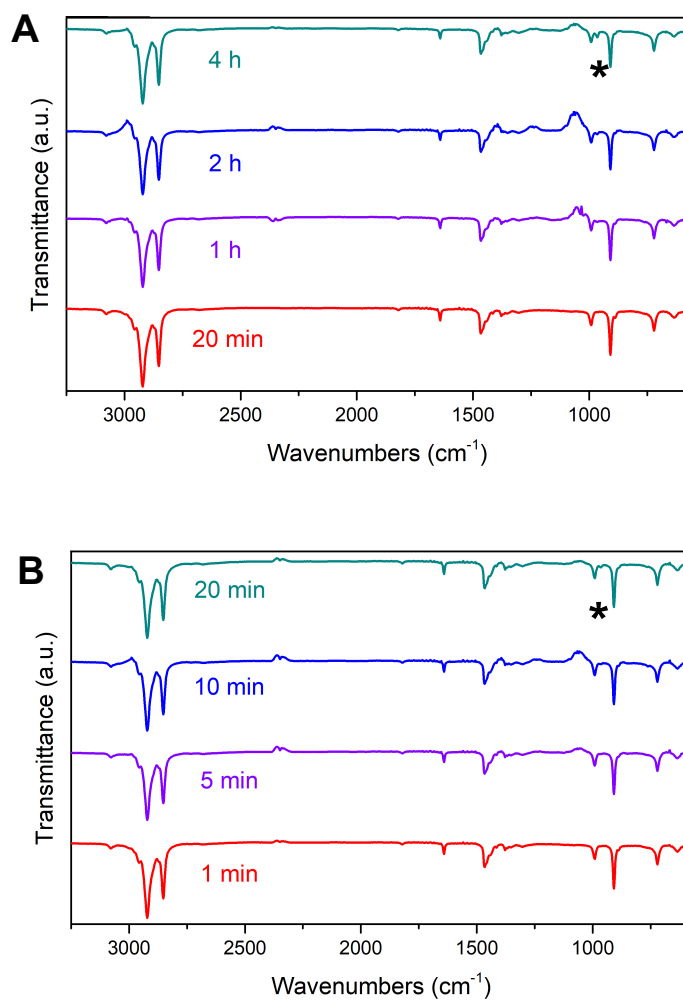


**Figure S5.3.** IR characterization of the reaction solution temporal aliquots for (A) *Indirect A* (Cu<sub>3</sub>P + Se/ODE headspace) and (B) *Indirect B* (Cu<sub>3</sub>P + H<sub>2</sub>Se).

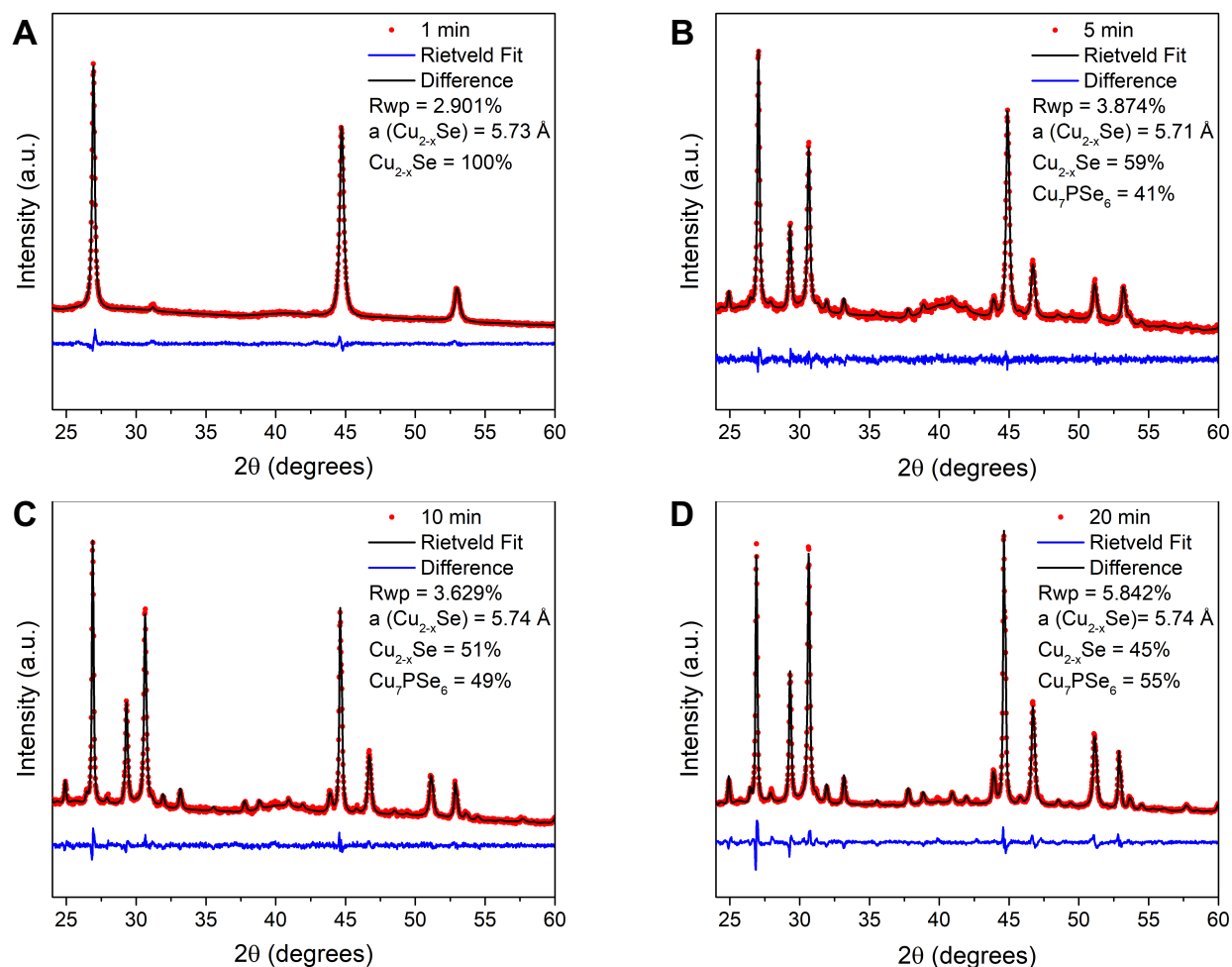


**Figure S5.4.** XRD pattern of  $\text{Cu}_3\text{P} + \text{H}_2\text{Se}$  reaction product analysed using the Rietveld method implemented in TOPAS v6 (Bruker AXS). The fitted parameters were limited to profile terms, background terms, and unit cell descriptions. The subtle peak shifts associated with the  $\text{Cu}_{2-x}\text{Se}$  phase are due to lattice parameter contractions (peaks move right in  $2\theta$ ) and expansions (peaks move left in  $2\theta$ ) as a result of Cu leaving and entering the crystal structure, confirmed by lattice parameter refinements. Refinements also indicated the increased growth of ternary product over time. All peaks were indexed to a  $\text{Cu}_7\text{PSe}_6$  reference (ICSD Coll. Code 280374) and to a  $\text{Cu}_{2-x}\text{Se}$  reference (ICSD Coll. Code 150758), and a good fit was observed.

#### **B.4. Identifying the Reaction Pathway of Cu<sub>3</sub>P to Cu<sub>3</sub>PSe<sub>4</sub> as Thermodynamic or Kinetic**

The high temperature of 300 °C for the standard reaction conditions was originally motivated to encourage H<sub>2</sub>Se production. However, if H<sub>2</sub>Se is not necessarily the sole active species, if at all, perhaps the Se/ODE reaction conditions optimized by Bullen et al. (5 h at 180 °C)<sup>4</sup> are sufficient to yield the target ternary. According to the authors' data, the reaction parameters of 5 h at 180 °C presumably does not generate H<sub>2</sub>Se until after 5 h and/or temperatures above 180 °C.<sup>4</sup>

A one-pot synthesis of Cu<sub>3</sub>P, Se, and ODE at these reaction conditions yielded Cu<sub>0.87</sub>Se (Figure S5.5A), supporting the importance of speciation on the sensitivity of this reaction. Alternatively, however, it is important to consider that Cu<sub>0.87</sub>Se could be an intermediate or a thermodynamic sink in the reaction landscape that leads to the synthesis of Cu<sub>3</sub>PSe<sub>4</sub>. This provides a unique opportunity to probe if the pathway is kinetic or thermodynamic.<sup>5,6</sup> Perhaps we are unable to synthesize the ternary at 180 °C for 5 h because the reaction required a longer time to overcome an activation barrier from the Cu<sub>0.87</sub>Se to the final product Cu<sub>3</sub>PSe<sub>4</sub> (thermodynamically controlled pathway). On the other hand, the appropriate conditions could be required to access species that lower the activation barrier and drive the reaction route to the ternary (kinetically controlled pathway). The reaction was held at 180 °C for 24 h (Figure S5.5B). It is important to note that because the chalcogenide speciation of the reaction evolves as time progresses, mainly evolution of H<sub>2</sub>Se, these proposed thermodynamic and kinetic pathways are simplistic.

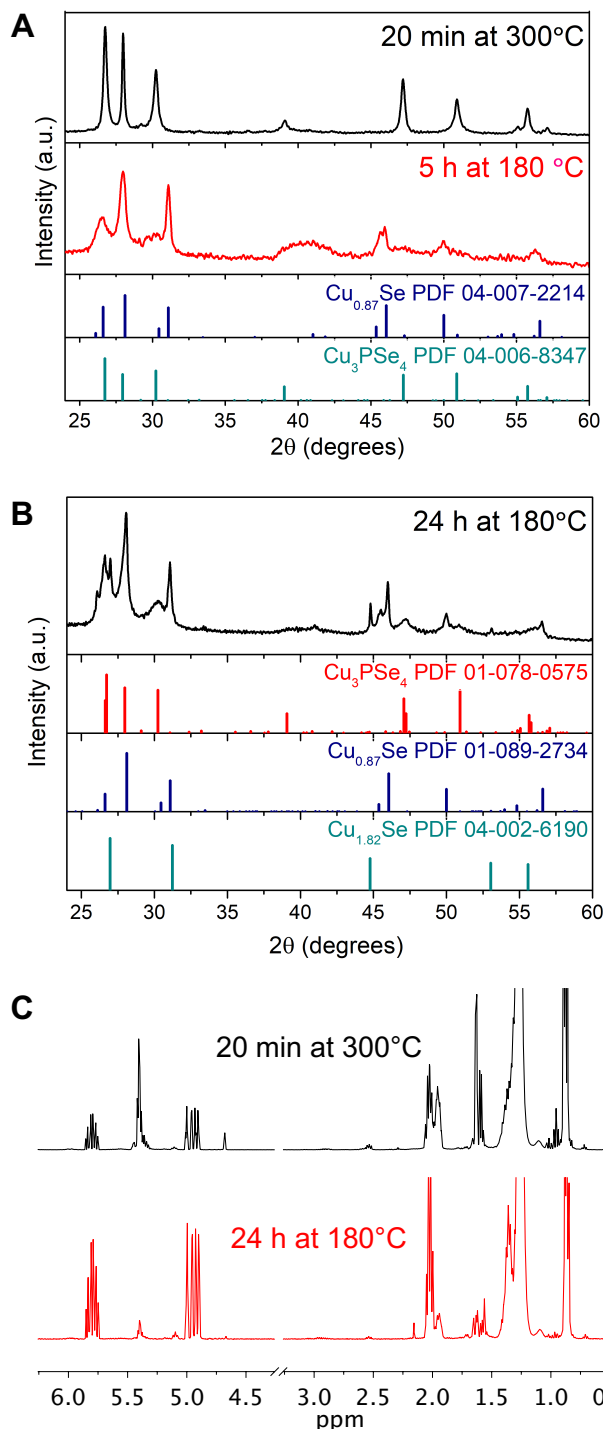


**Figure S5.5.** (A) XRD patterns of the product synthesized from standard conditions (20 min at 300 °C) and the product synthesized from Bullen et al.'s optimized Se/ODE conditions (5 h at 180 °C). Optimized Se/ODE conditions yielded  $\text{Cu}_{0.87}\text{Se}$  and no ternary product. (B) XRD pattern of the reaction product synthesized by exaggerated Bullen et al. conditions (180 °C for 24 h). (C)  $^1\text{H}$  NMR spectra comparisons of the end reaction solutions as a result of different reaction parameters: 20 min at 300 °C (total reaction) vs. 24 h at 180 °C (exaggerated Bullen et al. conditions).

The XRD data demonstrates that the pathway towards  $\text{Cu}_3\text{PSe}_4$  is indeed accessible after a long time. The reaction was also noted by the presence of  $\text{Cu}_{0.87}\text{Se}$ , demonstrating it could be an intermediate toward the synthesis of the ternary and that the reaction did not meet completion. However, the additional formation of a  $\text{Cu}_{2-x}\text{Se}$  phase suggests the speciation between the two reaction conditions (180 °C for 24 h and 300 °C for 20 min) are still quite varied. Indeed, differences were observed between the  $^1\text{H}$  NMR spectra of the remaining reaction solutions after the NPs were centrifuged away (Figure S5.5C). For the 24 h sample, the multiplet at 5.40 ppm (corresponding to the alkene protons on  $\text{SeR}_2$ ) was less intense but broader relative to the signals for ODE than in the 20 min sample. Thus, not only was less  $\text{SeR}_2$  present, the R-groups could be polymerized or  $\text{SeR}_2$  underwent vulcanization in which bridging chalcogenide chains formed between the monolefins.<sup>4</sup> Further, the associated 1.61 ppm signal (corresponding to protons adjacent to Se on  $\text{SeR}_2$ ) is correspondingly less intense and broader. However, the sharpness of the peak at 1.36 ppm in the 24 h sample is more reminiscent of tech. grade ODE than in the 20 min sample in which the same peak is broad, suggesting that ODE is oligomerized but distinct from poly(ODE) which resonates at 1.19 ppm. There is a peak at 2.15 ppm for the 24 h sample that is not present in the 20 min sample, and a peak at 4.62 ppm in the 20 min sample that is not present in the 24 h sample.

All in all, running the reaction at 180 °C showed that  $\text{Cu}_{1-x}\text{Se}$  is a potential intermediate toward  $\text{Cu}_3\text{PSe}_4$  and specific conditions are required to synthesize phase-pure  $\text{Cu}_3\text{PSe}_4$ . Running the reaction at 180 °C for 24 h did produce  $\text{Cu}_3\text{PSe}_4$ , suggesting there could've been a thermodynamic barrier not overcome at a lower temperature, but it could have also been due to the varied speciation as observed by  $^1\text{H}$  NMR and XRD. Ultimately, varied speciation of molecular species in solution leads toward different reaction pathways.

## B.5. Direct Characterization of Se Monomers via Mass Spectrometry

Mass spectrometry was used to not only probe for the ODE dimer but also as a complementary technique to capture/deconvolute as many other hydrocarbon and chalcogenide species as possible. Preliminarily, GC-MS by solid phase microextraction (SPME) was performed on samples extracted from the reaction headspace only at 300 °C to detect gaseous and colorless Se monomers that evolve when Se powder dissolves in ODE. The incorporated use of SPME resolved more peaks due its increased ability to adsorb more species as compared to traditional GC-MS sampling methods. Results showed mass/charge ( $m/z$ ) ratios that likely corresponded to  $H_2Se$  fragmentation, suggesting that  $H_2Se$  was present as a species in the reaction flask headspace. However, higher  $m/z$  ratio fragmentations were also observed (Figure S5.6).

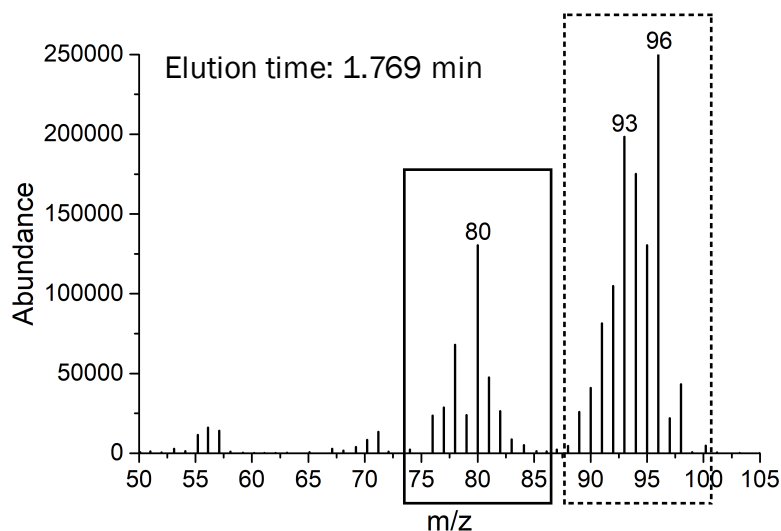


**Figure S5.6.** Mass spectrum of eluted peak at 1.769 min. The solid box indicates fragmentation appropriate for the compound  $H_2Se$ . However, the dashed box indicates fragmentation not associated with the assignment of  $H_2Se$ . This spectrum suggests that  $H_2Se$  was not isolated or may not be identified as  $H_2Se$ .

This could be attributed to the presence of a trace Se isotope with a higher mass or, more likely, that  $H_2Se$  is eluted with heavier species and is difficult to isolate. The distribution of higher  $m/z$  fragments correspond well to that expected for  $(CH_3)SeH$  ( $m/z$ : 95.95, 93.95, 91.95). Without

much context on potential processes in the molecular regime, further identification of monomers by GC-MS was extremely difficult considering the complexities of the total reaction which were inevitably riddled with convolutions in the data. However, what we could glean were differences in the peaks observed and the peak elution times in the mass chromatograms, elucidating that the reaction headspace was compositionally different from that of the control (Figure S5.7).

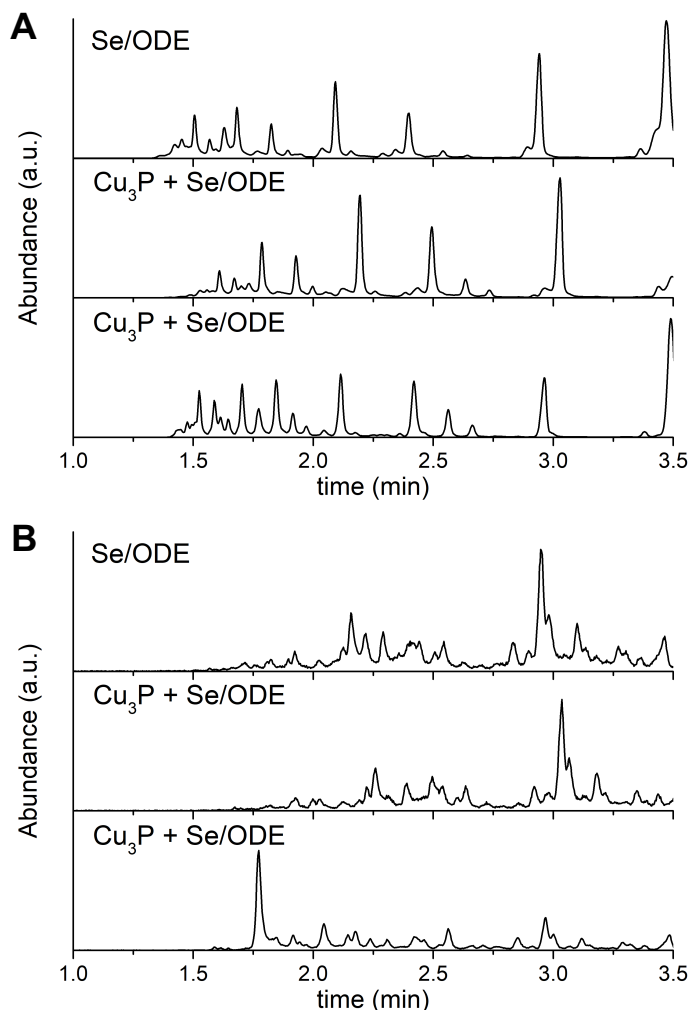


**Figure S5.7.** GC-MS chromatograms of gaseous species sampled with SPME fibers. (A) Raw data and (B) Data filtered/extracted for peaks that contain ion fragment with  $m/z = 81$ , which corresponds to H<sub>2</sub>Se.

Control samples subjected to Cu<sub>3</sub>PSe<sub>4</sub> synthesis conditions were tested to grasp the reactivity of each reactant and ODE (Figure S5.8A). Each peak in the individual chromatograms represents a different species coming off the column. In common, all the chromatograms showed

a majority peak around 12.499 min (Figure S5.8A) representing untransformed ODE (Figure S5.8B). The chromatograms of ODE/Cu<sub>3</sub>P, ODE/Se, and the total reaction but not ODE, additionally eluted a peak around 12.568 min, representing the *cis*-conformation of ODE. A kink somewhere along the carbon backbone gives rise to a slight change in polarity, giving it a close but not overlapping elution off the column as the *trans*-conformation of untransformed ODE.

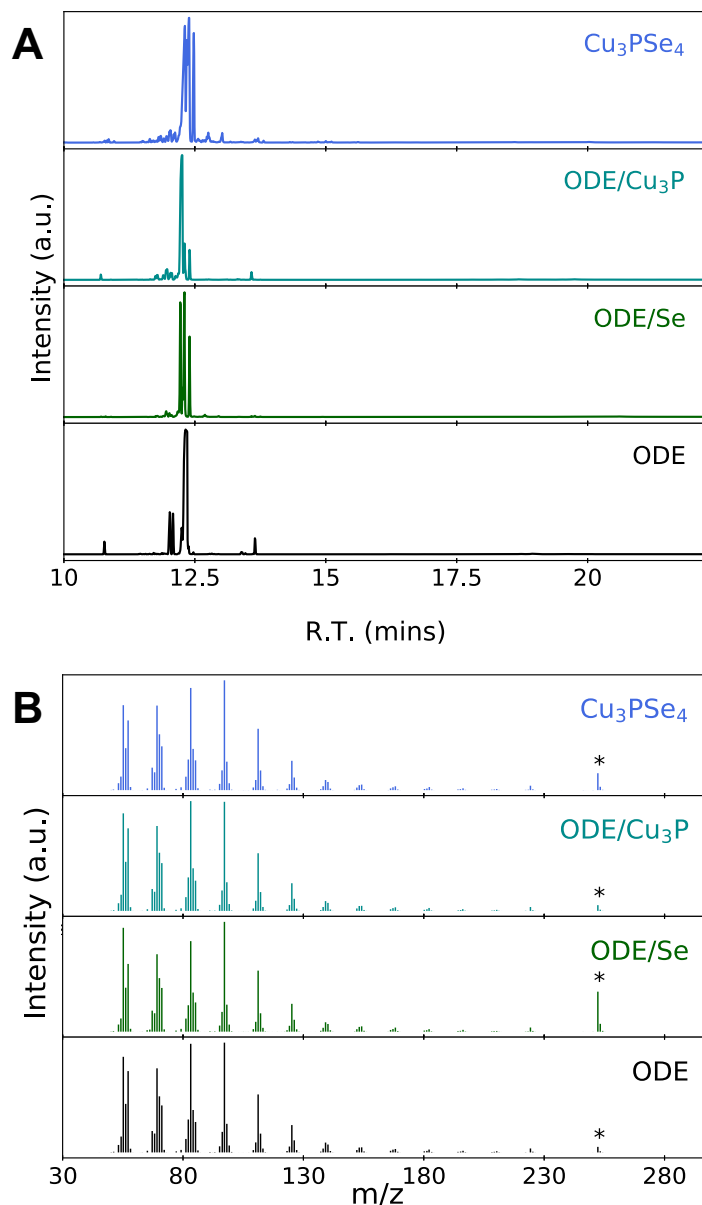


**Figure S5.8.** (A) Chromatograms of the control and total Cu<sub>3</sub>PSe<sub>4</sub> reaction solution collected after reaction completion. (B) Mass spectra of the major peak at 12.5 min which corresponds to ODE due to the molecular ion peak at 252.3 along with the fragmentation pattern that aligns with long chain aliphatic molecules.

Under the same conditions of the  $\text{Cu}_3\text{PSe}_4$  reaction, ODE and ODE/ $\text{Cu}_3\text{P}$  showed very little conversion, aligning with other characterization techniques that demonstrated very little reactivity between the other reagents. The sole presence of untransformed ODE and no presence of higher  $m/z$  fragments in the ODE chromatogram suggests that poly(ODE) is not a significant presence in our reactions although the nature of small sampling could mean that trace amounts were not detected. While the ODE/ $\text{Cu}_3\text{P}$  sample showed some divergence from ODE only, these are likely from labile surface surfactants consistent with  $^1\text{H}$  NMR data. For example, the retention peaks at 10.9, 12.25, and 13.8 mins for both ODE and ODE/ $\text{Cu}_3\text{P}$  controls represent 1-hexadecene, isomerized octadecene, and eicosane, respectively.

Of interest among the controls is ODE/Se. The dissolution of Se in ODE leads to a variety of species, as seen in the ODE/Se mass spectrum from retention time (R.T.) of 20.843 min (Figure S5.9). Of note is the characterization of species *iv* which corresponds to 2ODE+Se or  $\text{Se}(\text{C}_{18}\text{H}_{36})_2$ , confirming its presence as a Se monomer in our reaction solution. Diversity in Se monomers is further identified by overlaying its chromatogram with that of the total reaction (Figure S5.10).

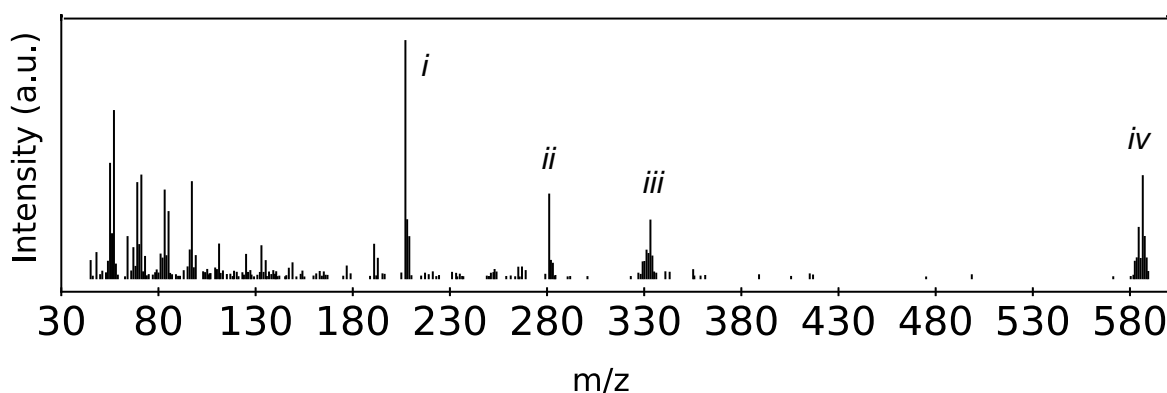


**Figure S5.9.** Mass spectrum of ODE+Se at R.T. = 20.843 min. Species *i* and *ii* are C-based species, noted by their fragmentation patterns and permutation analysis that only allow for C-based possibilities. Species *iii* is a Se monomer with  $m/z$  of 331 which corresponds to ODE+Se. This can be represented by  $\text{HSe}(\text{C}_{18}\text{H}_{36})$ , which can form by the same Se radical mechanism as  $\text{Se}(\text{C}_{18}\text{H}_{36})_2$ , or a selenoxide species in which Se is inserted into a terminal olefin to form an epoxide structure. Species *iv* is 2ODE+Se or  $\text{Se}(\text{C}_{18}\text{H}_{36})_2$  with is the dialkyl selenide species of interest in our studies. This species forms when an isomerized ODE moiety bonds to a Se-R moiety through the 1-carbon by a 2-electron oxidation to generate  $\text{H}_2\text{Se}$ .

Overlay of the chromatograms demonstrates the diversity of speciation in the flask and the contributions of each reagent to the overall reaction (Figure S5.11). Significant changes in solution compared to the other controls support that the interaction of precursors and the solution are essential to form  $\text{Cu}_3\text{PSe}_4$ . However, it does not necessarily reveal their roles to direct the reaction pathway toward  $\text{Cu}_3\text{PSe}_4$ .

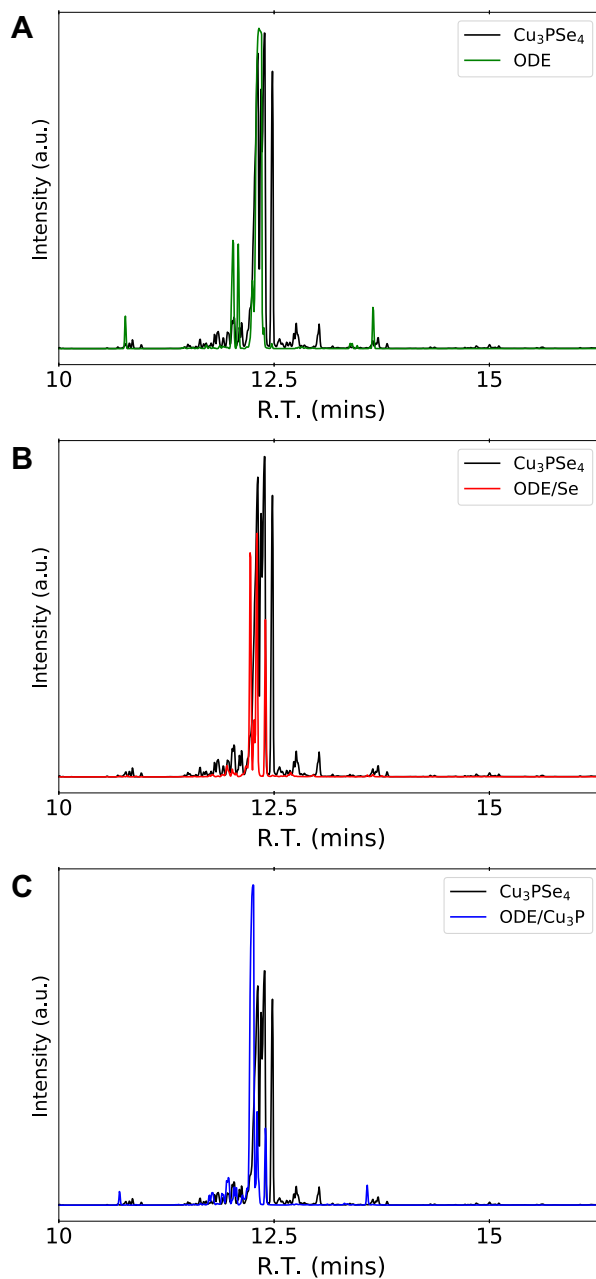


**Figure S5.10.** Overlay of the total reaction chromatogram over the individual control chromatograms: (A) *ODE*, (B) *ODE+Se*, and (C) *ODE+Cu<sub>3</sub>P*.

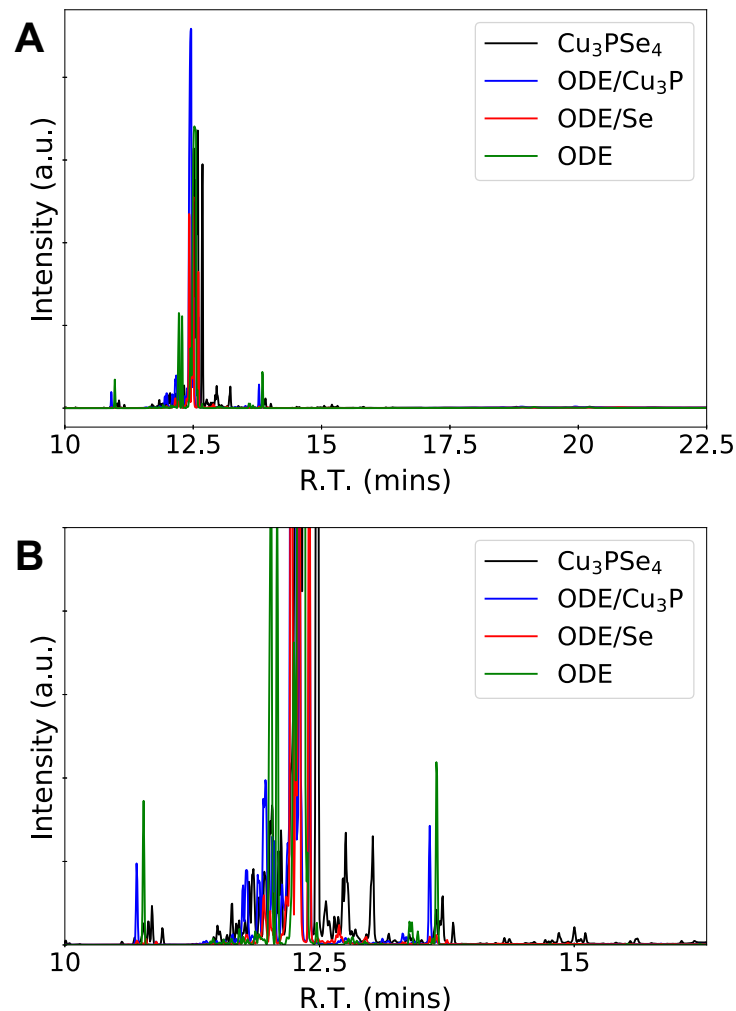


**Figure S5.11.** (A) Overlay of the raw chromatograms for the control and total reaction solutions. (B) Zoomed in chromatograms at 12.5 min retention time to highlight the diversity of Se speciation in the different reaction samples.

Certain limitations were experienced with EI-GC MS due to the limited separation of species in the sample. Implementation of ODE as the solvent leads to a high presence of the 12.498 retention time peak, corresponding to ODE. This drowns the signal and the sensitivity of detection for trace but important participating species, especially high molecular weight species that may remain stuck on the column or low molecular weight species which might elute off the column rapidly beyond detection. Further, the sample volume is significantly small considering the volume and heterogeneity of the reaction solution, which impacts what species are actually characterized. In order to have proper deconvolution and characterization of all species, the column must be

optimized for all species, but this is extremely taxing when we are blind to what species are actually present. This posits GC-MS as a great complementary technique that can confirm the presence of specific species of interest. Despite these limitations, we ultimately confirmed that our data is consistent with other techniques that demonstrate speciation changes.

#### B.4. Investigation of Solvent Role

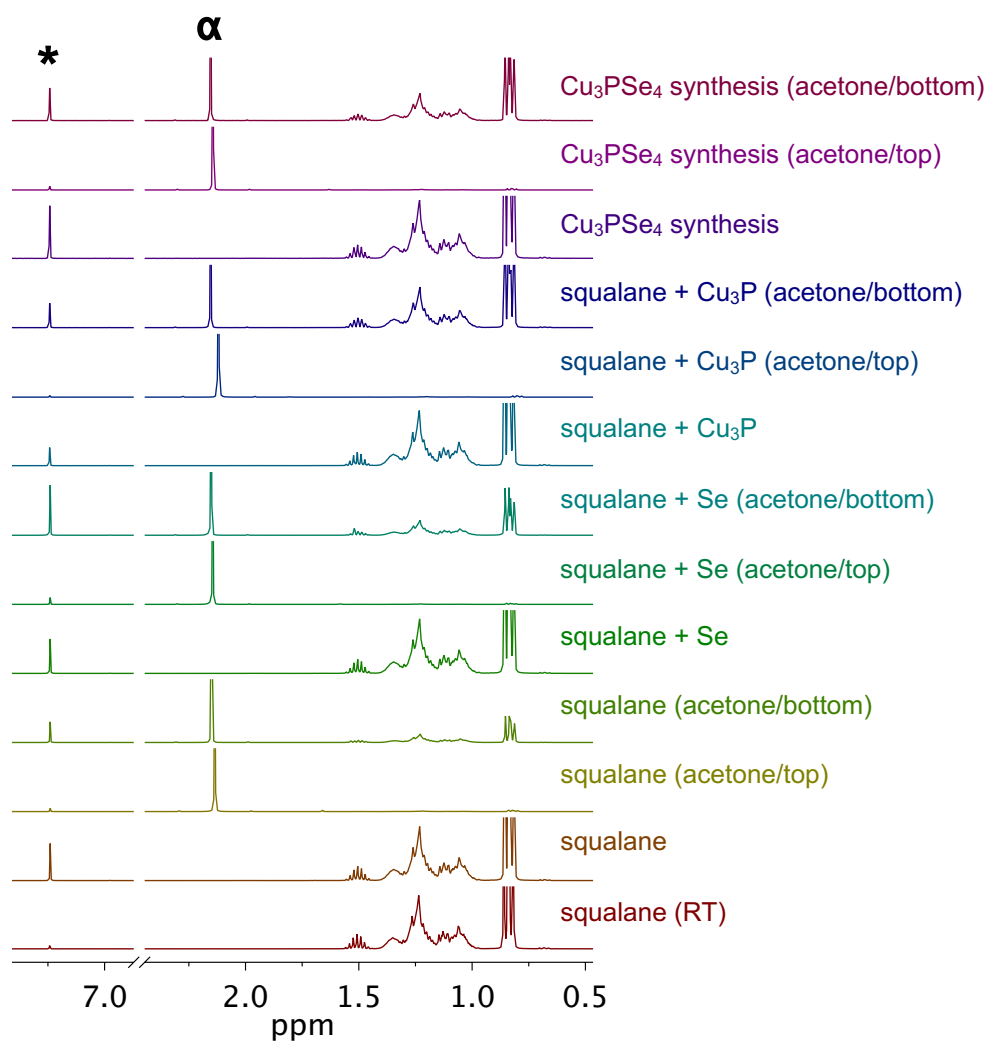


**Figure S5.12.** Squalane control and autopolymerization investigation via <sup>1</sup>H NMR. Similar to the studies with ODE, individual reagents were subjected to the reaction conditions (300 °C for 20 min) to determine if squalane is impacted by the presence of a specific reagent. No transformations were observed. All samples were washed with acetone and centrifuged to observe potential squalane autopolymerization. No species other than the expected acetone and squalane were observed. Asterisk (\*) is the reference peak for CDCl<sub>3</sub> at 7.24 ppm. The peak labelled with alpha (α) is the washing solvent acetone at 2.16 ppm.

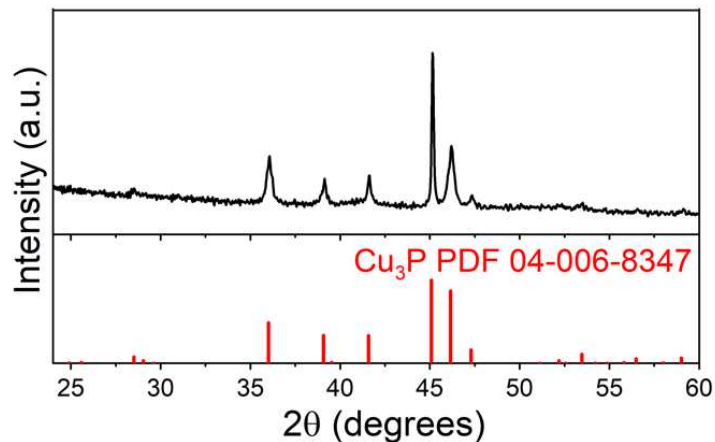


**Figure S5.13.** XRD characterization of the  $\text{Cu}_3\text{P}$  + squalane control product. No transformation in the crystalline identity was observed.

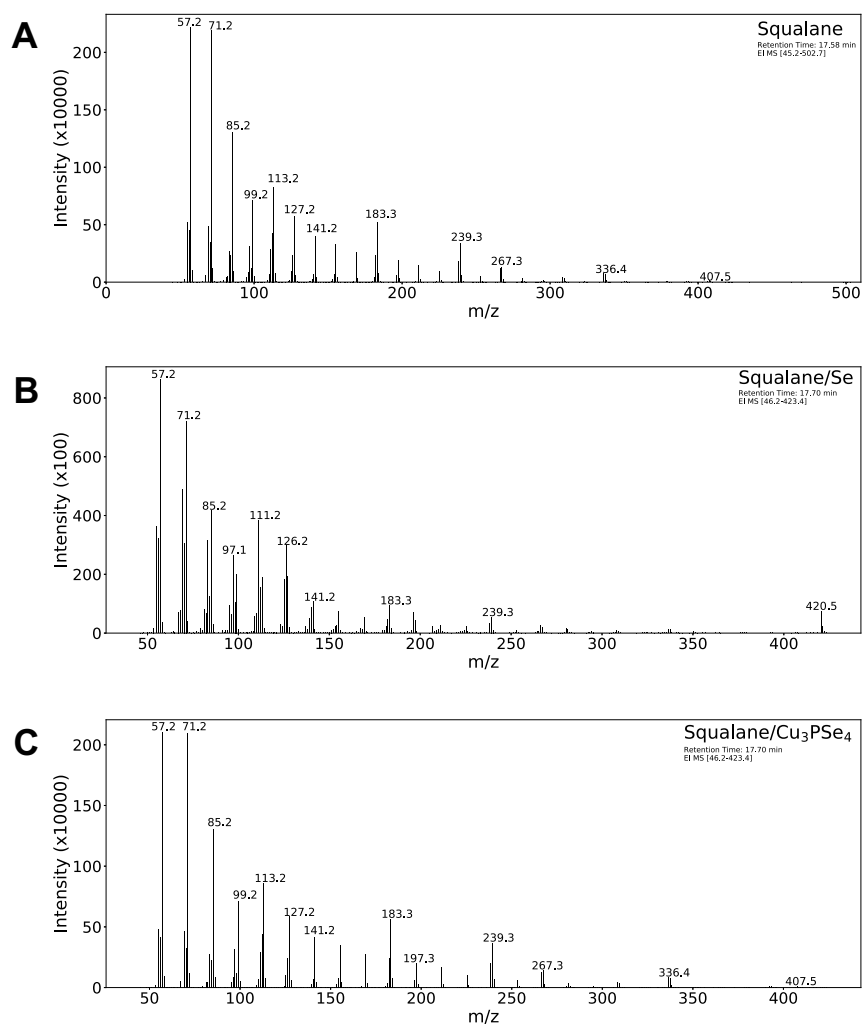


**Figure S5.14.** GC-MS characterization of (A) squalane, (B) Se powder in squalane, and (C) the  $\text{Cu}_3\text{PSe}_4$  synthesis with squalane solutions after subjection to the reaction conditions (300 °C for 20 min) and cooling. No transformations were observed.

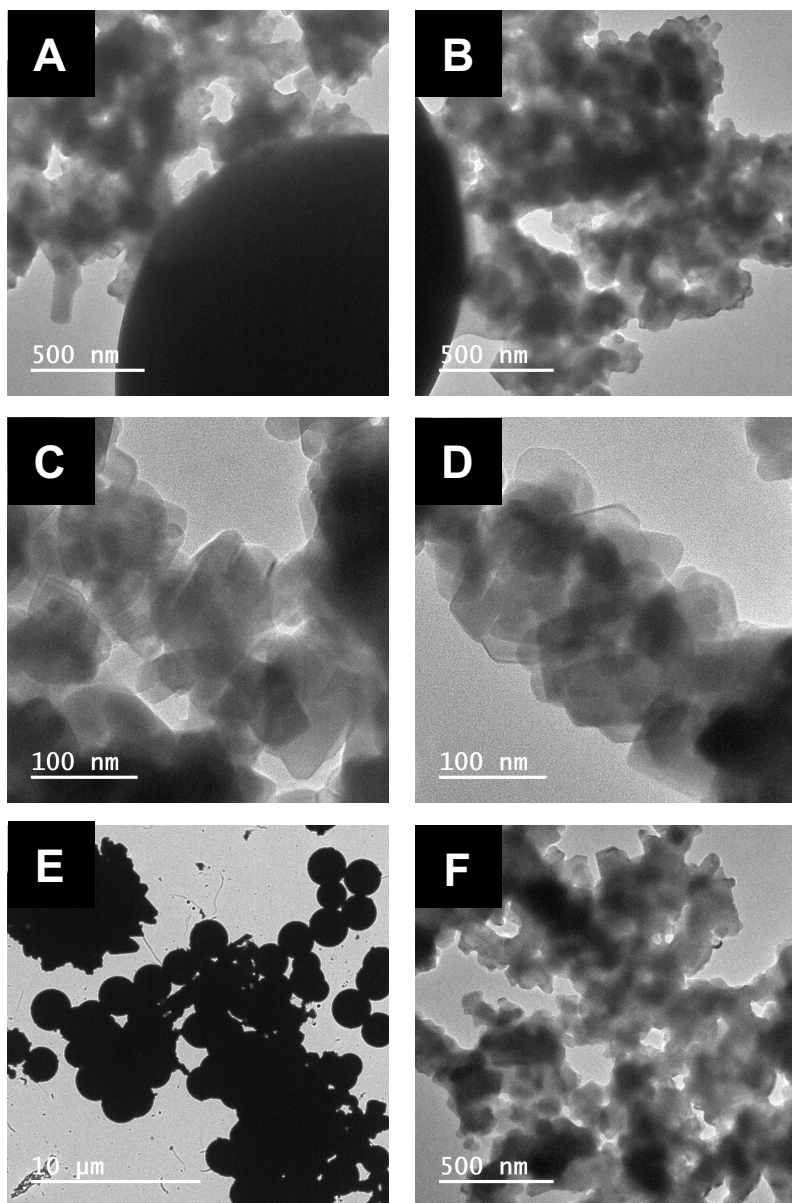


**Figure S5.15.** TEM images of the squalane reaction product.

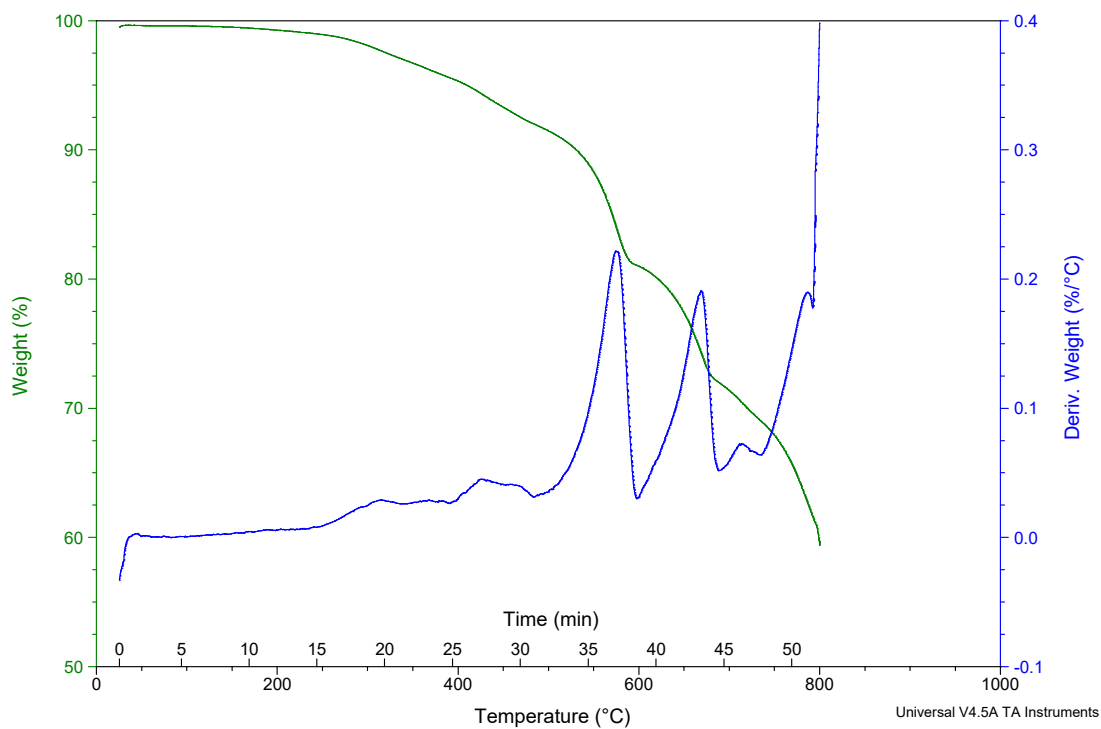


**Figure S5.16.** TGA of Cu<sub>3</sub>PSe<sub>4</sub> NPs which shows decomposition starting at 290 °C.

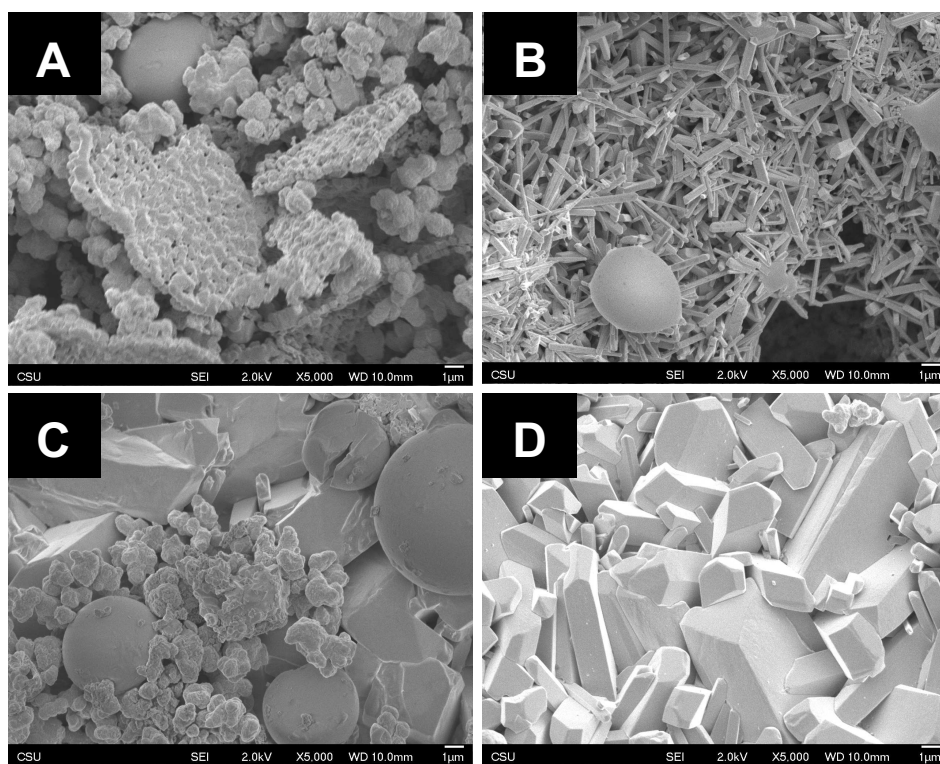


**Figure S5.17.** SEM images of the neat reaction product.

## REFERENCES

- (1) Liu, J.; Meyns, M.; Zhang, T.; Arbiol, J.; Cabot, A.; Shavel, A. Triphenyl Phosphite as the Phosphorus Source for the Scalable and Cost-Effective Production of Transition Metal Phosphides. *Chem. Mater.* **2018**, *30* (5), 1799–1807.
- (2) Dhaene, E.; Billet, J.; Bennett, E.; Van Driessche, I.; De Roo, J. The Trouble with ODE: Polymerization during Nanocrystal Synthesis. *Nano Lett.* **2019**, *19* (10), 7411–7417.
- (3) Henkes, A. E.; Schaak, R. E. Trioctylphosphine: A General Phosphorus Source for the Low-Temperature Conversion of Metals into Metal Phosphides. *Chem. Mater.* **2007**, *19* (17), 4234–4242.
- (4) Bullen, C.; van Embden, J.; Jasieniak, J.; Cosgriff, J. E.; Mulder, R. J.; Rizzardo, E.; Gu, M.; Raston, C. L. High Activity Phosphine-Free Selenium Precursor Solution for Semiconductor Nanocrystal Growth. *Chem. Mater.* **2010**, *22* (14), 4135–4143.
- (5) Chamorro, J. R.; McQueen, T. M. Progress toward Solid State Synthesis by Design. *Acc. Chem. Res.* **2018**, *51* (11), 2918–2925.
- (6) Martinolich, A. J.; Neilson, J. R. Toward Reaction-by-Design: Achieving Kinetic Control of Solid State Chemistry with Metathesis. *Chem. Mater.* **2017**, *29* (2), 479–489.

# APPENDIX C

## DESK MOTIVATION

